Harnessing the Power of Gravitational Lensing: Resolved Star Formation at Redshift 1 - 4

LIVERMORE, RACHAEL,CLAIRE

How to cite:

LIVERMORE, RACHAEL,CLAIRE (2013) *Harnessing the Power of Gravitational Lensing: Resolved Star Formation at Redshift 1 - 4*, Durham theses, Durham University. Available at Durham E-Theses Online: http://etheses.dur.ac.uk/7744/

Harnessing the Power of Gravitational Lensing: Resolved Star Formation at $1 < z < 5$

Rachael Livermore

A Thesis presented for the degree of

Doctor of Philosophy

Extragalactic Astronomy
Department of Physics
University of Durham
UK

June 2013

Dedicated to

Mum

for teaching me that being a grown-up is optional

and John

for making this possible.

Harnessing the Power of Gravitational Lensing: Resolved Star Formation at $1 < z < 5$

Rachael Livermore

Submitted for the degree of Doctor of Philosophy

June 2013

Abstract

In the coming decade, new observational facilities will enable galaxies seen in the first half of the Universe's history ($z > 1$) to be mapped on $\sim 100\,\mathrm{pc}$ scales routinely for the first time. As a preview of the science capabilities of these facilities, we can use clusters of galaxies, the largest gravitationally-bound structures in the Universe, as natural telescopes. Using this technique, we examine star formation within galaxies at $1 < z < 5$, during the peak epoch of cosmic star formation density.

We begin in Chapter 3 by targeting Hα emission with narrowband imaging from *HST*/WFC3 in eight lensed galaxies at $z = 1-1.5$. We identify star-forming clumps in these galaxies and compare their properties directly to those of local spirals.

In Chapter 4 we consider the fuel for star formation, with a search for molecular gas in a $z \sim 5$ lensed galaxy. We obtain a tentative detection that implies a gas fraction $M_{\mathrm{gas}}/\left(M_{\mathrm{gas}} + M_*\right) = 0.59^{+0.11}_{-0.06}$, suggesting slow evolution at $z > 2$.

In Chapter 5, we present the largest survey to date of gravitationally-lensed galaxies observed with integral field spectroscopy. We present observations of 12 new galaxies, increasing the total sample to 17 lensed galaxies at $1 < z < 4$ observed on $100\,\mathrm{pc}$ scales, and investigate the global disc dynamics and map the star formation.

With these combined observations, we present a simple theoretical model in which star formation in galaxy discs is driven by the same physical processes at all redshifts. We find that the scale of collapse depends on the galaxy's gas content and kinematics, and show that our observations are consistent with the necessary evolution in these properties.

Declaration

The work in this thesis is based on research carried out at the Department of Physics, Durham University, UK. No part of this thesis has been submitted elsewhere for any other degree or qualification and it is all my own work unless referenced to the contrary in the text.

In Chapters 1 and 2, figures from other work are presented for comment or illustration. Credit is given in the captions where appropriate.

Portions of this thesis have been published or submitted for publication as follows:

- Chapter 3: Hubble Space Telescope Hα imaging of star-forming galaxies at $z \sim 1 - -1.5$: evolution in the size and luminosity of giant HII regions

  R. C. Livermore, T. Jones, J. Richard, R. G. Bower, R. S. Ellis, A. M. Swinbank, J. R. Rigby, Ian Smail, S. Arribas, J. Rodriguez Zaurin, L. Colina, H. Ebeling and R. A. Crain

  2012 MNRAS 427 688

  T. Jones, R. S. Ellis, J. R. Rigby, S. Arribas, J. Rodriguez Zaurin and L. Colina provided additional data for comparison. J. Richard provided the lens models and assisted with the telescope proposal and data reduction. H. Ebeling provided the targets. R. G. Bower, A. M. Swinbank, Ian Smail and

R. A. Crain commented on the text and assisted with the theoretical interpretation. R. C. Livermore drafted the telescope proposal, performed the data analysis and wrote the text.

- Chapter 4: Observational Limits on the Gas Mass of a $z = 4.9$ Galaxy

  R. C. Livermore, A. M. Swinbank, Ian Smail, R. G. Bower, K. E. K. Coppin, R. A. Crain, A. C. Edge, J. E. Geach and J. Richard

  2012 ApJ 758 L35

  K. E. K. Coppin and A. C. Edge provided technical expertise for the observations and analysis. J. Richard produced the lens model. A. M. Swinbank, Ian Smail, R. G. Bower, R. A. Crain and J. E. Geach commented on the text. R. C. Livermore wrote the proposal, performed the data reduction and analysis and wrote the text.

- Chapter 5: Resolved spectroscopy of gravitationally-lensed galaxies: global dynamics and star-forming clumps on $\sim 100\,\mathrm{pc}$ scales

  R. C. Livermore, T. A. Jones, A. M. Swinbank, J. Richard, R. G. Bower, T.-T. Yuan, A. C. Edge, R. S. Ellis, L. J. Kewley and Ian Smail.

  2013 MNRAS submitted

  T. A. Jones, T.-T. Yuan, R. S. Ellis and L. J. Kewley provided parts of the data. J. Richard produced the lens models. A. M. Swinbank, R. G. Bower, A. C. Edge and Ian Smail offered comments on the text. R. C. Livermore wrote the proposals, prepared the observations, performed the data reduction and analysis and wrote the text.

The author has also contributed to or been involved in the following work:

- High-resolution Study of the Cluster Complexes in a Lensed Spiral at Redshift 1.5: Constraints on the Bulge Formation and Disk Evolution
  A. Adamo, G. Östlin, N. Bastian, E. Zackrisson, **R. C. Livermore**, L. Guaita
  2013 ApJ 766 105

- Metallicity Gradient of a Lensed Face-on Spiral Galaxy at Redshift 1.49
  T.-T. Yuan, L. J. Kewley, A. M. Swinbank, J. Richard, **R. C. Livermore**
  2011 ApJ 732 14

- The emission line properties of gravitationally lensed $1.5 < z < 5$ galaxies
  J. Richard, T. A. Jones, R. S. Ellis, D. P. Stark, **R. C. Livermore**, A. M. Swinbank
  2011 MNRAS 413 643

Acknowledgements

If it takes a village to raise a child, then there must be at least a hamlet responsible for a thesis.

I must begin by thanking Kristine Larsen, who cannot have had any idea that a random conversation with a geeky accountant in a convention bar would change said accountant's life so drastically. She most likely has no memory of me, but this was my inspiration not only to go back to school, but also to get involved in outreach in the hope that I will one day pay the favour forward.

And to my mother, whose response to my flying out to see her on a whim and declaring, out of the blue, that I'd had enough of being an accountant and wanted to have a go at this physics thing, my thanks for being encouraging despite not understanding my interest in science. Sincere thanks also to John, without whom it would literally not have been possible.

Thanks also to Leon Baruah back in Sussex, for that fatal coin-toss when I failed at making up my mind where I wanted to go for my PhD. If nothing else, that gave me someone else to blame when the northern winters got to be too much!

It has been a privilege to work with Richard Bower for the past four years. My thanks for being so memorable in that whirlwind interview (first impressions are sometimes right!), for giving me the opportunity to come to Durham, and for

encouraging me to do so despite my misgivings about the climate (although, four apocalyptic winters later, I feel I was somewhat falsely reassured in that regard). Richard's boundless enthusiasm is inspiring, and his patience in dealing with such a headstrong student is admirable.

I have benefited enormously from the open, helpful culture at Durham. Among those who have provided valuable advice and direct assistance along the way are Ian Smail, Mark Swinbank, Alastair Edge, Julie Wardlow, John Stott and, last but by no means least, Johan Richard for being my on-call LENSTOOL support desk.

There is also a substantial group of people who have made Durham worth living in despite the winters (and, frankly, the so-called "summers"). Thanks especially to Lynne, the real head of the Physics department, for keeping us all caffeinated. Thanks also to Sarah Hutton and Alice Danielson for all the outreach hijinks, to Danny Farrow and Mark Lovell for the regular escorts to coffee, and to Ben Lowing for indulging my theatre habit.

Away from Durham, my (dubious) sanity has been maintained for the last four years by too many people to name. In particular, thanks to Anna Damski and Fiona Scarlett, both of whom have not only provided London retreats but have also whisked me off to sunnier climes when needed. And also on the 'whisking' front, thanks to Heidi Tandy for insisting I spend Christmas in Florida during one of those especially harsh winters. Whether my obsession with the weather will continue once I am at more hospitable latitudes remains to be seen.

And thanks go above all to the Universe, for having the decency to be so endlessly fascinating.

Contents

3 Hubble Space Telescope Hα imaging of star-forming galaxies at $z \simeq 1 - 1.5$ 63

List of Figures

List of Tables

Chapter 1

The History of Astronomy

1.1 Overview

The work in this thesis is concerned with the extragalactic Universe; that is, that which lies beyond the reaches of the Milky Way galaxy. Extragalactic astronomy has existed as a science for fewer than a hundred years, but required the accumulation of thousands of years of observations, improvements in technology, and theoretical modelling to reach its present stage.

The history of how our current model of the Universe developed has formed a critical part of the author's outreach work, with the aim of communicating to the public how scientific ideas develop. In this chapter, we give a summary of the work of the many giants on whose shoulders we must stand if we are to study the most distant reaches of the cosmos.

1.2 Modelling the Solar System

The first known model of the Solar System that resembles our own, with the Sun at the centre and the Earth and other planets orbiting around it (known as a 'heliocentric' model), is that of Aristarchus of Samos (310 - 230 BCE) published in his *On the Sizes and Distances*. In this work, Aristarchus used geometrical arguments based on solar and lunar eclipses to derive the sizes and distances of the Sun and Moon in terms of Earth radii. Limitations in the accuracy of observations led to the distances being underestimated (the distance to the Sun was calculated to be $\sim 380\,R_\oplus$, where $R_\oplus$ is the radius of the Earth, compared to the modern value of $23,500\,R_\oplus$); nonetheless, this was one of the first applications of geometry to derive physical properties and the earliest known attempt to derive a physical scale for the cosmos.

Although the heliocentric nature of Aristarchus' model is often assumed to have been novel and controversial, it is likely that the concept pre-dated him and he was merely its most prominent proponent. Christianidis et al. (2002) argue that geocentric and heliocentric universes were equally valid from a mathematical standpoint as a means of describing astronomical phenomena, and it was not until later that physical and philosophical considerations became a concern.

The 'Universe,' in the model of Aristarchus, was supposed to be the volume contained within the sphere that carried the 'fixed stars.' To be consistent with the assumption of heliocentrism, this sphere had to be located at a sufficiently large distance that no apparent movement would be observed as the Earth orbited the Sun (known as 'parallax'); in fact, Aristarchus declared it to be infinite. The first attempt to estimate a finite physical scale for the volume of the Universe as a whole was by Archimedes in his work *The Sand Reckoner*, written some time before 216 BCE. The aim of this work was to set out a system of numerical notation that could express arbitrarily large numbers, and this was demonstrated through an argument that attempted to calculate the number of grains of sand that could fit into the Universe. This calculation relied on the assumption that the ratio of the diameter of the sphere of fixed stars to the size of the Earth-Sun orbit was equal to the ratio of the Earth-Sun orbit to the diameter of the Earth. He then derived a diameter for the sphere of fixed stars of 10^{14} stadia; in modern units, this equates to $\sim 2 \times 10^{13}$ km, or $\sim 120,000$ Astronomical Units.

The measurement of distances improved in accuracy with the work of Hipparchus of Nicaea (c. 190 - 120 BCE), who created the first star catalogue. He also expanded on the work of Aristarchus to derive the distance to the Moon using a solar eclipse. Using an eclipse that was total in Syene and partial in Alexandria, and assuming that the parallax of the Sun was negligible in comparison to that of the much closer Moon, he was able to derive an Earth-Moon distance remarkably consistent with modern values. The distance to the Sun is more difficult to calculate, as with the naked eye it has no observable parallax. The original work has not survived, but Toomer (1974) suggests that Hipparchus assumed an upper limit of 7' for the parallax of the Sun to derive a lower limit on its distance of $490R_{\oplus}$.

Two centuries later, Ptolemy used another method for determining the lunar parallax. As an observer at a fixed position on the Earth's surface rotates around its centre (or equivalently in a geostationary model, the Moon and fixed stars rotate around the Earth), the apparent position of the Moon changes with respect to the fixed stars. As the Moon is the closest body to the Earth, its parallax is large - $\sim 1^\circ$ - and so was measurable without a telescope. The resulting distance to the Moon was 33 - 64 Earth radii, $R_\oplus$ (compared to the modern mean value of $60\,R_\oplus$). The distance to the Sun was derived geometrically using a combination of solar and lunar eclipses, and at $1,160 - 1,260\,R_\oplus$ was again a vast underestimate (Carman, 2009).

Ptolemy, like Hipparchus before him, favoured a geostatic, geostationary Universe in which the Earth is embedded in a series of concentric spheres carrying the Moon, Sun and other planets in circular orbits. In common with the preceding models, the outer edge of the Ptolemaic Universe was a fixed sphere upon whose surface were embedded the stars. Ptolemy firmly rejected the notion of a heliocentric Universe:

> "Certain people, [propounding] what they consider a more persuasive view... supposed the heavens to remain motionless, and the Earth to revolve from west to east about the same axis [as the heavens]... However, they do not realise that, although there is perhaps nothing in the celestial phenomena that would count against that hypothesis, at least from simpler considerations, nevertheless from what would occur here on Earth and in the air, one can see that such a notion is quite ridiculous."
> (as quoted by Toomer, G. J., 1998)

A portion of the objection to heliocentrism was that it contradicted religious doctrine; Plutarch relates in his *On the face which appears in the orb of the Moon* that "Cleanthes used to think that the Greeks should have had served [the writ of heresy] upon Aristarchus of Samos, for shifting the hearth of the Universe" (as quoted by Prickard, 1911). Nonetheless, the overriding objection of astronomers such as Hipparchus and Ptolemy to the notion of a heliocentric Universe was scientific. Heliocentrism required by definition that the Earth be subject to two rapid rotations; one about its axis and another around the Sun. It seemed unthinkable that these movements would not be physically apparent. Furthermore, the lack of observable parallax in the fixed stars even when observed at six monthly intervals (i.e. when the Earth has moved its maximum distance around the Sun, known as 'annual parallax') implied that the stars were unreasonably distant, even based on the underestimate of the Earth-Sun distance.

Thus, the adoption of a geocentric Universe made sense scientifically at the time. Indeed, we shall see that scientists throughout history have struggled with the enormity of the Universe, and that the error of rejecting a hypothesis on the grounds that it rendered the Universe unreasonably large would continue to be repeated by astronomers almost two millennia later.

The overwhelming success of the Ptolemaic model, published in the *Almagest* in the second century AD, was that it was able to accurately predict the future positions of the planets. To do this, he had the Sun orbit the Earth in a circle almost (but not precisely) centred on the Earth, while the motion of the planets was a combination of a large eccentric circle called a 'deferent' and a smaller circle, called an 'epicycle,' whose centre moves along the deferent. The Ptolemaic model was remarkably successful, predicting the future positions of the planets to within an accuracy of 8', perfectly sufficient for naked-eye observations (Fitzpatrick, 2010).

Ptolemy even attempted the first calculation of the distances to the planets, in his *Planetary Hypotheses*. The basis of his argument was that the planetary spheres nest inside one another with no gaps in between them, "for it is not conceivable that there be in Nature a vacuum, or any meaningless and useless thing" (translation by Goldstein, 1967). With the derived distances to the Moon and Sun - and assuming that only Mercury and Venus lay closer than the Sun - he used the ratios of the minimum and maximum distances of each planet to construct a series of nested spheres such that the maximum distance of one body was equal to the minimum distance of the next one. This resulted in a distance to the fixed sphere of stars of $20,000\,R_\oplus$; we now know this to be less than the distance to the Sun.

Although much derided by modern astronomers for its supposed complexity, Ptolemy's *Almagest* remained the definitive work on astronomy for around 1,500 years, making it arguably the most successful cosmological model in history.

One of the biggest problems with the Ptolemaic model was the orbits of Venus and Mercury. It was known from Euclid's work on geometry, *Optics*, that the further away a planet was, the longer it would take to complete one period, under the assumption that all of the planetary spheres rotated at the same speed. This was the basis for the order of the planets chosen by Ptolemy, but it caused a problem for Mercury and Venus, both of which appeared to have periods of one year. Ptolemy's reason for placing them closer than the Sun was purely to fill in the large gap between the maximum distance of the Moon and the least distance of the Sun, under the nested spheres principle. In the fifth century AD, Martianus Capella noted that Mercury and Venus remain within 22° and 46° of the Sun respectively, and thus suggested that they in fact orbited the Sun (Eastwood, 2001). This model of the Universe remained geocentric, but the Earth was no longer the only centre of rotation; Mercury and Venus orbited the Sun, which in turn carried them about the Earth. The three known supra-solar planets - Mars, Jupiter and Saturn - retained the Earth as their centre of motion.

The problem of the orbits of Mercury and Venus led Copernicus (1473-1543) to take this notion a step further. He found that the only way to order the planets such that they obeyed a distance-period relation was to return to a heliocentric model (Goldstein, 2002). Copernicus is believed to have first presented his heliocentric model before 1514, in his *Commentariolus*. However, knowing his theory would be controversial, he delayed publication of his full work, *De revolutionibus orbium coelestium (On the Revolutions of the Heavenly Spheres)* until his death in 1543.

There is evidence that *De revolutionibus* was widely read by contemporary astronomers (Gingerich, 2004), but it was not immediately accepted by the scientific community. Besides the solution to the distance-period problem, the Copernican model offered only one notable improvement over geocentrism: by this time, the Ptolemaic model had been modified to introduce non-uniform motion in the form of 'equants,' which Copernicus was able to eliminate. Otherwise, it was not obvious that heliocentrism offered an improvement over the the geocentric model of Ptolemy: Copernicus still required epicycles (called 'epicyclets' to distinguish them from Ptolemaic epicycles) in order to maintain his principle that all motion should be uniform and circular, and he was not able to predict the motions of planets any more accurately than the Ptolemaic system.

Nonetheless, the Danish astronomer Tycho Brahe (1546 - 1601) admired Copernicus, hailing him a "second Ptolemy," and praising his elimination of the equant (Blair, 1990). However, he objected to the Earth's motion in the Copernican model on two points: firstly, that the Earth should move and yet its motion be undetectable, and secondly that its motion should not cause any measurable parallax in the fixed stars. The brightest stars were observed to have diameters of up to 3', and this was not understood at the time to be an effect of atmospheric distortion. For an object with such a large observed size to be sufficiently distant that no parallax was observable would require that its intrinsic size be greater than the size of the Earth-Sun orbit. This was considered unphysical. As a secondary objection to the implications of the Earth's movement, he raised the "unquestionable authority of the holy scriptures" (Blair, 1990), which held the Earth to be stationary.

Tycho Brahe was deeply critical of Copernicus' skills as an observer, and embarked upon an ambitious new project to 'restore' astronomy by obtaining new, more accurate measurements and fitting to them a hypothesis of his own devising. He was granted by King Frederick II of Denmark the island Hven in Oresund and funding for a new observatory, where he made new, more accurate measurements of almost all the observable celestial bodies.

His new model was published as *De mundi aetherei recentioribus phaenomenis liber secundis* in 1588. It was a geo-heliocentric model, essentially an expansion of the theory of Capella, in which the stationary Earth was orbited by the Moon and the Sun, and the five planets (Mercury, Venus, Mars, Jupiter and Saturn) orbited the Sun. In this way, the Tychonic model was mathematically equivalent to the Copernican model, with the exception that it eliminated the perceived problems introduced by the movement of the Earth (see Graney (2012) for a complete analysis of the weight of evidence in favour of the Tychonic model).

The real revolution in favour of a heliocentric model was brought about by Johannes Kepler (1571 - 1630). The difference in Kepler's approach was that he sought a *physical* explanation for the motion of the celestial bodies (Stephenson, 1987). He disliked the notion of epicycles on the basis that they had no centre to their motion; thus, even decades before Newton's theory of gravity, Kepler knew that there had to be some body providing the force which drove the motions of the celestial bodies (Kokowski, 2006). On this basis, he sought a modification to the Copernican hypothesis that would place the Sun at the centre of the planets' motion (the Sun itself was slightly offset from the centre of the Copernican model, a result of requiring that the orbits were perfect circles). He needed an accurate measurement of the eccentricity of the orbit of Mars, and so went to work with Tycho Brahe, who had the most sophisticated equipment available. In his *Astronomia Nova (New Astronomy; 1609)*, Kepler says:

> "God's goodness has granted us such a diligent observer in Tycho Brahe that his observations convicted the Ptolemaic calculation of an error of 8' of arc. It is therefore right that we should with a grateful mind make use of this gift to find the true celestial motions."

With the benefit of Brahe's observations, Kepler was able to determine that the force governing the motion of the planets fell in proportion to the square of the distance. With detailed examination of the orbit of Mars, he determined that the orbits were not circular, but rather elliptical in nature (Gingerich, 1972). This modification to the Copernican model finally produced a heliocentric model which was more accurate than the geocentric model.

Kepler is now best remembered for his three laws of planetary motion:

1. The orbit of every planet is an ellipse with the Sun at one of the two foci.
2. A line joining a planet and the Sun sweeps out equal areas during equal intervals of time.
3. The square of the orbital period of a planet is proportional to the cube of the semi-major axis of its orbit.

The first two of these laws were published in the *Astronomia Nova*; the third was added in 1619 in *Harmonicus Mundi (Harmony of the World).* These three laws follow naturally from Newton's law of universal gravitation, which would be published in 1687, with the assumption that the planets' masses are negligible compared to the mass of the Sun. It is remarkable that Kepler arrived at such precise descriptions of planetary motion without knowledge of universal gravitation, and he has accordingly been referred to as "the first astrophysicist" (Gingerich, 1972).

Until the sixteenth century, astronomy had been concerned solely with the Solar System. One thing all of the models of the Universe had in common was that the stars were fixed at a single distance upon one sphere, and the Aristotelian view was that they were eternal and immutable. This view was challenged in 1572 when a new star appeared in the constellation of Cassiopeia. Tycho Brahe attempted to measure the movement of this new star - now known to have been a supernova, known as Tycho's Supernova or SN 1572 - but was unable to determine any motion with respect to the background stars. This meant the nova had to lie beyond the planetary spheres, and thus the heavens could not be immutable (Gingerich, 2005).

The same supernova was observed in England by Thomas Digges, a Member of Parliament. At the time, no one knew what the supernova was, and it was referred to only as 'the Phenomenon.' Digges, who like Brahe attempted without success to measure its parallax, was convinced that it was "a new starre in the eyghte sphere" (the fixed sphere of stars; Pumfrey, 2011).

Digges favoured the Copernican model, but took it one step further. Since the rotation of the Earth no longer required the stars to maintain a rapid twenty-four hour period of rotation, there was no longer any reason to suppose that they were positioned on a fixed sphere. He published *A Perfit Description of the Caelestiall Orbes according to the most aunciente doctrine of the Pythagoreans, latelye revived by Copernicus and by Geometricall Demonstrations approved* in 1576, the first translation of Copernicus' work into English, and added to it his own modification in which the stars extended outwards to infinity (see Figure 1.1).

Digges was the son of mathematician Leonard Digges, who is believed to have invented the first reflecting telescope (Ronan, 1991). It has been suggested that it was his observations with telescopes, revealing faint stars that were invisible to the naked eye, that may have convinced him that the stars were scattered to infinity (Sawyer Hogg, 1952). In *A Perfit Description of the Caelestiall Orbes*, he wrote:

> "...that fixed Orbe garnished with lightes innumerable and reachinge vp

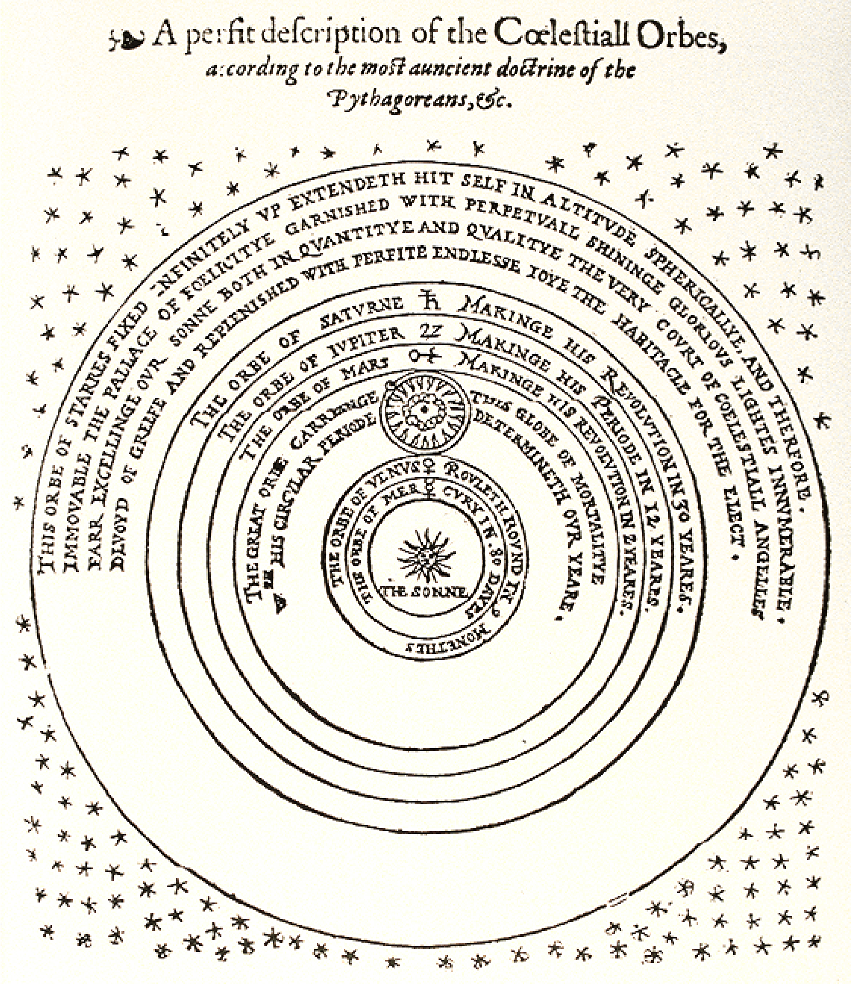

Figure 1.1. The Universe according to Thomas Digges, reproduced from his *A Perfit Description of the Caelestiall Orbes according to the most aunciente doctrine of the Pythagoreans, latelye revived by Copernicus and by Geometricall Demonstrations approved*, published in 1576. Digges modified the Copernican model so that instead of lying on a fixed sphere, the stars extended to infinity.

> in Sphcericall altitude without ende. Of whiche lightes Celestiall it is to bee thoughte that we onely behoulde such as are in the inferioure partes of the same Orbe, and as they are hygher, so seeme they of lesse and lesser quantity, euen tyll our sighte beinge not able farder to reache or conceyue, the greatest part rest by reason of their wonderfull distance inuisible vnto vs." (as quoted by Johnson et al., 1934)

Digges therefore not only posited an infinite Universe for the first time, but foresaw the wealth of discoveries that would be made in the age of the telescope.

1.3 The stars

One thing that all of the competing cosmological models of the sixteenth century had in common was that the stars - whether finite or otherwise - were fundamentally different from anything in the Solar System. This notion was challenged by Giodarno Bruno (1548 - 1600), who suggested for the first time an infinite and homogeneous Universe in which the stars were distant Suns, each orbited by their own system of planets and comets. It follows that in an infinite Universe, there can be no centre and no absolute position (Boulting, 1972).

Bruno was burned at the stake for heresy in 1600, but his work was communicated to Johannes Kepler by Imperial Counsellor Wackher von Wackenfels (Granada, 2008). In *De stella nova*, Kepler's work on the 1604 supernova, he dismisses Bruno's conclusion as "madness." Nonetheless, the discovery by Galileo of four moons orbiting Jupiter in 1610 initially caused Kepler some alarm, for, as he wrote in his reply to Galileo's announcement (translation from Rosen, 1965):

> "if four planets have hitherto been concealed up there, what stops us from believing that countless others will be hereafter discovered in the same region, now that this start has been made? Therefore, either this world is itself infinite, ...or...there is an infinite number of other worlds (or earths, as Bruno puts it) similar to ours."

It transpired that the discoveries of Galileo did not confirm Bruno's theory, for they orbited a planet rather than a star. Relieved, Kepler wrote:

> "I rejoice that I am to some extent restored to life by your work... by reporting that these four planets revolve, not around one of the fixed stars, but around the planet Jupiter, you have for the present freed me from the great fear that gripped me as soon as I heard about your book from my opponent's triumphal shout." (*ibid.*)

Thus, Bruno's hypothesis remained in need of confirmation:

> "In the first place, suppose that each and every fixed star is a sun. No moons have yet been seen revolving around them. Hence this will remain an open question until this phenomenon too is detected by someone equipped for marvellous refined observations." (*ibid.*)

Such "marvellous refined observations" have in fact only become possible in recent decades, and so Kepler remained unconvinced of Bruno's view of the Universe. Bruno did have his supporters, though; most notably, Christiaan Huygens (Granada, 2008) and Isaac Newton, who in an incomplete and unpublished paper *On the Sun and Fixt Starrs* wrote:

> “The Universe consists of three sorts of great bodies, Fixed Stars, Planets, and Comets... The fixt Stars are very great round bodies shining strongly with their own heat and scattered at very great distances from one another throughout the whole heavens... Our Sun is one of ye fixt Stars and every fixt Star is a Sun in its proper region. For could we be removed as far from ye Sun as we are from ye fixt stars, the Sun by reason of its great distance would appear like one of ye fixt stars. And could we approach as neare to any of ye fixt Stars as we are to ye Sun, that Star by reason of its nearness would appear like our Sun... For ye milky way being viewed through a good Telescope appears very full of very small fixt stars and is nothing else then ye confused light of these stars. And so ye fixt clouds and cloudy stars are nothing else then heaps of stars so small and close together that without a Telescope they are not seen apart, but appear blended together like a cloud” (as quoted by Hall & Hall, 1978).

The nature of the Milky Way as the combined light of many distant stars may have been settled, but as telescope technology improved over the next century, a new class of nebulous object began to cause controversy.

1.4 Measuring the Universe

The existence of nebulae had been known for centuries: the Persian astronomer Abd al-Rahman al-Sufi noted the "little cloud" that became known as Andromeda as early as 964 AD (Jones, 1991).

In 1750, Thomas Wright of Durham published *An Original Theory or New Hypothesis of the Universe*, in which he postulated that there may exist many stellar systems like the Milky Way. This idea was, he noted, "made evident by the many cloudy spots, just perceivable by us, as far without starry regions in which through visibly luminous spaces, no one star or particular constituent can possibly be distinguished; those in all likelihood may be external Creations, bordering upon the known one, too remote for us to reach" (as quoted by Gushee, 1941).

As Wright was an amateur astronomer, his work received little attention from contemporary scientists. However, it did come to the attention of the German philosopher Immanuel Kant, who has been credited as the originator of the "island universe" theory of the nebulae (Kant, 1755).

The most well-known catalogue of nebulae was compiled by Messier (1781) as a by-product of his search for comets, but the first dedicated catalogue, consisting of a thousand nebulous objects, was compiled by Herschel (1786).

Another idea with which Wright has been credited is that the Milky Way consists of a flat disc of stars. Gushee (1941) disagrees with this reading of Wright's original text, but this meaning was clearly inferred by Kant (1755), who attributed the origin of the idea to him, and took it further to suggest that the flattening was due to rotation.

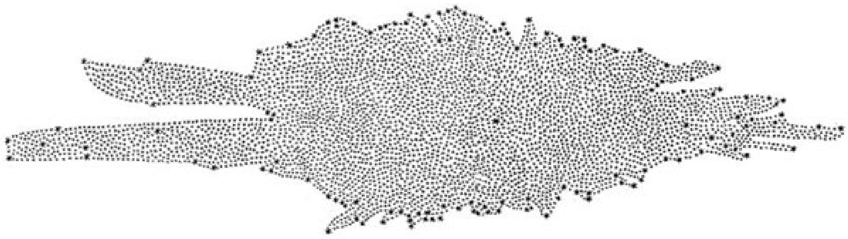

Figure 1.2. Herschel's diagram of the Milky Way, illustrating its disc-like structure, from Herschel (1785)

Observational confirmation of this theory came from William Herschel (1738-1822) and his sister Caroline (1750-1848), who used reflecting telescopes instead of the traditional refracting lenses. These were easier to manufacture in larger sizes and thus could collect more light, allowing the study of fainter objects. One of Herschel's projects was to measure the positions and distances of stars. They did this using the assumption that all stars are of equal intrinsic brightness, and therefore that their different magnitudes are due to their varying distances. Although we now know this assumption to be incorrect, it was sufficiently accurate on average for Herschel to determine that the Milky Way consists of a disc of stars, as illustrated in Figure 1.2.

Another of Herschel's major projects was the nature of the nebulae, defined then as any extended object. He initially believed that all nebulae consisted of unresolved stars, similar to the Milky Way, even remarking that "an extended nebular... cannot be otherwise than of a wonderful magnitude, and may well outvie our milky-way in grandeur" (Herschel, 1785).

Yet, as he studied the nebulae further, Herschel eventually came to change his mind. Herschel (1791) puts forward two theories regarding the nature of the nebulae: either they were collections of stars at a vast distance, or they were a single star embedded in "a shining fluid, of a nature totally unknown to us." He concluded:

> "I can adopt no other sentiment than the latter, since the probability is certainly not for the existence of so enormous a body as would be required to shine like a star of the 8th magnitude, at a distance sufficiently great to cause a vast system of stars to put on the appearance of a very diluted, milky nebulosity."

Thus, it was once again unwillingness to conceive of an unreasonably vast Universe that informed scientific theory.

Another suggestion for the nature of the nebulae was put forward by Pierre-Simon Laplace, who thought they supported his nebular hypothesis for the formation of the Solar System. Laplace believed that the central bright regions of the nebulae were stars, around which a cloud of gas was forming into an infant solar system (Nichol, 1846).

The study of the nebulae was transformed again when an even larger telescope than those of Hershel was built by William Parsons, Third Earl of Rosse, in the 1840s. The 'Leviathan of Parsonstown' was a reflecting telescope with a 1.8m aperture, and it enabled Lord Rosse to study the nebulae with unprecedented sensitivity and resolution. An indication of the achievement of Rosse's telescope can be seen from the comparison in Figure 1.3 of his first drawing of M51, made in 1845, with a modern image from the *Hubble Space Telescope* in 2005.

Lord Rosse's observations of M51 revealed for the first time that it had a spiral structure. The observations were eloquently described by Nichol (1846):

> "...although in one sense nothing can be more memorable than the conversion of these dim streaks of light into burning and rolling orbs, even

Figure 1.3. *Upper:* Lord Rosse's first drawing of M51, made in 1845. *Lower:* The view of M51 from the *Hubble Space Telescope* in 2005 (Credit: NASA). The similarity between the two demonstrates the unprecedented resolving power of Lord Rosse's Leviathan telescope.

> a feat so grand and triumphant, in regard of the science and art of Man, has an attraction infinitely less than the transforming of a shape apparently simple, into one so strange and complex that there is nothing to which we can liken it, save a scroll gradually unwinding, or the evolutions of a gigantic shell! How passing marvellous is this Universe! And unquestionably that form would seen stranger still, if, rising farther above the imperfections of human knowledge, we could see it as it really is – if, plunging into its bosom and penetrating to its farther boundaries, we could develop the structure of its still obscure nebulosities, which doubtless are streams and masses of gorgeous related Stars!"

Nichol, who said of himself that "for his sagacity any more than for his daring, no speculation was too high" even goes on to suggest that these galaxies could be subject to some evolution:

> "bearing them onward from the condition of collections of stars comparatively sparse, to ripened spheres whose centres approach towards an uninterrupted blaze of light. The elevation to which this idea leads us is, indeed, far aloft from the usual haunts of human thought: and yet why not the empire of Mutability, even over those dread Infinitudes, as well as among the mere shows and transiencies of Earth?"

Thus, though the idea seemed highly speculative at the time, Nichol foresaw the science of galaxy evolution. Yet despite his exuberance, there was no evidence that the spiral nebulae were extragalactic in nature, as there was no known method of measuring the distance to them.

In the 1830s, there was a race between astronomers to be the first to measure a stellar parallax. The race was won by Bessel (1838), who measured the parallax of 61 Cygni as 0”.3136, implying a distance of 10.4 light years, a difference of $< 10\%$ from the present-day value of 11.41 light years.

Within weeks, two further parallax measurements were published: Friedrich von Struve measured a parallax of 0.2619” for Vega (revised upwards from an initial estimate of 0”.129, which was within 3% of the current value), and Thomas Henderson, working from the Cape of Good Hope Observatory in South Africa, measured 1.26” for Alpha Centauri (Webb, 1999).

These measurements were possible because they targeted our closest stars, i.e. those with the largest parallax. Even so, the measurements implied distances of hundreds of thousands of times the Earth-Sun distance (by definition, 1 Astronomical Unit (AU)). The more distant stars, and the spiral nebulae, were beyond the reach of the parallax measurement, and so the question of their distances would remain unanswered until a new development in the twentieth century.

In 1893, Henrietta Leavitt came to work at the Harvard College Observatory, initially as an unpaid volunteer, and later as a “computer,” employed to make measurements from photographic plates. One of Leavitt’s tasks was to measure the brightness of variable stars in the Magellanic Clouds.

The stars Leavitt was measuring were known as Cepheid variables, discovered by John Goodricke in 1784 and named after the star Delta Cephei. They are a class of giant yellow stars whose luminosity oscillates in a regular manner. Their variability is now understood to be due to the ionisation of their atmospheres. As the stars

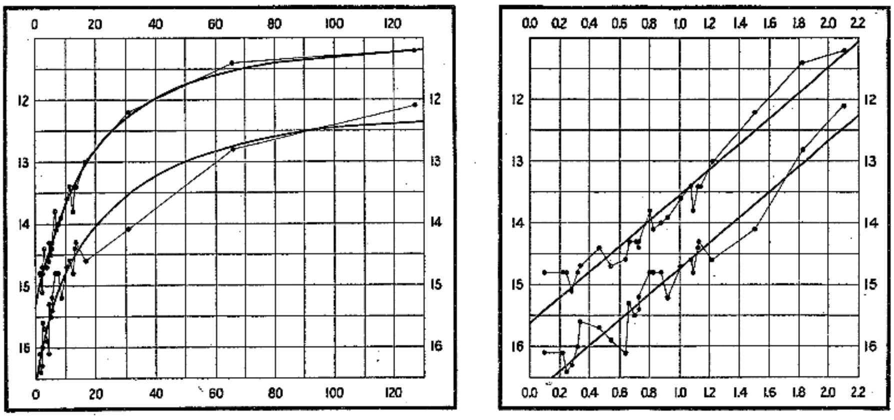

Figure 1.4. The left-hand figure shows the magnitudes at maxima and minima against the period in days, resulting in two smooth curves. In the right-hand figure, the magnitudes are plotted against the logarithm of the period (Leavitt & Pickering, 1912)

radiate energy, some of the singly ionised Helium, HeII, becomes doubly ionised to HeIII, causing the atmosphere to become more opaque. This in turn decreases the amount of energy leaving the star and heats up the atmosphere, causing it to expand and increasing the star's luminosity. As the gas expands, it cools and the HeIII converts back to HeII. The resulting decrease in opacity of the atmosphere causes the atmosphere to shrink again, and the luminosity to decrease.

While compiling her catalogue, Leavitt noticed that there was a correlation between the peak brightness of Cepheid variables and their period, noting that those with longer periods tended to be brighter (Leavitt, 1908). When measurements of further stars yielded the same result, she was able to quantify the relation, noting that "the logarithm of the period increases by about 0.48 for each increase of one magnitude in brightness" (Leavitt & Pickering, 1912, see Figure 1.4).

Since the stars being observed were all in the Magellanic Clouds and therefore at roughly the same distance from Earth, she concluded that the periods were related to their absolute magnitudes. This was a crucial discovery, for if Leavitt's relation could be calibrated, she had discovered a 'standard candle'; an object of known absolute magnitude whose apparent magnitude can thus be used to determine its distance.

Commenting on the significance of her results, Leavitt & Pickering (1912) said, "It is to be hoped...that the parallaxes of some variables of this type may be measured." This problem was first addressed by Hertzsprung (1913), who carried out a statistical parallax analysis of thirteen known Cepheids using Leavitt's slope. He was thus able to arrive at the first relation between absolute magnitude and period, providing the first calibration of the period-luminosity relation and thus the first estimate of an extragalactic distance.

1.5 Island Universes

With a method of measuring distances beyond the reach of stellar parallax now available, the question of the nature of the spiral nebulae could be addressed. In the early decades of the twentieth century, there were two leading theories: either the spiral nebulae were contained within the Galaxy, or they were "island universes," similar in size to the entirety of the Milky Way but so far removed in distance as to appear nebulous.

The first step in resolving this dichotomy was to establish a physical scale for the Milky Way system. Shapley (1919) used Leavitt's period-luminosity relation to calculate the distance to globular clusters, and from their distributions inferred the shape and size of the Milky Way. For the first time, he placed the Sun outside the centre of the Milky Way, which he estimated to be 100,000 pc in diameter. This overstates the current accepted value by a factor of ~ 3, but was $100\times$ greater than previous estimates. Shapley believed that the increased size of the Milky Way was evidence that the spiral nebulae had to be contained inside it:

> “so long as the diameter of the galactic system was thought to be only a thousand light-years or so, we had a fairly plausible case for the “island universe” hypothesis. But... any external “universe” must now be compared with a galactic system probably more than three hundred thousand light-years in diameter” (Shapley, 1919).

Shapley was so convinced by this evidence that he argued the case for the Milky Way as the entire Universe at the Great Debate of 1920, held at the Smithsonian Museum of Natural History. He argued that if spiral nebulae were separate galaxies, they would have to be located at vast distances, far greater than astronomers of the time were willing to accept. He contended that these spirals did not even consist of stars, but were nebulous objects.

On the other side of the debate was Heber D. Curtis of Lick Observatory, who had spent nearly a decade photographing nebulae and was an active proponent of the “island universe” theory. He argued that Shapley had overestimated the size of the Milky Way by a factor of ten, and that spiral nebulae were separate galaxies much like our own. Furthermore, it had been suggested that our own galaxy had spiral structure and Curtis concluded that this was “not improbable” (Hoskin, 1976).

Also presented in favour of the “island universe” hypothesis was the fact that the spiral nebulae appeared unlike any Galactic object in distribution and dynamics.

The nebulae were preferentially found outside the plane of the Milky Way, in contrast to the stars. Even more troubling, Slipher (1917) had taken spectra of 25 of them in order to measure their radial velocities and found they all but four were receding, and at unprecedented velocities; an average of $570\,\mathrm{km\,s^{-1}}$. Nonetheless, Shapley & Shapley (1919) insisted that this was not inconsistent with their being part of the Galaxy, though he had to invoke some new repulsive force acting exclusively upon the nebulae.

Although hyped as a "Great Debate," there were no conclusions reached at the Smithsonian, for there was no method known to calculate the distance to Andromeda or any other spiral nebula.

The debate continued in correspondence between the two astronomers, but was not settled until 1925 when Edwin Hubble discovered "definite evidence of actual stars involved in spirals," including many variables with the characteristic light-curves of Cepheids. From this, he was able to determine a distance to Andromeda of 285 kpc (Hubble, 1925). With modern measurements, this is now believed to have been a vast underestimate, with the true distance around 785 kpc (McConnachie et al., 2005). Nonetheless, Hubble's measurement was far larger than any estimate of the size of the Milky Way. It was thus sufficient to confirm Andromeda as a galaxy separate to our own, and thus revolutionised our view of the scale of our Universe.

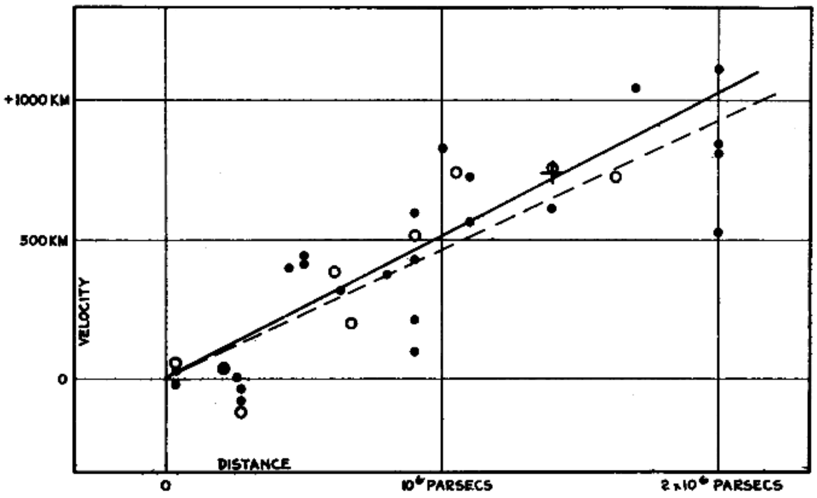

Figure 1.5. The relation between distance and radial velocity (Hubble, 1929).

1.6 The Big Bang

Things would change again by the end of the decade, as Hubble combined new distance measurements with Slipher's radial velocities. At the time, radial velocities were available for 46 galaxies but distances for only 24. Nonetheless, Hubble (1929) was able to determine a remarkable linear correlation between the two (see Figure 1.5).

The constant of proportionality became known as the Hubble constant, H, where H_0 denotes its current value. Hubble's (1929) results gave $H_0 = 500\ \mathrm{km\,s^{-1}\,Mpc^{-1}}$, which is significantly higher than its currently accepted value. However, although the value of H_0 has been under near-constant revision in the intervening decades, the linear relationship discovered by Hubble remains intact and is now known as Hubble's Law.

This relationship provided the first observational evidence that the Universe was expanding, and therefore that it must have been much smaller in the past, possibly originating in a single point. Hubble himself, however, never commented on the remarkable nature of his discovery or its implications; indeed, he favoured a model in which no expansion existed, and maintained that the observed redshifts represented "a hitherto unrecognised principle of nature" (Sandage, 1989).

Despite Hubble's own misgivings, his work remains accepted as evidence of the expansion of the Universe, and an accurate determination of H_0 became one of the primary goals of cosmology.

From Hubble's estimate of $H_0 = 500\,\mathrm{km\,s^{-1}\,Mpc^{-1}}$, increasingly accurate measures of distance and recognition of bias in luminosity measurements led to ever-decreasing values of H_0. By 1962, four independent methods placed H_0 in the range $75 - 125\,\mathrm{km\,s^{-1}\,Mpc^{-1}}$ (Sandage, 1962).

Work to pin down H_0 began in earnest from about 1975, and various methods placed the value between 50 and 100, but preferentially towards the two extremes. This dichotomy resulted in a long, drawn-out disagreement between Allan Sandage, who thought the value was close to 50 (e.g. Sandage, 1999) and Gérard de Vaucouleurs who claimed a value of around 100 (e.g. de Vaucouleurs, 1972). This dispute culminated in a debate between Gustav Tammann and Sidney van den Bergh in 1996, reminiscent of the 1920 Great Debate between Shapley and Curtis.

The need to resolve this rift and determine H_0 accurately was one of the prime motivations behind the building of the *Hubble Space Telescope* (*HST*). The *HST* offered numerous advantages over ground-based telescopes; its high image quality allowed Cepheids to be observed at much greater distances than were possible before, and without the effects of atmospheric seeing. With *HST*, Cepheids were found to calibrate Type 1a Supernovae (another distance indicator discussed in detail later in this section) for the first time, allowing the distance scale to be calibrated more accurately than had been possible before.

Utilising Cepheid variables and a number of secondary distance indicators, including Type 1a Supernovae, the *HST* Key Project found a value of $H_0 = 72 \pm 8\,\mathrm{km\,s^{-1}\,Mpc^{-1}}$ (Freedman et al., 2001). This value has since been slightly reduced by the *Planck* mission to $H_0 = 67 \pm 1.2\,\mathrm{km\,s^{-1}\,Mpc^{-1}}$ (Planck Collaboration et al., 2013a).

The 1920s began with a debate over whether the Milky Way constituted the entire Universe, and ended with the discovery that not only was the Universe far larger than even the most ambitious had imagined, but it was getting larger all the time. Yet the idea that it had originated in a single point - or indeed had an origin at all - did not immediately gain universal acceptance.

Sir James Jeans (1928) proposed a ‘steady state’ theory, based on the idea of a ‘perfect’ cosmological principle; that the Universe should be homogeneous and isotropic not only in space, but also in time. The discovery of the expansion of the Universe presented a difficulty for this theory, requiring that matter be spontaneously created so as to maintain a constant density as space expanded. Nonetheless, this was seen as a lesser problem than the instantaneous creation of the entire Universe at some point in the past. As Hoyle (1948) put it:

> “...through continuous creation of matter it might be possible to obtain an expanding universe in which the proper density of matter remained constant. This possibility [seems] attractive, especially when taken in conjunction with aesthetic objections to the creation of the universe in

> the remote past. For it is against the spirit of scientific enquiry to regard observable effects as arising from "causes unknown to science," and this in principle is what creation-in-the-past implies."

To differentiate between the two competing theories, some observational difference was needed. Gamow (1954) pointed out that that in a steady-state Universe, galaxies should not age on average, and so the probability that our closest large galaxy, Andromeda, would be of a similar age to the Milky Way was very low. In response, Hoyle & Narlikar (1962) objected that uncertainties in age determination were high, and there was as yet no theory concerning the structural evolution of galaxies from one morphological type to another.

The crucial factor would prove to be the prediction of Alpher et al. (1948) that a Big Bang Universe would have a blackbody background radiation, a remnant of the 'surface of last scattering,' or the point at which the early Universe became transparent. They predicted that the expansion of the Universe would have cooled this background radiation to 50 K, a figure that was later revised to $\sim 5\,\mathrm{K}$ by Alpher & Herman (1948). Several groups began searching for this background radiation, which would provide a 'smoking gun' confirming the Big Bang hypothesis.

Arguably, the Cosmic Microwave Background (CMB) had already been discovered; McKellar (1941) reported that the excitation of CN emission lines in the interstellar medium implied a background temperature of 2.3 K. However, this result went unnoticed. The result that came to the attention of the scientific community and became accepted as the discovery of the CMB came not from any of the groups dedicated to searching for it, but from Bell Labs in New Jersey, where Arno Penzias and Robert Wilson were experimenting with a sensitive 6-metre horn antenna designed to detect faint radio signals from communications satellites. In order to increase the sensitivity sufficiently to detect such faint signals, they measured and eliminated any possible sources of interference. Nonetheless, a faint, steady signal persisted, invariant in time and spread evenly across the sky. Since there was no change in the signal in the directions of the Sun or the Galactic centre, they concluded that the origin had to be extragalactic in nature. They had unwittingly discovered the sought-after remnant of the Big Bang. The results were published simultaneously by Penzias & Wilson (1965), giving the observational results, and Dicke et al. (1965) giving the theoretical background. The accidental nature of the discovery notwithstanding, Penzias and Wilson were awarded the 1978 Nobel Prize for Physics for their work.

1.7 The development of ΛCDM

The discovery of the CMB presented a problem for theories of the formation of galaxies, however. The prevailing theory for structure formation was that the early Universe consisted of a photon-baryon fluid, which would be compressed as it clumps together under gravity into overdense regions that arise due to random fluctuations. As the fluid condensed, its pressure would increase, counteracting the force of gravity until the fluid is forced apart. It would then expand until the pressure decreased sufficiently for gravity to dominate once more, and this process repeated until the Universe became transparent to photons, forming the surface of last scattering that is observed as the CMB. Different regions of the CMB should therefore have different temperatures depending on where in this cycle different parts of the Universe were at the time the photons decoupled, and these fluctuations are measures of the initial density perturbations that went on to form large scale structure in the Universe.

The problem was that baryonic matter only becomes electrically neutral at the epoch of recombination. Prior to this, electrostatic forces oppose gravity, and so baryonic matter only condenses efficiently after recombination. The CMB as measured by Penzias and Wilson and numerous successive ground-based experiments was uniform across the sky to within the measurement sensitivity. These low upper limits on the initial density perturbations were a concern, as they were so small that structures of the form observed would not have had time to form (e.g. Partridge, 1980).

One possible solution to this problem is to invoke a form of electrically neutral matter that could begin the process of structure formation before recombination. The idea that there was a significant amount of matter in the Universe that could not be seen was not a new one. From observations of the Coma cluster, Zwicky (1937) noticed a discrepancy between the mass implied by the light and that derived from the virial theorem from their velocities of two orders of magnitude. The galaxies were moving so quickly that clusters ought to be flying apart, yet their prevalence suggested that they were not transitory structures. Much of the analysis behind this work was published four years previously in a German-language paper in which Zwicky (1933) specifically attributed this discrepancy to missing mass, noting "...das dunkle Materie in sehr viel grösserer Dichte vorhanden ist als leuchtende Materie" (the density of dark matter is far greater than that of luminous matter), and even using the phrase ‘cold dark matter’ (“*dunkle (kalte) Materie*”), albeit not in the modern sense.

The same result was achieved for the Virgo cluster by Smith (1936), who posited a vast quantity of “internebular material” within the cluster. In the Local Group, too, Kahn & Woltjer (1959) deduced from the motions of the Milky Way and Andromeda that there must be an “appreciable” quantity of intergalactic matter, assumed by them to be ionised gas.

Separately, similar results were arising from the study of internal galaxy dynamics. Babcock (1939) measured the rotation curve of Andromeda and derived mass-to-light ratios that increased by more than an order of magnitude from the inner part of the galaxy to the outer regions, requiring extreme variations in dust obscuration or “new dynamical considerations” to reduce the mass towards the outer parts of the galaxy. Rubin & Ford (1970) found a similar rotation curve by measuring the velocities of 67 HII regions in Andromeda, concluding that the enclosed mass had to increase approximately linearly with radius in the outer regions. Roberts & Whitehurst (1975) extended this out to 30 kpc using the 21cm Hydrogen line. Even at these high radii, they found that the rotation curve in the outer parts of the galaxy was flat, though they considered an excess of dwarf stars in the outer parts of the galaxy sufficient to explain the extreme mass-to-light ratios.

Andromeda was by no means an isolated example; Oort (1940) found that “the distribution of mass in [NGC3115] appears to bear almost no relation to that of light.” Furthermore, following the study of rotation curves in 21 galaxies during the 1970s, Rubin et al. (1980) said that “the conclusion is inescapable that non-luminous matter exists beyond the optical galaxy."

A suggestion for the geometry of this unseen matter came from numerical simulations. Ostriker & Peebles (1973) found that flattened disc galaxies were dynamically unstable unless embedded in a spherical halo, citing the rotation curve observations as evidence for the existence of sizeable quantities of dark matter. Observational support for galaxies being embedded in spherical halos came from X-ray observations of elliptical galaxies, which found evidence for halos of dark matter similar to those inferred for groups and clusters (Forman et al., 1985).

Both observations and theory had converged on the same idea, that most of the matter in the Universe was dark. Yet, what is the dark matter? The dynamics of galaxies, groups and clusters could be adequately explained by a large quantity of dwarf stars and intergalactic gas, but the CMB observations suggested that it might consist of another form of matter entirely, something that interacted via gravity but only weakly via electromagnetism.

A possible solution was presented when a finite rest mass of 30eV was found for the electron neutrino (Lyubimov et al., 1980). Gershtein & Zel'dovich (1966) had argued that if neutrinos had a non-zero rest mass, they would create large-scale perturbations in the early Universe. After recombination, baryonic matter would fall into these perturbations. This had the advantage of reducing the expected amplitude of CMB perturbations observed in baryonic matter. Zel'dovich (1970) showed that large-scale perturbations would collapse into a filamentary structure which closely resembles the distribution of galaxies, so this provided a compelling explanation both for the missing mass problem and for the apparent absence of structure in the CMB. This model became known as "Hot Dark Matter," because the neutrinos were relativistic when they decoupled in the early Universe.

Concerns were swiftly raised about this model, however. The measurement of the neutrino rest mass proved to be erroneous; current estimates place the combined mass of neutrinos at less than 0.23 eV (Planck Collaboration et al., 2013b). Moreover, numerical simulations showed that free streaming of relativistic particles in the early Universe would wipe out too much small-scale structure (White et al., 1983), and Peebles (1982) showed that the perturbations resulting from cold (non-relativistic) dark matter were consistent with the upper limits of observations.

One of the most important differences in the predictions of the competing models was in the scales of perturbations in the CMB. Observations that were sensitive to one part in 10^5 were required, and searching for these fluctuations was one of the drivers of the COsmic Background Explorer (COBE) satellite, launched in 1989. The improved sensitivity revealed anisotropies in the CMB (Smoot et al., 1992) and resulted in the awarding of the 2006 Nobel Prize in Physics to John Mather and George Smoot.

Cold Dark Matter became the preferred model for the evolution of structure in the Universe, and cosmology entered a 'precision' era in which estimates of key parameters could be made to increasing accuracy thanks to the improving sensitivity of observations, as illustrated in the evolving CMB maps in Figure 1.6.

The picture of the Universe remained incomplete, however. Although the Universe was known to be expanding, the history - and future - of that expansion remained in question.

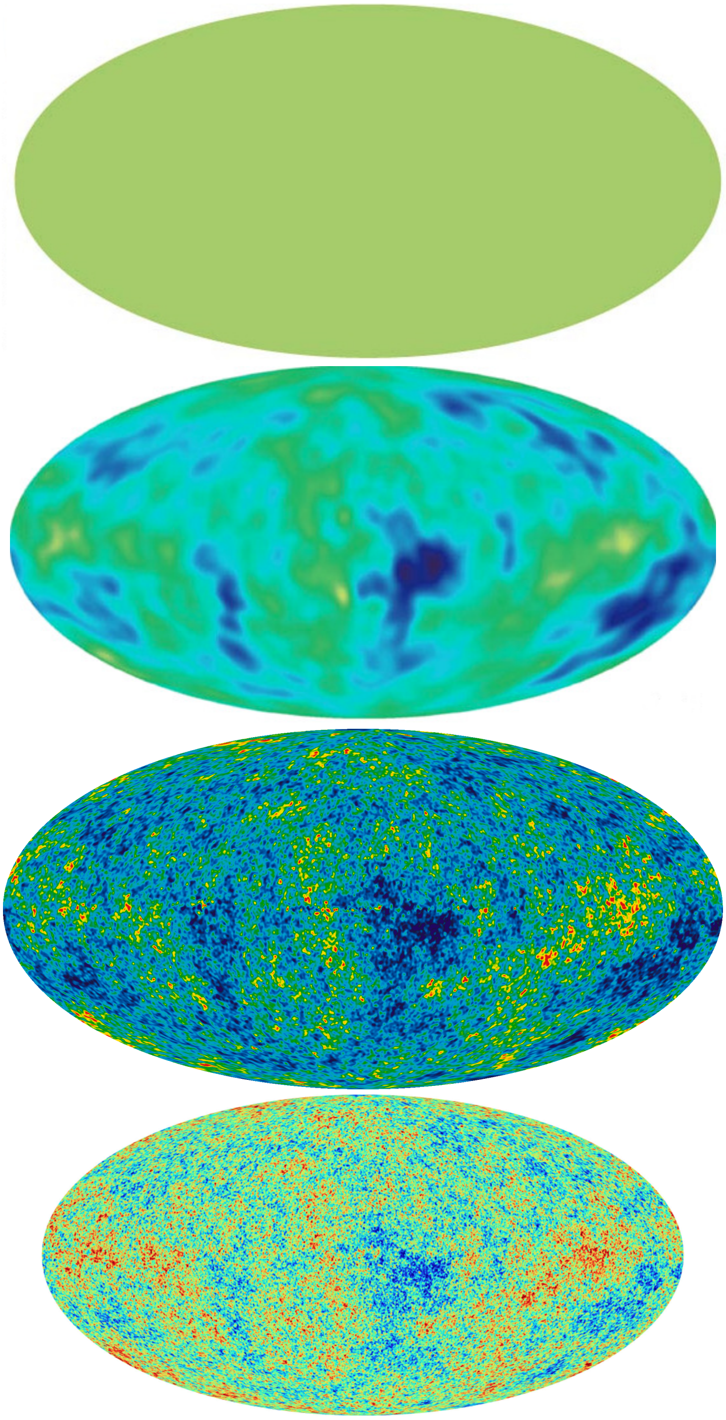

Figure 1.6. The improving sensitivity of Cosmic Microwave Background maps. From top to bottom: Penzias and Wilson (1965), the COsmic Background Explorer (COBE) 4-year mission (1996), the Wilkinson Microwave Anisotropy Probe 9-year data (2012) and the first year of Planck data (2013). Image credits: NASA/ESA

In a Universe consisting only of matter and a cosmological constant, with densities $\Omega_{\rm m}$ and Ω_Λ respectively, it can be shown that the deceleration parameter is

$$q_0 = \frac{\Omega_m}{2} - \Omega_\Lambda. \tag{1.7.1}$$

The deceleration parameter was so defined because, prior to the late 1990s, it was assumed that the Universe was matter-dominated and that gravity would be acting to slow down the expansion. As such, q_0 was expected to be positive, and the rate of expansion decreasing. From Equation 1.7.1, it can be seen that if $\Omega_\Lambda < \Omega_m/2$, then $q_0 > 0$ and the Universe would be decelerating, as was assumed to be the case.

The method for measuring q_0 comes from the luminosity distance D_L, defined as the apparent brightness of an object as a function of redshift z, which is given by

$$D_L \approx \frac{c}{H_0}\left[z + z^2\left(\frac{1-q_0}{2}\right)\right]. \tag{1.7.2}$$

From Equation 1.7.2, it can be seen that for small $z << 1$, D_L is roughly proportional to z. As we go to higher z, however, D_L becomes dependent on q_0. Measurements of q_0 therefore require observations of the most distant objects possible, for which distance and redshift can be independently measured. It was therefore surmised by Colgate (1979) and Tammann (1979) that distant supernovae were the best candidates.

Supernovae are the bright explosions of stars, which over a short period can outshine an entire galaxy. As more supernovae were observed, it became apparent that they could be divided into subsets, Type I and Type II, according to their spectra (Baade, 1938). The Type I supernovae were later further subdivided, with one class - known as Type 1a - proving to have remarkably homogenous light curves (Kowal, 1968).

It is now understood that this uniformity is due to their having almost identical progenitors. When a star of less than approximately ten solar masses exhausts its supply of hydrogen, its outer layers are ejected leaving a dense remnant known as a white dwarf. Chandrasekhar (1931) showed that there is a limit to the mass that can be supported by electron degeneracy pressure in such a star, which equates to approximately 1.44 $M_\odot$, where $M_\odot$ is the mass of the Sun. If the white dwarf accretes mass above this limit, the star will explode as a Type 1a supernova (SN1a). This defined mass results in consistent absolute magnitudes, with a scatter of no more than 0.25 mag (Branch & Tammann, 1992).

Since their calibration relies on Cepheid distances, SN1a can only serve as secondary distance indicators. Nonetheless, it is believed that they are accurate to within 8% (Perlmutter & Schmidt, 2003), making them one of the best standard candles known so far.

While SN1a are in theory perfect standard candles, a number of factors make them difficult to observe. Firstly, they are rare; a typical galaxy such as the Milky Way has only a few per millennium. They are also random, and so cannot be predicted, and do not last long; the period from being unobservable to peak brightness is only a few weeks. As such, it was almost impossible to schedule telescope time to observe them. Norgaard-Nielsen et al. (1989), for instance, recorded only one Type 1a supernova in two years of observations, and that was weeks past its peak brightness.

To overcome these problems, two independent, systematic searches for supernovae were set up: the Supernova Cosmology Project (SCP) and the High-z Supernova Search (HZSNS) Team. Both teams reported the same unexpected result: distant supernovae were fainter than expected, which implied a negative q_0, i.e. the expansion of the Universe is accelerating (Perlmutter et al., 1999; Riess et al., 1998).

The acceleration of the Universe has been attributed to a cosmological constant, Λ, which appears to comprise $\sim 70\%$ of the mass-energy density of the Universe (Knop et al., 2003; Tonry et al., 2003). To date, there has been no definitive answer as to what the cosmological constant might represent or why it has the value it does, or what particles comprise the dark matter. The matter we understand, the baryons that make up stars and galaxies, makes up only around 4% of the Universe. Nonetheless the ΛCDM (Λ- Cold Dark Matter) model is now known as the concordance model of cosmology, and it is this framework in which the work set out in this thesis is set.

Chapter 2

Galaxies

2.1 Galaxy properties

In Section 1.2, we saw how our understanding of the Universe expanded from our local Solar System, to a galaxy of billions of solar systems, and finally to a vast collection of billions of such galaxies.

The existence of galaxies has been understood for less than a century and so the study of their evolution is a relatively young science, relative to astronomy as a whole, yet its progress has been swift in an era of rapidly improving technology.

The first stage in understanding any newly-discovered object is to classify it into subgroups, so that key properties may be highlighted and perhaps an evolutionary sequence identified. The earliest classification systems in use were descriptive in nature only, and identified variations in the properties of the spiral arms. One of the clearest examples is that of Wolf (1908) shown in Figure 2.1, which used letters to denote the sequence from amorphous nebulae to developed spirals.

The most well-known classification is that of Hubble (1926), who devised the

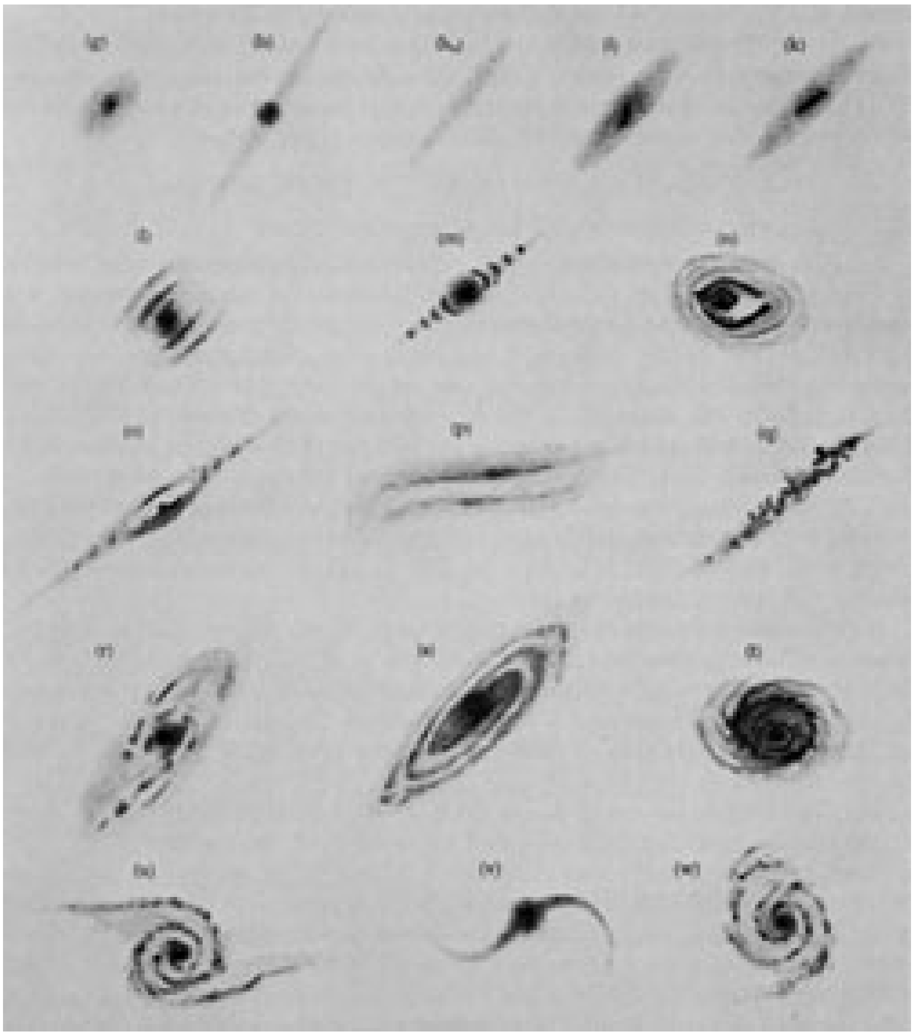

Figure 2.1. The classification system of Wolf (1908), as reprinted by Sandage et al. (1975), omitting the first line which consisted of Galactic nebulae, not known at the time to be a different class of object. In this system, letters were used to identify various types of spirals. This was the first classification system to use a linear sequence, progressing from featureless morphologies (*d* to *k*) to grand design spirals (*r* to *w*).

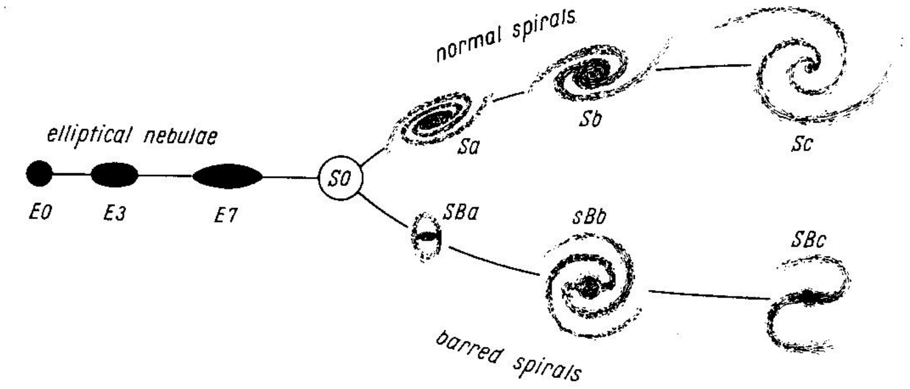

Figure 2.2. Hubble's 'tuning fork' classification system. From left to right, elliptical galaxies were classified as E0-E7, where the number denotes their ellipticity. The spheroidal S0 galaxies are discs with no spiral arms, and at that point the diagram diverges with Sa-Sc on the upper branch representing spirals with tightly wound and open spiral arms respectively. On the lower branch, the SBa-SBc classes represent the same sequence but with a bar in place of a spheroidal bulge.

famous 'tuning fork' illustrated in Hubble (1936, see Figure 2.2), but it was not immediately adopted. The level of detail in the Wolf system meant that it was widely used as late as the 1940s; Danver (1942) commented: "As to the Hubble classes, these [appear to constitute] a division along a line of development. This is certainly a great advantage, but if a conception of the appearance of the object is desired, it is better to designate the types according to Wolf."

However, the problem of an overcomplicated system was noted by Wolf (1908), who remarked "Es gibt kein zwei Nebelflecken am Himmel, die sich gleichen" (no two galaxies are alike). The broader categories of Hubble's system lent themselves more easily to the classification of the vast majority of galaxies; for example, in the catalogue of 338 galaxies published by Arp (1966), only 45 could not be classified according to the Hubble system. The tuning fork thus became the most popular

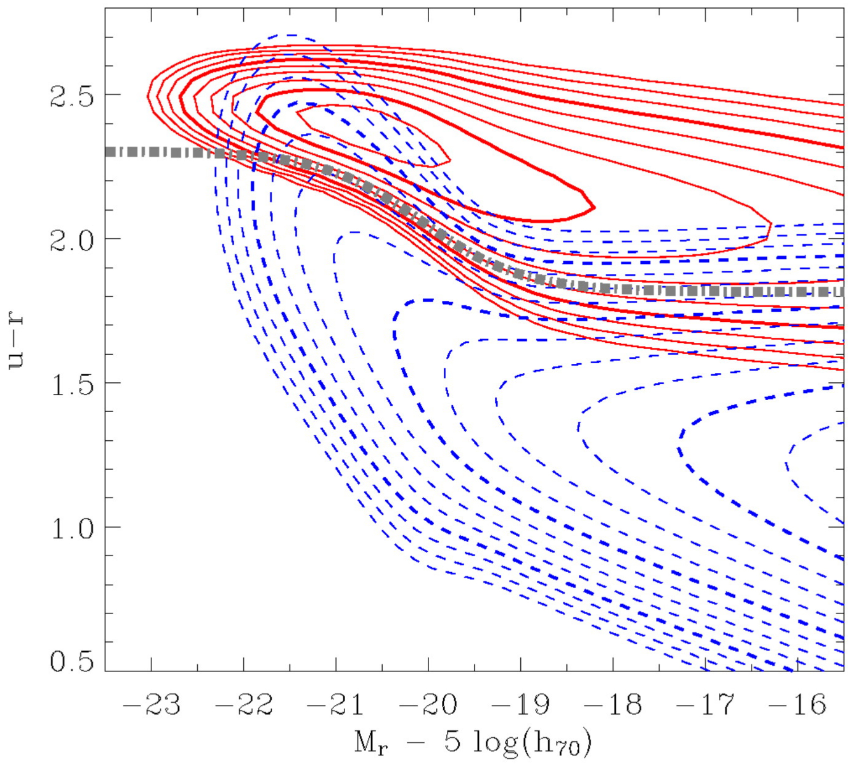

Figure 2.3. The colour-magnitude diagram for SDSS galaxies from Baldry et al. (2004). The solid red contours show the density distribution of red galaxies and blue dashed lines the blue galaxies. The thick dash-dotted line is an empirical divider between the two distributions. The galaxy population can be broadly divided into the 'blue cloud,' consisting primarily of spiral galaxies, and the 'red sequence' composed mainly of ellipticals.

classification method, and is still widely used today. A particular advantage of the Hubble classification scheme is that the physical properties of galaxies vary systematically along the sequence. These properties include:

- **Morphology:** The most immediately apparent difference between galaxies along the Hubble sequence is their physical shape. Elliptical galaxies are ellipsoidal, supported by random motions of stars, whereas spiral galaxies are thin discs supported by rotation. There are also combinations of the two: most spiral galaxies have a bulge component similar in properties to an elliptical galaxy, and some ellipticals have discs. This can be quantified with a bulge/disc ratio, which can be interpreted as a tracer of the galaxy's formation history (e.g. Baugh et al., 1996).

- **Luminosity:** A useful means of quantifying the statistical galaxy population is a luminosity function, a measure of the distribution of galaxies as a function of their luminosity. Large surveys have shown that the luminosity density of the Universe is dominated by spirals similar to the Milky Way. Although fewer in number, elliptical galaxies are systematically brighter (e.g. Nakamura et al., 2003).

- **Size:** Measurements of the size of a galaxy are difficult to make, as galaxies do not have a clear cut-off point, and their observed sizes are subject to the depth of the observations. A commonly used quantity (and one used in this thesis) is the 'half-light radius,' $r_{1/2}$, or the radius that encompasses half the light at the specified wavelength. Galaxy surveys have found that brighter galaxies tend to be larger, with spiral galaxies at a given luminosity systematically larger than ellipticals (Shen et al., 2003).

- **Gas fraction:** As the fuel for star formation, the fraction of a galaxy's mass in the form of gas is an important factor in its evolution. Generally, elliptical galaxies are observed to have smaller gas fractions than spiral galaxies; thus, most star formation occurs in spirals (e.g. Roberts & Haynes, 1994).

- **Colour:** The colour of a galaxy is broadly related to its age, as older stars are redder in colour. However, it is also affected by metallicity - the presence of more metals reddens the colour of a galaxy - and its dust content, as light is absorbed by dust and re-radiated at longer wavelengths (i.e. redder colours). The property of 'colour' is quantified in astronomy as the difference in flux between two filters of differing wavelengths. Galaxy populations exhibit a bimodal colour distribution, with elliptical galaxies appearing redder than spirals (e.g. Baldry et al., 2004; Blanton et al., 2003, see Figure 2.3).

- **Environment:** It was noticed early on that different types of galaxies are preferentially found in different environments: ellipticals are more common in clusters, whereas spirals are found more often in the field (Dressler, 1980).

Even the fastest processes involved in galaxy formation take place on timescales much longer than the human lifespan. In order to understand how galaxies evolved to their present state, we must therefore examine the observable properties of statistical populations and try to piece together the underlying physical processes.

2.2 Galaxy evolution

One fortuitous aspect of the expansion of the Universe is that we are able to observe galaxies in the past, and can therefore quantify how their properties evolve with time as well as present-day composition. As discussed in Section 1.2, Hubble's primary contribution to the science of extragalactic astronomy was his relation between the distance of a galaxy and its recession velocity, which became known as 'Hubble's law.' A corollary of this law is that galaxies with high recession velocities - or high redshift - are also at the highest distances and therefore, due to the finite speed of light, seen the furthest in the past. By studying galaxies with high redshifts, we can therefore see them in early stages of formation.

In the ΛCDM paradigm, the first structures to form in the early Universe were dark matter halos. Gas then cooled inside these halos to form galaxies (White & Rees, 1978). The classical picture of how galaxies acquired their morphologies was that it depended on their rates of star formation during their initial collapse (Eggen et al., 1962; Struck-Marcell & Tinsley, 1978). Stars are collisionless, so if they are formed quickly then they will maintain their initial motions as they collapse, leading to random orbit orientations and an ellipsoidal morphology. If more of the mass is in the gas phase then energy will be dissipated during collapse via shocks and cooling, leading to a disc morphology supported by rotation. An appealing aspect of this picture is that it provides a natural explanation for the morphology-density relation, due to gas collapsing more quickly in the largest overdensities in the early Universe, leading to faster star formation and hence more elliptical galaxies in denser environments (Gott & Thuan, 1976).

High resolution imaging with the *Hubble Space Telescope*, however, revealed that there were more spiral galaxies in the cores of clusters in the past than there are today (Couch et al., 1998; Dressler et al., 1997). This lends support to an alternative picture in which gas cooling in a dark matter halo spins up as it conserves angular momentum during collapse, and thus will always form as a rotating disc (Fall & Efstathiou, 1980). Mergers between disc galaxies will then cause them to lose their disc structure and create ellipticals (Toomre & Toomre, 1972). As mergers are naturally more common in dense environments, this picture explains both the present-day morphology-density relation and its evolution with redshift.

The ability of improved facilities to probe further into the past has revealed that the morphology-density relation was in place as early as $z = 1$, when the Universe was just half its present age, and that the fraction of ellipsoidal galaxies in cluster environments has increased steadily since then (Smith et al., 2005). The early establishment of the morphology-density relation, combined with its evolution, may suggest that a more accurate picture is a mixture of these two hypotheses: rapid star formation in the largest overdensities in the early Universe may have set the density-morphology relation, with subsequent evolution due to environmentally-driven processes.

A great deal of progress in understanding the complex processes that combine to create galaxies has been made in recent decades with semi-analytic modelling, which applies empirical laws and scaling relations to dark matter distributions in order to predict a range of galaxy properties at different epochs. A particularly important result of modelling is that there must be one or more processes at work to suppress the formation of stars. If all gas is permitted to cool within halos until its self-gravity dominates, upon which it fragments and collapses into stars, then the process of star formation is too efficient, resulting in far more stars than are observed. This has resulted in the introduction of feedback due to energy injected into the gas by supernovae or Active Galactic Nuclei (AGN; rapidly accreting black holes). The former acts to reduce star formation at the faint end, while the later is important in preventing star formation in the most massive galaxies (Benson et al., 2003; Bower et al., 2006; Croton et al., 2006).

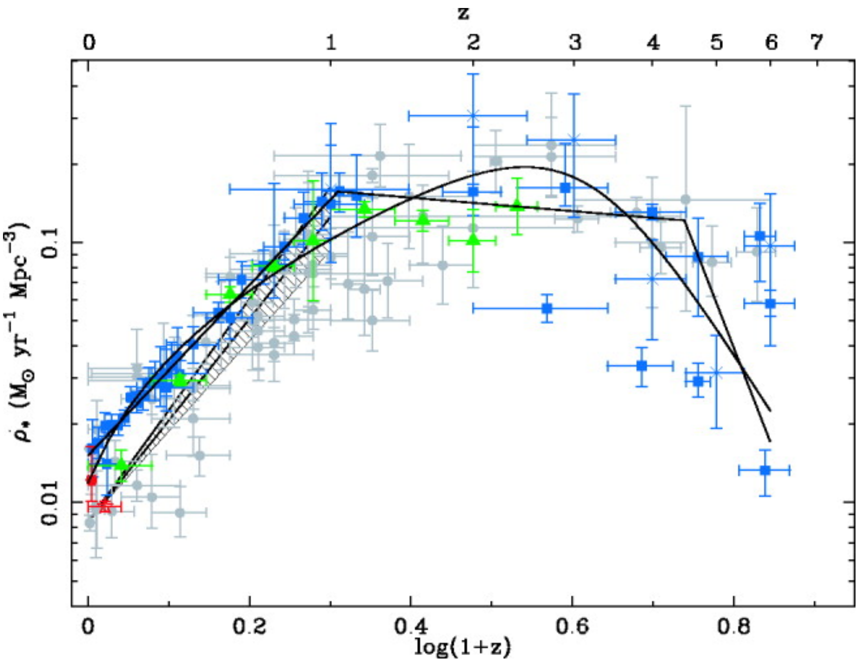

Figure 2.4. A compilation of measures of the star formation density history of the Universe, from Hopkins & Beacom (2006). Most of the star formation happened in the first half of the Universe's history (at $z > 1$), with star formation density decreasing by an order of magnitude by $z = 0$.

It can therefore be seen that galaxy formation is a complex process. Nonetheless, accumulating surveys that are deep enough to probe most of the history of the Universe or cover a wide enough area to provide a large statistical sample, have provided us with a picture of how galaxies have assembled over cosmic time.

Perhaps surprisingly, it appears that the majority of stars in the Universe formed at $z > 1$, when the Universe was less than half its current age (Dickinson et al., 2003; Patel et al., 2013). Furthermore, the cosmic star formation rate density seems to have peaked at $z \sim 1$, and declined by an order of magnitude in the latter half of the Universe's history (Hopkins, 2004; Hopkins & Beacom, 2006; Lilly et al., 1996; Madau et al., 1996, see Figure 2.4).

In order to understand the formation of galaxies, it is therefore important to understand how the processes driving star formation differed in the first half of the Universe's history ($z > 1$) to the quiescent star formation seen today. The large surveys have given us a picture of how the overall properties of galaxies have evolved with cosmic time; the goal now is to understand the underlying processes by probing inside the galaxies themselves to uncover where the stars are forming, and how - or if - the process of star formation differs from that seen in local galaxies.

The subject of this thesis is therefore to study $z > 1$ galaxies in detail, to map their star formation on small scales. There are, however, a number of inherent difficulties in making detailed observations of high-redshift galaxies.

Firstly, the expansion of the Universe reduces the observed surface brightness of distant galaxies. The expansion of space in between photons being emitted from the target galaxy and being observed means that they are received less frequently than they are emitted, which reduces the observed flux. In addition, they are shifted to lower energy, which means that the same filter effectively receives a smaller portion of the galaxy's total energy distribution. Combined, these effects cause cosmological surface brightness dimming $\propto (1+z)^4$.

The fact that photons are received at lower energies than they are emitted also means that we observe the galaxies in a different rest-frame band. In the optical, for instance, we observe rest-frame UV emission, which can be faint due to dust absorption or a lack of young, hot stars. This effect, known as the k-correction, can make high-redshift galaxies difficult to detect (although it can also work in the opposite direction, for example in the case of submilimetre galaxies). This can also change the apparent morphology of a galaxy, as light is distributed differently at different wavelengths (known as a morphological k-correction).

In addition, galaxies at high redshift are seen in an earlier phase of their evolution, and so are intrinsically smaller than those seen locally.

The combination of these difficulties means that detailed work on high-redshift galaxies is by necessity restricted to the most extreme objects: the largest, the most massive and those with the highest star formation rates. The more representative galaxies are currently beyond the reach of observational facilities.

In advance of future giant telescopes, there is a way of accessing the small and sub-luminous galaxy population at high redshift, if they happen to lie behind massive galaxy clusters that bend their light in such a way as to magnify them. In the following section, we will discuss gravitational lensing and how it may be used to achieve detailed observations of distant galaxies.

2.3 Gravitational lensing

This thesis makes use of the effect of gravitational lensing to magnify distant galaxy images. As we use lensing as a tool rather than studying the effect itself, a detailed discussion of the theoretical aspects is beyond the scope of this work. However, we discuss here some of the background and introduce the terminology that will be used throughout the work.

The idea that the path of light should be deflected by matter has been known since the work of Newton, though he lacked sufficient understanding of light to formalise the concept. When Einstein (1916) formulated his General Theory of Relativity, he realised that there must be an additional contribution to this deflection due to the 'equivalence principle,' the idea that there is no discernible difference between gravity and acceleration. In an accelerating frame, the path of a beam of light would appear curved; therefore, this must also be true in a gravitational potential. The angle of deflection, $\vec{\alpha}$, in General Relativity, can be shown to be

$$|\vec{\alpha}| = \frac{4\,G\,M}{c^2 \xi}, \tag{2.3.1}$$

for a photon passing a spherically symmetric mass M enclosed within the radius of the impact parameter ξ. This is a factor 2× higher than that predicted under Newtonian gravity, and initially gravitational lensing was considered interesting only insofar as it provided a test of Einstein's theory of General Relativity. Such a test was conducted during the solar eclipse of May 29, 1919, when Dyson et al. (1920) observed the predicted displacement in stars in the Hyades cluster.

The first practical use for lensing was suggested by Zwicky (1937), who realised

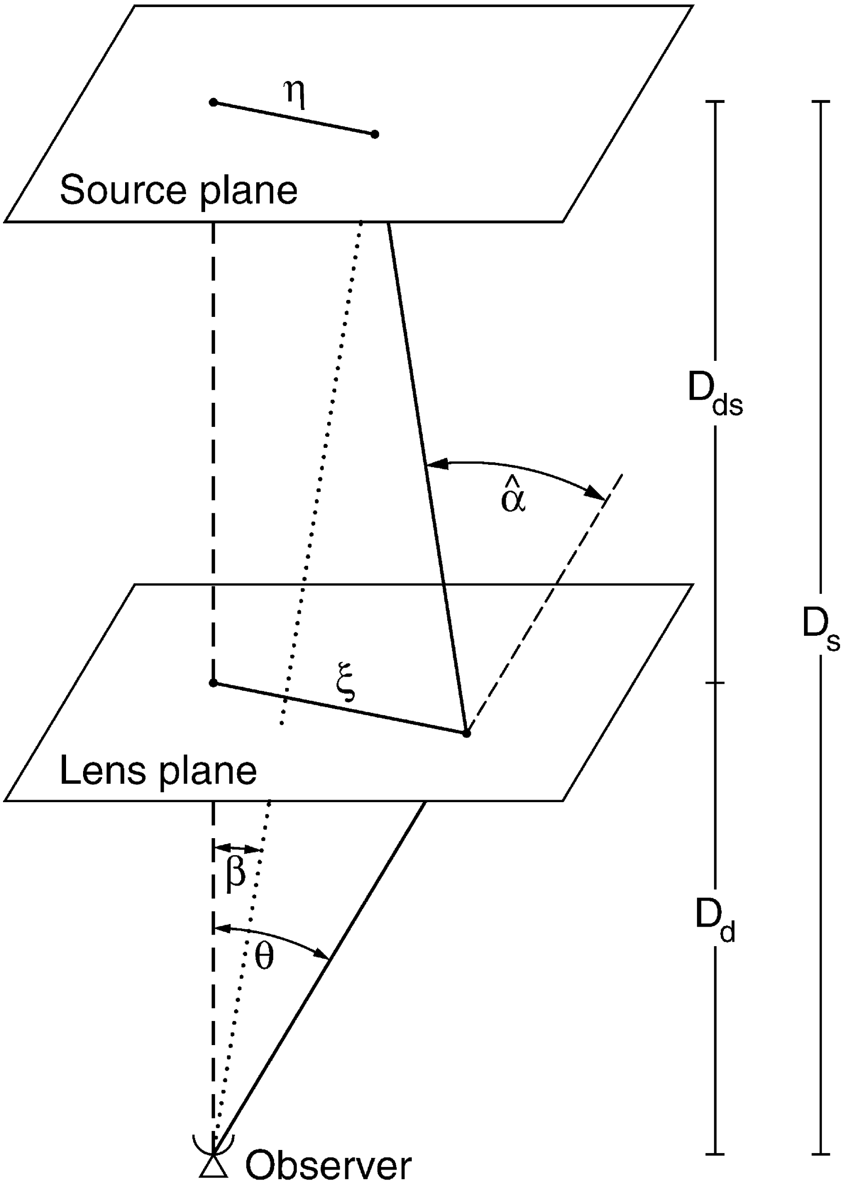

Figure 2.5. The geometry of a lensing system, defined by a source at a distance D_s from the observer, whose light is deflected by a lens at a distance D_{ds} from the source and D_d from the observer. The relation between the angular position of the source, $\vec{\beta}$, the observed angular position of the image, $\vec{\theta}$, and the deflection angle, $\vec{\alpha}$, is described in the text. Figure from Bartelmann & Schneider (2001).

that it could be used to measure the mass of galaxy clusters, though he, in common with Einstein (1916), believed it would never be measurable in practice.

According to Einstein (1916), light follows null geodesics - effectively, the shortest path in a curved spacetime. In the case that there is more than one solution for a null geodesic, the result will be multiple images of the lensed source. Furthermore, as can be seen from Equation 2.3.1 for the simple case of a point mass, the deflection depends on the impact parameter, with photons passing more closely to the lensing mass being more strongly deflected. This results in differential deflection across an image, which causes it to appear 'stretched' on the sky. The number of photons does not change, so surface brightness in conserved while size is not, which means that the total flux is magnified.

Gravitational lensing acts over two regimes, *weak* and *strong*. In the weak case, the distortions are too slight to be individually measurable, and must be computed statistically over a large sample. In the strong case, sources can be highly magnified and multiply imaged. While both effects can be used to measure the cluster mass, the strong case is the one we require in order to use the lensing effect to study the background galaxies, taking advantage of the source magnification.

Figure 2.5 illustrates the geometry of a lensing system in which a source lies at a distance D_s from the observer, with an intervening lensing potential at a distance D_d from the observer and D_{ds} from the source. The first assumption we make is that the distances between the source, lens and observer are much larger than the sizes of the source or lens. Therefore, we can consider the lens as being confined to a thin sheet; this is known as the *thin lens approximation*. Thus, the mass distribution can be fully described by a surface density on a thin sheet at a distance D_d from the observer. For strong lensing, the projected mass density, Σ must exceed some critical mass density, $\Sigma_{\rm crit}$, where

$$\Sigma_{\rm crit} = \frac{c^2 D_s}{4\pi G D_d D_{ds}} \tag{2.3.2}$$

For a source at $z \sim 2$ behind a lens at $z \sim 0.5$, $\Sigma_{\rm crit} \sim 1\,{\rm g\,cm^{-2}}$, so the use of clusters as strong lenses requires that they exceed this projected density.

The discovery of a lensed arc behind the cluster Abell370 (Lynds & Petrosian, 1986; Soucail et al., 1987) demonstrated that galaxy clusters do have sufficient mass surface density to act as strong gravitational lenses. Many lensed arcs are now known, and have driven the development of mass modelling techniques (e.g. Coe et al., 2008; Jullo et al., 2007; Jullo & Kneib, 2009).

For a lens with $\Sigma > \Sigma_{\rm crit}$, a critical line is produced at the Einstein radius, θ_E, given by

$$\theta_E = \sqrt{\frac{4\,G\,M\,D_s}{c^2\,D_d\,D_{ds}}} \tag{2.3.3}$$

so θ_E is governed by the enclosed mass M. The critical line represents a region of theoretically infinite magnification, though in practice the sources are extended so the actual magnification is large but finite. Most of the lensed galaxies presented in this thesis straddle the critical lines of their lensing clusters, and are therefore highly magnified. The line in the source plane that maps to the critical line in the image plane is known as the caustic.

In order to account for the lensing magnification and study the intrinsic properties of the lensed galaxies, the mass distribution must be known. This thesis makes use of published mass models for galaxy clusters, which are derived using the precise positions and redshifts of multiply-imaged sources in the cluster. Using a Markov chain Monte Carlo (MCMC) sampler, the open-source software LENSTOOL (Jullo et al., 2007; Kneib, 1993) can estimate the enclosed mass of the cluster to within $\sim 5\%$ given *HST*-quality imaging. The accuracy of the mass model depends on the number of constraints, i.e. how many lensed sources behind the cluster have known spectroscopic redshifts. The models can also be well constrained where there are multiple images straddling the critical line, as this allows the position of the line to be carefully pinpointed, which in turn gives the enclosed mass from Equation 2.3.3. It can be seen from Equation 2.3.1 that the deflection angle is linear with mass. This means that deflection by multiple sources (as in a galaxy cluster) can be calculated as a superposition of the lensing masses.

In practice, of course, the mass distribution is unlikely to be spherically symmetrical. For an asymmetric mass distribution, the deflection angle becomes

$$\vec{\hat{\alpha}} = \frac{2}{c^2} \int d\lambda \vec{\nabla}_{\perp} \Phi, \tag{2.3.4}$$

over the light path λ, where Φ is the gravitational potential of the lensing mass. This result is valid provided the gravitational field is weak ($|\Phi| \ll c^2$), and the lensing mass moves slowly ($|\vec{v}| \ll c$), both of which are true for galaxy clusters.

Once the mass distribution of the lensing cluster is known, the lensing distortion can be inverted so that the lensed galaxy can be studied in its intrinsic, unlensed, configuration. To do this, each pixel must be ray-traced back through the cluster potential to the source plane. In order to apply this ray-tracing, we must define the lens equation.

Considering a system with the geometry illustrated in Figure 2.5, we first make the assumption that all of the angles involved are small, so that the small angle approximation, $\sin(\theta) \sim \theta$, is valid. We then define an optic axis perpendicular to the lens plans and intersecting with the observer. On the source plane, a galaxy with angular position $\vec{\beta}$ is located at a distance $\vec{\eta} = \vec{\beta}\, D_s$ from the optic axis.

A photon from this source intersects with the lens plane with impact parameter $\vec{\xi} = \vec{\theta}\, D_d$, where $\vec{\theta}$ is the observed angular position of the image.

From basic geometry, the deflection angle $\hat{\vec{\alpha}}$ is related to the source position $\vec{\beta}$ and observed position $\vec{\theta}$ as

$$\vec{\theta}\, D_s = \vec{\beta}\, D_s + \hat{\vec{\alpha}}\, D_{ds}. \tag{2.3.5}$$

We also define a reduced deflection angle

$$\vec{\alpha}\left(\vec{\theta}\right) = \frac{D_{ds}}{D_s}\,\hat{\vec{\alpha}}\left(\vec{\theta}\right), \tag{2.3.6}$$

and we then have the lens equation

$$\vec{\beta} = \vec{\theta} - \vec{\alpha}\left(\vec{\theta}\right). \tag{2.3.7}$$

Combining Equations 2.3.4 and 2.3.7, we have

$$\vec{\beta} = \vec{\theta} - \frac{2\, D_{ds}}{c^2\, D_s} \int d\lambda \vec{\nabla}_{\perp}\Phi. \tag{2.3.8}$$

Using the thin lens approximation, we can also write the integral of the potential along the light path as a projected two-dimensional potential:

$$\int \Phi d\lambda = \phi\left(\vec{\eta}\right) = D_d \phi\left(\vec{\theta}\right), \tag{2.3.9}$$

and we define the lensing potential, φ, as

$$\varphi = \frac{2\, D_{ds}\, D_d}{c^2\, D_s}\phi. \tag{2.3.10}$$

Substituting Equations 2.3.9 and 2.3.10 into 2.3.8, we obtain the original angular position of the source, $\vec{\beta}$ in terms of its observed image position $\vec{\theta}$ and lensing potential, φ, as

$$\vec{\beta} = \vec{\theta} - \vec{\nabla}\varphi. \tag{2.3.11}$$

The work in this thesis involves using Equation 2.3.11 for images lensed by a cluster with a previously-derived potential. By applying this to each point over the galaxy image, we can reconstruct its appearance in the source plane, prior to being lensed. The stretching effect of gravitational lensing means that these source-plane images are higher resolution than could be obtained in the absence of lensing with current facilities, enabling us to study the properties of sub luminous galaxies at high redshift.

2.4 Techniques used in this work

In Section 2.2, we have discussed the need to understand star formation within $z > 1$ galaxies. Here, we briefly introduce the observational techniques used to measure star formation in galaxies, and the theoretical interpretation of disc instabilities used throughout this work.

2.4.1 Observational star formation tracers

There are a number of tracers used to measure star formation rates (SFRs) in galaxies, reviewed by Kennicutt (1998a) as follows:

- **Broadband colours:** The spectrum of a galaxy is a composite of its stellar populations, with optical wavelengths dominated by A, F, G and K stars (which are high- to low-mass and hence short- to long-lived respectively). The optical colours can therefore be used to estimate the fraction of young stars and hence the approximate SFR over the last Gigayear. Stellar population synthesis models are used to calibrate the colours, but are prone to errors due to the differing effects of dust, metallicity and star formation history. This method is primarily used as a computationally efficient means of comparing average SFRs across a large sample.
- **Ultraviolet:** At ultraviolet (UV) wavelengths ($1250 - 2500\mathring{A}$), the light is dominated by young stars, so there is a linear relationship between luminosity and SFR. For local galaxies, atmospheric absorption precludes the use of UV from ground-based telescopes, but these wavelengths are accessible in distant

galaxies in which the rest-frame UV is redshifted into optical bands, and space-based telescopes such as the *Hubble Space Telescope* have made it possible to observe local galaxies as well. However, UV measurements are particularly sensitive to dust obscuration.

- **Nebular recombination lines:** Massive stars ($> 10\,M_\odot$, where $M_\odot$ is the mass of the Sun) with lifetimes of $< 20\,\mathrm{Myr}$ ionise the clouds of (primarily hydrogen) gas in which they are embedded. As the hydrogen atoms recombine, they produce bright emission lines. The lines of the Balmer series are the most useful for measuring the SFR; the 3-2 transition gives rise to the Hα emission line at $6562.8\mathring{A}$, and the 4-2 transition gives Hβ at $4861\mathring{A}$. As only the shortest-lived stars contribute significantly to the ionising flux, these lines are a very sensitive tracer of instantaneous star formation. However, they are also sensitive to dust obscuration, which is typically $A_{\mathrm{H}\alpha} = 0.8 - 1.1$ magnitudes, though to a lesser degree than the UV.

- **Far infrared continuum:** The absorption of dust peaks in the ultraviolet, and this absorbed emission is then re-emitted in the infrared. The far-infrared (FIR) luminosity can therefore be used as a tracer of the UV emission, and hence of the young stellar population. Uncertainties with this method arise due to variations in the contribution to dust heating from old stars, and in the temperature and optical depth of the dust.

All of the above SFR tracers depend ultimately on measuring the emission from young, massive stars. They all therefore carry an additional systematic uncertainty due to assumptions regarding the initial mass function (IMF), which dictates what fraction of the total star formation is in these massive stars.

The simplest form of the IMF is that of Salpeter (1955), which is a pure power law. More recent work has refined this, primarily by restricting the contribution from low-mass stars (Baldry & Glazebrook, 2003; Chabrier, 2003; Kroupa, 2001;

Scalo, 1986).

Throughout this thesis, we make use of the nebular emission lines Hα and Hβ to trace star formation, assuming a Chabrier (2003) IMF. In addition to the advantages noted above of the sensitivity of the emission lines to the most massive stars, these lines are also accessible at a wide range of redshifts in the near-infrared.

In addition to measuring the ongoing formation of stars, we can consider their fuel. Star formation requires large clouds of gas to collapse under gravity, so the gas must be cold, around 10 K. At these temperatures, the gas becomes molecular. Stars therefore form in dense molecular clouds.

The majority of the molecular gas is hydrogen, H_2, but as a symmetric molecule H_2 does not have a permanent electric dipole. It therefore does not have any radiative rotational transitions (it does have lower-probability transitions, but these are inherently weak and so cannot be measured at high redshift). However, we can use the second most abundant molecule, CO, to trace the distribution of H_2 (Sanders et al., 1984; Solomon & Vanden Bout, 2005, e.g.). According to the Bohr model of the atom, angular momentum - and hence rotational energy - is quantised. Therefore, rotation of the molecule will result in discrete emission lines.

In the CO molecule, rotational transitions occur at approximately integer multiples of 115 GHz (the precise value depends on the distance between the carbon and oxygen atoms, which increases at higher rotational energy levels due to increased forces on the nuclei). This places the rotational transitions of CO at millimetre wavelengths, which corresponds to windows of atmospheric transmission; the higher-order CO transitions are even accessible at high redshift.

2.4.2 Disc stability

Throughout this thesis, we refer to the Toomre (1964) stability parameter, Q, which is defined as

$$Q = \frac{\sigma\,\kappa}{\pi\,G\,\Sigma} \tag{2.4.12}$$

where σ is the turbulent velocity dispersion, $\kappa \sim \sqrt{2}v_{\rm rot}/r$ is the epicyclic frequency for rotation velocity $v_{\rm rot}$ and disc scale length r, and Σ is the max surface density of the disc.

If $\sigma\,\kappa > \pi\,G\,\Sigma$ then the energy from turbulent and rotational motion dominate over the gravitational energy, so the disc will be stable against collapse. If $\pi\,G\,\Sigma > \sigma\,\kappa$ (i.e. $Q < 1$) then the gravitational energy dominates, and the disc will fragment. Therefore, a disc is described as 'Toomre-stable' if it has $Q > 1$ and unstable if $Q < 1$. A marginally stable disc has $Q \sim 1$.

2.5 Organisation of this work

We begin in Chapter 3 by isolating the Hα emission line in two redshift windows, $z \sim 1$ and $z \sim 1.5$ with narrowband filters available on the Wide Field Camera 3 (WFC3) installed on the *Hubble Space Telescope* in 2009. In Chapter 4, we turn to examining the fuel for star formation, with observations of molecular gas in our highest-redshift target at $z \sim 5$. We then compile the largest sample to date of lensed galaxies with spatially resolved spectroscopy to map star formation in lensed galaxies at $1 < z < 4$ in Chapter 5, to study the relation between star formation and galaxy dynamics. A summary of our findings and an outline for future work is presented in Chapter 6.

Chapter 3

Hubble Space Telescope Hα imaging of star-forming galaxies at $z \simeq 1 - 1.5$

3.1 Overview

We present *HST*/WFC3 narrowband imaging of the Hα emission in a sample of eight gravitationally-lensed galaxies at $z = 1 - 1.5$. The magnification caused by the foreground clusters enables us to obtain a median source plane spatial resolution of 360pc, as well as providing magnifications in flux ranging from $\sim 10\times$ to $\sim 50\times$. This enables us to identify resolved star-forming HII regions at this epoch and therefore study their Hα luminosity distributions for comparisons with equivalent samples at $z \sim 2$ and in the local Universe. We find evolution in the both luminosity and surface brightness of HII regions with redshift. The distribution of clump properties can be quantified with an H II region luminosity function, which can be fit by a power law with an exponential break at some characteristic luminosity, and we find that the luminosity of the break evolves with redshift. We therefore conclude that 'clumpy' galaxies are seen at high redshift because of the evolution of the characteristic mass; the galaxies themselves follow similar scaling relations to those at $z = 0$, but their H II regions are larger and brighter and thus appear as clumps which dominate the morphology of the galaxy. A simple theoretical argument based on gas collapsing on scales of the Jeans mass in a marginally unstable disc shows that the clumpy morphologies of high-z galaxies are driven by the competing effects of higher gas fractions causing perturbations on larger scales, partially compensated by higher epicyclic frequencies which stabilise the disc.

3.2 Introduction

Observations of star-forming galaxies at high-z have shown that a significant fraction of the population have turbulent, clumpy, rotating discs with clump masses of $\sim 10^{8-9}\mathrm{M}_{\odot}$, a factor of $\sim 100\times$ the typical Giant Molecular Cloud (GMC) locally (e.g. Cowie et al., 1995; Elmegreen & Elmegreen, 2005; Elmegreen et al., 2009, 2004; Förster Schreiber et al., 2009). The clumps are thought to form from gravitational instabilities in gas-rich discs (Bournaud et al., 2010; Elmegreen et al., 2009, 2007; Genzel et al., 2008).

Some recent numerical simulations have suggested that the majority of massive, high-z galaxies accrete their gas via 'cold flows,' in which the gas is accreted smoothly along filaments. These cold flows are less disruptive than a major merger, and hence offer a route to maintain marginally stable discs (Toomre parameter $Q \sim 1$) without disrupting the structure and dynamics. Cold-flow accretion is expected to be a dominant mode of mass assembly above $z \simeq 1$, and thus accounts for the ubiquity of large clumps at high redshift (e.g. Bournaud et al., 2011; Bournaud & Elmegreen, 2009; Dekel et al., 2009).

In this picture, the clumps are considered to be transient features, forming in marginally unstable discs at high-z and fed by smooth accretion of gas onto the galaxy. Clumpy galaxies therefore represent a phase in the evolution of present-day spiral discs.

There is a need to test the internal physical properties of the interstellar medium (ISM) observationally, to determine whether the clumps are scaled-up analogues of local HII regions or represent a different 'mode' of star formation, and whether they can explain the strong evolution of star formation rate density with redshift. However, sufficient spatial resolution is required to resolve the ISM on the scales of star-forming regions. Even with the use of adaptive optics, spatially resolved studies of high-redshift galaxies to date have been limited to a resolution of ~ 1.5kpc (e.g. Förster Schreiber et al., 2009; Genzel et al., 2006); using the *Hubble Space Telescope (HST)*, only the largest starburst complexes can be resolved, on scales of ~ 1kpc (Elmegreen et al., 2007). On these scales, it is possible to probe the dynamics of galaxies on large scales, and Genzel et al. (2011) found evidence that $Q < 1$ in the regions of galaxies where clumps are found, lending observational support to the theory that the clumps form from internal gravitational instabilities. In order to study the clumps in detail, we need to resolve high-redshift discs on the scales of individual star-forming regions; in the local universe, this is ~ 100pc.

The required spatial resolution can currently only be achieved by exploiting gravitational lensing. By targeting galaxies that lie behind foreground cluster lenses, it is possible to benefit from linear magnification factors (along one direction) of up to 50× (e.g. Jones et al., 2010; Swinbank et al., 2007, 2009), and to isolate HII regions of order ~ 100pc out to $z \sim 5$ (Swinbank et al., 2009). Regions were found with star formation surface densities $\Sigma_{\rm SFR} \sim 100\times$ higher than those found locally (Jones et al., 2010; Swinbank et al., 2009). These regions of dense star formation are comparable to the most intensely star-forming interacting systems in the local Universe (Bastian et al., 2006), yet appear to be ubiquitous in non-interacting galaxies at high redshift.

It is not known what drives these regions of intense star formation at high-z, although Jones et al. (2010) suggest a combination of higher gas density, increased star formation efficiency and shorter star-formation timescales. In addition, their data give the appearance of a bimodal distribution of HII region surface brightnesses, although there is no known physical process that might drive this. In order to understand this result further, we require a sample at intermediate redshift ($z \sim 1-1.5$) with which we can probe the evolution of star formation density with redshift at higher sensitivity so that regions comparable to those at $z = 0$ are detectable.

Previous work on high-z clumps has made use of Integral Field Units such as Keck/OSIRIS (Jones et al., 2010; Wisnioski et al., 2012a), Gemini/NIFS (Swinbank et al., 2009) and *VLT*/SINFONI (Förster Schreiber et al., 2009). These allow detailed mapping of the nebular emission lines, but at lower sensitivity than is achievable with imaging from space, depending on the width of the emission line, the spectral resolution and the available filters. An alternative means of identifying star-forming regions with high sensitivity is to take imaging through narrowband filters. The Wide Field Camera 3 (WFC3) on the *HST* presents an opportunity to study the star formation in galaxies at $z \sim 1$ and $z \sim 1.5$, as there are narrowband filters available which correspond to the wavelength of the Hα emission line at these redshifts. Combining the sensitivity and high spatial resolution of *HST*/WFC3 with the magnification afforded by gravitational lensing by foreground clusters, we can map the internal star formation distribution and so identify the frequency and properties of giant HII regions.

In this chapter, we therefore study the star formation morphologies of eight galaxies at $z \sim 1 - 1.5$. We present the sample in §3.3, present the properties of the galaxies and their star-forming clumps in §3.4, discuss the implications in §3.5 and present our conclusions in §3.6. Throughout, we adopt a ΛCDM cosmology with $H_0 = 70\,\mathrm{km\,s^{-1}\,Mpc^{-1}}$, $\Omega_\Lambda = 0.7$ and $\Omega_m = 0.3$. Star-formation rates are calculated from Hα luminosity $L_{\mathrm{H}\alpha}$ using the prescription of Kennicutt (1998a) adjusted to a Chabrier (2003) IMF.

3.3 Sample and Observations

Our sample comprises eight lensed galaxies, each with spectroscopically-confirmed redshifts between $1 < z < 1.5$ such that the Hα emission line falls within the high-transmission region of the narrowband filters on WFC3. The associated cluster lenses are massive systems from the X-ray selected BCS and MACS samples (Ebeling et al., 2007, 1998, 2001, 2010) with well-constrained mass models (see references in Table 3.1), so that the effects of lensing can be accounted for.

The positions and properties of the sample are given in Table 3.1. We observed each target in the narrowband filter covering Hα for a typical exposure time of 6 ks (2 orbits), using a 3- or 4-point linear dithering pattern of ±5 arcsecs in both directions to improve the detection and removal of cosmic ray hits and bad pixels. At the same time, three of the targets (MACS J0947, MACS J0159 and MACS J1133), which did not have WFC3 data in the archive, were observed in the corresponding broadband filter using the same sequence of observations as their corresponding narrowband data, for a total of 3 ks (1 orbit). The narrowband data and new broadband observations were obtained in Cycle 18 under Program 12197 (PI:Richard), with the exception of Abell 2390, for which the broadband and narrowband data were taken in Cycle 17 under Program 11678 (PI:Rigby). The remaining broadband data were obtained under Cycle 17 Program 11591 (PI:Kneib) or Cycle 18 Program 12065-9 (PI:Postman) as indicated in the notes to Table 3.1.

All of the WFC3 data were reduced using the multidrizzle software (Koekemoer et al., 2002) under PyRAF to perform a cosmic-ray rejection, sky subtraction, and drizzling onto an output pixel scale of 0.05”. Drizzling combines a stack of undersampled images taken from different dithering positions to correct for geometric distortion, remove cosmic rays and bad pixels, and restore the full spatial resolution of the telescope while maximising the field of view. The narrowband and broadband images of the same cluster were aligned using the location of ~ 20 bright stars. A narrowband excess image was constructed by direct pixel-to-pixel subtraction between the narrowband and broadband images, including an arbitrary scaling factor. We calibrated this scaling factor by checking that all bright cluster members, which are featureless elliptical galaxies with no emission lines in the respective filters, became consistent with the background in the excess image. For Abell 773 and Abell 68, the broadband images available in the archive did not directly overlap the Hα emission line, so an estimate of the broadband continuum was made by linear interpolation between the adjacent F110W and F160W filters.

The narrow and broad filters used for each target are indicated in Table 3.1. The $z \sim 1$ targets were observed in either the F126N or F132N narrowband filters as appropriate for their redshifts. These filters have widths of 118Å and 131Å respectively, compared to 3015Å for the corresponding F125W broadband filter, where ‘width’ is defined as the full width at 50% transmission. The $z \sim 1.5$ targets were observed in either F164N or F167N, at 175Å and 172Å respectively, with the corresponding broadband filter F160W having a width of 2879Å. The equivalent widths of the Hα emission lines are typically 80-100Å, and so contribute $\sim$ 3.5% of the broadband flux. This contribution introduces errors into the broadband subtraction, although we attempt to minimise this using the residual minimisation technique described above. Two galaxies have Hα equivalent widths above this range; these are MACS J0159 at 330Å and Abell 773 at 375Å. The former thus has higher potential errors in the broadband flux estimate ($\sim$ 12%), but in the latter case the Hα line is not included in the broadband filter.

The flux calibration of each image was verified using 2MASS stars in the fields, and in all cases was found to agree to within 15%, which is sufficient precision for our purposes.

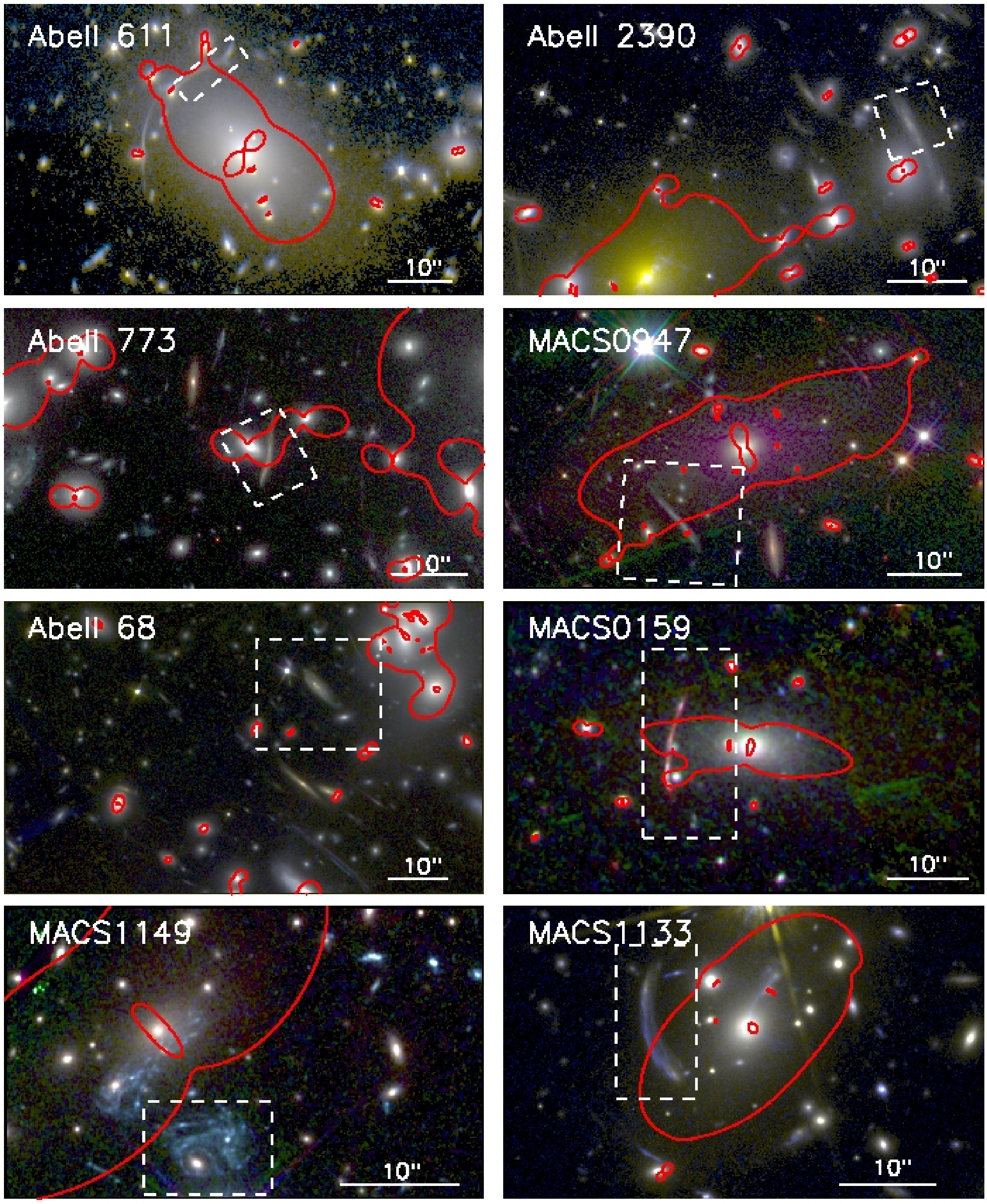

Figure 3.1. HST/ACS and WFC3 three-colour images of the observed clusters with the critical line at the redshift of the target arc overlaid, showing the positions of the target arcs. The arcs are contained within the white dashed boxes which denote the regions extracted in Figure 3.2.

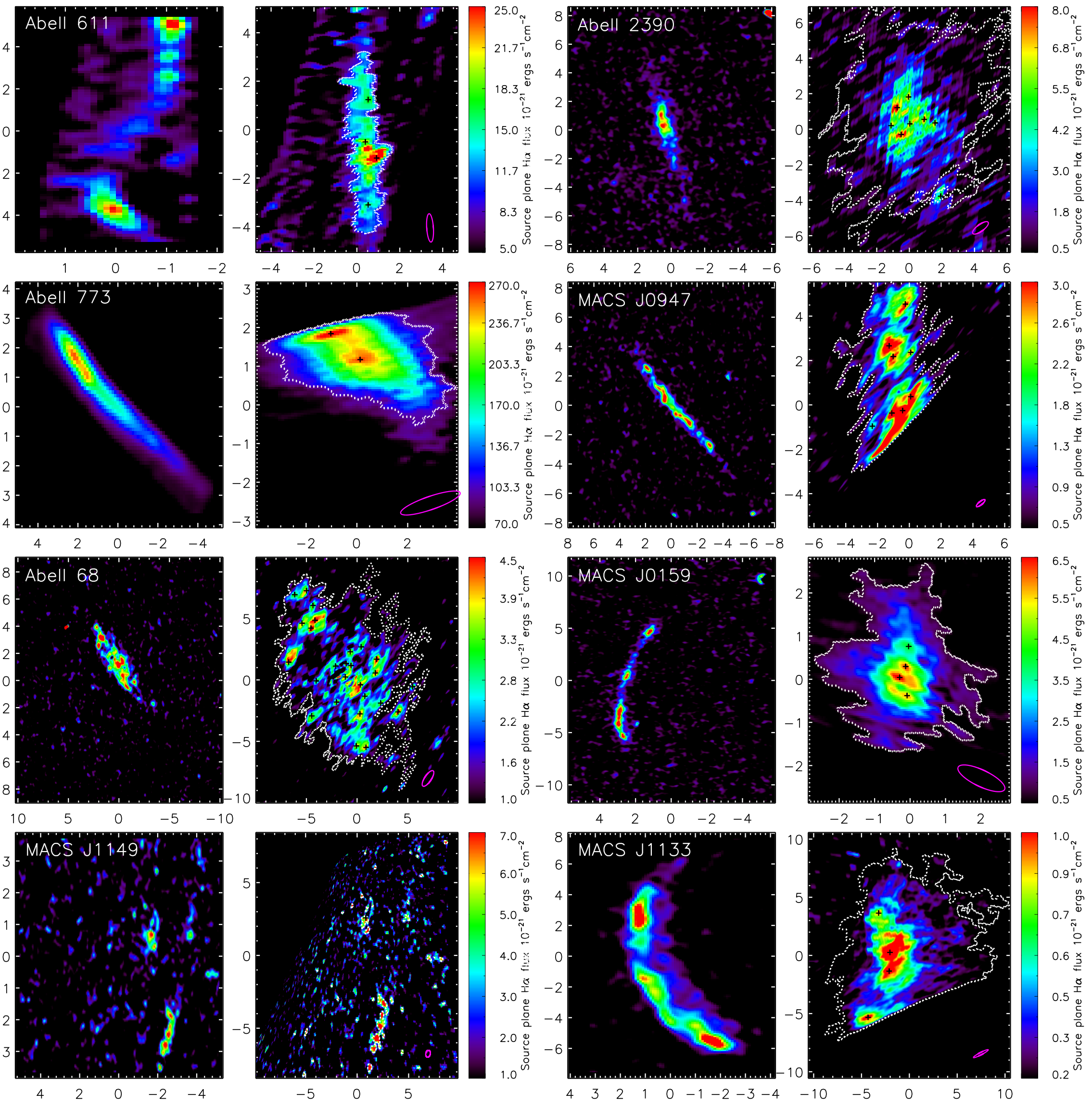

Figure 3.2. Hα excess images in the image plane (left) and reconstructed in the source plane (right). The image scales are in arcseconds in the image plane and in kpc in the source plane. Identified clumps are indicated in the source-plane images by black crosses, and the magenta ellipse shows the FWHM of the effective source-plane PSF, as described in the text.

Target cluster	Arc position		z	Hα flux	Magnification		Resolution	Broadband	Narrowband	Lens
	RA	Dec		(intrinsic)	$\mu_x \times \mu_y$ (PA)	μ	(pc)	filter	filter	model
	(J2000)	(J2000)		(10^{-18}erg/s/cm^2)						reference
Abell 611	08:00:57.30	+36:03:37.0	0.908	30 ± 5	$10.4 \times 2.7\,(1^\circ)$	28 ± 5	338	F125W[a]	F126N	[1]
Abell 2390	21:53:34.55	+17:42:02.4	0.912	39 ± 6	$5.5 \times 2.3\,(73^\circ)$	12.6 ± 1.9	435	F125W[b]	F126N[b]	[2]
Abell 773	09:17:58.80	+51:43:42.3	1.010	274 ± 49	$7.0 \times 1.0\,(61^\circ)$	7 ± 1	336	F110W & F160W[c]	F132N	[1]
MACS J0947.2+7623	09:47:15.26	+76:23:02.9	1.012[d]	8.5 ± 2.2	$3.0 \times 17.7\,(51^\circ)$	53 ± 14	172	F125W	F132N	[3]
Abell 68	00:37:04.91	+09:10:21.0	1.017	119 ± 11	$3.0 \times 1.7\,(41^\circ)$	5.1 ± 0.5	615	F110W & F160W[e]	F132N	[4]
MACS J0159.8-0849	01:59:04.68	-34:13:03.4	1.488[e]	7 ± 1	$10.7 \times 3.0\,(111^\circ)$	32 ± 4	592	F160W	F164N	[3]
MACS J1149.5+2223	11:49:35.30	+22:23:45.8	1.490[f]	11 ± 2	$4.5 \times 3.5\,(140^\circ)$	15 ± 3	315	F160W[b]	F164N	[5]
MACS J1133.2+5008	11:33:14.31	+50:08:39.7	1.550	8 ± 1	$1.1 \times 12.7\,(67^\circ)$	14 ± 2	68	F160W	F167N	[6]

Table 3.1. Properties of the redshift-selected sample. Lensing magnifies the image by a factor μ_x at a position angle PA, with a transverse magnification μ_y. The total magnification factor μ is calculated from the amplification of Hα flux, and the resolution given is the highest achievable along the most magnified direction, calculated from the FWHM of a star under the same lensing transformation as that applied to the galaxy, as described in the text. All observations were obtained under Program 12197 (Cycle 18, PI:Richard) unless otherwise stated.

[a] Program 12065-9 [b] Program 11678 [c] Program 11591 [d] Ebeling et al. (2010) [e] Ebeling et al. in prep [f] Ebeling et al. (2007).

[1] Richard et al. (2010), [2] Pello et al. (1991), [3] Richard et al. in prep, [4] Richard et al. (2007), [5] Smith et al. (2009), [6] Sand et al. (2005)

Colour *HST* images of the clusters are shown in Figure 3.1, with the critical lines at the redshift of the target arc overlaid. We use the transformation between image and source plane mapping from the best-fit cluster mass models (for details of the mass models, see references in Table 3.1) with LENSTOOL (Jullo et al., 2007; Kneib, 1993) to reconstruct the images in the source plane, and show these in Figure 3.2. In order to reconstruct the source plane morphology, LENSTOOL uses the mapping between the image and source planes on a cluster-by-cluster basis and ray-traces the galaxy image. The lensing effect is to stretch the galaxy image - in most cases along one direction - and so the reconstruction cannot 'create' new HII regions, but rather the lensing has acted to extend them. As surface brightness is conserved by lensing, we then apply this conservation to obtain the intrinsic source plane flux. The total magnification is then simply the ratio of the image- to source-plane flux. To obtain the errors on the magnification, we use the family of best fit lens models which adequately describe the cluster potential, derived by sampling the posterior probability distribution of each parameter of the model (see Richard et al. (2010) for more details). For each acceptable lens model, we reconstruct the arc and remeasure the amplification. We give the resulting magnification factors, μ, and associated errors in Table 3.1.

In cases where the target is multiply-imaged, the images were reconstructed separately and then adjusted for small differences in position and orientation before being combined. For MACS J0159, which consists of five images, only the first three were used due to the high magnification gradients in the fourth and fifth images resulting in high distortion in the source plane reconstructions. In the case of Abell 611, we use only the northernmost arc due to high distortion by a foreground galaxy lying close to the line of sight of the southern arc.

We derive total magnification factors by comparing the total luminosities of the image- and source-plane Hα excess images. The intrinsic Hα luminosities are in the range $0.45-15\times10^{41}\mathrm{erg\,s^{-1}}$ corresponding to SFRs of $0.4-12\mathrm{M_{\odot}yr^{-1}}$. These are at the faint end of the Hα luminosity function for this redshift range (see Figure 3.3), and probe fainter galaxies than the $z\sim2$ sample of Jones et al. (2010), which covers the range $2.5-32\times10^{41}\mathrm{erg\,s^{-1}}$, although the two samples overlap in luminosity. Due to the increased sensitivity provided by the lensing magnification, both of the lensed samples cover a lower range of intrinsic Hα luminosities than the sample of SINS galaxies studied by Förster Schreiber et al. (2011), which were selected to have bright Hα and lie in the range $28-43\times10^{41}\mathrm{erg\,s^{-1}}$, making them rare, intensely star-forming galaxies. Thus, by harnessing gravitational lensing we are able to probe the more 'normal' star-forming population.

Since gravitational lensing can preferentially shear one direction, we estimate the effective source-plane resolution by reconstructing the image of a star from the field repositioned to lie at the centre of the target. The maximum linear resolution, derived from the FWHM of the reconstructed star in the direction of greatest magnification, is 68–615pc with a median of 360pc, sufficient to resolve giant HII regions.

3.3.1 Comparison samples

In order to interpret our high-z data, we exploit the Hα narrowband imaging from the *Spitzer* Infrared Nearby Galaxies Survey (SINGS, Kennicutt et al., 2003), which comprises Hα imaging of 75 galaxies with corrected SFRs of up to $11\,\mathrm{M_{\odot}yr^{-1}}$. We use the publicly available continuum-subtracted Hα narrowband imaging and restrict the sample to those with Hα detections with signal-to-noise of > 5 that have no significant defects in the galaxy images (determined by visual inspection). This restricts the SINGS sample to 41 galaxies with SFR $> 4 \times 10^{-4}\,\mathrm{M_{\odot}yr^{-1}}$.

To ensure a fair comparison, we rebin the SINGS images so that the resolution is comparable to the high-z data and then threshold to the median surface brightness limit of the $z \sim 1 - 1.5$ observations. It is worth noting that thresholding the images in this manner excludes $10 - 50\%$ of the total star formation. This should not affect the comparison between samples which have the same surface brightness-limit, but may serve as an indication of the fraction of star formation missed in high-z observations.

To provide a comparison to local galaxies which are more actively star-forming, we use the VIMOS Hα imaging spectroscopy of Rodríguez-Zaurín et al. (2011), which includes 38 LIRGs and ULIRGs at $z < 0.13$ with spatial resolution of $130\,\mathrm{pc}-1.2\,\mathrm{kpc}$ and SFR $\lesssim 25\,\mathrm{M_{\odot}yr^{-1}}$.

We also compare the $z \sim 1 - 1.5$ sample to the $z \sim 2$ lensed arcs of Jones et al. (2010), which were observed with Keck/OSIRIS. In order to provide a fair comparison, we have constructed narrowband images by summing the OSIRIS cubes over 100 Å (observed-frame) around the redshifted Hα emission line, matching the width of the WFC3 narrowband filters. The resulting images are then corrected for lensing using the same image-to-source plane mapping as Jones et al. (2010) in order to obtain the intrinsic galaxy properties.

3.3.2 Determination of galaxy properties

The total Hα luminosities of the galaxies in all samples are determined by constructing an image mask from an isophotal contour at a signal-to-noise of > 3 in a sky-subtracted image, in order to give the best possible match to IFU surveys in which flux is summed over pixels in which a line fit is obtained (e.g. Förster Schreiber et al., 2009; Jones et al., 2010). In the case of the SINGS galaxies, each image was checked by visual inspection and any foreground sources and defects masked. The resulting luminosities were then compared to the published values and found to agree to within $\sim 20\%$.

We convert Hα luminosity to SFR using the Kennicutt (1998a) prescription, corrected to a Chabrier (2003) IMF, which reduces the SFR by a factor of 1.7×. As we do not have constraints on the dust extinction, we adopt an estimate of $A_{\mathrm{H}\alpha} = 1$ in all samples. This assumption is widely used in the literature although it is the subject of some disagreement. Garn et al. (2010) suggest a luminosity-dependent $A_{\mathrm{H}\alpha}$ is more appropriate; were we to adopt their relation, we would obtain $A_{\mathrm{H}\alpha} = 0.7 - 1.6$ with a median $A_{\mathrm{H}\alpha} = 1.15$. However, we also note that recent work by Domínguez et al. (2013) suggests that galaxies with $L_{\mathrm{H}\alpha} \lesssim 4 \times 10^{41}\,\mathrm{erg\,s^{-1}}$ may be consistent with having $A_{\mathrm{H}\alpha} = 0$, and that above this threshold extinction increases in a luminosity-dependent way. Had we adopted this correction instead, the SFRs

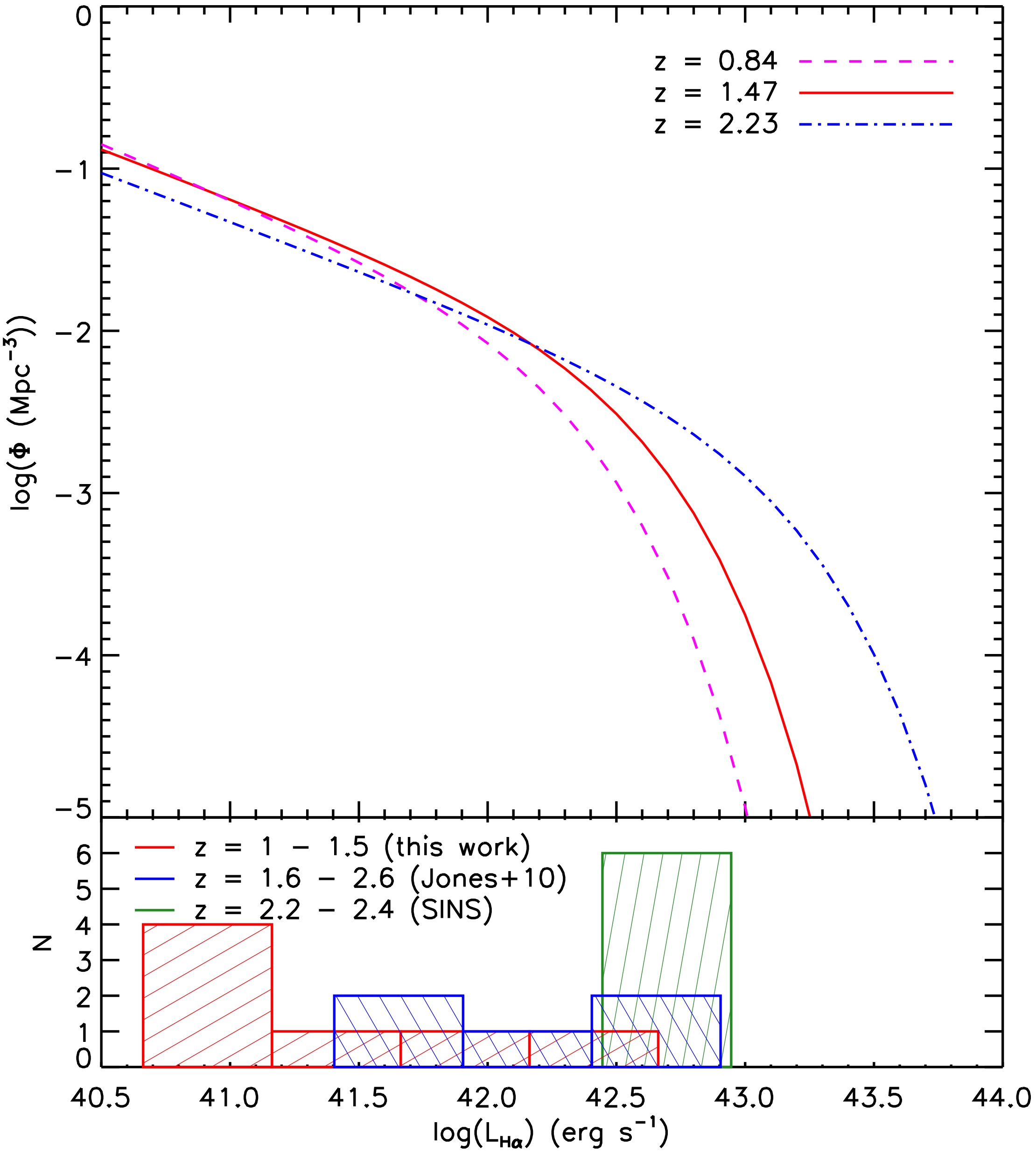

Figure 3.3. Intrinsic Hα luminosities of the high-z samples compared to Hα luminosity functions from HiZELS (Sobral et al., 2012a). Also shown is the range of Hα luminosities of the Förster Schreiber et al. (2011) sample from the SINS survey at $z \sim 2$. The two lensed samples overlap in luminosity and are both at the faint end of the luminosity function, with the median of the $z \sim 1 - 1.5$ WFC3 sample lower than that of the $z = 1.6 - 2.6$ OSIRIS sample by a factor of 6.6×, while the unlensed SINS galaxies cover a range of higher Hα luminosities.

of the majority of our galaxies would be reduced by a factor of 2.5×. The exceptions are the three brightest $z \sim 2$ galaxies, in which the SFRs would increase by factors of $1.3 - 1.8\times$, and the $z \sim 1$ galaxies Abell 68 and Abell 773; the former would be a factor of 1.8× lower, while the latter would be unchanged. Qualitatively, there is no significant impact on our results, as adopting either luminosity-dependent extinction relation would serve to increase the evolution we observe in §3.4.2. For simplicity and reproducibility, we adopt $A_{\mathrm{H}\alpha} = 1$ throughout.

We define the sizes of the galaxies as twice the half-light radius. The half-light radius is determined using the continuum images to find the shape (i.e. the centre and major to minor axis ratio of an ellipse that best fits the galaxy), and then adjusting the semi-major axis of the ellipse until it encompasses half of the total Hα luminosity calculated in the manner described above. The galaxy-averaged star formation surface density, Σ_{SFR} is defined from the total luminosity per unit area enclosed within two half-light radii.

3.4 Results and Analysis

3.4.1 The Spatial Distribution of Star Formation

A common theme in the recent literature is that high redshift galaxies are “clumpier” than galaxies in the local universe. This concept originates from the frequent appearance of “chain” galaxies in the high redshift universe (e.g. Cowie et al., 1995; Elmegreen & Elmegreen, 2005; Elmegreen et al., 2004). Even without looking at the properties of individual star forming regions, it is interesting to compare the morphologies of the star-forming regions across the samples.

From visual inspection, it is clear that there are significant differences between the samples. In particular, the surface brightness distributions of the galaxies show distinct differences in the different samples. In Fig. 3.4, we show the fraction of star formation in pixels above a given Σ_{SFR} for the $z \sim 1 - 1.5$ and $z \sim 2$ samples, with the interquartile range of the thresholded SINGS sample shown for comparison.

To allow for the differing surface brightness limits of the samples, we only show star formation above a surface brightness of $\Sigma_{\mathrm{SFR}} = 0.001\,\mathrm{M}_{\odot}\,\mathrm{yr}^{-1}\,\mathrm{kpc}^{-2}$. This enables us to compare the star formation occurring in bright regions in a consistent manner. From the peaks - i.e. the maximum of the cumulative histograms on the horizontal axis - we can see that the samples are different, with the $z \sim 2$ galaxies having peak surface brightnesses of around an order of magnitude higher than the lower-z samples. Similarly, the $z \sim 1 - 1.5$ sample is systematically brighter than SINGS sample, with the exception of MACS J1133, which is similar to the fainter $z = 0$ galaxies, MACS J0947 which is similar to the median of the $z = 0$ sample, and Abell 773 which appears similar to the $z \sim 2$ galaxies.

As a statistical measure of the clumpiness of galaxies, we investigate using the Gini coefficient, G, which is used in economics to measure the inequality of wealth in a population (Gini, 1912). It has values from 0 to 1, where at the extremes $G = 0$ for a completely uniform distribution, and $G = 1$ if there is only one non-zero value. Following Förster Schreiber et al. (2011), we use it to quantify the distribution of flux in an image, so a value close to one indicates that the profile has a single peak (in the case of $G = 1$, all of the flux would be in a single pixel), a galaxy with multiple

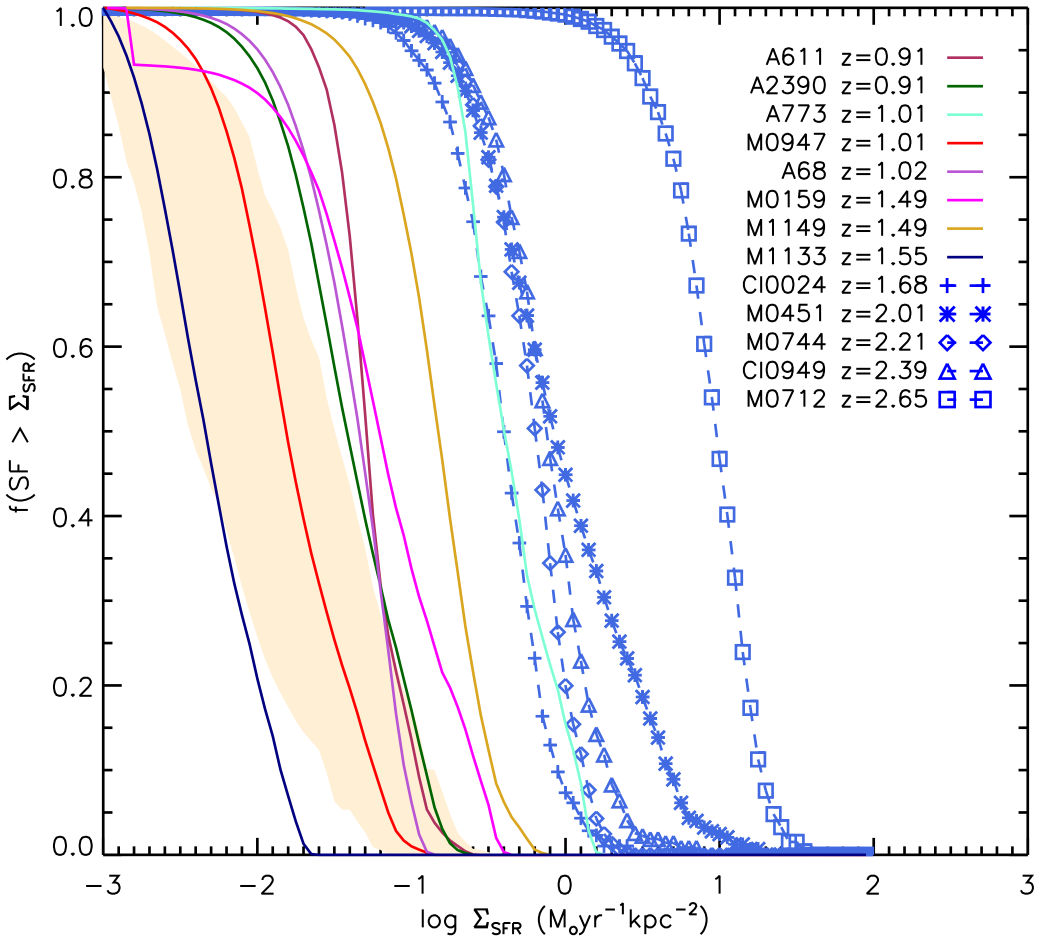

Figure 3.4. The fraction of star formation within each galaxy occurring above a given surface brightness, for the $z \sim 1-1.5$ and $z \sim 2$ samples. The shaded region is the interquartile range of the SINGS $z \sim 0$ sample. There are two galaxies, MACS J1133 and MACS J0947, from the $z \sim 1-1.5$ sample with similar surface brightnesses to the $z = 0$ sample, and the remainder are systematically brighter. The $z \sim 2$ sample has significantly higher surface brightnesses. Hence, there is clear evolution in the surface brightnesses of galaxies with redshift.

clumps would have a lower G, and at the extreme, a galaxy with completely uniform surface brightness would have $G = 0$.

In the $z \sim 1 - 1.5$ sample, we find a narrow range of $0.25 \leq G \leq 0.39$ with a median of $G = 0.34$. The $z \sim 2$ sample is marginally higher, with $0.42 \leq G \leq 0.56$ and a median of $G = 0.43$. The $z = 0$ SINGS sample has a similar median $G = 0.45$ but a much wider range of $0.05 \leq G \leq 0.82$, and the low-z ULIRGs have $0.38 \leq G \leq 0.85$ with the highest median $G = 0.70$. On the basis of the Gini coefficient there are no clear differences between the samples. Comparing the Gini coefficients with the visual appearance of the galaxies, the lack of distinction reflects the fact that a low Gini coefficient may arise from either a smooth distribution of star formation or from star formation that is concentrated into a large number of distinct clumps. Furthermore, we find no strong correlations between G and any of the properties of the galaxies. Clearly, to progress further we will have to compare the properties of individual clumps. In particular, we will show that the clump luminosity function provides a good means of distinguishing different galaxy star formation morphologies.

3.4.2 Properties of star-forming clumps

Definition of Clumps

Studies of HII regions or star-forming clumps have used a variety of methods to define and separate clumps from the background emission of the galaxy. Usually an isophote is defined at 3σ above the background noise (e.g. Gonzalez Delgado & Perez, 1997; Jones et al., 2010). However, this method is clearly dependent on the noise properties of the image, and thus is problematic when comparing local and high-redshift observations. In particular, as high-redshift galaxy images tend to have high relative noise levels and low dynamic range, the choice of isophote tends to select only the brightest regions in the galaxy, neglecting any lower-surface brightness clumps and underestimating their sizes.

An alternative is the IRAF task DAOFIND as employed by Förster Schreiber et al. (2011), which is designed to locate point sources in images. However, we found that it did not perform well on our sample. This is likely to be because DAOFIND requires an expected size of features to look for. As the clumps of Förster Schreiber et al. (2011) are largely unresolved, they were able to use the PSF of their observations as the expected size. As our clumps are resolved, the routine does not work reliably. For this chapter, we therefore use the 2D version of CLUMPFIND (Williams et al., 1994), which uses multiple isophotes to define clumps. We defined the contour levels with respect to the rms noise in the image, starting at 3σ and increasing in 1σ intervals until the peak value of the image is reached. The data are first contoured at the highest level to locate clumps, and the algorithm then works down in brightness through the contour levels. Any isolated contours are defined as new clumps, while others extend existing clumps. If a contour surrounds one existing peak, they are allocated to that clump, and any which enclose two or more are divided using a 'friends-of-friends' algorithm. The advantages of this approach are that it enables a consistent clump definition to be applied to multiple data sets, lower surface brightness clumps are not excluded, and there is no assumption made about the clump profile.

The clumps identified by CLUMPFIND were all confirmed by visual inspection to remove any sources not associated with the target galaxy, of particular importance in the case of the SINGS images where foreground sources lie close to or overlap the target galaxies. The area A of the clump is then obtained from the number of pixels assigned to it, multiplied by the source-plane pixel scale, and from this we define the effective radius $r = \sqrt{A/\pi}$. We only accept clumps where $2r$ is larger than the FWHM of the PSF, so all clumps are resolved.

Due to the manner in which clumps are 'grown,' their sizes returned by CLUMPFIND tend to be larger than those obtained by other methods. As a comparison, we also fit a 2D elliptical Gaussian profile to each peak and measure the FWHM. A comparison of the clump radii found by the two methods is shown in Figure 3.5. The rms difference between the two radii is $\sim$ 100pc, and on average we find that CLUMPFIND outputs sizes 25% higher than the FWHM. Wisnioski et al. (2012a) note that sizes defined through isophotes can be unreliable due to the level of 'tuning' required to select an appropriate isophote level in a given galaxy. This is less significant with CLUMPFIND because this tuning is not required; the use of multiple isophote levels in all galaxies allows the levels to be defined in a consistent way across a large sample. We therefore find much lower scatter between the isophotal sizes output by CLUMPFIND and the clump FWHM than they do in their sample. Throughout this work, we use the CLUMPFIND size for all samples, and give error bars that encompass the FWHM of the clumps.

The sizes and Hα-derived SFRs of the $z \sim 1 - 1.5$ clumps are given in Table 3.2. We analyse these properties in comparison to the other samples below.

Table 3.2. Properties of clumps identified in the $z \sim 1 - 1.5$ sample, determined as described in §3.4.2.

Clump	radius (pc)	SFR ($M_\odot\,yr^{-1}$)
MACS J0947-1	350 ± 56	0.054 ± 0.010
MACS J0947-2	324 ± 22	0.0328 ± 0.0086
MACS J0947-3	384 ± 48	0.045 ± 0.012
MACS J0947-4	334 ± 39	0.0350 ± 0.0092
MACS J0947-5	318 ± 38	0.0339 ± 0.0089
MACS J0947-6	376 ± 6	0.0347 ± 0.0091
MACS J0947-7	311 ± 17	0.0261 ± 0.0068
MACS J0947-8	149 ± 9	0.0050 ± 0.0013
MACS J0159-1	402 ± 89	0.282 ± 0.060
MACS J0159-2	370 ± 77	0.203 ± 0.043
MACS J0159-3	530 ± 130	0.355 ± 0.076
MACS J0159-4	468 ± 13	0.170 ± 0.036
Abell 611-1	730 ± 180	0.370 ± 0.083
Abell 611-2	560 ± 160	0.181 ± 0.041
Abell 611-3	630 ± 140	0.200 ± 0.045
Abell 611-4	390 ± 59	0.065 ± 0.015
Abell 68-1	378 ± 26	0.081 ± 0.016
Abell 68-2	132 ± 8	0.0075 ± 0.0015
Abell 68-3	375 ± 24	0.076 ± 0.015

Continued on next page

Table 3.2 – continued from previous page

Clump	radius (pc)	SFR ($M_\odot\,yr^{-1}$)
Abell 68-4	354 ± 25	0.070 ± 0.014
Abell 68-5	509 ± 31	0.114 ± 0.023
Abell 68-6	337 ± 33	0.062 ± 0.013
Abell 68-7	386 ± 61	0.099 ± 0.020
Abell 68-8	205 ± 42	0.0273 ± 0.0055
Abell 68-9	348 ± 44	0.069 ± 0.014
Abell 68-10	299 ± 89	0.066 ± 0.013
Abell 68-11	328 ± 31	0.057 ± 0.012
Abell 68-12	312 ± 15	0.0476 ± 0.0097
Abell 68-13	412 ± 60	0.100 ± 0.020
Abell 68-14	293 ± 16	0.0429 ± 0.0087
Abell 68-15	263 ± 5	0.0302 ± 0.0061
Abell 68-16	280 ± 50	0.0454 ± 0.0092
Abell 68-17	169 ± 7	0.0132 ± 0.0027
Abell 68-18	195 ± 33	0.0215 ± 0.0044
Abell 68-19	224 ± 6	0.0199 ± 0.0040
Abell 68-20	239 ± 51	0.0344 ± 0.0070
Abell 68-21	135 ± 5	0.0069 ± 0.0014
Abell 68-22	163 ± 23	0.0142 ± 0.0029
Abell 68-23	112 ± 2	0.00489 ± 0.00099

Continued on next page

Table 3.2 – continued from previous page

Clump	radius (pc)	SFR ($M_\odot\,yr^{-1}$)
Abell 68-24	171 ± 31	0.0161 ± 0.0033
Abell 68-25	98 ± 5	0.00416 ± 0.00085
Abell 68-26	122 ± 8	0.0066 ± 0.0013
Abell 2390-1	352 ± 59	0.115 ± 0.025
Abell 2390-2	404 ± 68	0.136 ± 0.030
Abell 2390-3	409 ± 6	0.086 ± 0.019
Abell 2390-4	366 ± 26	0.067 ± 0.015
Abell 2390-5	463 ± 9	0.111 ± 0.024
Abell 2390-6	347 ± 13	0.059 ± 0.013
Abell 2390-7	470 ± 1	0.093 ± 0.020
Abell 2390-8	341 ± 73	0.069 ± 0.015
Abell 773-1	1040 ± 200	5.6 ± 1.3
Abell 773-2	1430 ± 180	9.6 ± 2.2
MACS J1133-1	1120 ± 100	0.118 ± 0.025
MACS J1133-2	890 ± 160	0.068 ± 0.015
MACS J1133-3	790 ± 280	0.057 ± 0.012
MACS J1133-4	835 ± 4	0.0334 ± 0.0072
MACS J1149-1	174 ± 34	0.084 ± 0.020

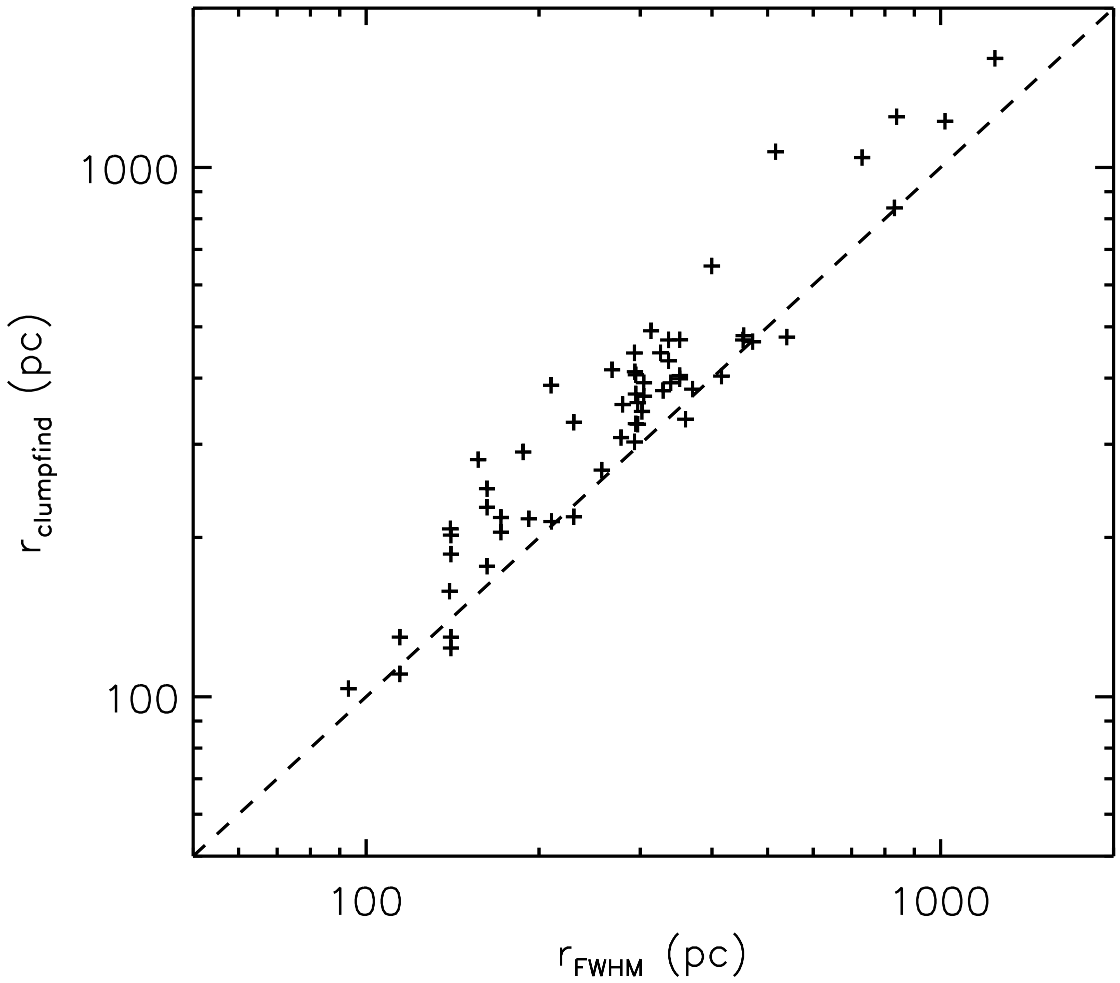

Figure 3.5. Comparison of the clump size $r_{\mathrm{clumpfind}}$ output by CLUMPFIND with the size r_{FWHM} obtained by taking the FWHM of a 2D Gaussian profile fit. On average, CLUMPFIND outputs sizes 25% larger than the FWHM. For consistency, we adopt the isophotal size output by $r_{\mathrm{clumpfind}}$ in all samples.

Clump properties

One way of quantifying the 'clumpiness' of a galaxy is to consider the fraction of a galaxy's total Hα luminosity contained within clumps. We find medians of 31% in SINGS, 36% for the $z < 0.13$ ULIRGs, 50% for the $z \sim 1-1.5$ sample and 68% for the $z \sim 2$ sample. Thus, as expected, the higher-z galaxies are clumpier than their local counterparts.

We now consider the properties of the clumps themselves, and first compare the Hα-derived SFR to the clump radius, as shown in Figure 3.6. Locally, there is a well-defined relationship between these properties, as found by Kennicutt (1988) who found almost constant surface brightness in local HII regions, except in merging and interacting systems (Bastian et al., 2006). The situation at high-z, though, appears different; Swinbank et al. (2009) and Jones et al. (2010) found clumps with SFRs of $\sim 100\times$ higher at a given size than found locally, in systems with no evidence of interactions.

Figure 3.6 is an updated version of one presented in Jones et al. (2010), where we have re-analysed the $z \sim 2$ and SINGS galaxies using CLUMPFIND so that clumps are defined consistently across all samples, and we have added the results from our new $z \sim 1-1.5$ data set and the $z < 0.13$ ULIRGS as well as the $z = 1-2$ results from SHIZELS (Swinbank et al., 2012) and WiggleZ (Wisnioski et al., 2012a). We show lines of median surface brightness in the samples, and vertical offsets from these lines represent differences in the surface density of star formation, $\Sigma_{\rm SFR}$, in the clumps. We will explore the relation of these offsets to global galaxy properties in Section 3.5.

We note that the clumps we identify in the SINGS galaxies are derived from images which have been degraded to comparable resolution to the high-z data, and we find the effect of this is to decrease the surface brightness by a factor of $\sim 2\times$, as the size increases more than the luminosity. The points in Figure 3.6 move along the vector labelled 'A'. Defining clumps in the $z = 0$ sample in this way ensures the fairest possible comparison with the high-z data.

Upon re-analysis using CLUMPFIND, we find some lower Σ_{SFR} regions in the Jones et al. (2010) sample, but they all remain separated from the local relation by a factor of $\sim 100\times$. This confirms the large differences between the local and high redshift population already noted by Swinbank et al. (2009) and Jones et al. (2010).

Our new $z \sim 1 - 1.5$ sample fits in between the SINGS and $z \sim 2$ samples, with the exception of the two regions from the most compact source Abell 773, which have Σ_{SFR} similar to the $z \sim 2$ sample, and the four regions from MACS 1133, which are similar to $z = 0$ clumps. This indicates clear evolution in clump surface brightness, Σ_{SFR}, with redshift.

The surface brightness limit of the $z \sim 2$ data means that we cannot identify the low star formation rate clumps in that sample. We show a dotted line representing the lower limit at which we define clumps in the $z \sim 2$ galaxies. It is likely that there are additional clumps which lie below this limit and are undetected; however, such clumps make only a small contribution to the total SFR, as we shall discuss in Section 3.4.3.

Selection effects have no impact on the lack of high surface brightness regions in the lower redshift samples, however. The intense star-forming regions are clearly

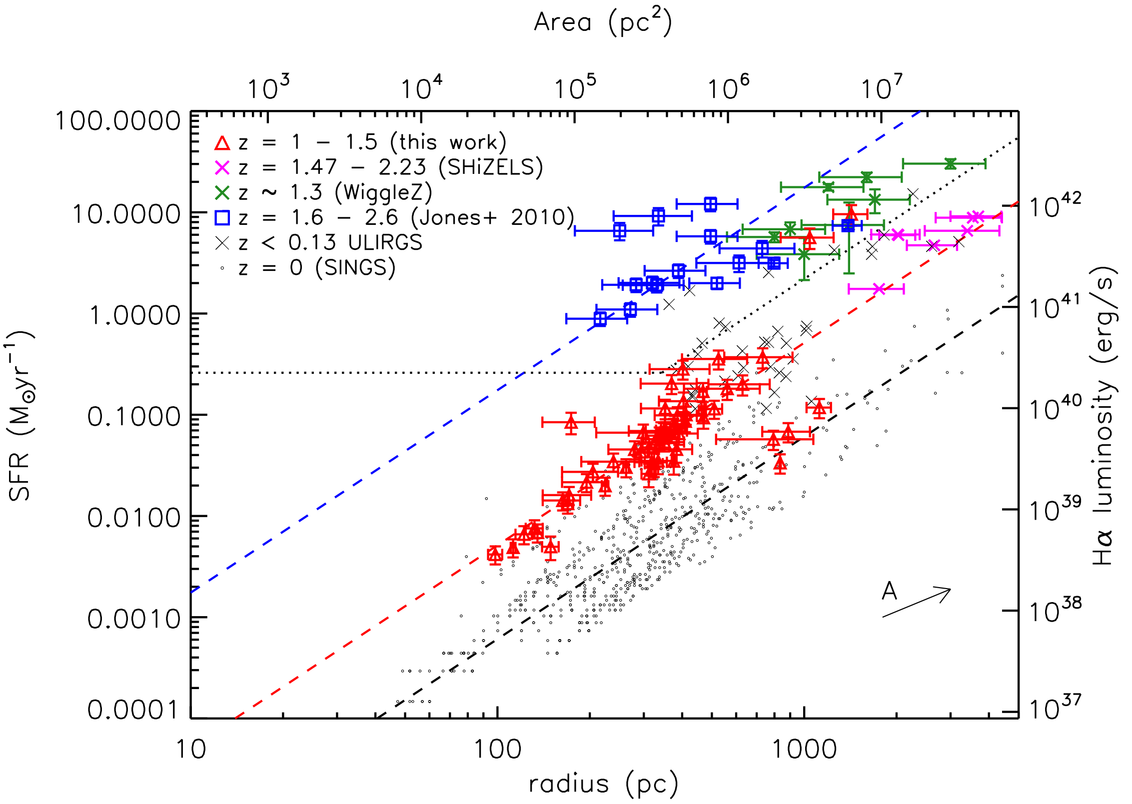

Figure 3.6. Hα SFR for extracted HII regions as a function of size, compared to the lensed $z \sim 2$ sample of Jones et al. (2010), high-z unlensed samples from SHiZELS (Swinbank et al. in prep) and WiggleZ (Wisnioski et al., 2012a), low-z ULIRGs from Rodríguez-Zaurín et al. (2011) and the $z = 0$ SINGS galaxies (Kennicutt et al., 2003). Star formation rates are calculated using the Kennicutt (1998a) prescription adjusted for a Chabrier IMF with a dust extinction $A_{\mathrm{H}\alpha} = 1$ in all samples, and the error bars of the high-z lensed sources are dominated by the uncertainty in the lensing magnification. Dashed lines show the median surface brightnesses in the SINGS, $z \sim 1-1.5$ and $z \sim 2$ samples. The black dotted line indicates the sensitivity limit of the $z \sim 2$ OSIRIS observations. The arrow indicates the effect of degrading the image resolution, as discussed in the text. The four lowest surface brightness clumps in the $z \sim 1-1.5$ sample come from one galaxy (MACS J1133), and the two brightest regions are from Abell 773, the most compact galaxy in the sample. The remaining galaxies have clumps with surface brightnesses in between those of the $z = 0$ and $z \sim 2$ samples, similar to local ULIRGs.

more common in high-z galaxies; they are found only in extreme systems such as the Antennae locally, but exist in all five of the $z \sim 2$ galaxies and one of the eight $z \sim 1 - 1.5$ sample.

As noted in § 3.3.1, the $z \sim 2$ galaxies have 'normal' SFRs for their redshift, below the knee of the Hα luminosity function. The offsets seen in the figure emphasise the importance of analysing clumps in terms of their surface brightness. This is even more evident if the clumps belonging to a single galaxies are examined separately. Rather than being distributed across the plot at random, individual galaxies form a much tighter sequence with all the clumps sharing a common surface brightness, particularly in the low redshift sample. Thus the spread in clump properties in Figure 3.6 appears to be driven by *global* differences in the galaxies.

We therefore next compare the clump $\Sigma_{\rm SFR}$ to the properties of their host galaxies in Figure 3.7. In the left-hand panel, we correlate the clump properties with the total star formation rate of the galaxy. For clarity, we plot the median clump $\Sigma_{\rm SFR}$ in each individual galaxy, and the error bars encompass the central 68% of clumps within each galaxy (i.e. $1\,\sigma$ if they follow a Gaussian distribution). There is evidence for correlation between the clump $\Sigma_{\rm SFR}$ and the galaxy Hα luminosity (which we assume to be proportional to the total SFR); we find a Spearman rank correlation coefficient $\rho = 0.69$, representing a $5.8\,\sigma$ deviation from the null hypothesis of no correlation. This suggests that the star-formation in the high-z sample follows a similar trend to the local sample, and that the differences seen in Fig. 3.6 may arise from the higher total star formation rates of the high redshift galaxies.

For the majority of the samples, an even stronger relation arises if we compare

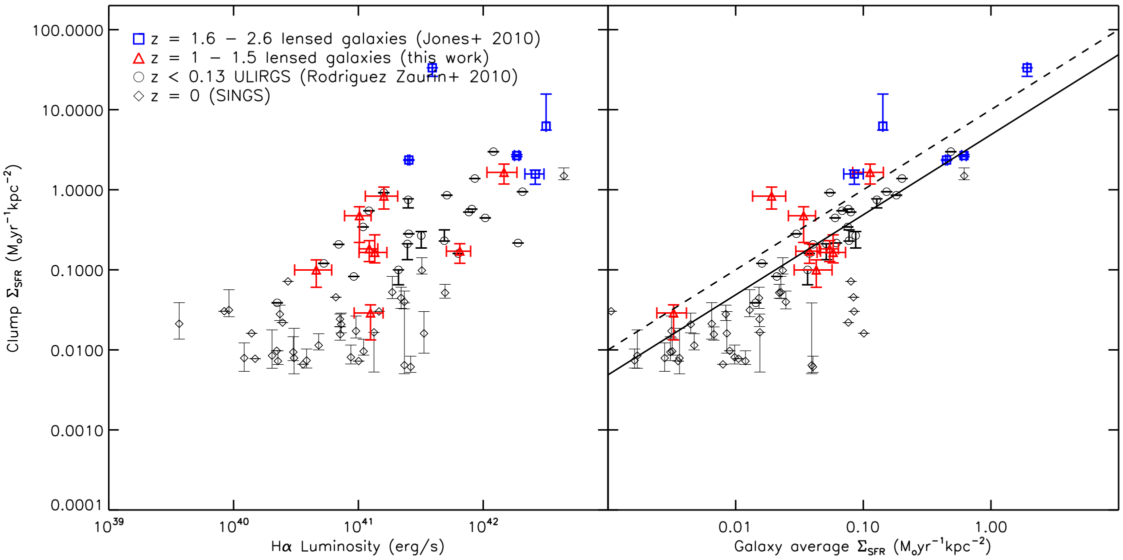

Figure 3.7. Comparisons between the star formation surface density Σ_{SFR} of star-forming clumps within each galaxy and the intrinsic Hα luminosity and galaxy-averaged Σ_{SFR}. The clump Σ_{SFR} shown is the median for each galaxy, with error bars encompassing the full range of Σ_{SFR} for all clumps within each galaxy. The solid line is the best fit to the data, and the dashed line illustrates the clump Σ_{SFR} expected from theory, discussed in Section 3.5. We find that both are correlated at the 5σ level, implying that we find more high-Σ_{SFR} at high redshift because there are more high-SFR and Σ_{SFR} galaxies at this epoch.

the clump Σ_{SFR} to the galaxy-averaged Σ_{SFR}. This is shown in the right-hand panel of Figure 3.7, and has a correlation coefficient $\rho = 0.79$ with $6.6\,\sigma$ significance. The ratio of clump-to-average Σ_{SFR} can be thought of as a measure of the 'clumpiness' of the galaxy.

We conclude that the properties of star-forming clumps in a galaxy are strongly dependent on the global Σ_{SFR} of the galaxy. Galaxies with higher overall Σ_{SFR} have higher clump surface densities and are correspondingly offset in the clump size – star formation rate relation. While this accounts for some of the differences seen in Fig. 3.6, it is also clear that there are more bright clumps in the higher redshift galaxies. We quantify this below.

3.4.3 HII region luminosity functions

A quantitative measure of the clump brightness is to construct a luminosity function (LF) of HII regions. In the local universe, the HII LF is presented in Kennicutt et al. (1989) and Gonzalez Delgado & Perez (1997). They demonstrate that the LF can be fitted by a broken power-law, or by a power-law with an exponential break. In order to be consistent with our definitions of clump sizes, we reanalyse the local data in order to construct our own LF. The results are shown in Figure 3.8. The left panel of the figure shows the cumulative number of regions per galaxy as a function of Hα luminosity. The normalisation of each bin takes into account the different surface brightness limit of the galaxies, with error bars computed from the Poisson error in counting regions. The slope of the power-law part of the mass function is ~ -0.75, so that although the LF appears steep in this representation, most of the

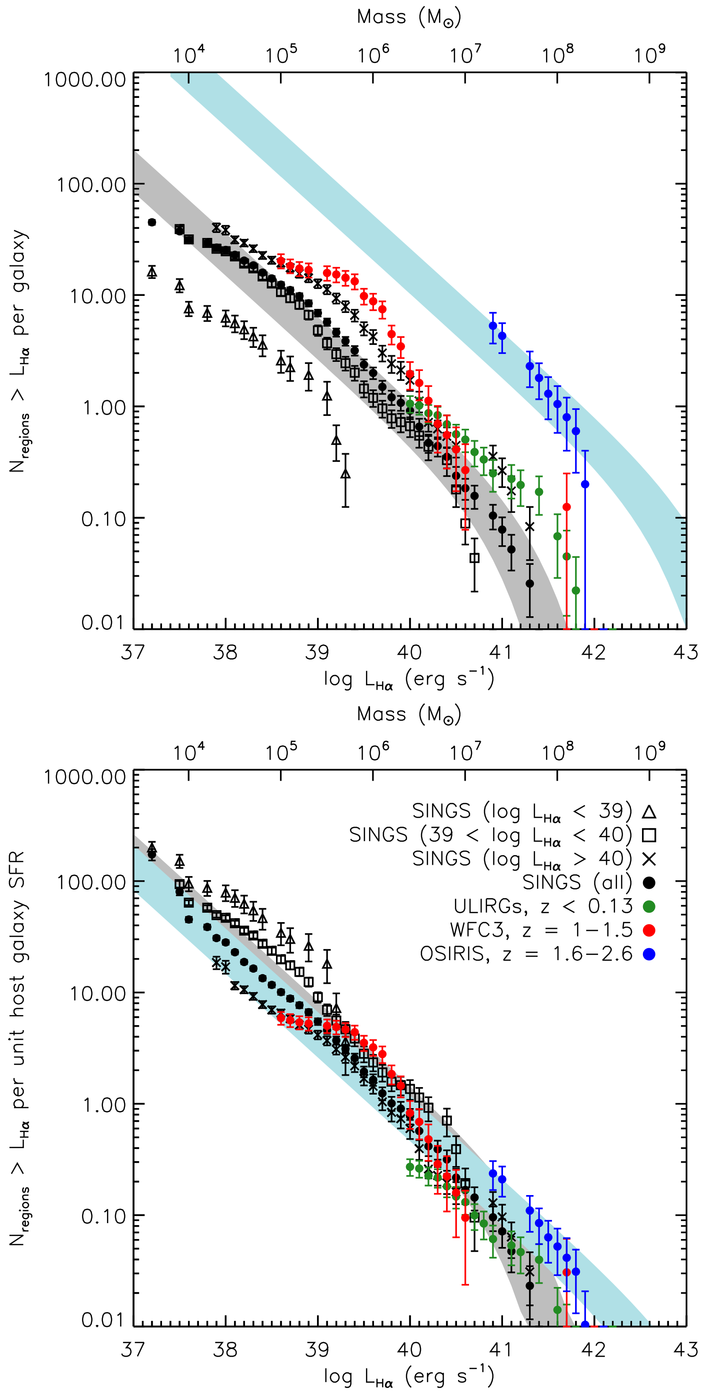

Figure 3.8. Cumulative luminosity functions of HII regions in the SINGS, $z \sim 1 - 1.5$ and $z \sim 2$ samples, shown as a mean per galaxy (*upper*) and normalised by total galaxy Hα luminosity (*lower*). We plot the SINGS sample as a whole and subdivided into three luminosity bins. The shaded regions illustrate model predictions from the GMC mass functions of Hopkins et al. (2012) for Milky Way-like (grey) and high-z (blue) simulations. We find evolution in the HII region luminosity function with redshift, which seems to be driven by the gas fraction of the disc.

total luminosity is contributed by the brightest HII regions.

Solid black points show the average of all SINGS galaxies. However, since we will be comparing the galaxies covering a range of luminosities and redshifts, we have separated the galaxies from the SINGS sample into 3 total Hα luminosity bins. At a fixed luminosity, galaxies with lower total emission have fewer regions, but the shape of the luminosity function is similar. In order to emphasise the similarity of the mass function, we normalise each of the curves by the total star formation rate of the host galaxies, and show this in the right-hand panel. The similarity of all the HII region LFs is now clear.

There is a striking similarity between the LF of the $z \sim 1 - 1.5$ sample and that of the highest SFR galaxies in the low-z SINGS sample. The excess of very bright regions ($L \sim 10^{41}\,\mathrm{erg\,s^{-1}}$) is down to one galaxy, Abell 773, which is the same compact galaxy for which we found the clump surface brightnesses to be more typical of the highest redshift galaxies. The low luminosity slope of the LF tends also to be flatter than that seen in the low redshift galaxies, but it is hard to quantify this difference without directly comparable surface brightness limits and is likely to be affected by unresolved regions which are excluded. In any case, these faint regions contribute little to the total flux.

In both panels, the HII region LF for the highest redshift galaxies is strongly offset from the relation seen in the low redshift SINGS sample and from the sample at $z \sim 1 - 1.5$, but is similar to the low-redshift ULIRGs. Although the data do not probe the low-luminosity slope of the LF, these galaxies have much brighter regions than are seen at lower redshift. The right-hand panel emphasises that this is not because they contain many more regions overall.

In order to compare our data to models of mass functions, we must relate the measured Hα luminosities to model clump mass, M. As an estimate, we use the Hα-derived SFR and adopt SFR ($M_\odot \mathrm{yr}^{-1}$) $= 4.6 \pm 2.6 \times 10^{-8} M_\odot$ (Lada et al., 2010). This empirical relation is based on local molecular clouds and applies to the high-density gas where $A_K > 0.8\,\mathrm{mag}$. However, we note that this relation is consistent with the far-infrared-derived star formation rate and CO-derived gas masses of star-forming clumps reported in a lensed $z = 2.3$ galaxy by Swinbank et al. (2011), but clearly more high-resolution CO observations of high-z galaxies are required to confirm this. As a guide, we include this conversion on the upper axis of Figure 3.8.

The shapes of the LFs can be approximated by a power law with an exponential break at some characteristic high luminosity or mass. The difference between the samples' LFs is then best described by a pure luminosity evolution, so that the break shifts to higher luminosity/mass at higher redshift.

To demonstrate this, we include shaded regions representing a Schechter function of the form

$$N\left(>M\right) = N_0 \left(\frac{M}{M_0}\right)^{\alpha} \exp\left(\frac{-M}{M_0}\right), \qquad (3.4.1)$$

where we adopt the median value of $\alpha = -0.75$ from Hopkins et al. (2012). The normalisation N_0 is arbitrary, so we fit N_0 to the $z = 0$ data and then keep it fixed while allowing M_0 to vary in order to find best-fit values of in the different samples. The fit is carried out on the cumulative LF in order to match Hopkins et al. (2012). The best-fit values are $M_0 = 4.6^{+3.1}_{-2.0} \times 10^7\,M_\odot$ at $z = 0$, $M_0 = 8.0^{+11.0}_{-4.3} \times 10^7\,M_\odot$ at

$z \sim 1-1.5$ and $M_0 = 1.5^{+2.2}_{-1.0} \times 10^9\,M_\odot$ at $z \sim 2$, where the errors are found with a bootstrap method. We shade the best-fit Schechter functions at $z = 0$ and $z \sim 2$ in grey and blue respectively in Figure 3.8. The normalisation of the model in the lower panel is obtained by summing the luminosities of the clumps. The result is in remarkably good agreement with our observations.

Not only do the highest-redshift galaxies have HII regions that are higher surface brightness, but the characteristic luminosity of the regions is higher too. We suggest that the presence of high-luminosity regions may be a good operational definition of the clumpiness of a galaxy.

3.5 Discussion

In the previous section, we presented an analysis of star forming regions in galaxies at $z = 0$, $z \sim 1-1.5$ and $z \sim 2$. We find that the luminosities of the regions in $z = 1$ galaxies are similar to those of bright ($L > 10^{40}\,\mathrm{erg\,s^{-1}}$) galaxies at low redshift, but the surface brightnesses are systematically higher. At higher redshifts, the properties of the galaxies change, with the galaxies having clumps that are both much higher surface brightness and shifted to higher total luminosities. This accounts for the qualitative impression that the most distant galaxies are "clumpier."

We also noted that the increase in the surface brightness of HII regions tracks the increase in the average star formation rate surface density, Σ_{SFR}, of the galaxies. The observations are consistent with the changing properties of the HII regions being driven by changes in the overall Σ_{SFR} of the galaxies. We can link the increase in the observed Σ_{SFR} to an increase in the gas surface density of these galaxies by assuming that the Kennicutt-Schmidt law holds at $z \sim 2$ as well as at $z = 0$. In this case, we have an emerging picture that the changes we see are likely driven by greater gas surface densities at higher redshift.

The connection between the increasing surface density of clumps and the greater peak brightness arises naturally from this picture (Hopkins, 2012). The clump mass required for collapse on scale R from a turbulent ISM is given by the Jean's mass, M_J:

$$\rho_c = \frac{3}{4\pi R^3} M_J \approx \frac{9}{8\pi R^2 G} \sigma_t(R)^2, \tag{3.5.2}$$

where $\sigma_t(R)$ is the line of sight turbulent velocity dispersion. Assuming a turbulent velocity power spectrum $E(k)$, the velocity dispersion $\sigma_t(R)$ for wavenumber $k = 1/R$ is

$$\sigma_t(R)^2 = kE(k) \propto R^{p-1}, \tag{3.5.3}$$

where $p \approx 2$ for supersonic turbulence appropriate to the ISM (Burgers, 1974; Schmidt et al., 2009).

To determine the normalisation of the relation, we assume that the clumps are located in a marginally unstable disc. We note that the available kinematic data for the $z \sim 2$ sample and for MACS J1149 support this assumption, as do larger surveys (Genzel et al., 2011); nonetheless, clearly this is uncertain without dynamical data for the entire sample. However, if we make the assumption that the galaxies are rotating discs with Toomre parameter $Q \approx 1$, we can relate the epicyclic frequency, κ of the disc to its scale height, h: $\kappa \approx \sigma_t(h)/h$ (Hopkins, 2012).

$$Q = \frac{\kappa \sigma_t(h)}{\pi G \Sigma_0} \approx \frac{\sigma_t(h)^2}{\pi G \Sigma_0 h}. \tag{3.5.4}$$

Since the stability of the disc is a global phenomenon, we will associate Σ_0 with the average surface density of the star forming disc, Σ_{disc}, and treat the quantities appearing in Eq. 3.5.4 as appropriate global disc averages. Since the disc is made up of both stars and gas, we must take an appropriate average of the surface densities in the two components. Following Rafikov (2001), and focussing on the largest unstable fluctuations, the appropriate combination of gas and star surface densities (denoted Σ_g and Σ_*) is

$$\Sigma_{\mathrm{disc}} = \Sigma_g + \left(\frac{2}{1+f_\sigma^2}\right)\Sigma_*, \tag{3.5.5}$$

where $f_\sigma = \sigma_*/\sigma_t$ is the ratio of the velocity dispersion of the stellar component to that of the gas.

Assuming $Q \approx 1$, we can write,

$$\sigma_t^2(R) = (\pi G \Sigma_{\mathrm{disc}} h)\left(\frac{R}{h}\right)^{p-1} \approx \pi G \Sigma_{\mathrm{disc}} R, \tag{3.5.6}$$

where we have used Eq. 3.5.3 to relate $\sigma_t(h)$ to $\sigma_t(R)$ as $\sigma_t(R)^2/R^{p-1} = \sigma_t(h)^2/h^{p-1}$. Combining with Eq. 3.5.2 gives a critical density for collapse of

$$\rho_c(R) = \frac{9}{8}\Sigma_{\mathrm{disc}}\frac{1}{R}. \tag{3.5.7}$$

Assuming that the cloud contracts by a factor ≈ 2.5 as it collapses (Murray et al., 2011), the post-collapse surface density is

$$\Sigma_{\mathrm{cloud}} \approx 10\rho_c R \approx 10\,\Sigma_{\mathrm{disc}}. \tag{3.5.8}$$

Thus, for the turbulent power spectrum $p \approx 2$, the surface density of collapsed clouds is independent of radius and proportional to the surface density of the disc. The normalisation of the relation follows from the collapse factor and the requirement that the disc is marginally stable. This model provides a good description of clouds in the Milky Way (Larson's laws) as discussed in Hopkins (2012), and predicts that the surface brightnesses of clouds should increase as the gas surface density (and thus overall average star formation rate surface density) increases. If we assume a constant Kennicutt-Schmidt law of the form $\Sigma_{\rm gas} \propto \Sigma_{\rm SFR}^{1.4}$ (Kennicutt, 1998b), we can compare Eq. 3.5.2 to our data; we therefore overplot this line on Figure 3.7 and find that it is in good agreement with the observations.

Moreover, the model predicts that the most massive clouds should increase in size with the average gas surface density. This follows from the marginal stability condition (Eq. 3.5.4), since density structures on scales greater than h will tend to be stabilised by disc rotation.

This can be demonstrated formally by examining the dispersion relation for a finite thickness disc (Begelman & Shlosman, 2009). Hopkins (2012) shows that this leads to an exponential cut-off of the clump mass function above a mass

$$M_0 \approx \frac{4\pi}{3}\rho_c(h)h^3 = \frac{3\pi^3 G^2}{2}\frac{\Sigma_{\rm disc}^3}{\kappa^4}, \tag{3.5.9}$$

where we have used Equations 3.5.3 and 3.5.4 to express h as a function of $\Sigma_{\rm disc}$ and $\kappa = \sqrt{2}\, v_{\rm disc}/R_{\rm disc}$ (where $v_{\rm disc}$ is the disc circular velocity and $R_{\rm disc}$ is half-mass radius of the disc). Expressing κ in units of $100\,{\rm km\,s^{-1}\,kpc^{-1}}$ we obtain a normalisation of

$$\frac{M_0}{M_\odot} = 8.6 \times 10^3 \left(\frac{\Sigma_{\rm disc}}{10\,M_\odot\,{\rm pc}^{-2}}\right)^3 \left(\frac{\kappa}{100\,{\rm km\,s^{-1}\,kpc^{-1}}}\right)^{-4}. \tag{3.5.10}$$

We can check that this results in a reasonable value of M_0 in the Milky Way by using a gas surface density $\Sigma_{\rm gas} \sim 10\,M_\odot\,{\rm pc}^{-2}$ and a gas fraction of 10% with

$f_\sigma = 2$ (Korchagin et al., 2003) to obtain an effective $\Sigma_{\rm disc} \sim 35\,M_\odot\,{\rm pc}^{-2}$. With $\kappa = 36.7\,{\rm km\,s^{-1}\,kpc^{-1}}$ (Feast & Whitelock, 1997), this gives $M_0 \sim 10^7 M_\odot$, in good agreement with the characteristic mass of the largest Galactic GMCs (Stark & Lee, 2006).

Eq. 3.5.10 shows that the mass function break depends strongly on the disc surface density — the higher the surface density, the more massive the clumps that are able to form. This trend can, however, be opposed by the stabilising effect of angular rotational speed. For a fixed disc radius, a higher circular velocity tends to reduce the mass of the largest clumps.

For low-redshift galaxies, simple theoretical models suggest that $R_{disc} \propto v_{\rm disc}$ since halo spin is weakly dependent on the halo mass (Mo et al., 1998), and thus we should expect the dependence on the disc surface density to be the dominant trend controlling the characteristic clump mass. This is confirmed by analysis of the observed properties of galaxies. For example, Dutton et al. (2011) find

$$\frac{R_{\rm disc}}{\rm kpc} \approx 2.5 \left(\frac{v_{\rm disc}}{100\,{\rm km/s}}\right)^{1.2} \tag{3.5.11}$$

in the local universe. Combining this with the observed dependence of the disc rotation velocity on galaxy mass

$$\frac{M_*}{10^{10} M_\odot} = 0.25 \left(\frac{v_{\rm disc}}{100\,{\rm km/s}}\right)^{4.5}, \tag{3.5.12}$$

we obtain

$$\frac{\kappa}{100\,{\rm km/s\,kpc^{-1}}} \approx 0.38 \left(\frac{M_*}{10^{10} M_\odot}\right)^{-0.04}, \tag{3.5.13}$$

which shows that κ is very weakly dependent on the galaxy mass, and the variation in the clump mass functions of local galaxies is driven is driven by the disc surface density.

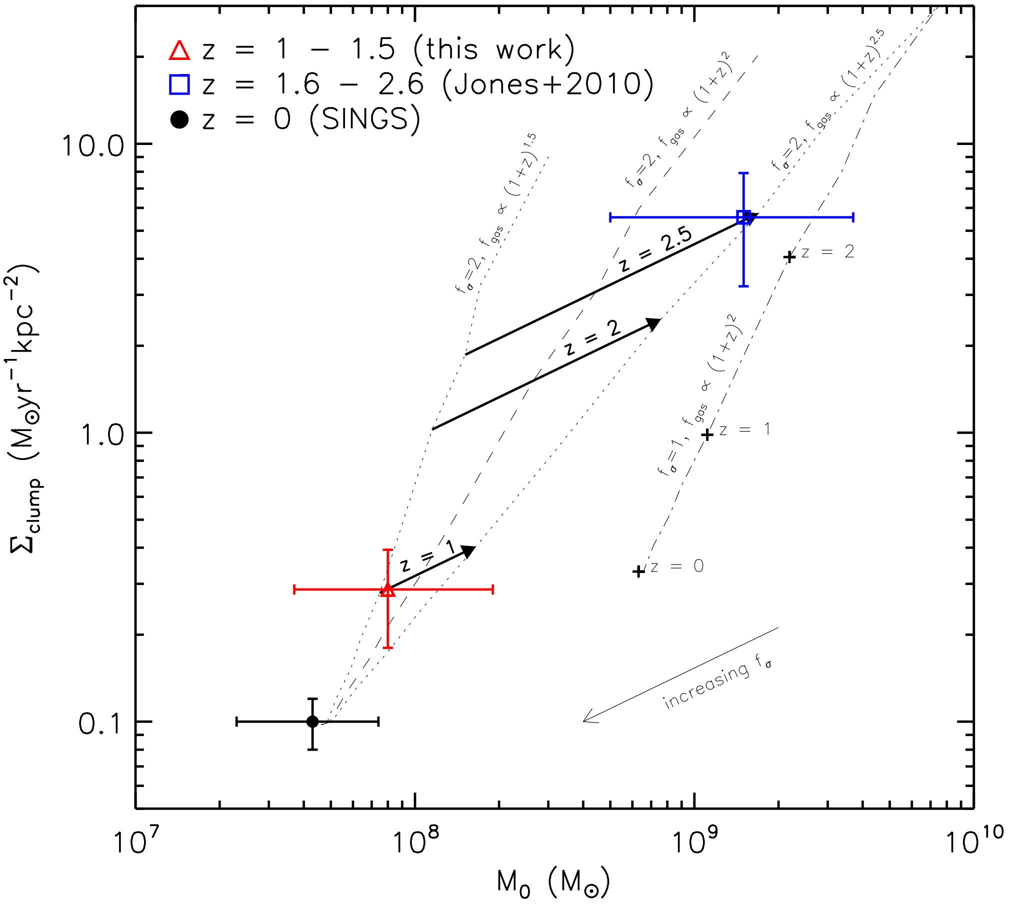

Figure 3.9. The evolution of characteristic mass M_0 and clump surface density $\Sigma_{\rm clump}$ in comparison with model predictions (equation 3.5.10). The model is strongly dependent on the assumed evolution of gas fraction with redshift; we show tracks for $f_{\rm gas} \propto (1+z)^{2\pm0.5}$ and the thick arrows show the effect of increasing the gas fraction. We also show a track for $f_\sigma = 1$ - i.e. assuming that the gas and stars have the same velocity dispersion. This makes the disc unstable on larger scales and would lead to higher-mass clumps at low-z than are observed. The impact of this is reduced at higher-z where gas dominates the disc dynamics. As f_σ increases, the points move in the direction of the arrow in the lower right corner. The model provides a good fit to the data, demonstrating that larger, higher surface brightness clumps at high-z are a natural consequence of increasing gas fractions, which explains the observed morphologies of high-z galaxies.

We also note that in a disc of constant circular velocity, κ scales with radial distance r as $\kappa \propto r^{-1}$, while the gas surface density profiles are shallow, with $\Sigma_{\rm gas} \propto r^{-4/3}$ (Fu et al., 2010). Thus from Eq. 3.5.10 there is no dependence of M_0 on r; while the surface density is higher towards the centre of the galaxy, this is balanced by the higher rotational frequency. This explains the observations that clump properties appear to be driven by the global properties of their host galaxies rather than by local conditions, and this allows us to use disc-averaged values of κ and Σ.

We have no measurements of the gas contents of our samples, but dynamical information available for the $z \sim 2$ sample permits us to predict the characteristic mass in these galaxies from our model if we estimate $\Sigma_{\rm disc}$ from the dynamical mass. Using the measurements reported in Jones et al. (2010, see their Table 2), we compute a characteristic mass ranging from $3.3 \times 10^6 - 3.1 \times 10^9\,M_\odot$ for the $z \sim 2$ sample. The median value is $5 \times 10^7\,M_\odot$, approximately 5× higher than the Milky Way value. We therefore expect that the $z \sim 2$ sample should contain clumps of higher mass and luminosity, as observed. However, the uncertainty in the characteristic mass for the $z \sim 2$ sample is very large due to uncertainties in $\Sigma_{\rm disc}$ and κ, which prevents us from making a precise comparison of the characteristic mass in the different samples.

To understand how the clumpiness of galaxies evolves, we must therefore use simulations to estimate the evolution of their scaling relations. Dutton et al. (2011) present a simple analytic model that seems to describe the observational data well (Förster Schreiber et al., 2009; Trujillo et al., 2006; Williams et al., 2010). We use their scaling relations for mass, size and rotational frequency with redshift in combination with Eq. 3.5.8 and Eq. 3.5.10 to predict how the characteristic mass and clump surface brightness should evolve with redshift. Figure 3.9 illustrates this evolution for a gas fraction evolution of $f_{\rm gas} \propto (1+z)^{2\pm0.5}$ (Geach et al., 2011). The arrows show how altering the assumed gas fraction changes the model. This suggests that the changing clump properties are a natural consequence of increasing gas fractions dominating high-z galaxy dynamics. The high gas fractions probably arise from high gas infall rates at high redshift (Bournaud et al., 2011; Bournaud & Elmegreen, 2009; Krumholz & Dekel, 2010); however, our observations do not directly rule in or out cold flows. Our results merely require high gas fractions, and cold flows are a method of maintaining the gas supply. Crucially, we note that this effect is tempered by the more compact nature of galaxies, which leads to higher epicyclic frequencies that limit the collapse on larger scales. The need to include the κ term is apparent from our HII region luminosity functions: without it, a factor 10 increase in disc surface density would correspond to an increase in clump luminosity of 1000×, and we do not observe such a large increase.

To summarise, we find that our simple theoretical model is in good agreement with the observations and suggests that the evolving 'clumpiness' of galaxies is a manifestation of the different characteristic mass of the HII region luminosity function, which is driven by evolution in the gas fraction with redshift.

3.6 Conclusions

We have used *HST/WFC3* to obtain narrowband Hα imaging of eight gravitationally lensed galaxies at $z \sim 1-1.5$. The magnification provided by the lensing enables us to reach spatial resolutions in the source plane of $68-615\,\mathrm{pc}$. In addition, to provide comparisons we have re-analysed the lensed $z \sim 2$ sample observed with Keck/OSIRIS by Jones et al. (2010), the Rodríguez-Zaurín et al. (2011) sample of $z < 0.13$ (U)LIRGs observed with VLT/VIMOS and the Hα narrowband imaging of the $z = 0$ SINGS survey (Kennicutt et al., 2003).

The high-z samples have 'clumpy' morphologies, dominated by a few large regions of high Hα luminosity, which we use as a proxy for the SFR. We have extracted star-forming clumps from the galaxies in each sample and examined their properties. The clumps follow similar SFR-size scaling relations in all samples, but the normalisation of the relation exhibits systematic offsets to higher surface brightness at higher redshifts. The normalisation appears to be approximately constant within a given galaxy, implying that this relation is driven by global galaxy properties.

On comparison with the properties of the host galaxies, we find that all samples follow approximately the same scaling relations between the clump surface brightness and both the host galaxy's total Hα luminosity, $L_{\mathrm{H}\alpha}$, and its average surface density of star formation, Σ_{SFR}, and that they evolve along this relation in decreasing $L_{\mathrm{H}\alpha}$ and Σ_{SFR} with decreasing redshift.

We have measured the luminosity function of clumps in the samples, and shown that the $z \sim 1-1.5$ sample is similar to the higher-$L_{\mathrm{H}\alpha}$ members of the SINGS sample. When normalised by the host galaxies' total SFR, the SINGS and $z \sim 1-1.5$

samples can be fit by the same Schechter function, while the ULIRGs and $z \sim 2$ samples are offset horizontally. This shift can be explained by an increase in the characteristic mass of the HII region luminosity functions of the ULIRGs and $z \sim 2$ discs.

We present a simple theoretical model which shows that the evolution in luminosity and surface brightness are connected, and are driven by the competing effects of disc surface density $\Sigma_{\rm disc}$ and the epicyclic frequency κ. Galaxies at high redshift tend to have higher $\Sigma_{\rm disc}$, which increases the maximum mass of clumps that are able to form; however, this is tempered by the more compact nature of high-z galaxies, implying higher κ, which impedes collapse on the largest scales.

We have shown that this model is consistent with the evolution in clump properties seen in our data. We therefore conclude that the clumps observed in high-z galaxies are star-forming regions analogous to those found locally but with higher masses and surface brightnesses. As HII regions in the distant Universe are larger and brighter, they give rise to the 'clumpy' appearance. The increase in clump luminosity is driven primarily by increasing gas fractions at high-z. This clearly motivates further study with ALMA to better quantify the evolution of gas properties in high-z galaxies.

Chapter 4

Observational limits on the gas mass of a $z = 4.9$ galaxy

4.1 Overview

We present the results of a search for molecular gas emission from a star-forming galaxy at $z = 4.9$. The galaxy benefits from magnification of $22 \pm 5\times$ due to strong gravitational lensing by the foreground cluster MS1358+62. We target the CO(5–4) emission at a known position and redshift from existing *Hubble Space Telescope*/*ACS* imaging and Gemini/NIFS [OII]3727 imaging spectroscopy, and obtain a tentative detection at the $4.3\,\sigma$ level with a flux of $0.104 \pm 0.024\,\mathrm{Jy\,km\,s^{-1}}$. From the CO line luminosity and adopting a CO-H$_2$ conversion factor $\alpha = 2\,\mathrm{M_\odot}\ (\mathrm{K\,km\,s^{-1}\,pc^2})^{-1}$, we derive a gas mass $M_{\mathrm{gas}} \sim 1^{+1}_{-0.6} \times 10^9\,\mathrm{M_\odot}$. Combined with the existing data, we derive a gas fraction $M_{\mathrm{gas}}/\left(M_{\mathrm{gas}} + M_*\right) = 0.59^{+0.11}_{-0.06}$. The faint line flux of this galaxy highlights the difficulty of observing molecular gas in representative galaxies at this epoch.

4.2 Introduction

Extensive studies of optically-selected star-forming galaxies seen at the epoch of peak cosmic star-formation density ($z \sim 2$) have revealed star-formation rates (SFRs) of 10-100 $\mathrm{M_{\odot} yr^{-1}}$ and stellar masses of $\sim 10^{10-11} \mathrm{M_{\odot}}$ (e.g. Daddi et al., 2010a; Förster Schreiber et al., 2009; Law et al., 2009; Tacconi et al., 2010). If these SFRs have been continuously maintained, then these galaxies must have undergone their first major epoch of stellar mass assembly 1–2 Gyr earlier, at $z \sim 5$, when the bulk of the star-forming population was $\sim 5\times$ less massive (McLure et al., 2009; Stark et al., 2010; Verma et al., 2007).

The star formation within these galaxies is fuelled by reservoirs of predominantly cold molecular hydrogen, H_2. Since the H_2 is not directly detectable, CO emission at millimetre wavelengths has been employed to trace the cold molecular gas. However, exploring gas properties of galaxies beyond $z \sim 3$, is challenging; not only does the apparent surface brightness reduce as $(1 + z)^{-4}$, but the galaxies themselves also appear systematically smaller and intrinsically fainter making detections of their molecular gas emission difficult.

To date, studies of molecular line emission at $z > 3$ have been limited to extreme populations such as gas-rich quasars (e.g. Walter et al., 2009) and submillimetre galaxies (SMGs; Carilli et al., 2010; Coppin et al., 2010; Riechers et al., 2011). Detecting typical star-forming galaxies at $z > 3$ has proven difficult because the CO line luminosities are usually below the sensitivity limits of current facilities (Davies et al., 2010; Stanway et al., 2008).

However, it is still possible to study less active high-z galaxies which are strongly gravitationally lensed by massive galaxy clusters. The magnification provided by gravitational lensing has enabled detections of molecular gas in a number of star-forming galaxies up to $z \sim 3$ (e.g. Baker et al., 2004; Coppin et al., 2007; Danielson et al., 2011; Riechers et al., 2011), and more recently $z \sim 4-6$ (e.g. Combes et al., 2012; Cox et al., 2011). The physical properties of the interstellar medium appear similar to those in local ULIRGs, with high gas fractions, high densities and intense UV radiation fields.

Franx et al. (1997) reported the detection of a multiply-imaged $z = 4.9$ galaxy which is gravitationally lensed by the massive galaxy cluster MS 1358+62. Correcting for lensing, this galaxy (hereafter MS1358-arc) appears to be representative of the star-forming population at this epoch (its lensing-corrected apparent magnitude is I_{AB}=24.9, marginally brighter than the characteristic luminosity of $\mathrm{I}_{AB} = 25.3$ at $z \sim 5$; Ouchi et al. 2004). Swinbank et al. (2009, hereafter S09) carried out a detailed study of one image of the MS1358-arc system, using optical and infrared imaging combined with integral field spectroscopy, revealing a rotating system across 2 kpc in projection, with star formation occurring in five bright clumps.

In this chapter, we report observations with the Plateau de Bure Interferometer to search for CO(5-4) emission in MS1358-arc. Throughout, we adopt a ΛCDM cosmology with $H_0 = 70\,\mathrm{km\,s^{-1}\,Mpc^{-1}}$, $\Omega_\Lambda = 0.7$ and $\Omega_m = 0.3$.

4.3 Observations and Data Reduction

The MS1358+62 system is illustrated in Figure 4.1, with the positions of the two images of MS1358-arc marked (Table 4.1). We estimate the amplification of each image using the lens model of Richard et al. (2008) with LENSTOOL (Jullo et al., 2007; Kneib, 1993), with errors accounting for the magnification gradient across the image. The combined magnification factor for Image 1 and 2 is $\mu = 22 \pm 5$.

To search for the CO(5–4) emission, we observed MS1358-arc with the IRAM Plateau de Bure Interferometer (PdBI; Guilloteau et al., 1992), using six antennae in D (compact) configuration. The pointing centre was $\alpha_{2000}, \delta_{2000} = 13:59:48.7, +62:30:48.34$, and the frequency was tuned to the CO(5–4) transition (rest frame 576.2679 GHz) redshifted to 97.185 GHz (based on the [OII]-derived systemic redshift of $z = 4.9296 \pm 0.0002$ from S09). The observations were made between 2010 June 4 and 2010 June 6 with total on-source time of 10 hours, using WIDEX, the new high-bandwidth correlator, with a resolution of 2.5 MHz. The star MWC349 was observed as the primary flux calibrator, with the quasars 1749+096, 0923+392 and 2145+067 as secondary flux calibrators. Receiver bandpass calibration was performed against 0923+392 and 3C454.3, and 1435+638 and 1418+546 were used for phase and amplitude calibration.

The data were reduced with the GILDAS software package (Guilloteau & Lucas, 2000) and resampled to a velocity resolution of 38.6 km s^{-1}. The synthesised beam is a Gaussian ellipse with a FWHM size of $5.6 \times 4.3''$ at a position angle of 111^o.

The PdBI observations were centred on the two brightest images of the $z \sim 5$ galaxy. The images are both within 6” of the pointing centre, whereas the primary beam of PdBI at 3mm is 50”; we have therefore not corrected for primary beam attenuation, which is negligible. First, we construct a channel map from a 90km s^{-1} window around the CO(5–4) emission line centred at the systemic redshift, and

Table 4.1. Positions of the three images of MS1358-arc within the Plateau de Bure field of view and the mean linear magnification factor (μ). The position of the third image is included for completeness, but is excluded from our analysis as it lies outside the primary beam.

Image	RA (J2000)	Dec (J2000)	μ
Image 1	$13^h59^m48.684^s$	$62^o30'48.54''$	12.4 ± 3
Image 2	$13^h59^m49.430^s$	$62^o30'45.13''$	9.5 ± 4
Image 3	$13^h59^m54.746^s$	$62^o31'5.21''$	2.9 ± 0.1

show as an inset in Figure 4.1, with contours at $\pm 1\sigma$ intervals. The positions of the images within the PdBI cube are determined by aligning the cube with the *HST* image and taking the centre of the corresponding pixels.

We also extract spectra from these positions and show these in Figure 4.2. Individually, the two images are clearly extremely faint; by comparing the $\Delta\chi^2$ of a Gaussian profile to that of a continuum-only fit, measuring the noise over a $1200\,\mathrm{km\,s^{-1}}$ channel, the significances of the CO(5–4) emission lines in Images 1 and 2 are 3.3σ and 2.7σ respectively. However, since they are separated by more than one beam width, we can improve the signal to noise by coadding the spectra at the two positions using uniform weights (Figure 4.2); we then obtain a 1σ rms channel sensitivity of 0.4 mJy. Again comparing the χ^2 of a Gaussian profile fit to that of a continuum-only fit, we use the $\Delta\chi^2$ to derive a significance level of $4.3\,\sigma$ for the coadded CO(5–4) emission line.

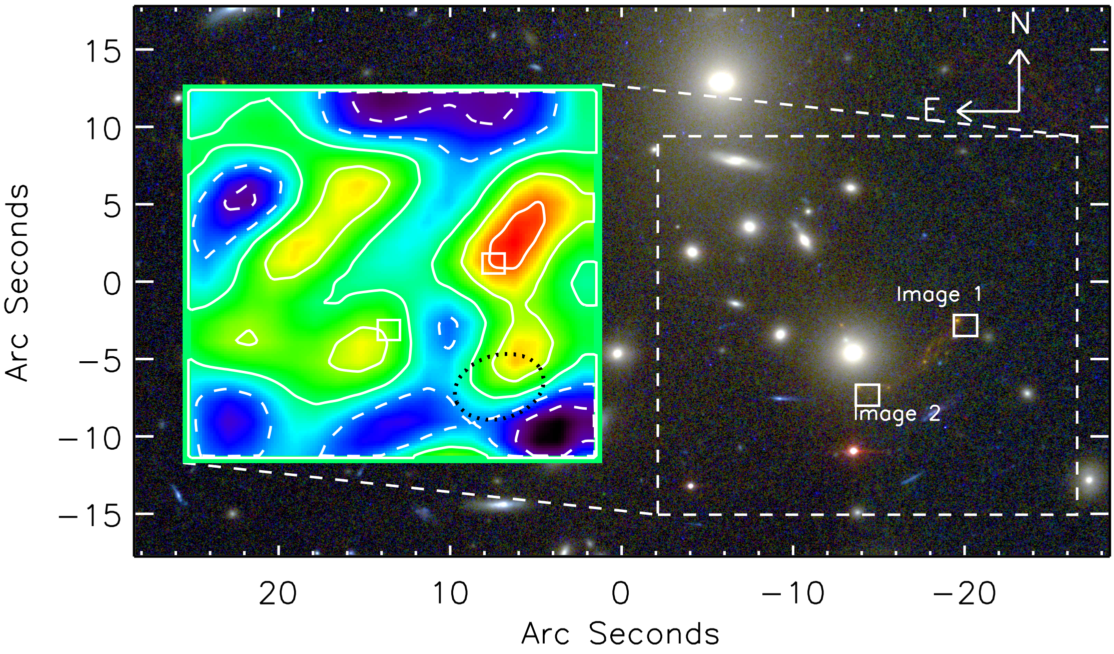

Figure 4.1. *Hubble Space Telescope (HST)/ACS* image of the core of MS1358+62. The squares mark the extent of the pixels in the PdBI cube used to extract the spectra shown in Figure 4.2. A Plateau de Bure channel map constructed from a 90km s^{-1} window around the systemic velocity of the CO(5-4) line is shown as an inset. The PdBI synthesised beam size is indicated by the dotted ellipse in the inset. Contours are shown in $\pm 1\sigma$ intervals, with negative contours indicated by dashed lines. The origin of the *HST* image coordinate system is $(\alpha_{2000}, \delta_{2000}) = (13^h 59^m 51.4^s, +62^o 30' 52.5'')$.

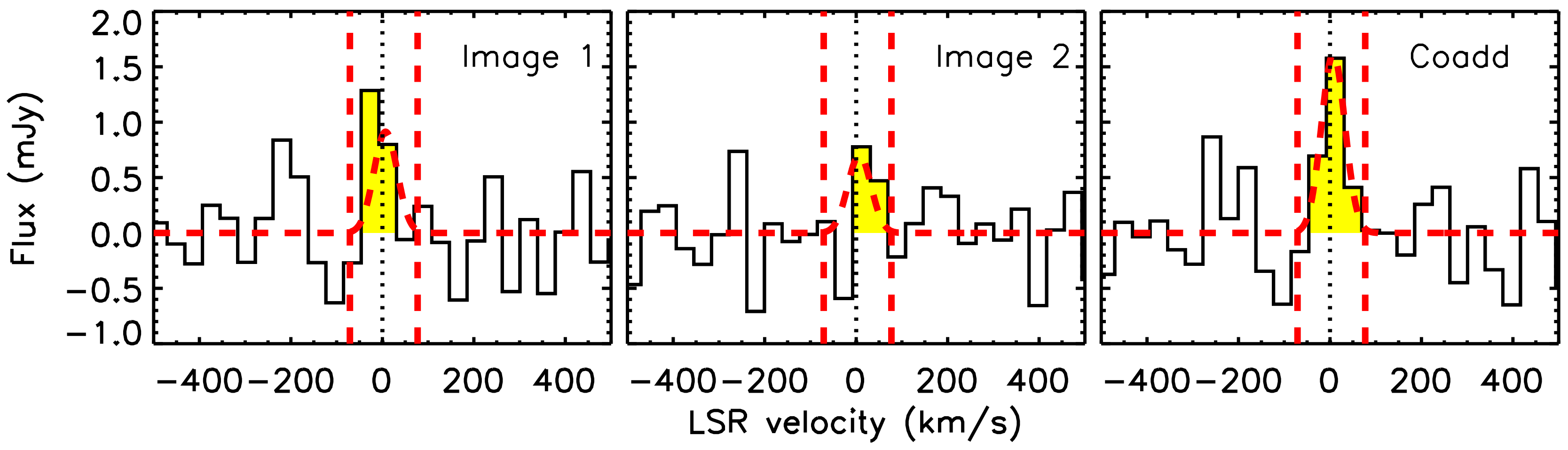

Figure 4.2. The CO(5–4) spectra extracted from the two images of MS1358-arc and the coadd of these spectra. The velocity scale is centred on the systemic redshift $z = 4.9296$, and the expected position of the CO(5–4) emission line is indicated by a black dotted line. The spectra are binned into $38.6\,\mathrm{km\,s^{-1}}$ channels. The best-fit Gaussian profile to the coadded spectrum is overlaid as a guide, scaled to the relative amplifications of the two images, and the velocities of the two brightest star-forming clumps measured by S09 are indicated by vertical lines. Each image shows positive flux at the systemic redshift of MS1358-arc, but individually they are only detected at $\sim 3\sigma$ significance.

Whilst the emission line centroid is extremely well-matched to the best-fit redshift of the nebular emission, the line is weak, highlighting the difficulty of these observations even with long integrations. We perform a number of tests to validate the robustness of the detection. First, we check how often a detection is made when coadding two random spectra from the original (non-coadded) cube. We generate 1000 combinations of two randomly-selected pixels on the map (excluding pixels which lie within one beam of MS1358-arc), then fit a Gaussian profile to the resulting coadded spectrum and compare this to a continuum-only fit. The probability of finding an emission line of equal significance to the target from two randomly-selected positions with a velocity centroid lying within $\pm 150\mathrm{km\,s^{-1}}$ of the redshift of MS1358-arc and a line width in the range $\sigma = 30 - 250\,\mathrm{km\,s^{-1}}$ is 0.05%.

The CO(5–4) emission line we measure is centred at $z = 4.9297 \pm 0.0001$ with a line flux of $0.104 \pm 0.024\,\mathrm{Jy\,km\,s^{-1}}$ and Full Width at Zero Intensity of FWZI $= 150 \pm 20\,\mathrm{km\,s^{-1}}$, comparable to the velocity gradient measured across the source by S09. Error bars are obtained by fitting a Gaussian profile to the line and perturbing it in intensity, velocity and width to obtain a $\Delta\,\chi^2 = 1$ error surface, using a Monte Carlo routine with 10^5 realisations centred on the best fit.

We also construct a coadded channel map from the PdBI cube by extracting regions centred on the two images and co-adding them. The coadded cube is then spatially convolved with the PdBI beam, and spectrally convolved with a Gaussian with FWHM $= 100\,\mathrm{km\,s^{-1}}$. We estimate the noise at each spatial position using the off-line spectrum at that position, and divide the signal in the on-line slice of the convolved datacube by this noise map to construct a signal-to-noise map, shown in

Figure 4.3. We find that 99.95% of the pixels have lower signal-to-noise than the target. This is equivalent to a detection significance of $3.5\,\sigma$.

In the following analysis, we treat the line flux as $0.104 \pm 0.024\,\mathrm{Jy\,km\,s^{-1}}$, but discuss the implications of treating it as an upper limit in Section 4.5.

4.4 Results, Analysis and Discussion

4.4.1 CO Dynamics, Luminosity and Molecular Gas Mass

Using the combined spectrum of Images 1 and 2, we first estimate the line luminosity and gas mass. Following Solomon & Vanden Bout (2005), the line luminosity is $L'_{\mathrm{CO(5-4)}} = (3.6 \pm 0.8) \times 10^9\,\mathrm{K\,km\,s^{-1}\,pc^2}$. Adopting a magnification factor of $\mu = 22 \pm 5$, this indicates an intrinsic $L'_{\mathrm{CO(5-4)}} = (1.6 \pm 0.5) \times 10^8\,\mathrm{K\,km\,s^{-1}\,pc^2}$.

To convert this CO(5–4) luminosity to a total molecular gas mass, we must first estimate the corresponding CO(1–0) line luminosity. We therefore exploit recent observations of $z = 2 - 4$ galaxies where the ratio $L'_{\mathrm{CO(5-4)}}/L'_{\mathrm{CO(1-0)}}$ has been measured directly and adopt $L'_{\mathrm{CO(5-4)}}/L'_{\mathrm{CO(1-0)}} = 0.32 \pm 0.05$ (Bothwell et al., 2013), which we note is consistent with the ratios found by Danielson et al. (2011) and Carilli et al. (2010). Applying this ratio to MS1358-arc, we estimate $L'_{\mathrm{CO(1-0)}} = (5.0 \pm 1.7) \times 10^8\,\mathrm{K\,km\,s^{-1}\,pc^2}$.

To derive the molecular gas mass M_{gas} from $L'_{\mathrm{CO(1-0)}}$, we assume $M_{\mathrm{gas}} = \alpha L'_{\mathrm{CO(1-0)}}$ where α is the coefficient relating the CO to $\mathrm{H_2}$+He gas mass. We can derive an absolute lower limit for α by assuming that the molecular gas is enriched to solar metallicity and is optically thin to CO radiation. From Ivison et al. (2010),

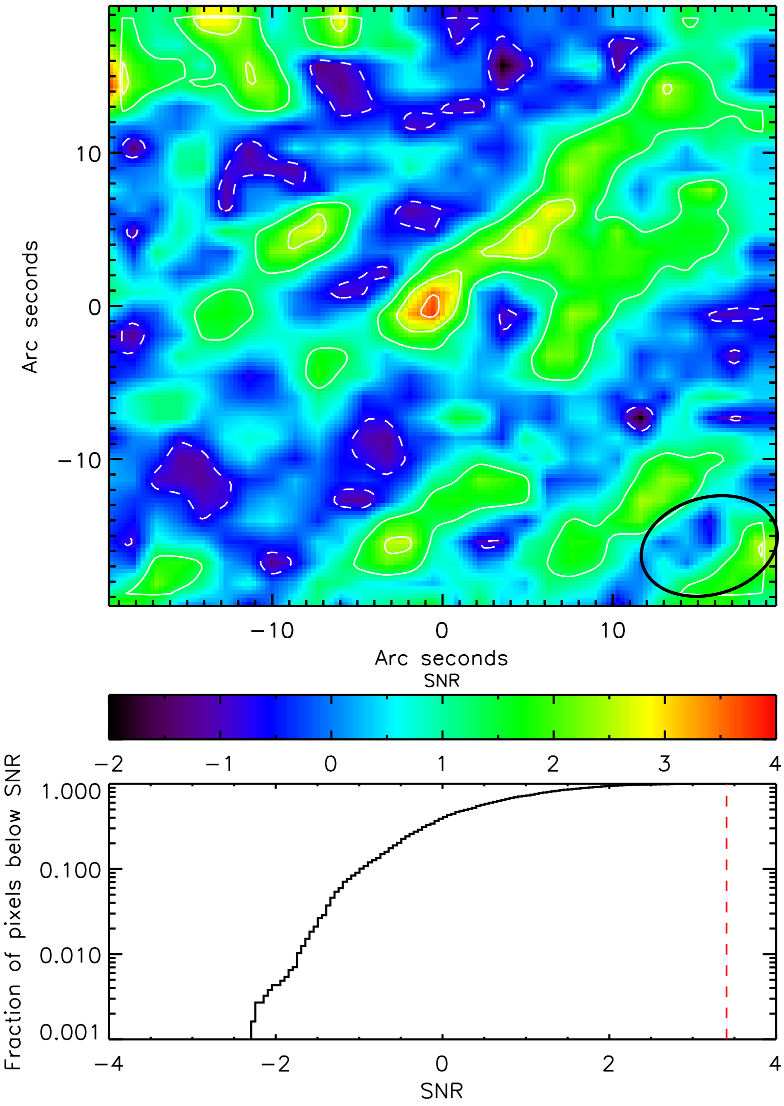

Figure 4.3. *Upper:* The coadded PdBI signal-to-noise channel map, constructed by extracting and coadding regions around each of the two images of MS1358-arc, convolved spatially with the beam and in the spectral direction with a Gaussian profile with FWHM= $100 \mathrm{km\,s}^{-1}$, and then dividing each pixel by its noise. The combined image of the two targets is located in the centre of the map. The solid lines are intensity contours in $\pm 1\sigma$ intervals, with negative contours indicated by dashed lines. The beam size is indicated by the black ellipse line in the lower right-hand corner. *Lower:* Cumulative histogram of the signal-to-noise in the map, with the central pixel marked as a red dashed line. We find that just 0.05% of pixels have higher signal-to-noise than the emission seen from the source, suggesting a 3.5σ detection.

we have $\alpha \gtrsim 0.7\,\mathrm{M}_\odot\ (\mathrm{K\,km\,s^{-1}\,pc^2})^{-1}$, which is consistent with the value $\alpha = 0.8\,\mathrm{M}_\odot\ (\mathrm{K\,km\,s^{-1}\,pc^2})^{-1}$ applied to local (Ultra) Luminous InfraRed Galaxies ((U)LIRGs; Solomon & Vanden Bout, 2005). However, recent studies of high-z star-forming galaxies have suggested that $\alpha \sim 2\,\mathrm{M}_\odot\ (\mathrm{K\,km\,s^{-1}\,pc^2})^{-1}$ may be a more appropriate conversion factor (e.g. Danielson et al., 2011; Ivison et al., 2011). Adopting this value, we find $M_{\rm gas} = 1^{+1}_{-0.6} \times 10^9\,\mathrm{M}_\odot$, where we conservatively estimate a factor of 2× uncertainty in α.

Combining our gas mass estimate with the stellar mass $M_* = 7 \pm 2 \times 10^8\,\mathrm{M}_\odot$ derived by S09, we obtain a total baryonic mass of $M_{\rm baryon} = M_* + M_{\rm gas} = 1.7^{+1.0}_{-0.6} \times 10^9\mathrm{M}_\odot$. This is consistent with the dynamical mass within 2kpc derived by S09 of $M_{\rm dyn} = 3 \pm 1 \times 10^9 \csc^2(i)\,\mathrm{M}_\odot$, if the inclination is high.

The gas fraction $f_{\rm gas} = M_{\rm gas}/\left(M_{\rm gas} + M_*\right)$ is typically $< 10\%$ in local large spiral galaxies (Young & Scoville, 1991), or $\sim 33\%$ in local ULIRGs (Solomon et al., 1997). Other studies of molecular gas in high-redshift galaxies are beginning to find a trend for higher gas fractions at higher redshifts (Geach et al., 2011; Tacconi et al., 2010), which is in line with expectations from hydrodynamical simulations (Crain et al., 2009). For MS1358-arc, we find $f_{\rm gas} = 0.59^{+0.11}_{-0.06}$. To determine the error bars, we use a Monte Carlo method taking random samplings from distributions of $M_{\rm gas}$ and M_* with Gaussian statistical errors on the measurements and a uniform distribution of values of α. The errors represent the interquartile range of the resulting distribution of gas fractions.

In Figure 4.4, we compare the gas fraction of MS1358-arc to samples at lower redshift (see also Geach et al., 2011). The sample size is currently too small to draw any firm conclusions, and there are of course significant selection effects involved. We therefore caution that there are limits to the extent of any physical interpretation of this result, although it clearly motivates a uniformly-selected survey of the gas properties of high-redshift star-forming galaxies.

We can also use the dynamics of the [OII] emission to test whether the molecular gas is colocated with the star formation. In Figure 4.2, we overplot the redshifts of the two brightest star-forming knots, which are located at $\pm 150\,\mathrm{km\,s^{-1}}$ from the dynamical centre. Hence, if the CO gas traced the [OII] emission we would expect a FWZI of $\sim 300\mathrm{km\,s^{-1}}$, higher than the observed line width. This may indicate that the CO emission is associated with the dynamical centre of the galaxy rather than being concentrated in the star-forming regions or associated with the outflowing Lyα and UV-ISM lines (S09).

4.4.2 Gas depletion timescales

S09 derived a star formation rate (SFR) of $42 \pm 8\,\mathrm{M_\odot\,yr^{-1}}$ using the Kennicutt (1998a) conversion from [OII] luminosity to SFR. We note that this conversion is consistent with the empirical correction to this calibration of Gilbank et al. (2010), which accounts for the metallicity dependence of the [OII]-derived SFR.

If MS1358-arc has sustained this SFR continuously, then the time taken to build up the current stellar mass of $7 \pm 2 \times 10^8\,\mathrm{M_\odot}$ is just $\tau_{\rm build} \sim 17\,\mathrm{Myr}$ (consistent with the age and star formation history used to derive the stellar mass). This suggests we may be seeing this galaxy in its first epoch of star formation. If this SFR is maintained at a constant level, the gas supply of $1 \times 10^9\,\mathrm{M_\odot}$ will be exhausted in

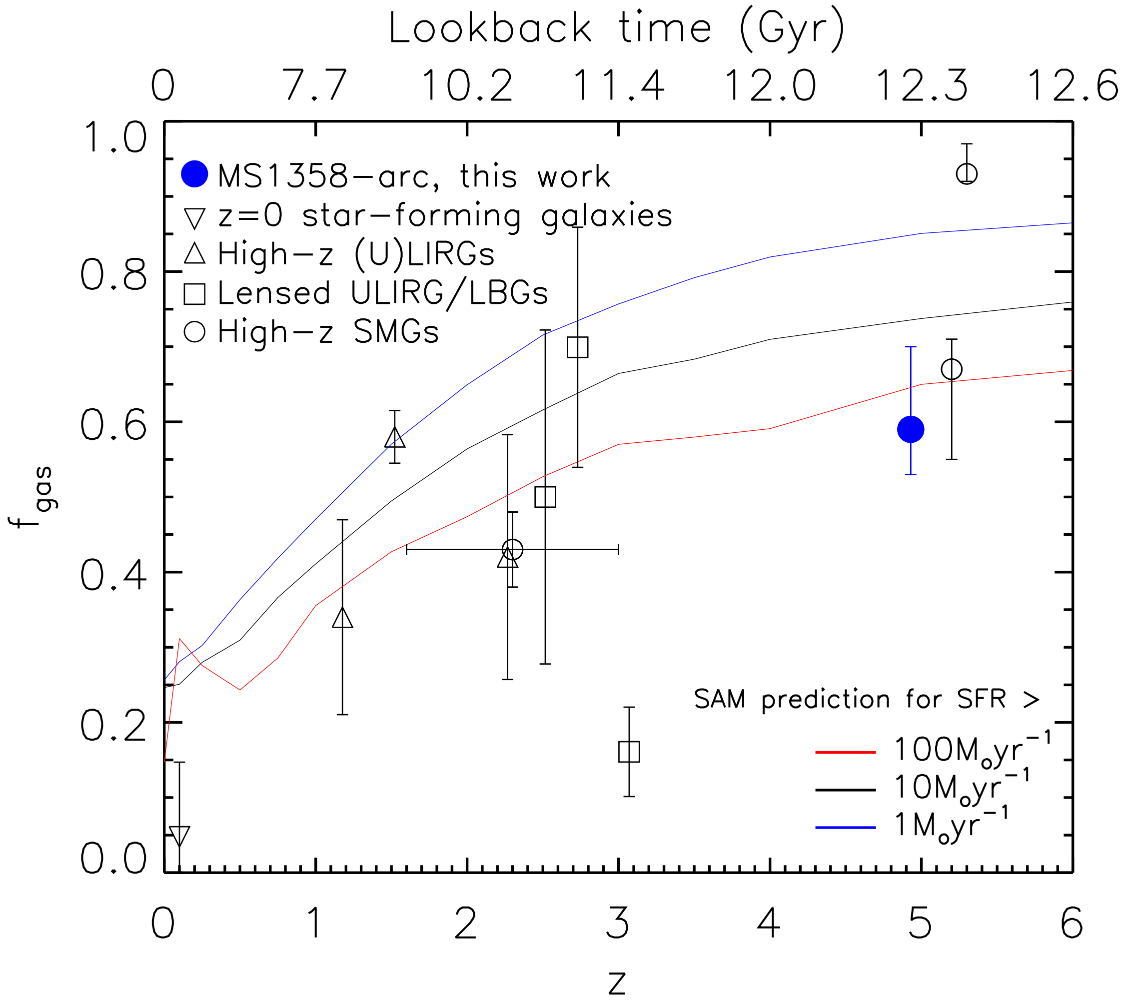

Figure 4.4. Evolution of the molecular gas fraction with redshift in star-forming galaxies. We compare MS1358-arc to the $z = 0$ sample of Leroy et al. (2008), the median gas fractions of the high-z LIRGs from Daddi et al. (2010b) and the median of each redshift bin of the Tacconi et al. (2010) (U)LIRG sample. We also use the lensed ULIRG from Kneib et al. (2005), lensed LBGs from Riechers et al. (2010) and high-z SMGs from Bothwell et al. (2013), Riechers et al. (2010) and Walter et al. (2012), all converted to $\alpha = 2\,\mathrm{M_\odot}\,\left(\mathrm{K\,km\,s^{-1}\,pc^{2}}\right)^{-1}$ for consistency. The lines are the predictions from semi-analytic models for galaxies with $SFR > 1, 10, 100\,\mathrm{M_\odot\,yr^{-1}}$ (Lacey et al. in prep). From the limited data available, there is apparent evolution in the molecular gas fraction with redshift, broadly consistent with the semi-analytic models.

$\sim$ 24 Myr, which would place the galaxy $\sim$ 40% of the way through its starburst. The star formation 'lifetime' of this galaxy would thus be very short compared to that inferred indirectly for the LBG population at $z = 4 - 6$, which have implied starburst lifetimes of $\lesssim$ 500 Myr (Stark et al., 2009), but is consistent with the lifetime of the starburst-triggered 'LBG phase' predicted by semi-analytic models (Gonzalez et al., 2011).

Finally, we note that the ratio between far-infrared luminosity and molecular gas mass, $L_{\mathrm{FIR}}/M_{\mathrm{H_2}}$, gives the star formation efficiency (SFE), relating the ongoing star formation to the available molecular gas.

Knudsen et al. (2008) obtained an upper limit on the 850 μm flux of MS1358-arc of $S_{850} < 4.8\,\mathrm{mJy}$ which, accounting for the lensing magnification and using the $S_{850} - L_{\mathrm{FIR}}$ calibration of Neri et al. (2003), suggests a far-infrared (FIR) luminosity $L_{\mathrm{FIR}} < 3.5 \times 10^{11}\,\mathrm{L_\odot}$ (we note that if we assume that the FIR flux is re-emitted light from dust-obscured star formation and apply the Kennicutt (1998a) relation to our [OII]-derived SFR, we obtain $L_{\mathrm{FIR}} = (2.3 \pm 0.9) \times 10^{11}\,\mathrm{L_\odot}$, which is consistent with this upper limit). We thus obtain $SFE \lesssim 240\,\mathrm{L_\odot\,M_\odot^{-1}}$. For comparison, the median SFE in local ULIRGS is $49 \pm 6\,\mathrm{L_\odot\,M_\odot^{-1}}$ when corrected to $\alpha = 2\,\mathrm{M_\odot}\,(\mathrm{K\,km\,s^{-1}\,pc^2})^{-1}$, although this rises to $172 \pm 23\,\mathrm{L_\odot\,M_\odot^{-1}}$ if $\alpha = 0.8\,\mathrm{M_\odot}\,(\mathrm{K\,km\,s^{-1}\,pc^2})^{-1}$, which is the factor commonly applied to ULIRGs (Sanders et al., 1991), while SMGs give $SFE \sim 55^{+20}_{-15}\,\mathrm{L_\odot\,M_\odot^{-1}}$ for $\alpha = 2\,\mathrm{M_\odot}\,(\mathrm{K\,km\,s^{-1}\,pc^2})^{-1}$ (Bothwell et al., 2013). Our upper limit is consistent with these values.

4.5 Conclusions

We have used the IRAM Plateau de Bure Interferometer to search for the CO(5–4) emission in a $z = 4.9296$ galaxy lensed by the foreground cluster MS1358+62. We were able to observe two images of the galaxy simultaneously, with a total magnification factor of $22 \pm 5\times$. We measure a line flux of $0.104 \pm 0.024\,\mathrm{Jy\,km\,s^{-1}}$ at the position of the galaxy, yielding a detection at 3.5-4.3σ.

The molecular gas shows a relatively narrow velocity range around the systemic redshift, unlike the [OII] emission, which mainly arises from two clumps in the galaxy at $\pm150\,\mathrm{km\,s^{-1}}$. This may suggest that the gas is more centrally concentrated than the star formation.

We derive a total gas mass $M_{\mathrm{gas}} = 1^{+1}_{-0.6} \times 10^9\,\mathrm{M_\odot}$, suggesting that this galaxy has a gas fraction $f_{\mathrm{gas}} = 0.59^{+0.11}_{-0.06}$, which is similar to the most gas-rich galaxies at $z \sim 2$. This could imply that gas fractions do not continue to rise significantly beyond $z \sim 2$, though a larger sample is clearly needed to draw any conclusions.

Finally, given the tentative nature of the detection, we consider the implications of treating the measured flux as a 4σ upper limit. In this case, the resulting gas mass $M_{\mathrm{gas}} < 1 \times 10^9\,\mathrm{M_\odot}$ would be lower than expected given the stellar and dynamical masses derived by S09, and the gas fraction would be $f_{\mathrm{gas}} < 0.6$. This would also imply a gas depletion timescale of $< 24\,\mathrm{Myr}$, placing the galaxy more than 40% of the way through a short starburst.

Our observations highlight the difficulty of measuring gas properties of 'representative' star-forming galaxies at $z \sim 5$, an era when many of today's massive galaxies may be undergoing their first major episode of star formation. Probing their basic properties - their stellar and gas content and relation to star formation - will provide important physical quantities which galaxy formation models must reproduce.

Chapter 5

Resolved spectroscopy of gravitationally lensed galaxies at $1 < z < 4$

5.1 Overview

We present adaptive optics-assisted integral field spectroscopy around the Hα/[Nii] or Hβ/[Oiii] lines of 12 gravitationally-lensed galaxies obtained with VLT/SINFONI, Keck/OSIRIS and Gemini/NIFS. We combine these data with the previous observations of 5 lensed galaxies from Jones et al. (2010) and use the data to investigate the dynamics and star formation properties of 17 galaxies at $1 < z < 4$. The galaxies all benefit from magnification due to gravitational lensing by foreground clusters of $1.4-90\times$, resulting in effective spatial resolutions of $\sim 80-700$pc. The magnification also allows us to probe lower star formation rates and stellar masses than unlensed samples; our sample have dust-corrected SFRs derived from Hα or Hβ emission of $\sim 0.8 - 40\,\mathrm{M_\odot yr^{-1}}$, and stellar masses $M_* \sim 4\times10^8 - 6\times10^{10}\,\mathrm{M_\odot}$. All of the galaxies have velocity gradients, with 15 out of 17 exhibiting velocity profiles indicative of rotation, and 11/17 having centrally-peaked velocity dispersion profiles and high v/σ indicative of rotating disc systems. The rotating fraction of 65% is higher than that found in unlensed studies, which is likely due to the greater spatial resolution offered by the lensed sample. The merger fraction (29%) is similar to that found in unlensed studies. We find that v/σ increases with M_*, indicative of dynamical settling, and we show that the galaxies in our sample are consistent with the local stellar mass Tully-Fisher relation, with no evidence for evolution with redshift. We extract 50 star-forming clumps with sizes in the range 60 pc - 1 kpc from the Hα (or Hβ) maps, and find that their surface brightnesses, Σ_{clump} and the characteristic luminosity at the break of the luminosity functions, L_0, evolve to higher luminosities with redshift as $\log\left(\Sigma_{\mathrm{clump}}/\mathrm{M_\odot\,yr^{-1}\,kpc^{-2}}\right) = (3.5\pm0.5)\log(1+z) - (1.7\pm0.2)$ and $\log\left(L_0/\mathrm{erg\,s^{-1}}\right) = (2.0\pm0.7)\log(1+z) + (41.0\pm0.2)$ respectively. Following Livermore et al. (2012a), we show that this evolution can be described by fragmentation on larger scales in gas-rich discs, and is likely to be driven by evolving gas fractions, though this effect is partially offset by evolution in the epicyclic frequency that acts to stabilise the discs. Using the kinematic data, we demonstrate that the data are in line with the assumed evolution of disc dynamics. We also discuss the origin of the high velocity dispersion seen in high-redshift galaxies, and demonstrate that the sample is consistent with self-regulation to maintain a Toomre stability parameter $Q \sim 1$, with turbulence driven by a combination of gravitational instabilities and feedback from star formation.

5.2 Introduction

Advances in observational facilities and instrumentation over recent decades have led to a rapid accumulation of data on the statistical properties of galaxy populations and their evolution with cosmic time. Most notably, it is established that the cosmic star formation rate density peaked around $z \sim 1$ and has since declined by an order of magnitude (Hopkins & Beacom, 2006; Lilly et al., 1996; Madau et al., 1996; Sobral et al., 2012b), and that more than half of the present-day stellar mass had been formed by $z \sim 1$ (e.g. Dickinson et al., 2003; Patel et al., 2013).

The challenge now is to interpret these statistical trends and to uncover the underlying physical processes at work. How did these early galaxies form their stars, and what conditions have changed over time to result in the observed evolution of their integrated properties?

Star formation is a complex process driven by the interplay of competing effects: self-gravitating gas is supported against collapse by turbulent motion and by feedback in the form of radiation pressure from hot, young stars and active galactic nuclei. An understanding of the evolution of star-forming galaxies therefore requires an understanding of the evolving dynamics of galaxies at different epochs. A population of rapidly star-forming galaxies at high redshift implies the presence of large gas reservoirs. Since the dynamics of gas and stars are intrinsically different - stars comprise a collisionless system, while gas is collisional and can dissipate energy - it is to be expected that high-redshift galaxies will have systematically different dynamics to those found locally.

The advent of near-infrared Integral Field Units (IFUs) on 8-10m class telescopes presented the opportunity to study two-dimensional velocity fields, without the inevitable light losses inherent in long-slit spectroscopy. IFUs enable spectra to be obtained in each pixel of an image (or, equivalently, an image to be observed in a series of discrete wavelength channels). The near-infrared IFUs used in this chapter are:

- SINFONI (SINgle Faint Object Near-IR Investigation) on the ESO/VLT (European Southern Observatory/ Very Large Telescope). The SINFONI field of view is divided into 32 slices on the detector, resulting in 32×64 spectra of the imaged region. In this work we use the 0.125" × 0.250" plate scale, for a field of view of 8" × 8"
- NIFS (Near-infrared Integral Field Spectrometer) on Gemini-North. NIFS uses 29 spherical mirrors to reformat a 3" × 3" field of view into 29 slices, each with an effective slit width of 0.1".
- OSIRIS (OH-Suppressing InfraRed Imaging Spectrograph) at Keck. OSIRIS uses an array of lenslets to take 16×64 simultaneous spectra. The plate scale used here is 0.1" per lenslet, resulting in a field of view of 1.6" × 6.4".

At $z \gtrsim 1$, the optical nebular emission lines such as Hα are redshifted into the near-infrared, with [OII] visible out to $z \sim 5$, providing bright tracers of the underlying dynamics in ionised gas across a large redshift range.

IFU studies of the dynamics of high-z galaxies quickly revealed that a significant fraction, around 1/3, are rotating systems in place as early as $z \sim 2$, but that they show higher velocity dispersions than local galaxies and $\sim 1/3$ are 'dispersion dominated' non-rotators, with the remaining $\sim 1/3$ comprising merging systems (Epinat et al., 2009, 2012; Förster Schreiber et al., 2006; Genzel et al., 2006; Law et al., 2009, 2007; Wright et al., 2007, 2009, see Glazebrook, 2013 for a review).

A common feature in Hα maps of high-redshift galaxies from IFU studies is the irregular, clumpy morphology of the Hα emission. These have also been observed in high-resolution imaging (Cowie et al., 1995; Elmegreen & Elmegreen, 2005; Elmegreen et al., 2009, 2004) and termed 'clump cluster' or 'chain' galaxies. The prevailing view is that these clumps form from internal gravitational instabilities in gas-rich discs (Bournaud et al., 2010; Elmegreen et al., 2009, 2007; Genzel et al., 2008); their ubiquity in galaxies with ordered rotation supports this view, as clumps forming through major mergers would be expected to disrupt the dynamics (e.g. Bournaud et al., 2011; Bournaud & Elmegreen, 2009; Dekel et al., 2009).

The study of dynamics and star formation morphologies of high-redshift galaxies is hampered by spatial resolution. Even with adaptive optics, the current generation of telescopes can achieve resolution of $\sim 1-1.5\,\mathrm{kpc}$ at $z \sim 2$. This limits the number of spatial resolution elements, as not only are galaxies intrinsically smaller at high redshift, but cosmological surface brightness dimming $\propto (1+z)^4$ limits observations to the bright central regions. Beam-smearing also affects measurements of velocity dispersion, which includes contributions from the underlying velocity gradient as well as local turbulent motion, and can smooth out rotation curves to give slowly rotating galaxies the appearance of being dispersion-dominated (e.g. Newman et al., 2013; Wright et al., 2009).

Enhanced spatial resolution can be achieved with current facilities by targeting galaxies that benefit from strong gravitational lensing by massive foreground clusters. As well as stretching the galaxy images and thus increasing the spatial resolution of observations, lensing conserves surface brightness, which means that the total flux is effectively magnified. This enables us to study galaxies whose intrinsic luminosities lie below the detection limits of current surveys, opening up more 'normal' galaxies, where unlensed surveys have by necessity focused on the more extreme star-forming population.

By taking advantage of magnification due to strong gravitational lensing, high resolution dynamics in high-redshift galaxies have been observed, revealing a high fraction to have ordered rotation (Jones et al., 2010; Nesvadba et al., 2006, 2007; Stark et al., 2008; Swinbank et al., 2006, 2009). Star-forming clumps are also visible in these galaxies, and due to the high spatial resolution can be observed on $\sim 100\,\mathrm{pc}$ scales, enabling direct comparisons with the HII regions in which stars form in the local Universe (Jones et al., 2010; Swinbank et al., 2009). Livermore et al. (2012a) used Hα narrowband imaging to study clumps in star-forming galaxies at $0 < z < 2$ and showed that both their surface brightnesses and luminosity functions evolve with redshift, with the higher-redshift galaxies having more massive, brighter clumps with higher surface brightnesses. The high-z clumps can be explained by the same formation process as HII regions in local galaxies: a marginally stable disc fragments on scales related to the disc's Jeans mass. At high redshift, higher gas fractions cause collapse on larger scales, leading to clumps large enough to dominate the galaxy's morphology. This factor alone, however, overpredicts the luminosities of high-z clumps. Livermore et al. (2012a) therefore suggested a contribution from the epicyclic frequency, which is higher at high redshift and acts to stabilise the disc, causing collapse on smaller scales.

This model effectively explains the evolution in observed clump properties, but relies on the dynamics of the galaxies, which were derived from disc scaling relations and not measured in the data itself. In this chapter, therefore, we use integral field spectroscopy of lensed galaxies to examine the evolution of galaxy dynamics in combination with the properties of star-forming clumps. The chapter is organised as follows: we present the sample and describe the data reduction and derivation of galaxy properties in Section 5.3. In Section 5.4, we analyse the results and discuss first the dynamics and then the star-forming clumps. We discuss the formation and evolution of star-forming clumps in Section 5.5 before finishing with a discussion of the origin of the velocity dispersion. Finally, we summarise our conclusions in Section 5.6. Throughout, we adopt a ΛCDM cosmology with $H_0 = 70\mathrm{km\,s^{-1}Mpc^{-1}}$, $\Omega_\Lambda = 0.7$ and $\Omega_\mathrm{m} = 0.3$.

Table 5.1. Targets and observations.

Name	α_{2000}	δ_{2000}	z	μ	$\mu_{\mathrm{x}} \times \mu_{\mathrm{y}}$	Resolution (pc)	Instrument	Emission lines	Lens model ref
Notes:	(*a*)	(*a*)	(*a*)	(*b*)	(*b*)	(*c*)			(*d*)
MACSJ0744^e	07:44:50.90	+39:27:34.5	1.28	63 ± 22	21 × 3	134 ± 47	NIFS	Hα/[NII]	[1,2]
MACSJ1149^e	11:49:35.30	+22:23:45.8	1.49	16 ± 2	3 × 5	169 ± 21	OSIRIS	Hα/[NII]	[3]
MACSJ0451^e	04:51:57.22	+00:06:21.3	2.01	90 ± 7	63 × 1	84 ± 7	SINFONI	Hβ/[OIII]	[1]
Abell1413a	11:55:18.31	+23:23:55.5	2.04	24 ± 3	1 × 18	299 ± 37	SINFONI	Hα/[NII]	[4]
Abell1413b	11:55:18.31	+23:23:55.5	2.04	29 ± 2	1 × 21	265 ± 18	SINFONI	Hα/[NII]	[4]
Abell1835	14:01:00.99	+02:52:23.2	2.07	63 ± 3	2 × 37	118 ± 6	SINFONI	Hα/[NII]	[4]
MS1621+26	16:23:35.56	+26:34:29.1	2.14	8 ± 2	4 × 2	722 ± 165	SINFONI	Hα/[NII]	[5]
RXJ1720+26	17:20:10.26	+26:37:27.4	2.22	86 ± 18	14 × 6	560 ± 115	SINFONI	Hα/[NII]	[4]
Abell1689a	13:11:26.52	-01:19:55.5	2.54	15 ± 3	21 × 1	96 ± 19	SINFONI	Hβ/[OIII]	[6]
Abell1689b	13:11:26.43	-01:19:57.0	3.04	61 ± 11	25 × 2	249 ± 47	SINFONI	Hβ/[OIII]	[6]
Abell2895a	01:18:11.15	-26:58:03.9	3.40	7 ± 1	1 × 10	454 ± 88	SINFONI	Hβ/[OIII]	[7]
Abell2895b	01:18:10.45	-26:58:14.2	3.72	9 ± 2	7 × 1	167 ± 40	SINFONI	Hβ/[OIII]	[7]

Notes: (*a*) Positions and redshifts are given for the target lensed arcs. (*b*) μ is the total magnification of the source, derived from the ratio of the emission line flux in the image plane to that in the source plane. μ_{x} and μ_{y} are the linear magnifications along the direction of greatest magnification and perpendicular to that axis, derived as described in the text. (*c*) Resolution is given in the direction of greatest magnification. (*d*) References: [1] Jones et al. (2010), [2] Korngut et al. (2011), [3] Smith et al. (2009), [4] Richard et al. (2010), [5] Richard et al. (in prep), [6] Limousin et al. (2007), [7] May et al. (in prep). (*e*) To identify the arcs, we use truncations of the full cluster names: MACSJ0744.8+3927, MACSJ1149.5+2223, MACSJ0451.9+0006 (Ebeling et al., 2007, 2001).

Table 5.2. Observational log.

Name	Instrument	Date	Grating	Exposure time (s)	NINT	Total exposure (s)
MACSJ0744	NIFS	2010 11 14	H	600	4	2400
		2010 11 16	H	600	2	1200
		2010 11 22	H	600	14	8400
		2011 02 11	H	600	4	2400
		2011 02 12	H	600	4	2400
		2011 02 15	H	600	4	2400
MACSJ0451	SINFONI	2009 10 18	H	600	4	2400
		2009 10 19	H	600	4	2400
		2009 11 10	H	600	4	2400
		2009 11 11	H	600	4	2400
		2009 11 12	H	600	4	2400
		2009 11 17	H	600	4	2400
		2009 11 19	H	600	8	4800
Abell1413	SINFONI	2010 07 11	K	600	4	2400
		2011 05 26	K	600	4	2400
		2011 06 29	K	600	4	2400
		2012 02 12	K	600	4	2400
		2012 03 18	K	600	4	2400

Continued on next page

Table 5.2 – continued from previous page

Name	Instrument	Date	Grating	Exposure time (s)	NINT	Total exposure (s)
		2012 05 20	K	600	8	4800
		2012 06 02	K	600	4	2400
		2012 07 16	K	600	4	2400
Abell1835	SINFONI	2009 04 30	K	600	4	2400
		2009 05 16	K	600	12	7200
		2009 05 26	K	600	4	2400
		2009 06 28	K	600	4	2400
		2009 06 29	K	600	4	2400
		2009 07 24	K	600	4	2400
MS1621+26	SINFONI	2010 04 02	K	600	4	2400
		2010 07 13	K	600	4	2400
		2010 07 20	K	600	4	2400
		2010 07 22	K	600	4	2400
		2010 07 26	K	600	8	4800
		2010 07 27	K	600	4	2400
		2010 08 30	K	600	4	2400
		2011 03 05	K	600	4	2400
RXJ1720+26	SINFONI	2010 07 10	K	600	4	2400

Continued on next page

Table 5.2 – continued from previous page

Name	Instrument	Date	Grating	Exposure time (s)	NINT	Total exposure (s)
		2010 09 15	K	600	4	2400
		2011 04 02	K	600	4	2400
		2011 04 25	K	600	4	2400
		2011 05 02	K	600	8	4800
		2011 06 30	K	600	4	2400
		2011 07 29	K	600	4	2400
		2011 08 22	K	600	4	2400
		2011 08 24	K	600	4	2400
Abell1689	SINFONI	2009 05 09	H+K	600	8	4800
		2009 05 25	H+K	600	4	2400
		2009 05 27	H+K	600	8	4800
		2009 07 23	H+K	600	4	2400
		2010 03 16	H+K	600	8	4800
Abell2895a	SINFONI	2011 06 25	K	600	4 2400	
		2011 07 22	K	600	8	4800
		2011 08 24	K	600	8	4800
		2011 08 26	K	600	8	4800
		2011 09 04	K	600	4	2400

Continued on next page

Table 5.2 – continued from previous page

Name	Instrument	Date	Grating	Exposure time (s)	NINT	Total exposure (s)
Abell2895b	SINFONI	2011 09 04	K	600	4	2400
		2011 08 25	K	600	4	2400
		2011 08 28	K	600	4	2400
		2011 09 05	K	600	4	2400
		2011 09 08	K	600	8	4800
		2011 09 10	K	600	8	4800
		2011 09 12	K	600	4	2400
		2011 09 24	K	600	8	4800

5.3 Observations and Data Reduction

5.3.1 Integral Field Spectroscopy

Table 5.1 lists the galaxies in our sample, which were selected from clusters with existing mass models, and to have spectroscopically-confirmed redshifts that place their Hα or Hβ emission in windows of atmospheric transmission in the near-infrared and away from OH emission lines. In order to ensure detection in ~ 5 hours, we targeted galaxies with integrated emission line fluxes of $> 10^{-16}\,\mathrm{erg\,s^{-1}\,cm^{-2}}$, known either from prior spectroscopy or from pre-imaging (e.g. Richard et al., 2011).

The new sample comprises twelve galaxies, of which ten were observed with the SINFONI Integral Field Unit (IFU) on the ESO/VLT (Eisenhauer et al., 2003) between 2009 April 30 and 2012 July 16, as listed in Table 5.2. The SINFONI targets were selected to be close to sufficiently bright stars for the use of NGS+AO, resulting in a median FWHM $= 0.2''$. As the lensed arcs are extended, usually over several arcseconds, we used the $8'' \times 8''$ field of view with a spaxel size of $0.125''$. Due to the elongated shape typical of lensed arcs, the targets were kept in one half of the IFU and nodded across in an ABBA sequence. We observed each target for six ABBA sequences in the H or K-band filter according to the redshifted position of the target emission line (see Table 5.1).

The data were reduced using the ESOREX package, which performs flat-fielding and wavelength calibration and reforms the image into a data cube with two spatial and one spectral dimension. It also carries out sky subtraction by subtracting each B frame from its closest A frame, which with our observing strategy results in cubes that contain two images of the target, one positive and one negative. Standard stars were observed on the same nights and in the same filters as the science exposures, and were reduced in the same way. We used the standard stars to individually flux-calibrate each cube before combining them.

To combine the cubes, we first cut them in half to separate the two images of the target, and subtracted the negative image from the positive one. We then aligned the cubes by collapsing them into continuum images. As the targets all lie behind cluster lenses, they commonly have elliptical cluster members close to their line of sight. Where possible, a foreground elliptical galaxy was intentionally positioned within the SINFONI field of view to allow for careful alignment between cubes. Where this was not possible (in the case of Abell 2895), we aligned the cubes by centring on a bright feature within the lensed galaxy. Once aligned, the cubes were median-combined with the IRAF task `imcombine` with the `crreject` algorithm for cosmic ray rejection.

In addition to the ten targets observed with SINFONI, we observed a $z = 1.28$ galaxy lensed by the cluster MACSJ0744 with Gemini/ Near-Infrared Integral Field Spectrometer (NIFS; McGregor et al., 2003). As the target is too long to fit in the $3'' \times 3''$ field of view (see first panel of Figure 5.1), we observed in an ABC sequence, where two halves of the arc were positioned diagonally across the field in the A and C frames, and the B frame was a blank field used for sky subtraction. The A and C frames were chosen to overlap at the foreground elliptical in the middle of the arc to enable precise alignment of the A and C frames. We observed for 8 ABC sequences with the H-band filter. Data reduction was carried out using the `gemini` package in IRAF of both the science frames and standard stars observed on the same nights and with the same setup as the science observations. Each cube was then individually flux-calibrated and combined as for the SINFONI observations described above.

One further target, the spiral galaxy at $z = 1.49$ lensed by the cluster MACS J1149.5+2223, was observed with Keck/OSIRIS. The observations and data reduction are described by Yuan et al. (2011), who use the data to show that the galaxy's metallicity gradient is strongly negative.

Throughout this chapter we also make use of the sample of six lensed galaxies observed with Keck/OSIRIS from Jones et al. (2010). They presented the resolved kinematics of these galaxies, which we adopt in the first half of this chapter for comparison with our new data. They also demonstrated that individual star-forming clumps could be extracted from the data and discussed their properties in relation to local HII regions, deriving luminosity densities up to 100× higher than local star-forming regions. So that they can be combined with the new data in a self-consistent manner, we undertake a new analysis of the clump properties in this sample in the latter half of this chapter, but our results are entirely consistent with those presented by Jones et al. (2010). One of these galaxies - MACSJ0451, observed in Hα by Jones et al. (2010) - is also included in the SINFONI sample, where we observed it in Hβ and [OIII]. The combined sample of lensed arcs thus comprises 17 galaxies at $1.28 < z < 3.72$.

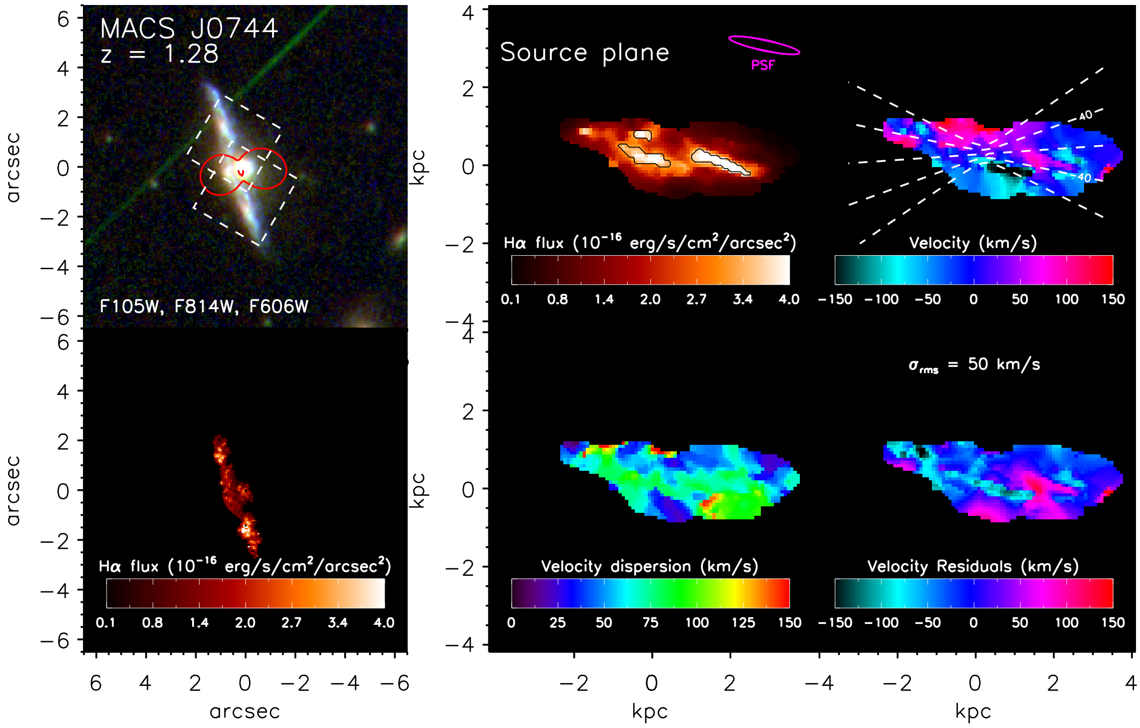

Figure 5.1. Image plane colour images and reconstructed source plane maps of the target galaxies. The top-left image in each panel shows an *HST* image of the arc constructed from archival *ACS* and/or *WFC3* data, in colour where there are multiple bands in the archive. The filters used are given in the lower-left corner of the image. The critical line at the target galaxy's redshift is overlaid in red. Where the IFU field of view cannot cover the entire arc, it is shown as a dashed white box. The lower-left image shows the Hα or Hβ emission line flux, aligned to the same astrometry as the *HST* image for context. The right four images in each panel show the source plane reconstructions: from top left to bottom right, they show the Hα or Hβ intensity maps, velocity fields, line-of-sight velocity dispersion and velocity field residuals after subtracting the best-fit disc model. The star-forming clumps are contoured over the intensity maps. Contours overlaid on the velocity field show the best-fit disc model after smoothing by the effective source plane PSF, shown by a magenta ellipse. As surface brightness is conserved by lensing, the image and source plane intensity maps are displayed in terms of surface brightness, with the same scaling.

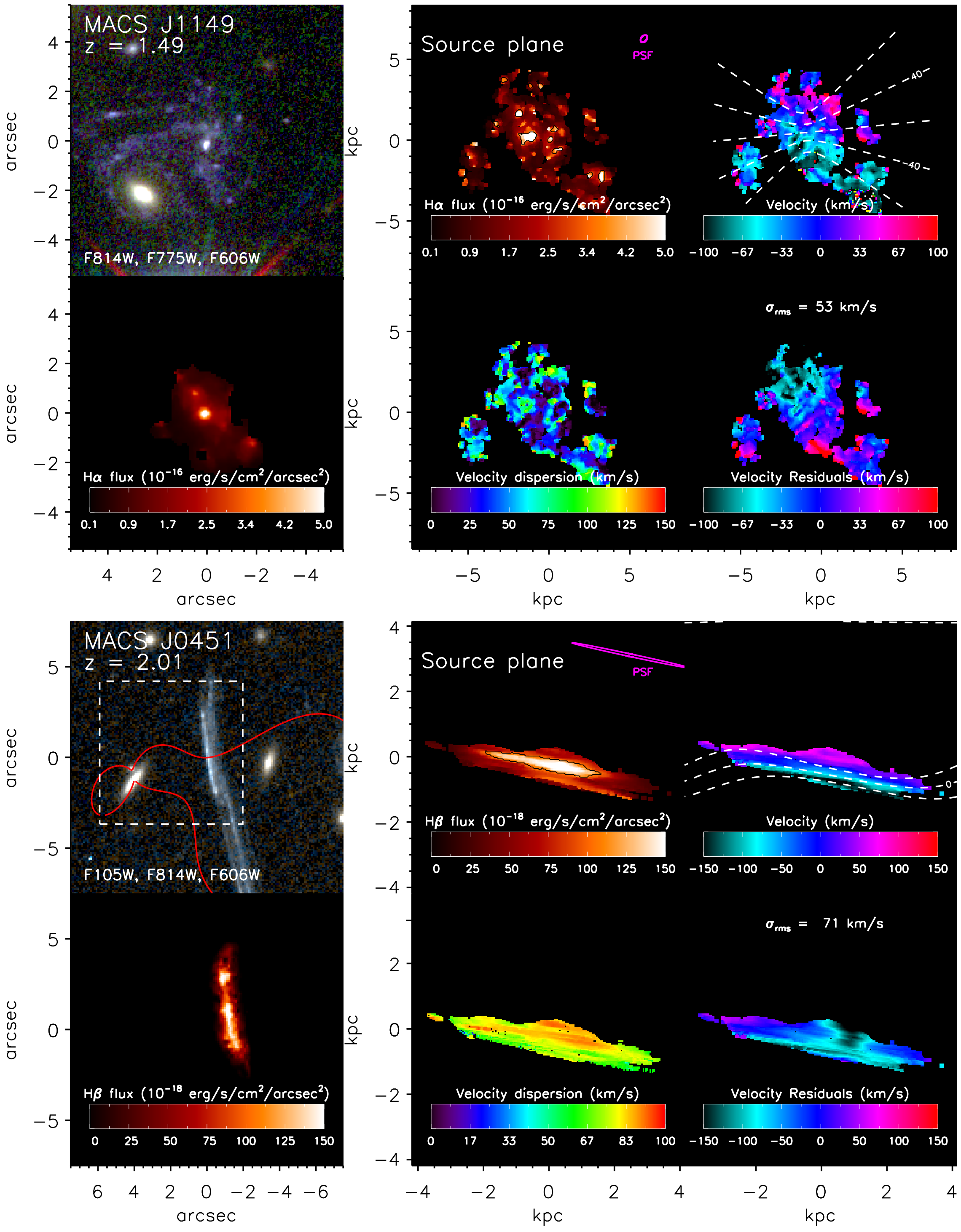

Figure 5.1 (continued)

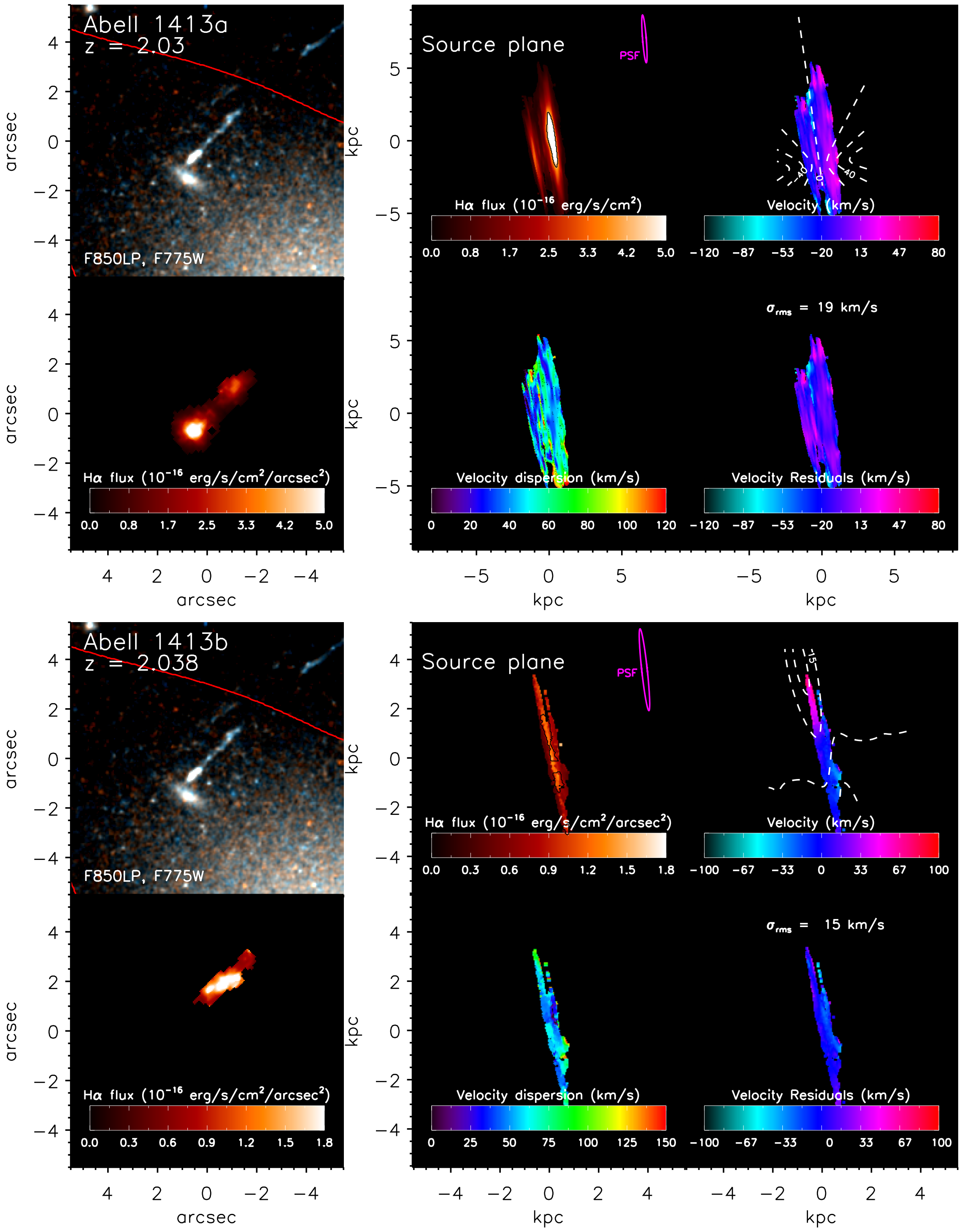

Figure 5.1 (continued)

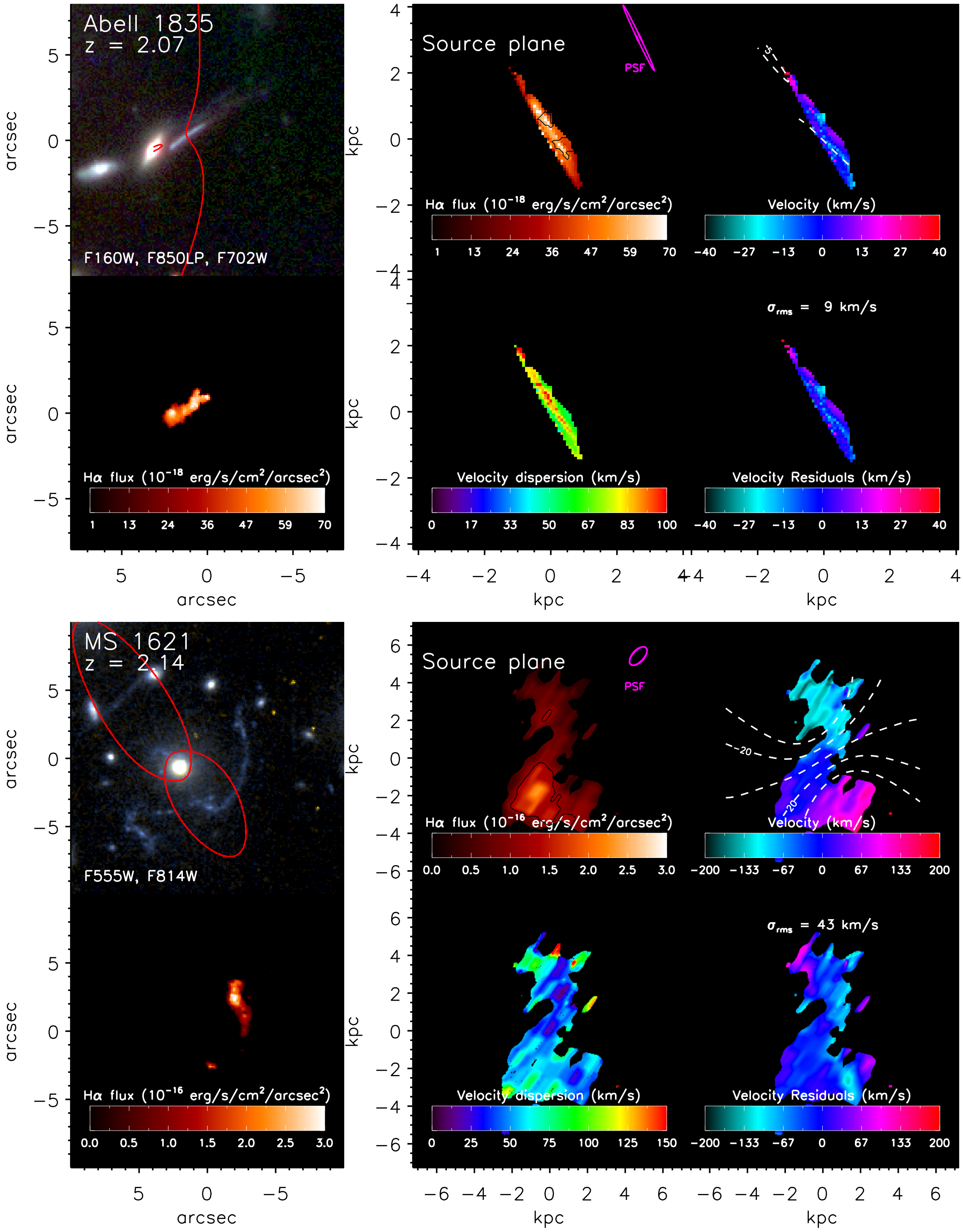

Figure 5.1 (continued)

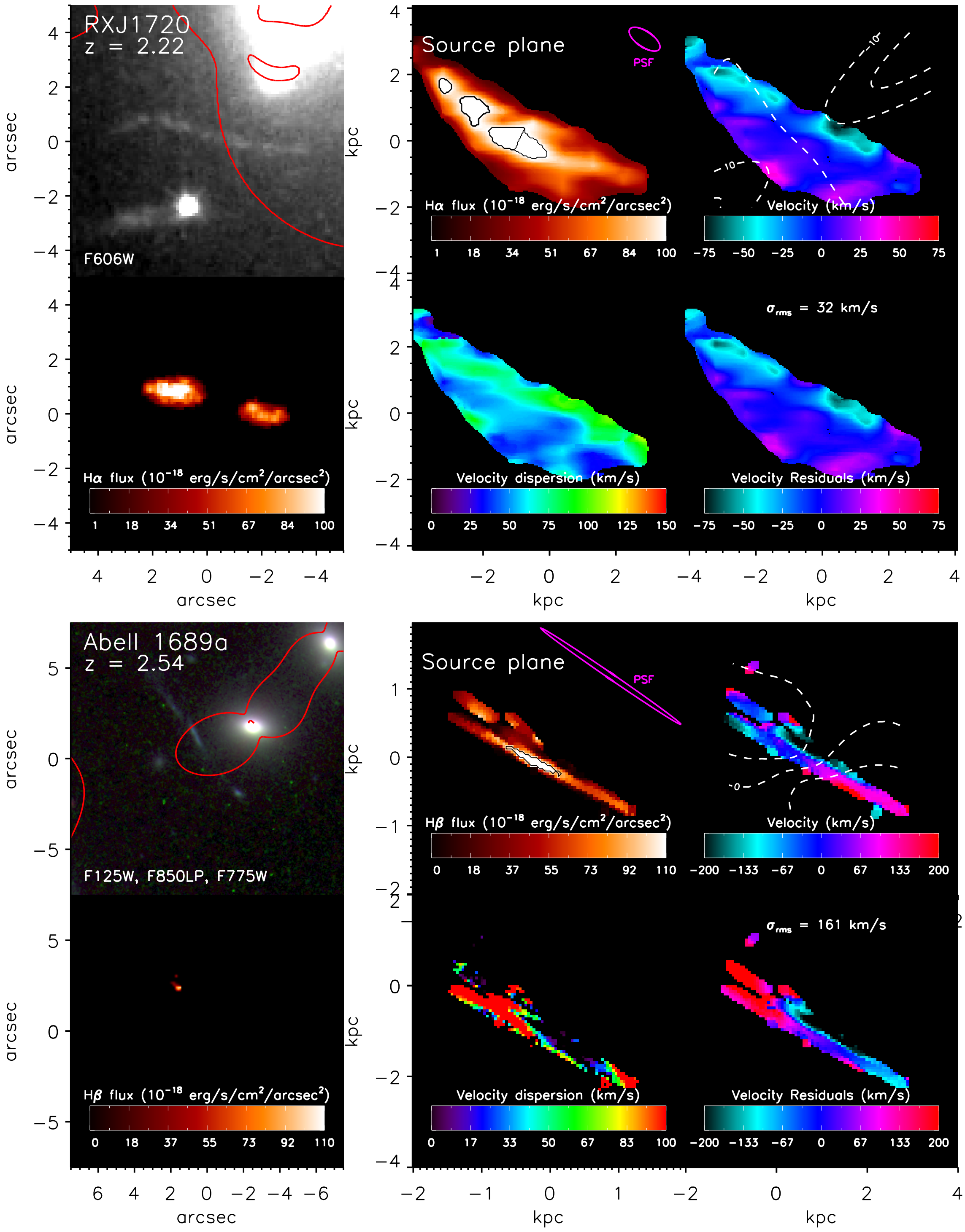

Figure 5.1 (continued)

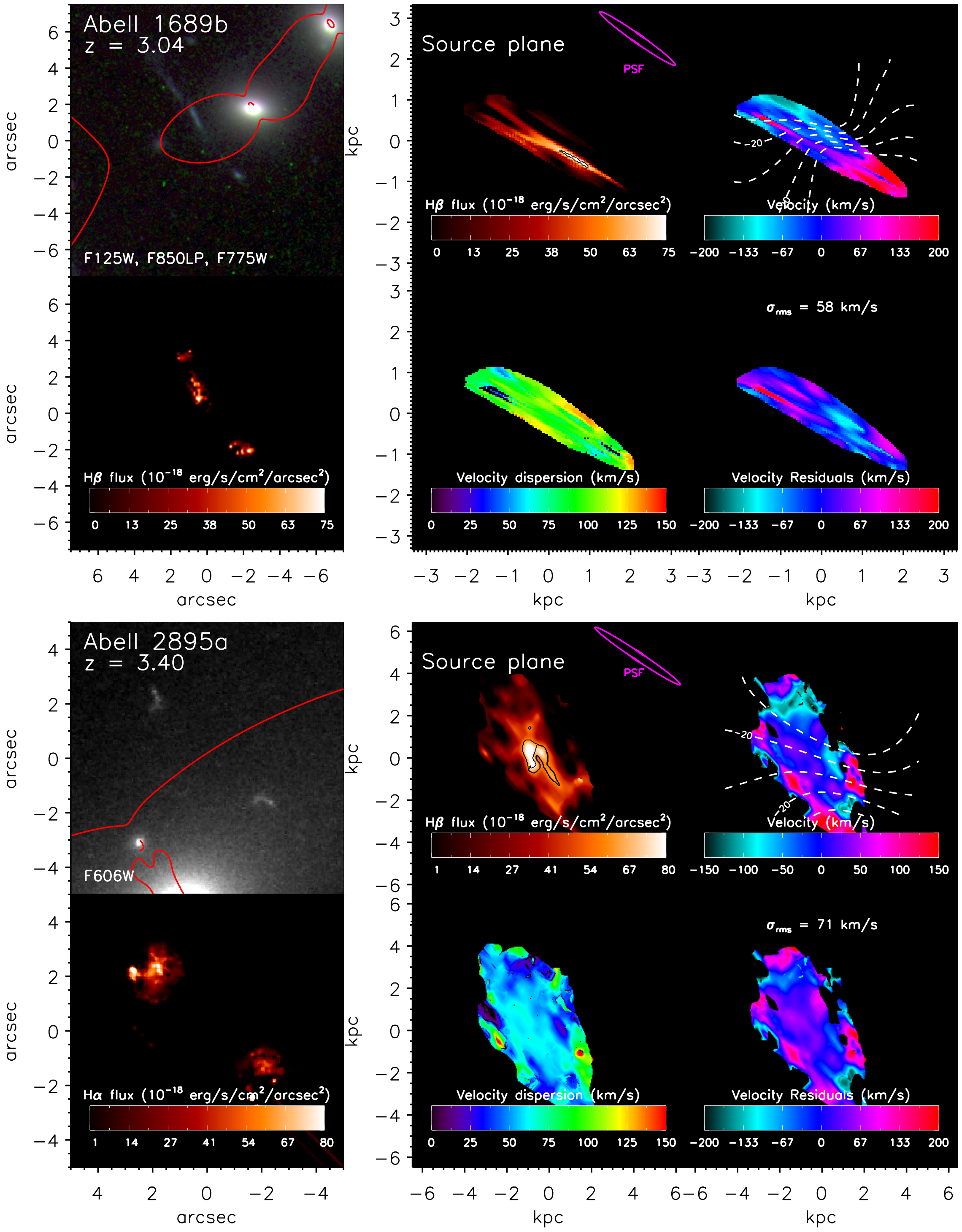

Figure 5.1 (continued)

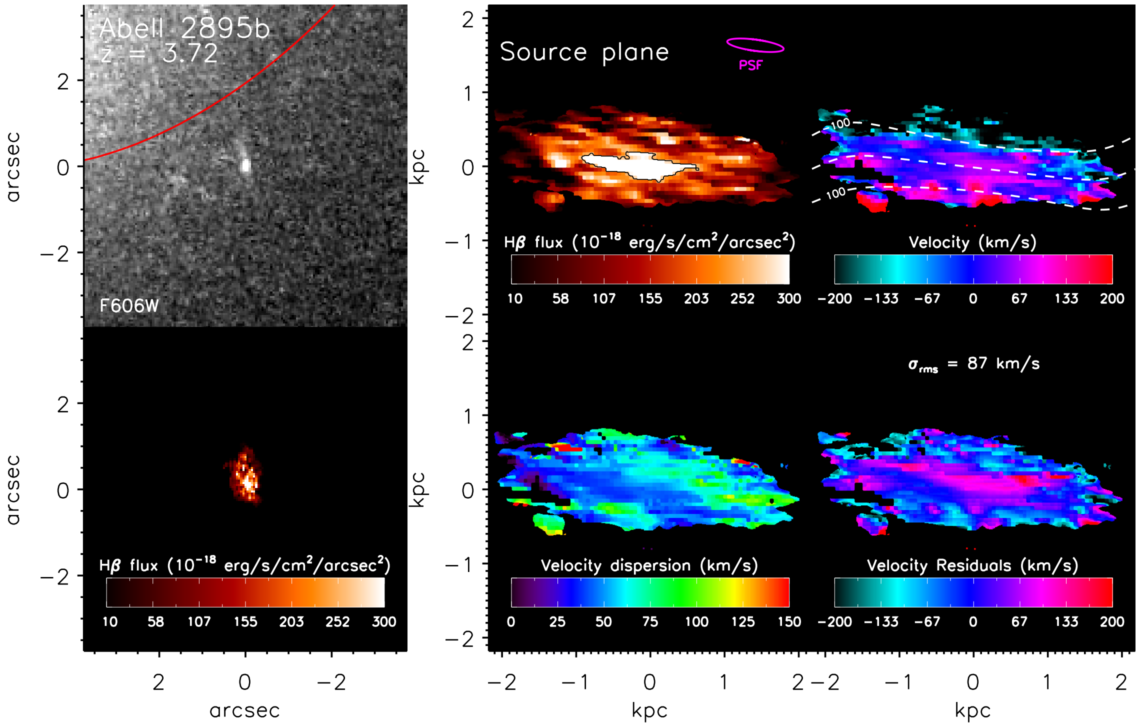

Figure 5.1 (continued)

5.3.2 *HST* imaging and lens modelling

Colour (where available) *HST* images of the target galaxies are shown in the top-left panels of Figure 5.1. In order to determine the intrinsic properties of the target galaxies, it is necessary to account for the effects of lensing. To do this, we use the best fit cluster mass models (for details of the models, see the references in Table 5.1). Where the cluster's critical line at the redshift of the lensed arc crosses the field, it is overlaid in red. The critical line denotes regions of theoretically infinite magnification, and arcs which cross this line are multiply imaged within the IFU field of view. To reconstruct the source-plane images of the galaxies, we use LENSTOOL (Jullo et al., 2007; Kneib, 1993) to ray-trace each pixel to its source-plane origin. After using a central pixel to obtain the position of the galaxy in the source plane, we construct a regular grid in the source plane, ray-trace each pixel to the image plane and obtain the spectrum in that position by interpolating between pixels in the IFU data cube. In the cases of Abell1835 and Abell2895b, the high magnification gradient in the vicinity of the critical line causes this method to omit data from the image plane. For these galaxies, we therefore carry out the process in reverse by ray-tracing each pixel from the IFU data cube to the source plane. This results in an irregular grid in the source plane, which is gridded into square pixels using a Delauney tessellation. Once the source plane cubes have been constructed, we apply conservation of surface brightness to each pixel to obtain the intrinsic source plane flux. The magnification factor μ for the galaxy given in Table 5.1 is then the ratio of image- to source-plane flux measured from the Hα or Hβ emission lines.

With both methods, the source plane pixel scale is chosen so that each pixel in the IFU data cube is represented in the source plane, and we impose a lower limit of 0.001" to ensure manageable file sizes. The pixel scale is therefore dictated by the direction or region of highest magnification. Gravitational lensing usually acts preferentially in one direction, and galaxies lying close to the critical line will experience strong magnification gradients. Hence, the source plane cubes are oversampled both in the direction of lower magnification and in regions of the galaxy that lie furthest from the critical line. To estimate the actual resolution achieved, we apply the same reconstruction as described above to the standard star observations and measure the FWHM in the image and source plane. The result is an ellipse, shown in magenta in Figure 5.1.

In order to estimate the errors on the magnification factors for each galaxy, we use the family of 100 best-fit lens models. We use LENSTOOL to reconstruct the Hα or Hβ intensity maps for each galaxy for each one of the possible lens models, and then measure the ratio of image- to source-plane flux in each. The 1σ deviation in the derived magnifications are given in Table 5.1 as the error on the total magnification. As we measure the magnification for the purpose of this chapter from the Hα (or Hβ) line intensity (effectively a weighted mean), the largest errors are found where there is a large magnification gradient across the arc without strong constraints on the mass distribution of the primary lensing source. The largest fractional error, 35%, is found in MACSJ0744, due to the strong magnification gradient across the image arising from lensing by the foreground cluster galaxy positioned along the line of sight to the arc. The smallest error, 5%, is found in Abell1835, which also has a strong magnification gradient, but in this case the two images straddling the critical line provide good constraints on the precise position of the line. We note that changing the lens model tends to result in the galaxy image being stretched differently, so that the effective resolution described above would change, but the underlying morphology cannot be materially altered. Crucially for the discussion in the latter half of this chapter, new features such as clumps cannot be created during the lensing reconstruction.

5.3.3 Dynamical maps

With both the image- and source-plane cubes, we fit the intensity, velocity and velocity dispersion of the emission lines in each pixel using a χ^2 minimisation technique. In each pixel, we simultaneously fit the Hα and [NII]λ6583 or Hβ and [OIII]$\lambda\lambda$4959,5007 lines. To reduce the number of parameters in the fit, we require all lines to be of the same velocity and velocity dispersion, and we impose a ratio of [OIII]$\lambda\,5007/\lambda\,4959 = 3$ (Storey & Zeippen, 2000). The fit is accepted if it results in a $\Delta\chi^2 > 25$ compared to a straight-line fit, equivalent to a signal-to-noise of $S/N > 5$. If no fit is obtained, we adaptively bin up to 3×3 pixels in the image plane, or the equivalent area of 3×3 PSF areas in the source plane. We deconvolve the velocity dispersion for spectral resolution by subtracting in quadrature the median width of sky lines measured from blank exposures taken with the standard stars. The high spatial resolution of the source-plane cube means that most of the contribution to the velocity dispersion of the velocity gradient across the galaxy is removed. To remove the remainder, we subtract in quadrature the velocity gradient across each pixel, measured over the PSF. For each parameter, we also estimate the errors in each pixel. Taking the best fit to the emission lines, we vary each parameter until we obtain a $\Delta\chi^2 \geq 1$. We do not find any emission lines that are well fit by multiple components at different velocities or line widths.

We show the resulting maps in Figure 5.1. In the bottom left of each panel is the Hα or Hβ emission line intensity from the image-plane IFU data, mapped to the same astrometry as the *HST* image. The source plane reconstructions are in the right-four images of each panel, showing the Hα or Hβ emission line intensity, the velocity and velocity dispersion maps and the velocity residuals after subtracting the best-fit disc models (contoured over the velocity map and described in Section 5.4.1). We note that as the velocity and velocity dispersion are fixed between multiple emission lines, their values are dominated by the line with the highest signal-to-noise. In the case of the Hβ/[OIII] observations, the [OIII]λ 5007 line is far brighter than the Hβ line; in some cases we thus obtain velocity and velocity dispersion values in pixels where no Hβ is measured. We note that the method above is the same as that used by Jones et al. (2010), so the properties derived from the two samples are self-consistent.

5.3.4 Disc modelling

To each of the velocity fields, we follow Jones et al. (2010) and attempt to fit a rotating disc model and hence infer the true disc rotation speed and inclination. The model is described by six parameters: the disc centre x and y, the asymptotic rotational velocity $v_{\rm asym}$, the turnover radius r_t, the position angle ϕ and inclination θ. The values of these parameters are constrained so that x and y are within the range of the data, and $r_t <$ 50kpc, and rotation is described by an arctan function

Table 5.3. Dynamical properties of the sample

Name	Inclination θ	PA	$v_{2.2}$ ($\mathrm{km\,s^{-1}}$)	σ ($\mathrm{km\,s^{-1}}$)	v/r ($\mathrm{km\,s^{-1}kpc^{-1}}$)	v/σ	Velocity field type
MACSJ0744	61	266	80 ± 10	60 ± 20	230 ± 30	1.4 ± 0.8	Disc
MACSJ1149	45	86	59 ± 3	50 ± 10	88 ± 4	2 ± 1	Disc
MACSJ0451	55	100	100 ± 10	77 ± 9	220 ± 30	1.6 ± 0.6	Disc
Abell1413a	50	172	17 ± 4	50 ± 10	24 ± 5	0.5 ± 0.3	Disc
Abell1413b	66	249	20 ± 3	60 ± 20	8 ± 1	0.6 ± 0.3	Merger
Abell1835	89	236	40 ± 10	70 ± 10	4 ± 1	0.2 ± 0.2	Dispersion Dominated
MS1621+26	84	247	126 ± 4	60 ± 20	47 ± 1	3 ± 1	Merger
RXJ1720+26	70	144	63.2 ± 0.5	60 ± 20	27.1 ± 0.2	0.4 ± 0.2	Merger
Abell1689a	81	38	64 ± 7	55 ± 1	180 ± 20	1 ± 1	Disc
Abell1689b	80	234	78 ± 4	90 ± 10	53 ± 4	1.3 ± 0.4	Merger
Abell2895a	85	260	60 ± 10	60 ± 20	62 ± 3	1.9 ± 0.7	Disc
Abell2895b	47	276	200 ± 10	60 ± 20	530 ± 30	4 ± 2	Disc
Cl0024+16	50	122	91 ± 8	63 ± 6	15 ± 3	2.6 ± 0.3	Disc
Cl0949	...	...	...	68 ± 7	16 ± 3	...	Merger
MACSJ0712	40	351	33 ± 3	75 ± 7	25 ± 3	0.81 ± 0.08	Disc
MACSJ0744b	45	124	118 ± 9	110 ± 10	210 ± 20	2.4 ± 0.2	Disc
MACSJ2135	55	113	51 ± 4	44 ± 4	55 ± 5	1.9 ± 0.2	Disc

Notes: Inclination and PA are derived from the best-fit disc models. $v_{2.2}$ is the velocity at $2.2r_{1/2}$, where $r_{1/2}$ is the half-light radius. Velocity dispersion, σ, is the luminosity-weighted mean local value, after deconvolving for local velocity gradient. The velocity gradient v/r is measured at $r_{1/2}$. Targets below the line are from Jones et al. (2010) with values reported in their Table 2, except for $v_{2.2}$, v/r and v/σ, which we measure for consistency with the new data. No values for θ, PA or $v_{2.2}$ are given for Cl0949 as this galaxy cannot be fit by a disc model.

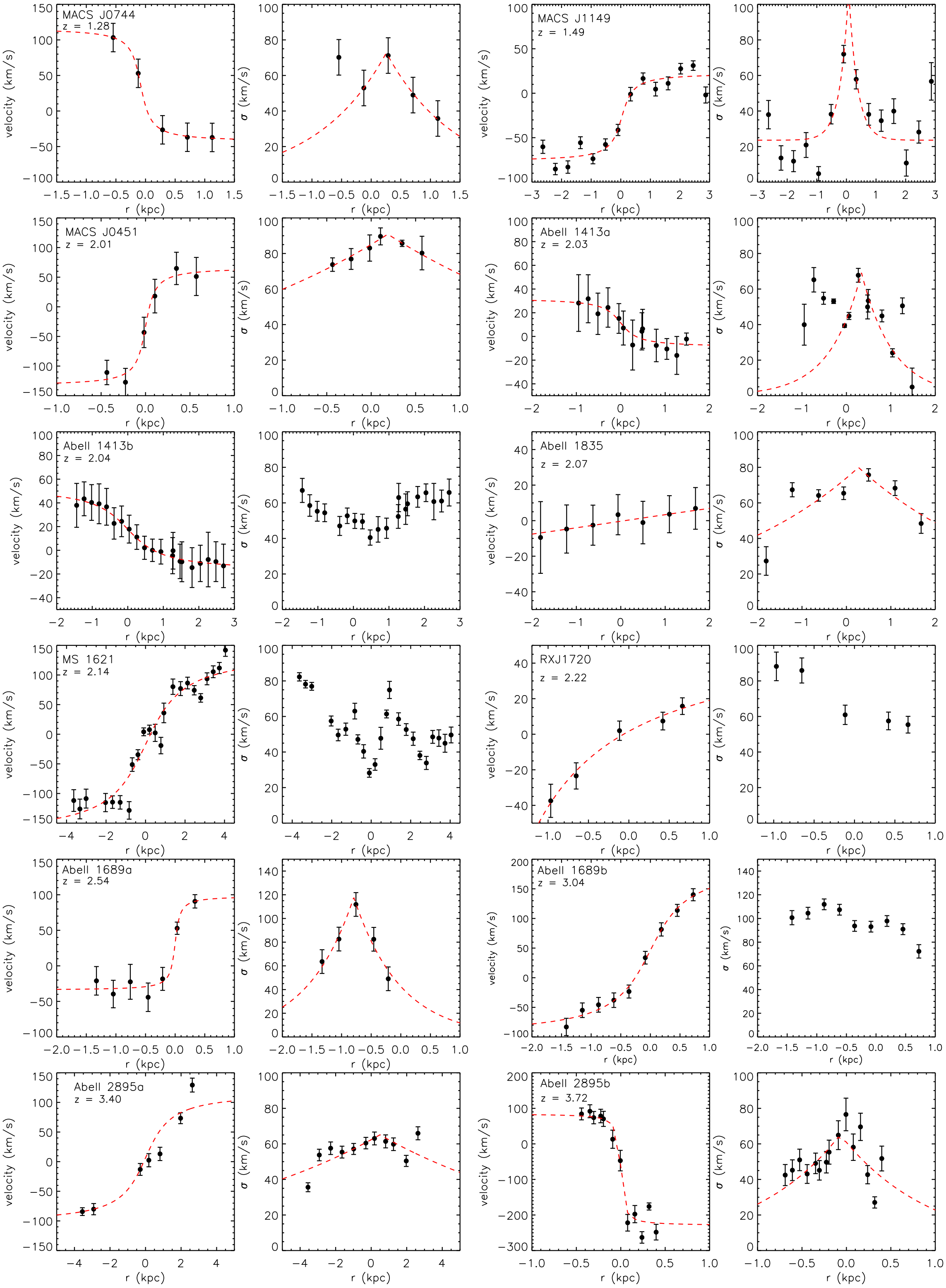

Figure 5.2. One-dimensional rotation curves (left) and velocity dispersion profiles (right), extracted from a slit aligned along the axis of the best-fit disc model. For the galaxies whose dynamics are well fit by a rotating disc model, we overlay the best-fit rotation curve and velocity dispersion profile.

(Courteau, 1997) of the form

$$v(r) = \left(\frac{2}{\pi}\right) v_{\mathrm{asym}} \arctan\left(\frac{r}{r_t}\right). \tag{5.3.1}$$

The fit is carried out with an iterative procedure whereby $10,000$ random sets of parameters are generated, and the resulting 2D velocity models are smoothed by the effective source plane PSF of the galaxy. The χ^2 is then calculated for each one. The parameter space is contracted by discarding up to 10% of the worst fitting models in each iteration. This process is repeated up to 100 times, and the fit is deemed to have converged once all models in a generation have $\Delta\chi^2 < 1$. The smoothed best-fit disc models are contoured on the observed velocity fields in Figure 5.1, and the velocity residuals after subtracting the best-fit disc model are shown in the bottom-right image of each panel. The dynamical properties of the sample are given in Table 5.3.

While it is always possible to fit a rotating disc model to the data, this is insufficient to determine that the galaxy is a rotating disc. A rotating disc should have symmetric velocity and velocity dispersion fields, the latter peaking in the centre of the galaxy. The traditional requirement that the velocity field form a ‘spider’ pattern is rarely found in lensed galaxies due to the asymmetric magnification (the contours overlaid in Figure 5.1 demonstrate how much smoothing by the elliptical source plane PSFs distorts even an idealised rotation field).

Jones et al. (2010) illustrate the symmetry of the kinematics in their sample by extracting one-dimensional profiles along the kinematic axis, concluding that 5/6 of the galaxies have velocity profiles indicative of rotation, with one likely merger

(Cl0949). In order to examine the symmetry in our new data, we extract a one-dimensional profile of the velocity and velocity dispersion from each galaxy. We do this by using the best-fit disc model to identify the dynamical centre and kinematic axis of the galaxy. The velocity and velocity dispersion are extracted along a slit five pixels wide, and binned into independent resolution elements along the long axis according to the galaxies' effective source plane PSF. The resulting dynamical profiles for the 12 galaxies in our sample are shown in Figure 5.2. The best fit one-dimensional rotation curves and exponential velocity dispersion profiles (where applicable) are overlaid in red.

All of the galaxies in the sample exhibit velocity gradients, and all but one (Abell2895a) are well-fit by an arctan function indicative of rotation. However, the velocity dispersion profiles are less ordered. In Figure 5.2 we attempt to fit an exponential profile to the velocity dispersions. In 50% of cases the exponential function is a good fit to the data. In two cases, Abell1413b and RXJ1720, there is no central peak. Abell1413b is probably interacting with the larger Abell1413a, from which it is offset by only $\sim$ 1000km s^{-1}, and the morphology of RXJ1720 with its extended tail suggests that it also may be an interacting system. In the remaining four galaxies - MACSJ0744, Abell1413a, MS1621 and Abell1689b - there are suggestions of a double peak in the velocity dispersion profile, which may also be indicative of a late-stage merger. Alternatively, the irregular and asymmetric profiles could be due to turbulence within the discs.

The kinematic properties of the galaxies are similar to those in the Jones et al. (2010) sample, which also exhibited rotation-like velocity fields with irregular velocity dispersion profiles. The galaxies in the new sample tend to be smaller than those from Jones et al. (2010), with median $r_{1/2} \sim 0.5\,\mathrm{kpc}$ and $1.2\,\mathrm{kpc}$ respectively, but both lensed samples probe systematically smaller galaxies than unlensed studies such as SINS+AO, SHiZELS and WiggleZ, which have median $r_{1/2} \sim 4.3\,\mathrm{kpc}$, $2.3\,\mathrm{kpc}$ and $2.5\,\mathrm{kpc}$ respectively (Newman et al., 2013; Swinbank et al., 2012; Wisnioski et al., 2011). The two lensed samples are closely matched in rotational velocity with median rotational velocity measured at $2.2\,r_{1/2}$ of $v_{2.2} \sim 64\,\mathrm{km\,s^{-1}}$ and $51\,\mathrm{km\,s^{-1}}$ for the new data and Jones et al. (2010) sample respectively (see §5.4.1 for a discussion of why $v_{2.2}$ is used). The median rotational velocity in the WiggleZ survey is marginally higher at $74\,\mathrm{km\,s^{-1}}$, with $\sim 110\,\mathrm{km\,s^{-1}}$ in SHiZELS and $\sim 150\,\mathrm{km\,s^{-1}}$ in the SINS AO sample. There are two factors that bias lensing surveys towards more slowly rotating systems: firstly, that they are sensitive to smaller galaxies, which tend to be slower rotators (e.g. Newman et al., 2013, see also Section 5.4.1), and secondly, the high spatial resolution enables us to measure small velocity gradients that would be flattened by beam smearing in unlensed data and thus categorised as non-rotating.

As the properties of the two lensed samples are similar, and differ systematically from the unlensed data, we discuss them in the remainder of this chapter as a combined sample. In the interest of providing a comparison to other studies, we give our best estimate of the nature of the galaxies in Table 5.3, but caution that these are by no means certain.

Table 5.4. *HST* optical photometry used for SED fitting. All fluxes are given in μJy and are corrected for lensing. Upper limits are given at the 3σ level.

Name	$F225W$	$F275W$	$F336W$	$F390W$	$F435W$	$F475W$	$F555W$	$F606W$	$F625W$	$F775W$
MACSJ0744	50 ± 10	80 ± 20	250 ± 50	160 ± 30	...	170 ± 30	200 ± 40	230 ± 40	...	410 ± 80
MACSJ1149	180 ± 30	240 ± 50	380 ± 70	370 ± 70	450 ± 90	430 ± 80	390 ± 70	420 ± 80	450 ± 80	440 ± 80
MACSJ0451	...	...	...	...	...	...	...	150 ± 30	...	...
Abell1413a	...	...	...	...	...	...	...	...	...	300 ± 60
Abell1413b	...	...	...	...	...	...	...	...	...	< 150
MS1621	...	...	...	...	...	...	210 ± 40	...	...	...
RXJ1720	...	...	...	...	...	...	...	120 ± 30	...	...
Abell1689a	...	< 290	< 66	...	...	...	...	...	...	100 ± 20
Abell1689b	...	< 290	< 70	...	...	...	...	...	...	170 ± 30
Abell2895a	...	...	...	...	...	...	...	170 ± 30	...	...
Abell2895b	...	...	...	...	...	...	...	50 ± 10	...	...

Table 5.5. *HST* near-infrared photometry used for SED fitting. All fluxes are given in μJy and are corrected for lensing. Upper limits are given at the 3σ level.

Name	$F814W$	$F850LP$	$F105W$	$F110W$	$F125W$	$F140W$	$F160W$
MACSJ0744	450 ± 80	...	700 ± 100	700 ± 100	480 ± 90	...	...
MACSJ1149	500 ± 100	700 ± 100	810 ± 150	880 ± 160	870 ± 160	920 ± 170	1000 ± 200
MACSJ0451	160 ± 30	...	...	280 ± 50	...	450 ± 80	...
Abell1413a	...	360 ± 70	...	...	...	...	...
Abell1413b	...	< 200	...	...	...	...	...
MS1621	320 ± 60	...	...	...	...	...	...
RXJ1720	...	...	...	...	...	...	...
Abell1689a	...	120 ± 20	...	...	120 ± 20	...	180 ± 30
Abell1689b	...	190 ± 40	...	...	120 ± 20	...	160 ± 30
Abell2895a	...	...	...	...	...	...	...
Abell2895b	...	...	...	...	...	...	...

5.3.5 SED fitting and stellar mass estimates

In order to estimate the extinction due to dust and the stellar masses of our sample, we model their spectral energy distributions (SEDs) from available archival *HST* and *Spitzer/IRAC* imaging. We first subtract any foreground cluster members lying close to the line of sight to the target galaxy, using the IRAF tasks `ellipse` and `bmodel`. We then degrade all of the imaging for each galaxy to the poorest resolution, that of the longest-wavelength *IRAC* band. We then extract the photometry using an elliptical aperture large enough to encompass the galaxy, with a 2" annulus for sky subtraction. We apply aperture corrections to the *IRAC* fluxes based on the area of the aperture used.

As the continuum light does not necessarily follow the same distribution as the nebular emission, we do not assume the same magnification factor from gravitational lensing; instead, the measured fluxes are corrected for lensing using the flux-weighted mean magnification within the aperture, from magnification maps created with LENSTOOL. The resulting magnification factors are within 1σ of the values given for the nebular emission in Table 5.1. The complete photometry, corrected for lensing, is given in Tables 5.4, 5.5 and 5.6. The number of available photometric bands per galaxy ranges from 2 to 19; those with fewer bands have correspondingly large errors in the quantities derived from the SED fit.

We perform the SED fitting using the CIGALE code (Noll et al., 2009). We use the stellar population models of Maraston (2005), allow either exponentially decreasing or continuous star formation histories and constrain the oldest stellar populations to be younger than the age of the Universe at the target redshift. The CIGALE code

Table 5.6. *Spitzer*/IRAC infrared photometry used for SED fitting. All fluxes are given in μJy and are corrected for lensing. Upper limits are given at the 3σ level.

Name	IRAC 3.6μm	IRAC 4.5μm	IRAC 5.8μm	IRAC 8μm
MACSJ0744	1900 ± 300	1400 ± 300	...	...
MACSJ1149	2000 ± 400	1500 ± 300	...	...
MACSJ0451	360 ± 70	380 ± 70	...	...
Abell1413a	480 ± 90	490 ± 90	...	...
Abell1413b	< 250	< 250	...	...
MS1621	...	...	...	...
RXJ1720	1900 ± 800	2200 ± 800	< 2500	< 1600
Abell1689a	< 340	< 270	< 700	< 700
Abell1689b	140 ± 30	140 ± 30	< 700	< 640
Abell2895a	< 400	< 500	...	...
Abell2895b	< 300	< 230	...	...

creates SEDs from the far-ultraviolet to the infrared based on a dust-attenuated stellar population, infrared dust emission and spectral line templates. The best-fit galaxy parameters are derived with a Bayesian-like analysis from the distribution of probability-weighted best-fit models.

The stellar masses and dust extinction, A_V, obtained for each galaxy from the SED fit is given in Table 5.7. We find stellar masses of $M_* = 4\times10^8 - 2\times10^{10}\mathrm{M}_\odot$; thus, lensing allows us to probe systematically lower mass galaxies than unlensed samples such as SINS (median $M_* \sim 3\times10^{10}\mathrm{M}_\odot$; Förster Schreiber et al., 2009) or SHiZELS (median $M_* \sim 2\times10^{10}\mathrm{M}_\odot$; Swinbank et al., 2012). The dust extinctions we derive are in the range $A_V = 0.3 - 1.1$ with a median $A_V \sim 0.8$, similar to those of SINS ($A_V \sim 0.8$; Förster Schreiber et al., 2009) and SHiZELS ($A_V \sim 0.9$; Swinbank et al., 2012).

The stellar masses and dust extinctions of the Jones et al. (2010) sample and Abell1835 of the new observations are derived by Richard et al. (2011) and given in their Table 4. We note that the method used is similar to the one we employ, so the results can be directly compared.

5.3.6 Integrated galaxy properties

We now derive some integrated properties of the sample, so that we can relate the lensed galaxies to the population as a whole and explore how their internal structures evolve as a function of their global properties.

A summary of the integrated properties of the sample is given in Table 5.7. Total fluxes of the Hα or Hβ emission lines are calculated by summing every pixel in the

Table 5.7. Integrated properties of the sample

Name	Intrinsic $f_{H\alpha}$	Intrinsic $f_{H\beta}$	SFR	$r_{1/2}$	$\log M_*$	A_V
	(10^{-18}erg s^{-1}cm^{-2})		($M_\odot yr^{-1}$)	(kpc)	($M_\odot$)	
MACSJ0744	18 ± 2		1.7 ± 0.2	0.3 ± 0.1	9.2 ± 0.4	0.9 ± 0.4
MACSJ1149	12 ± 2		1.2 ± 0.2	0.6 ± 0.2	9.3 ± 0.4	0.5 ± 0.3
MACSJ0451		5 ± 2	5 ± 2	0.18 ± 0.03	8.8 ± 0.3	0.7 ± 0.3
Abell1413a	34 ± 4		6.6 ± 0.7	0.46 ± 0.08	8.9 ± 0.4	0.4 ± 0.3
Abell1413b	10 ± 1		3.0 ± 0.3	0.8 ± 0.3	< 8.6	1.0 ± 0.5
Abell1835	2.6 ± 0.3		0.8 ± 0.2	0.6 ± 0.2	8.8 ± 0.2^a	1.1 ± 0.3^a
MS1621+26	32 ± 4		11 ± 1	2 ± 1	10.3 ± 1.0	1.0 ± 0.5
RXJ1720+26	3.7 ± 0.5		1.3 ± 0.2	0.7 ± 0.3	8.9 ± 0.9	0.9 ± 0.5
Abell1689a		0.7 ± 0.5	1.1 ± 0.2	0.3 ± 0.1	8.9 ± 0.6	0.7 ± 0.4
Abell1689b		1.0 ± 0.5	1.5 ± 0.3	0.23 ± 0.08	8.6 ± 0.4	0.3 ± 0.2
Abell2895a		10.4 ± 0.1	22 ± 4	0.5 ± 0.3	< 9.6	0.4 ± 0.3
Abell2895b		9 ± 3	27 ± 5	0.17 ± 0.09	< 9.4	0.5 ± 0.3
Cl0024+16	130 ± 30		27 ± 6	1.8 ± 0.2	10.4 ± 0.1^a	1.1 ± 0.2^a
Cl0949	50 ± 10		20 ± 6	3.5 ± 0.9	10.2 ± 0.5^a	1.0 ± 0.0^a
MACSJ0712		2.8 ± 0.6	5.0 ± 0.1	0.5 ± 0.2	10.5 ± 0.4^a	0.8 ± 0.2^a
MACSJ0744b	8 ± 2		2.4 ± 0.5	1.2 ± 0.2	10.0 ± 0.1^a	0.8 ± 0.2^a
MACSJ2135		18 ± 2	40 ± 5	0.8 ± 0.2	10.8 ± 0.1^a	0.7 ± 0.1^a

Notes: All quantities are corrected for lensing magnification. SFR is calculated from the Hα or Hβ luminosity corrected for dust extinction based on A_V. The half-light radius $r_1/2$ is based on the Hα or Hβ morphology as described in the text. A_v and M_* are estimated from SED fitting of broadband photometry as described in the text, except for those marked (*a*), which are from Richard et al. (2011). Targets below the line are from Jones et al. (2010), with SFRs given in their Table 2 and half-light radii reported by Richard et al. (2011).

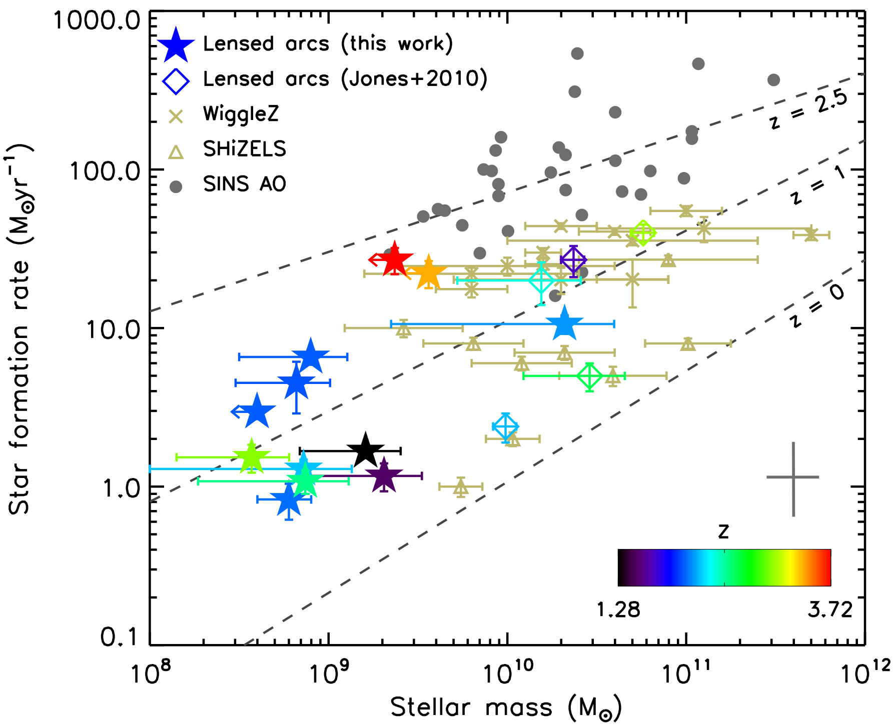

Figure 5.3. Total galaxy SFR against stellar mass for the lensed arcs, in comparison with other high-redshift kinematic studies. The lensed arcs are colour-coded by redshift. The dashed lines indicate the star-forming galaxy 'main sequence' at z = 0, 1 and 2.5 (Whitaker et al., 2012). Comparison data are from SHiZELS (Swinbank et al., 2012), WiggleZ (Wisnioski et al., 2011) and the SINS AO sample (Newman et al., 2013), and the grey cross indicates the typical error on the SINS points. The lensed arcs, as well as the WiggleZ and SHiZELS samples, are similar to $z \sim 1$ main sequence star-forming galaxies, though the lensed arcs probe the lower-mass end of the relation. The SINS AO sample covers higher specific star formation rates, similar to the $z \sim 2.5$ star-forming main sequence.

source plane cubes with signal-to-noise > 5. We measure the total flux by fitting a Gaussian profile to the emission lines, and the ratio of the total flux in the image plane to that in the source plane gives the total magnification given in Table 5.1.

Intrinsic star formation rates (SFRs) in Table 5.7 are calculated from the Hα (or Hβ, assuming case B recombination) flux, corrected for dust according to the extinction A_V derived from SED fitting, by applying the Kennicutt (1998a) prescription corrected for a Chabrier initial mass function (IMF), which reduces the SFR by a factor 1.7×.

To find the half-light radius $r_{1/2}$, we first construct an array in which each pixel value is the distance from the dynamical centre, $[i_c, j_c]$, based on an estimated position angle, ϕ, and inclination (θ); the derivation of the dynamical centre, position angle and inclination is discussed in Section 5.4.1). The result is a series of concentric ellipses with the galactocentric radius in pixel i, j given by

$$r_{i,j} = \sqrt{(x\cos\phi + y\sin\phi)^2 + \left(\frac{x\sin\phi - y\cos\phi}{\cos\theta}\right)^2}, \tag{5.3.2}$$

where $x = |i - i_c|$ and $y = |j - j_c|$. We then convolve this array with the flux-weighted source plane PSF, to account for the fact that the preferential direction of magnification causes the source plane images to appear stretched in one direction.

Starting from the dynamical centre, we then sum the flux within contours of constant r, incrementing r until half the total flux is enclosed. This then gives the half-light radius $r_{1/2}$ given in Table 5.7. The half-light sizes we find are in the range $r_{1/2} \sim 0.2 - 2.1\,\mathrm{kpc}$. The half-light radii of the Jones et al. (2010) sample are $r_{1/2} = 0.5 - 3.5\,\mathrm{kpc}$. As noted in Section 5.3.4, we find galaxies that are systematically smaller than those observed in unlensed samples due to the lensing magnification.

We illustrate the selection of the lensed galaxies in Figure 5.3 by comparing the SFRs and stellar masses of the lensed arcs to similar unlensed samples. The lensed sample covers a similar range of specific star formation rates (SSFR; SFR/M_*) to the unlensed SHiZELS and WiggleZ surveys, though the lensing magnification allows us to probe lower stellar masses and SFRs. The SSFRs of these samples are similar to the star-forming main sequence at $z \sim 1$ (Whitaker et al., 2012), whereas the SINS galaxies have systematically higher SSFR, similar to the $z \sim 2.5$ main sequence.

5.4 Results and Analysis

5.4.1 Dynamics

Dynamical properties of the sample

From our best estimates of kinematic classification given in Table 5.3, we estimate that 11/17 (65%) of the combined lensed sample are rotating discs, 5/17 (29%) are probable mergers, and the remaining one is dispersion-dominated. The merger fraction in our sample is very close to those in unlensed surveys, typically 1/3, but we find a higher fraction of rotating systems, which typically make up 33-44% of other samples (Epinat et al., 2012; Förster Schreiber et al., 2009; Law et al., 2009; Wright et al., 2009). While the merger classification adopted is relatively insensitive to spatial resolution, it is likely that many of the galaxies classed as 'dispersion-dominated' in unlensed studies would present with velocity gradients given higher spatial resolution. For example, Newman et al. (2013) found that when the same 34

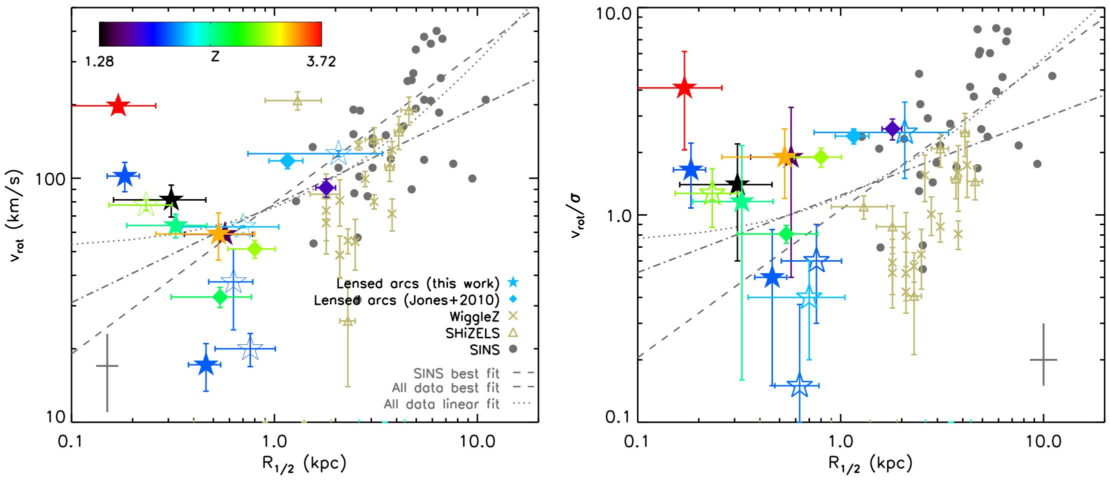

Figure 5.4. *Left:* Relation between rotational velocity and half-light radius. *Right:* $v_{\rm rot}/\sigma$ against half-light radius. The lensed arcs are colour-coded by redshift on the same scale in both plots, with filled symbols representing those galaxies identified as discs, and unfilled symbols mergers or dispersion-dominated systems. The lines show the best fits to the data assuming a linear relation and a power law. The dashed line is the fit to the SINS data from Newman et al. (2013), and the dot-dashed line is a fit to all of the samples. Comparison samples are included from the high-z lensed sources of Jones et al. (2010), and the unlensed high-z IFU surveys SHiZELS (Swinbank et al., 2012), WiggleZ (Wisnioski et al., 2011) and the SINS AO sample (Newman et al., 2013). The grey crosses indicate the average error on the SINS points. The best fit power law to the SINS data is also shown for comparison purposes. The intrinsically smaller lensed galaxies extend the relation found in the non-lensed samples to smaller sizes, but with a weaker correlation.

galaxies observed in seeing-limited conditions were re-observed with adaptive optics, the fraction classified as dispersion-dominated fell from 41% to $6-9\%$. The one lensed galaxy we classify as dispersion-dominated is Abell1835, but this galaxy lies on the critical line so it is possible that we have not observed the whole velocity gradient in this source. Alternatively, it could simply be a slow rotator.

The quantity $v_{\rm rot}/\sigma$ is a measure of the rotational support in a system. Galaxies exist on a continuum in $v_{\rm rot}/\sigma$; they all have some degree of rotation, but those with low $v_{\rm rot}/\sigma$ values have a larger fraction of their kinematic support from random motion rather than ordered rotation. Generally, a simple cut is applied, where galaxies with $v_{\rm rot}/\sigma > 0.4$ are considered rotating systems (Förster Schreiber et al., 2009). Of our combined sample, only Abell1835 falls beneath this cut, with $v_{\rm rot}/\sigma = 0.2 \pm 0.2$. However, as discussed above, we may not have observed the full velocity gradient in this galaxy. The galaxies that appear to be interactions or mergers - Abell1413a, Abell1413b and RXJ1720 - all have marginal $v_{\rm rot}/\sigma$ within 1σ of the boundary between rotation-dominated and dispersion-dominated systems.

In non-lensed galaxies observed with adaptive optics, Newman et al. (2013) found a correlation between $v_{\rm rot}/\sigma$ and the half-light radius $r_{1/2}$. This was suggested to be due to a relationship between $v_{\rm rot}$ and $r_{1/2}$, with larger galaxies having higher rotation velocities. We add our sample to these relationships in Figure 5.4. As gravitational lensing allows us to observe intrinsically smaller galaxies, we are able to extend these relations to smaller sizes, and we find that the correlations observed in non-lensed data continue, but with larger scatter. Between $v_{\rm rot}$ and $r_{1/2}$, we find a best fit relation of $\log{(v_{\rm rot})} = 0.36\,\log r_{1/2} + 1.9$, with a Spearman rank correlation coefficient of $\rho = 0.61$ (where $\rho = 0$ indicates no correlation, and $\rho = 1$ implies perfect correlation). This is a shallower relation than that found by Newman et al., who derive a slope of 0.73. While this could be an effect increasing the sample size, it may also be an indication that a linear relation is more appropriate. The best-fit linear relation is $v_{\rm rot} = 23\,r_{1/2} + 60$. This provides a much better fit to the data ($\Delta\,\chi^2 \sim 1300$), with a slope similar to that found in the SINS sample at large $r_{1/2}$, but accounting for a 'floor' in $v_{\rm rot}$ in smaller galaxies. It is also, as Newman et al. point out, more physically motivated. There is no apparent systematic difference between the disc-like (rotation-dominated) galaxies and those identified as mergers or dispersion-dominated systems.

Comparing $v_{\rm rot}/\sigma$ to $r_{1/2}$ in Figure 5.4 gives similar results; we find higher scatter at low $r_{1/2}$, but there remains a weak positive correlation (Spearman rank correlation coefficient $\rho = 0.52$) in the combined lensed and unlensed data. The best fit linear relation is $v_{\rm rot}/\sigma = 0.7 + 0.5\,r_{1/2}$. In this case, the data are better fit by a power law with $\log\left(v_{\rm rot}/\sigma\right) = 0.37\log\left(r_{1/2}\right) + 0.09$, but the difference between the two fits ($\Delta\,\chi^2 \sim 20$) is less significant. Disc-like galaxies typically have, by definition, higher $v_{\rm rot}/\sigma$ than non-rotation-dominated systems. If we consider only the rotation-dominated lensed arcs in Figure 5.4, there is some evidence for a flattening of $v_{\rm rot}/\sigma$ at low $r_{1/2}$.

In Figure 5.5, we plot stellar mass, M_*, as a function of $v_{\rm rot}/\sigma$, finding that our combined sample continues the relation observed in the non-lensed SINS+AO sample to lower stellar masses, although with significant scatter. However, there is little correlation with the unlensed SHiZELS and WiggleZ data. This could be because

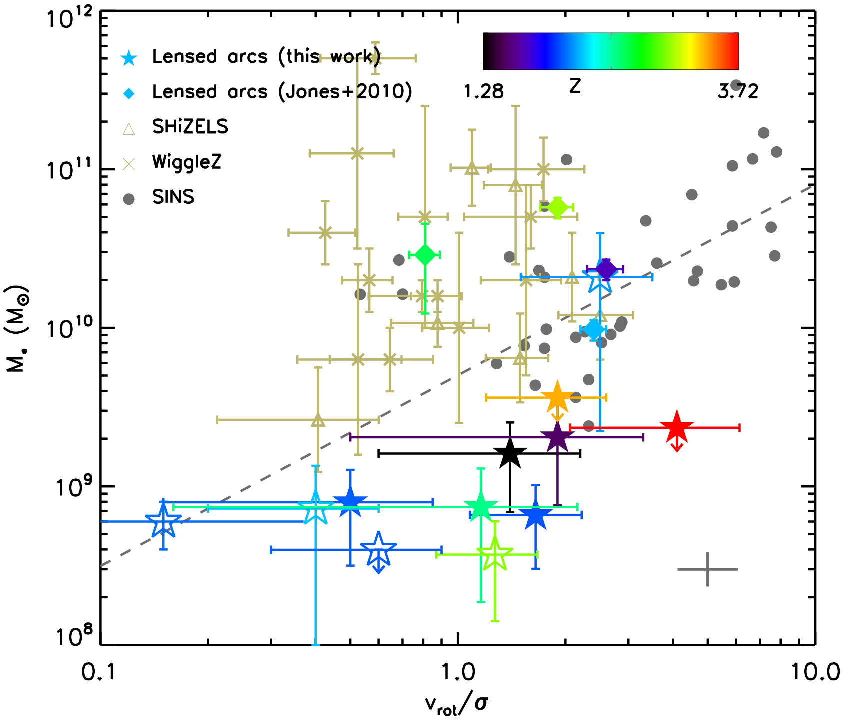

Figure 5.5. Relation between stellar mass, M_*, and $v_{\rm rot}/\sigma$. The rotational velocity $v_{\rm rot}$ is corrected for inclination, and σ is the luminosity-weighted mean velocity dispersion, corrected for beam smearing. The SINS AO sample (Newman et al., 2013), SHiZELS (Swinbank et al., 2012) and WiggleZ (Wisnioski et al., 2011) are also shown for comparison with higher stellar mass systems at high redshift. The grey cross indicates the typical error on the SINS data, and the dashed line is the best fit to the SINS + lensed samples. The lensed samples continue the relation observed in the SINS data to lower stellar masses, but there is little correlation observed in the SHiZELS and WiggleZ data, which are not so well resolved. We find that lensed galaxies with high $v_{\rm rot}/\sigma$ tend to have high M_*, indicating that galaxies become more dynamically 'settled' as they build up more mass.

they are observed with similar resolution to the SINS data, but have systematically smaller sizes, and thus a larger contribution from beam smearing. The best fit to the combined lensed and SINS+AO unlensed data is $\log(M_*) = 1.2\log(v_{\rm rot}/\sigma) + 9.7$. If we interpret $v_{\rm rot}/\sigma$ as a measure of the 'order' in a system, where $v_{\rm rot}$ measures the ordered rotation and σ constitutes turbulent or disordered motion, this relationship suggests that galaxies become more ordered as they build up higher stellar masses, a process described as 'kinematic settling' (Kassin et al., 2012).

The stellar mass Tully-Fisher relation

The Tully-Fisher relation relates the stellar content of galaxies to their rotational velocity (Tully & Fisher, 1977). In a model in which gas cools from a dark matter halo into a rotating disc, maintaining the angular momentum of its parent halo, the Tully-Fisher relation is interpreted as a relationship between the baryonic content of galaxies and the angular momentum of their dark matter halos. As such, it is a key parameter that models of galaxy evolution must reproduce.

Attempts to place observational constraints on the redshift evolution of the Tully-Fisher relation have had inconclusive results. Observations of the B-band Tully-Fisher relation at high redshift demonstrate modest evolution, but are affected by recent star formation and so evolution of the B-band mass-to-light ratio (Vogt et al., 1996, 1997). We therefore concentrate on the more physical stellar mass Tully-Fisher relation, but this too has produced mixed results, with no coherent evidence of evolution out to $z \sim 2$ (Conselice et al., 2005; Cresci et al., 2006; Flores et al., 2006; Kassin et al., 2007; Miller et al., 2011, 2012; Puech et al., 2008; Swinbank et al., 2012; Vergani et al., 2012). Miller et al. (2013) found that bulgeless galaxies at

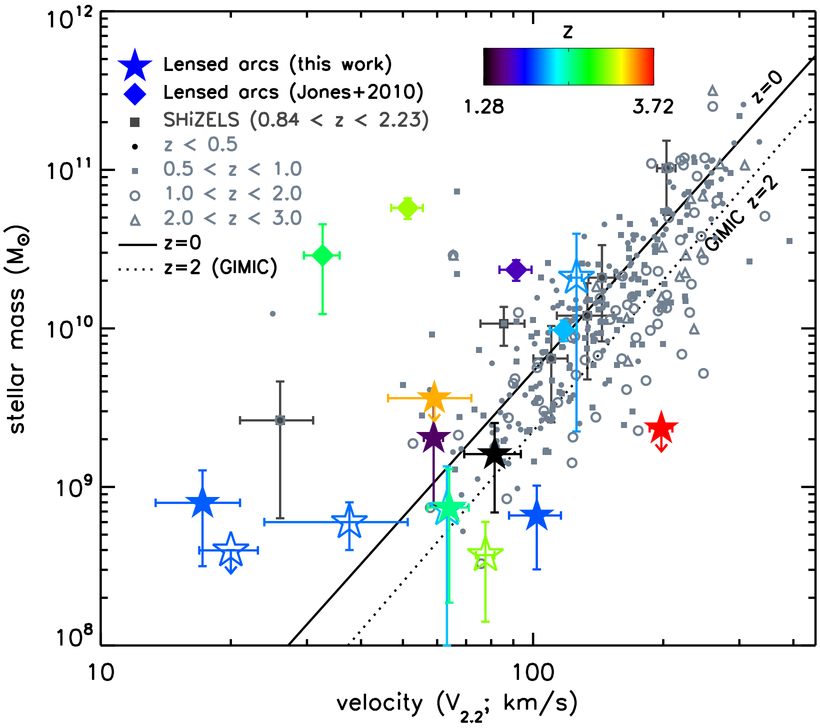

Figure 5.6. The stellar mass Tully-Fisher relation. The stellar mass, M_*, is estimated from SED fitting to the available *HST* and *Spitzer* imaging. The rotation velocity $v_{2.2}$ is measured from the model rotation curves interpolated at a radius of $r = 2.2\, r_{1/2}$, where $r_{1/2}$ is the half-light radius. The $z = 0$ data are from Pizagno et al. (2005), and the solid line is the best fit to these points. High-redshift comparison data are from the $z \sim 2$ lensed arcs of Jones et al. (2010), the $z = 1$ lensed arcs of Swinbank et al. (2006), the DEIMOS $z \sim 0.6$ and $z \sim 1.3$ samples of Miller et al. (2011, 2012), the $z \sim 2-3.5$ SINS and AMAZE surveys (Cresci et al., 2009; Gnerucci et al., 2011) and the SHiZELS $0.84 < z < 2.3$ sample of Swinbank et al. (2012). The dotted line indicates the predicted evolution of the Tully-Fisher relation at $z = 2$ from simulations (Crain et al., 2009). We colour-code our lensed arcs by redshift, and show rotating disc-like systems with filled symbols, and mergers and dispersion-dominated systems with open symbols. We find that most of our sample is largely consistent with the $z = 0$ relation, but with significant scatter discussed further in the text.

high-z are the ones that show the greatest offset from the local relation, which they interpret as evidence that these galaxies have yet to 'mature' onto the Tully-Fisher relation, perhaps related to higher gas fractions in their discs. Similarly, Gnerucci et al. (2011) investigated the stellar mass Tully-Fisher relation at $z \sim 3$ and found marginal evolution but with a large amount of scatter, concluding that the relation may not be in place at this epoch.

To compare different galaxies, it is important to measure $v_{\rm rot}$ in a consistent manner. Measurements of the rotation curve are naturally sensitive to the surface brightness of the galaxy and the depth of the observations. Courteau (1997) compared various methods of measuring $v_{\rm rot}$ and found that $v_{2.2}$ - the velocity interpolated from the model rotation curve at a radius $r = 2.2\,h$, where h is the disc scale length - performed best in terms of minimal internal scatter and residuals from the Tully-Fisher relation and provided the best match to radio (21cm) results. In high-redshift galaxies with clumpy and disturbed morphologies, the light does not follow a pure exponential disc profile, so we cannot strictly use this definition with our data. We therefore adopt the half-light radius, $r_{1/2}$, as a proxy for the disc scale length, and measure $v_{2.2}$ from the model rotation curve fits, corrected for inclination, at $r = 2.2\,r_{1/2}$. For consistency across the sample, we re-analyse the velocity fields of the Jones et al. (2010) sample in order to extract $v_{2.2}$ from these galaxies. Our derived $v_{2.2}$ values are slightly lower than the inclination-corrected $v_{\rm max}$ that they derive by an average of 20%.

We plot the stellar mass Tully-Fisher relation in Figure 5.6. We find that most of our lensed arcs are consistent with the Tully-Fisher relation observed in other

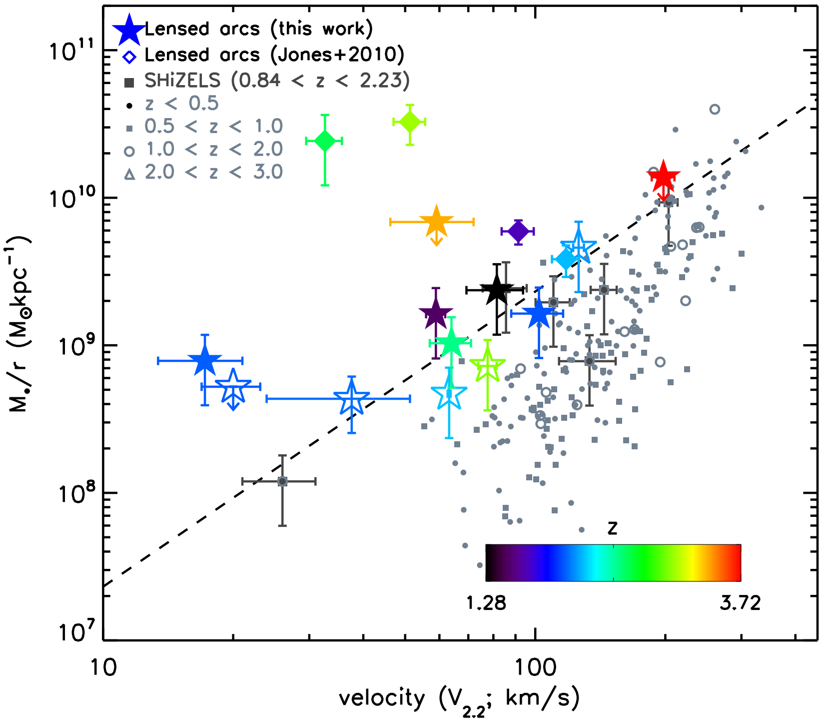

Figure 5.7. The ratio between stellar mass and galaxy radius as a function of rotational velocity, where radius is defined as 2.2 disc scale lengths and the velocity is corrected for inclination. Comparison data is from the same sources as in Figure 5.6. The dashed line indicates $v^2 = GM_*/r$. The lensed galaxies and some data from the other samples, in particular from SHiZELS, lie along this line, indicating that their dynamics are dominated by baryons in the discs. There is no apparent systematic difference between disc-like (filled symbols) and mergers/ dispersion-dominated systems (open symbols) in the lensed samples. Offsets from this line are likely related to the gas fractions of the galaxies.

samples, but with considerable scatter. Four galaxies lie well above the local relation, with low $v_{2.2}$ for their stellar masses. Of these, two are from the Jones et al. (2010) sample; these are Cl0949 and MACSJ2135 (the Cosmic Eye). The former was identified as a merger by Jones et al. (2010), though the latter appears to be a rotationally-supported disc (see Stark et al., 2008). The remaining two galaxies lying above the local relation are Abell1413a and Abell1413b, which appear to be an interacting pair.

In addition, MACSJ0451 ($z = 2.01$) and two of the higher-redshift targets (Abell1689a at $z = 3.04$ and Abell2895b at $z = 3.72$) have high $v_{2.2}$ for their stellar masses. This could be indicative of redshift evolution; simulations predict that the zero-point should decrease at high redshift (e.g. Crain et al., 2009; McCarthy et al., 2012, indicated by a dotted line in Figure 5.6). Semi-analytic models in which the disc dynamics are driven by the dark matter halo make a similar prediction (Dutton et al., 2011).

However, Benson (2012) predicts a modest *positive* increase in the zero-point at high redshift. As Miller et al. (2012) point out, the primary difference is that the Benson model has a larger contribution from baryons. High-redshift galaxies are intrinsically smaller than their present-day counterparts - especially in the lensed sample that probes the smaller, fainter population - and so we might expect the dynamics within $2.2r_{1/2}$ to be dominated by baryons (see also Miller et al., 2011). In the simplest case of orbital circular motion, we should see $v^2 = GM/r$ for total enclosed mass M. To test whether this is a better description of our data, we divide the y-axis of Figure 5.6 by $2.2r_{1/2}$ and show the result in Figure 5.7. The scatter is significantly reduced in comparison to Figure 5.6, and the line $v^2 = GM_*/r$ provides a good fit to the lensed and SHiZELS data. The varying gas fractions in the galaxies will contribute significantly to the scatter in this relation. The other comparison samples have a systematically higher velocities at a given M_*/r, perhaps suggesting that their dynamics do have contributions from the dark matter halo, whereas the dynamics of the lensed galaxies within the central few kpc are dominated by baryons.

5.4.2 Star-forming clumps

With the high spatial resolution afforded by gravitational lensing, it is possible to extract star-forming clumps from lensed galaxies on scales comparable to giant HII regions in local galaxies. It has long been noted that galaxies in the high-redshift Universe tend to be 'clumpier' then their local counterparts, with clumps often dominating the host galaxies' morphologies and giving rise to 'clump cluster' and 'chain' galaxies (e.g. Cowie et al., 1995; Elmegreen & Elmegreen, 2005; Elmegreen et al., 2004). Numerous high-redshift galaxy surveys have isolated clumps and analysed their properties on ~kpc scales (Förster Schreiber et al., 2011; Genzel et al., 2011; Swinbank et al., 2012; Wisnioski et al., 2012b), but to compare them directly to star formation in the local Universe, which takes place in HII regions on scales of ~ 100 pc, the spatial resolution afforded by gravitational lensing is required (Jones et al., 2010; Livermore et al., 2012a; Swinbank et al., 2011, 2009).

Table 5.8. Properties of the star-forming clumps.

Notes: All quantities are corrected for lensing where appropriate. (*a*): The clump radius is calculated as described in the text, using the area enclosed by an isophote and assuming circular symmetry. The error bar encompasses an alternative definition using the FWHM of the clump emission line profile. (*b*): SFR is calculated from the total Hα or Hβ flux enclosed in the isophote and is corrected for extinction. (*c*): The velocity dispersion, σ, is the mean local value within the clump and is deconvolved for the local velocity gradient.

Name	radius	SFR	σ
	pc	$\mathrm{M_{\odot} yr^{-1}}$	$\mathrm{km\,s^{-1}}$
Notes:	(*a*)	(*b*)	(*c*)
MACSJ0744-1	300 ± 100	0.26 ± 0.02	70 ± 7
MACSJ0744-2	300 ± 100	0.18 ± 0.01	84 ± 8
MACSJ0744-3	160 ± 30	0.04 ± 0.01	51 ± 8
MACSJ1149-1	450 ± 70	0.51 ± 0.05	74 ± 10
MACSJ1149-2	150 ± 50	0.15 ± 0.02	120 ± 19
MACSJ1149-3	160 ± 30	0.06 ± 0.01	134 ± 31
MACSJ1149-4	210 ± 50	0.12 ± 0.02	80 ± 17
MACSJ1149-5	180 ± 70	0.07 ± 0.01	95 ± 39
MACSJ1149-6	150 ± 20	0.05 ± 0.01	71 ± 17
MACSJ1149-7	160 ± 40	0.04 ± 0.01	123 ± 33
MACSJ1149-8	140 ± 50	0.03 ± 0.01	115 ± 30
MACSJ1149-9	140 ± 20	0.02 ± 0.01	122 ± 61
MACSJ0451-1	500 ± 200	1.2 ± 0.4	87 ± 6
MACSJ0451-2	300 ± 200	0.5 ± 0.2	84 ± 6

Continued on next page

Table 5.8 – continued from previous page

Name	radius	SFR	σ
	pc	$M_\odot yr^{-1}$	$km\,s^{-1}$
Notes:	(a)	(b)	(c)
Abell1413a-1	700 ± 300	2.3 ± 0.2	53 ± 8
Abell1413b-1	200 ± 100	0.18 ± 0.02	57 ± 9
Abell1413b-2	260 ± 60	0.15 ± 0.02	58 ± 10
Abell1413b-3	300 ± 100	0.26 ± 0.03	54 ± 9
Abell1413b-4	140 ± 40	0.02 ± 0.01	84 ± 32
Abell1835-1	90 ± 60	0.10 ± 0.01	77 ± 14
Abell1835-2	200 ± 100	0.12 ± 0.02	67 ± 13
MS1621+26-1	900 ± 400	3.1 ± 0.3	63 ± 9
MS1621+26-2	600 ± 200	0.8 ± 0.1	66 ± 11
MS1621+26-3	340 ± 70	0.18 ± 0.03	55 ± 12
MS1621+26-4	200 ± 100	0.08 ± 0.01	58 ± 12
RXJ1720+26-1	700 ± 200	0.77 ± 0.08	61 ± 8
RXJ1720+26-2	600 ± 100	0.59 ± 0.06	67 ± 10
RXJ1720+26-3	400 ± 100	0.28 ± 0.03	76 ± 11
RXJ1720+26-4	600 ± 100	0.65 ± 0.06	65 ± 9
RXJ1720+26-5	300 ± 100	0.23 ± 0.03	67 ± 12
Abell1689a-1	180 ± 60	0.2 ± 0.1	116 ± 45
Abell1689b-1	150 ± 80	0.13 ± 0.04	103 ± 16

Continued on next page

Table 5.8 – continued from previous page

Name	radius	SFR	σ
	pc	$\mathrm{M_{\odot} yr^{-1}}$	$\mathrm{km\,s^{-1}}$
Notes:	(*a*)	(*b*)	(*c*)
Abell2895a-1	400 ± 100	1.8 ± 0.7	63 ± 4
Abell2895a-2	500 ± 300	2.3 ± 0.8	61 ± 4
Abell2895a-3	60 ± 10	0.03 ± 0.01	57 ± 5
Abell2895b-1	290 ± 90	5 ± 2	51 ± 3
Cl0024+16-1	420 ± 70	5 ± 1	65 ± 11
Cl0024+16-2	600 ± 200	9 ± 2	60 ± 9
Cl0024+16-3	370 ± 50	4 ± 1	63 ± 14
Cl0024+16-4	400 ± 100	3.4 ± 0.8	62 ± 13
Cl0949-1	1000 ± 100	16. ± 4	72 ± 13
Cl0949-2	800 ± 300	10 ± 2	63 ± 8
Cl0949-3	800 ± 300	11 ± 3	56 ± 6
Cl0949-4	700 ± 100	8 ± 2	76 ± 14
MACSJ0712-1	220 ± 70	3.3 ± 0.8	74 ± 11
MACSJ0744b-1	300 ± 100	0.7 ± 0.2	93 ± 26
MACSJ0744b-2	300 ± 100	0.4 ± 0.1	136 ± 45
MACSJ0744b-3	300 ± 100	0.5 ± 0.1	118 ± 14
MACSJ2135-1	600 ± 100	25 ± 6	41 ± 15
MACSJ2135-2	500 ± 100	12 ± 3	40 ± 14

Different studies of star-forming clumps have used a variety of methods to detect and isolate them from their host galaxies. Discussions of the merits of various techniques can be found in Wisnioski et al. (2012b) and Livermore et al. (2012a). We adopt the same method as in Livermore et al. (2012a) and use the 2D version of CLUMPFIND (Williams et al., 1994). This routine uses multiple isophotes, starting by defining clumps in the brightest regions and then moving down through the isophote levels. Any isolated contours are defined as new clumps, and any which enclose an existing peak are allocated to that clump. A contour which encloses two or more existing peaks has its pixels divided between them using a 'friends-of-friends' algorithm. We define the lowest contour at 3σ, where σ is the standard deviation of pixels in the underlying galaxy. We then add additional contours in 1σ intervals up to the peak in the image.

For IFU data, Genzel et al. (2011) advocate defining clumps in slices in velocity. We test this method with our data and find that it produces similar results to using the integrated intensity maps, and where it does produce clumps that are not evident in the integrated maps, they are marginal detections found only in the lowest $(3 - 4\sigma)$ contour levels. We therefore use the integrated Hα (or Hβ) maps to define clumps. This has the added advantage of being the method most easily comparable to the narrowband imaging in Livermore et al. (2012a), where we used maps of Hα integrated over a wide velocity range.

To ensure self-consistency across the entire sample of lensed arcs, we reanalyse the intensity maps of the Jones et al. (2010) sample to extract clumps with

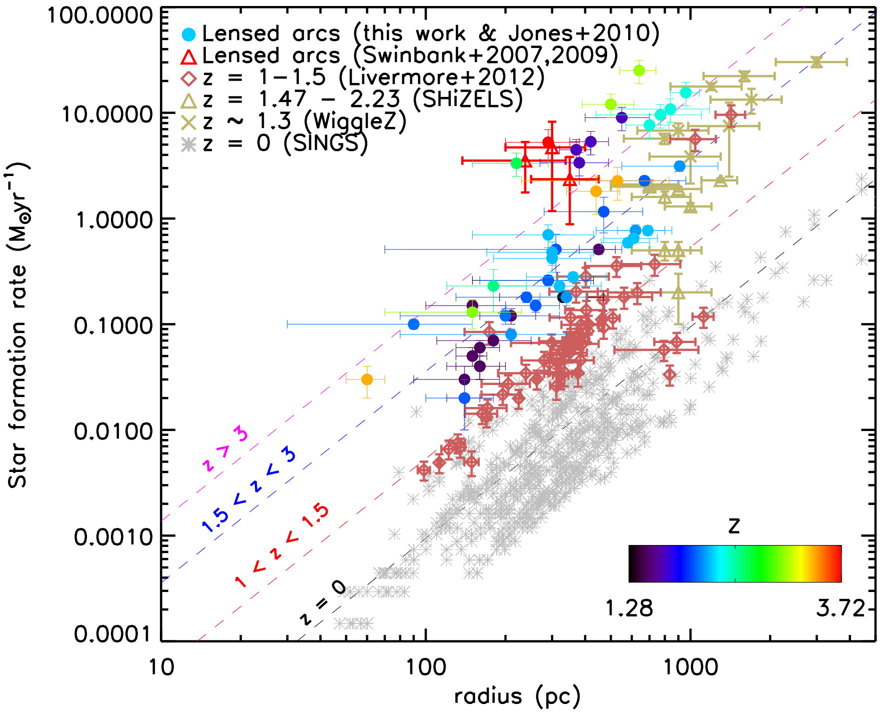

Figure 5.8. Relation between Star formation rate (SFR) in clumps and their sizes. The $z = 0$ sample from the SINGS survey (Kennicutt et al., 2003) and the $z \sim 1 - 1.5$ lensed arcs from Livermore et al. (2012a) are extracted from Hα narrowband imaging. We also show the $z \sim 5$ lensed arcs of Swinbank et al. (2007) and Swinbank et al. (2009) and the unlensed high-z samples from SHiZELS (Swinbank et al., 2012) and WiggleZ (Wisnioski et al., 2012b) for comparison. The clumps from our sample of lensed arcs are colour-coded by redshift. The dashed lines are contours of constant surface brightness with the zero-points fit in four redshift bins. We find evolution in this zero-point such that high-redshift galaxies host clumps of higher surface brightnesses.

CLUMPFIND. Jones et al. (2010) used a single isophote per galaxy to extract their clump properties, whereas the algorithm developed by Livermore et al. (2012a) used the noise properties of the image to robustly define a series of isophote levels in a way that does not require any fine tuning. The variation in methods means that the clumps extracted are not identical; a lower isophote will increase both the size and luminosity of the extracted clump, and vice versa. Generally, we use lower isophote levels than Jones et al. (2010), leading to larger sizes (but within $\sim 1\sigma$ of the published values) with correspondingly higher luminosities. The primary difference is that we also extract some smaller, lower-luminosity clumps that are missed when adopting a single isophote.

Once the clumps are defined, we sum the spectra in their component pixels and fit a Gaussian emission line (a single line for Hα or a triplet for Hβ and [OIII]) to obtain their intensity and velocity dispersion. For those galaxies observed in Hβ, we estimate the equivalent Hα intensity by assuming case B recombination and dust extinction based on the attenuation A_V estimated from the SED fitting. No additional extinction is assumed in the nebular lines. Thus, the estimated Hα luminosity, $L_{\mathrm{H}\alpha}$ is given by

$$L_{\mathrm{H}\alpha} = 2.86 \times 10^{\frac{A_V}{7.96}} L_{\mathrm{H}\beta}. \tag{5.4.3}$$

From $L_{\mathrm{H}\alpha}$, we calculate the SFR using the prescription of Kennicutt (1998a) adapted to a Chabrier (2003) initial mass function (IMF) and extinction $A_{\mathrm{H}\alpha} = 0.82\,A_V$.

The effective radius, r, of the clump is estimated by summing the area of all pixels contained in the clump, A. We then subtract the area of the effective source plane PSF in quadrature and define an effective radius

$$r = \sqrt{\frac{A}{\pi}}. \tag{5.4.4}$$

We identify 50 clumps in our sample, with between 1 and 9 clumps per galaxy, and list the derived properties in Table 5.8.

Jones et al. (2010) found that the clumps in high-redshift lensed galaxies had surface brightnesses that are higher than those of local HII regions by up to 100×. Such intense star-forming regions are found locally in merging systems such as the Antennae (Bastian et al., 2006), but appeared to be ubiquitous in isolated discs at high-z. Similar results were found at $z \sim 5$ (Swinbank et al., 2009) and in kpc-scale clumps from unlensed sources (Swinbank et al., 2012; Wisnioski et al., 2012a). To investigate the origin of these high-surface brightness clumps, Livermore et al. (2012a) observed 57 clumps in 8 galaxies with Hα narrowband imaging, and demonstrated that their surface brightnesses evolve with redshift. In Figure 5.8, we expand on this relation adding our new clumps. We note that one galaxy - MACSJ1149 - is included in both the current IFU sample and the narrowband imaging sample. Only one clump (the galaxy bulge) was observed in the narrowband sample, and we confirm that its luminosity is consistent with the previous observation within the measurement errors.

With the new data, the evolution in clump surface brightnesses is confirmed and extended out to $z > 3$. We show the mean surface brightness, $\Sigma_{\rm clump}$, in four redshift bins in Figure 5.8. The best fit to the redshift evolution of the clump surface brightness is

$$\log\left(\frac{\Sigma_{\mathrm{clump}}}{\mathrm{M}_{\odot}\,\mathrm{yr}^{-1}\,\mathrm{kpc}^{-2}}\right) = (3.5 \pm 0.5)\log(1+z) - (1.7 \pm 0.2)\,. \tag{5.4.5}$$

Clearly there is a selection effect involved, as we would not observe low-surface-brightness clumps in the high-z galaxies. However, there appears to be evolution in the properties of the brightest clumps, as these are not seen in isolated local galaxies but seem to be ubiquitous at high redshift. We will discuss this further in the context of the clump luminosity function along with implications of this evolution in §5.5.1.

The IFU data of our current sample allows us to add the extra dimension of velocity dispersion, σ, to this analysis. If the clumps are gravitationally bound, they should follow a relation of the form $L \propto \sigma^4$ (Terlevich & Melnick, 1981). However, not all studies of local star-forming regions have found this relation; Arsenault et al. (1990) found that it applied only to the brightest, 'first-ranked' regions in galaxies, with no $L-\sigma$ or $r-\sigma$ relation applying to their entire sample. Others have found a shallower $L-\sigma$ relation indicative of density-bounded regions, where only a fraction of the ionising photons are able to escape (Rozas et al., 2006, 2001). It is not clear that clumps should be expected to be virialised; indeed, Giant Molecular Clouds (GMCs) locally are not necessarily gravitationally bound (Dobbs et al., 2011).

In Figure 5.9, we plot σ as a function of both the clump size and luminosity. As a guide, we overlay the relations found by Swinbank et al. (2012):

$$\log\left(\frac{r}{\mathrm{kpc}}\right) = (1.01 \pm 0.08)\log\left(\frac{\sigma}{\mathrm{km\,s}^{-1}}\right) + (0.8 \pm 0.1) \tag{5.4.6}$$

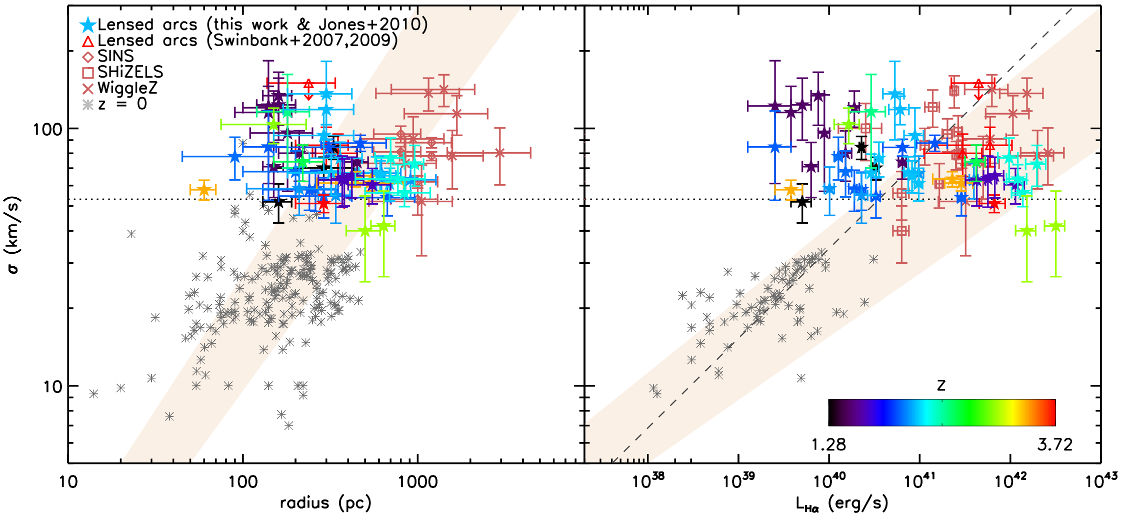

Figure 5.9. Velocity dispersion, σ, of star-forming clumps, as a function of clump size (*left*) and Hα luminosity (*right*). Clumps from the local Universe are taken from Terlevich & Melnick (1981), Arsenault et al. (1990), Bordalo & Telles (2011), Fuentes-Masip et al. (2000) and Rozas et al. (2006). The high-redshift comparison samples are from the $z \sim 5$ lensed arcs of Swinbank et al. (2007) and Swinbank et al. (2009) (with $L_{\mathrm{H}\alpha}$ estimated from the [OII]-derived SFRs), and the unlensed SINS (Genzel et al., 2011), WiggleZ (Wisnioski et al., 2012b) and SHiZELS (Swinbank et al., 2012) surveys. The shaded region shows the best fits from Swinbank et al. (2012), the dashed line is the best-fit $L_{\mathrm{H}\alpha} - \sigma$ relation from Rozas et al. (2006), and the dotted line indicates the estimated resolution limit (determined as described in the text). The addition of lensed galaxies extends the high-z samples to smaller sizes and lower luminosities while σ is similar to the unlensed samples. Although partially an effect of the spectral resolution limit, we find an excess of clumps with high resolved σ for their sizes and luminosities. This suggests that they are not necessarily virialised, and that the observed σ may contain contributions from a variety of processes such as star formation feedback.

$$\log\left(\frac{L}{\mathrm{erg\,s^{-1}}}\right) = (3.81 \pm 0.29)\log\left(\frac{\sigma}{\mathrm{km\,s^{-1}}}\right) + (34.7 \pm 0.4)\,. \tag{5.4.7}$$

Although our data scatter around these relations, we do not find any correlation between σ in our clumps and either r or L.

We first consider whether this is an effect of spectral resolution. We deconvolve σ for the instrumental resolution as measured from sky emission lines, but there is some lower limit at which we will not be able to measure the broadening of the line. To test where this limit is, we construct a set of 1000 Gaussian emission lines with varying widths of $< 100\,\mathrm{km\,s^{-1}}$ and add noise so that the final signal-to-noise, S/N$=5$ (this gives us a conservative estimate, as S/N>5 is the constraint we set to detect an emission line). We then convolve the resulting spectrum with the instrumental resolution, and apply the same emission line fitting routine used on the data to recover the line properties. We find that we consistently recover the input line width to within 20% at $\sigma > 53\,\mathrm{km\,s^{-1}}$. We show this line on Figure 5.9.

The clumps that lie close to this line may be affected by the resolution limit; however, there remains an excess of clumps at high-σ that are well-resolved and lie above the expected relations. It therefore appears that the clumps are not necessarily virialised, and the observed σ may contain contributions from a range of processes including gravitational instabilities and star formation feedback. We discuss the origin of the velocity dispersion in greater detail in §5.5.2. A further possible contribution to the high σ values could come from the superposition of multiple clumps along the line of sight. This is an additional source of uncertainty in all values derived from clumps, and motivates studies with higher spectral resolution so that any such multiple clumps can be separated.

5.5 Discussion

5.5.1 Clump formation

Livermore et al. (2012a) demonstrated that an effective means of quantifying the 'clumpiness' of a galaxy is the clump luminosity function. The luminosity function can be described by a Schechter function with a break at some characteristic luminosity L_0, which describes the brightest clumps. The presence of more bright clumps in a galaxy causes it to appear as 'clumpy.' Livermore et al. (2012a) showed that L_0 increases with redshift, giving rise to the appearance of more clumpy galaxies at high-redshift.

We show the luminosity functions in Figure 5.10 with the new data added. We account for the varying surface brightness limits of the observations by normalising each bin by the number of galaxies in which we should be able to identify clumps of that luminosity, and the error bars represent the Poisson error from counting clumps. The $z < 1.5$ bin combines the two $z < 1.5$ galaxies from the current sample with the seven galaxies from the Livermore et al. (2012a) narrowband imaging sample (MACSJ1149 is removed from the latter as it is duplicated in the current sample), and the $z > 3$ bin includes the two lensed $z \sim 5$ galaxies of Swinbank et al. (2007) and Swinbank et al. (2009).

To each redshift bin, we fit a Schechter function of the form

$$N\left(>L\right) = N_0 \left(\frac{L}{L_0}\right)^{\alpha} \exp\left(\frac{-L}{L_0}\right), \tag{5.5.8}$$

where the power-law slope is fixed to $\alpha = -0.75$ from Hopkins et al. (2012). We

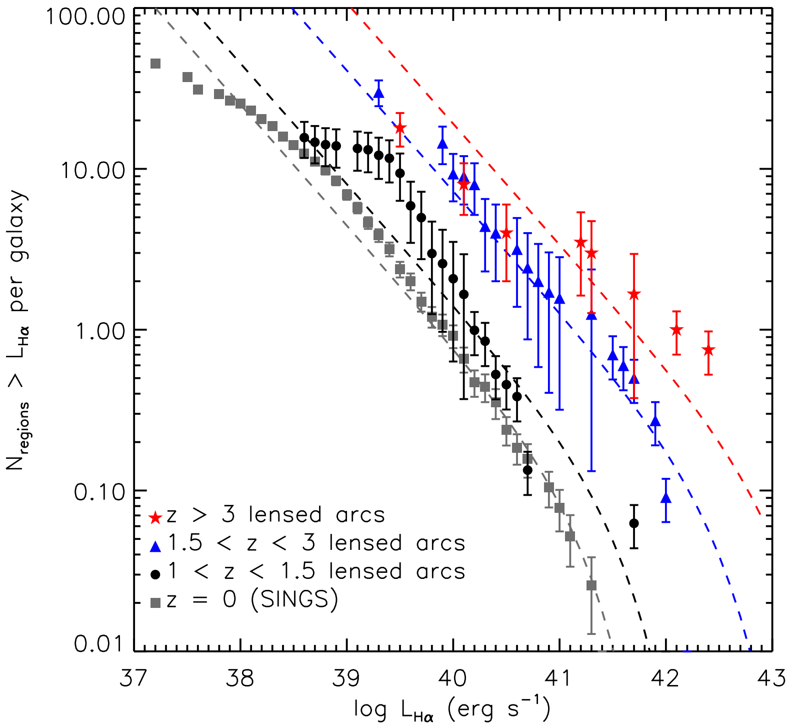

Figure 5.10. Cumulative clump luminosity functions. The $z = 0$ data are from the SINGS survey (Kennicutt et al., 2003), with clumps extracted by Livermore et al. (2012a). The $z < 1.5$ bin includes the narrowband imaging sample of Livermore et al. (2012a) combined with the two $z < 1.5$ galaxies from this work. Each luminosity bin is normalised by the number of galaxies contributing to that bin, accounting for variations in the depth of observations as described in the text. The dashed lines are Schechter function fits, where the $z = 0$ fit is from the simulations of Hopkins et al. (2012), and we keep the same normalisation but allow the characteristic luminosity to vary to fit the high-redshift data. We find that this characteristic luminosity evolves with redshift.

do not attempt to fit the faint-end slope as the sharp turnovers evident in Figure 5.10 are likely due to incompleteness and small number statistics in the faintest clumps. The normalisation N_0 is arbitrary, so we fit N_0 to the $z = 0$ data. We then keep N_0 and α fixed while allowing the characteristic luminosity L_0 to vary, and we find the best-fit L_0 for each bin with a χ^2 minimisation procedure. The best fits are

$$\frac{L_0}{\mathrm{erg\,s^{-1}}} = \begin{cases} 2.5^{+1.8}_{-1.2} \times 10^{41}, & z = 0 \\ 4.0^{+0.7}_{-0.7} \times 10^{41}, & 1 < z < 1.5 \\ 4^{+3}_{-3} \times 10^{42}, & 1.5 < z < 3 \\ 1.3^{+0.9}_{-0.8} \times 10^{43}, & z > 3 \end{cases}$$

where the errors are estimated using a bootstrap method.

We therefore find that the break of the clump luminosity function evolves with redshift, such that high-redshift galaxies have more high-luminosity clumps. The best fit to the redshift evolution of L_0 is

$$\log\left(\frac{L_0}{\mathrm{erg\,s^{-1}}}\right) = (2.0 \pm 0.7)\log(1+z) + (41.0 \pm 0.2)\,. \tag{5.5.9}$$

In combination with the evolution in clump surface brightness discussed in the previous section, it follows that high-redshift galaxies tend to have a higher number of bright, high surface-brightness star-forming clumps, which come to dominate the galaxy morphology and therefore give rise to the population of ‘clumpy’ galaxies seen at high redshift.

Livermore et al. (2012a) suggest that the cause of these bright clumps is a combination of high gas fractions at high redshift and the evolving galaxy dynamics.

Briefly, the argument is based on the assumption that clumps form in marginally stable discs described by a Toomre (1964) parameter Q where

$$Q = \frac{\kappa \sigma_t(R)}{\pi G \Sigma_0} \approx 1, \tag{5.5.10}$$

for epicyclic frequency $\kappa \approx \sqrt{2} v/r$ and velocity v at galactocentric radius r. Hopkins et al. (2012) argued that star-forming galaxies tend to self-regulate to maintain $Q \sim 1$; instabilities cause the gas to collapse to form stars, while feedback from the star formation stabilises the disc.

The mass required for collapse on a scale R is the Jeans' mass, M_J, given by

$$M_J = \frac{3R}{2G} \sigma. \tag{5.5.11}$$

If M_J is related to the characteristic mass of clumps in a galaxy, M_0 (i.e. the break of the mass function), then Livermore et al. (2012a) showed that combining Equations (5.5.10) and (5.5.11) with an assumed turbulent power spectrum gives

$$M_0 = \frac{3\pi^3 G^2}{2} \frac{\Sigma_0^3}{\kappa^4}. \tag{5.5.12}$$

Thus, M_0 depends on the disc surface density and epicyclic frequency. To relate this predicted mass to the observable $L_{\mathrm{H}\alpha}$, we use an empirical relation between the Hα-derived SFR and mass of local molecular clouds, $\mathrm{SFR}(M_\odot \mathrm{yr}^{-1}) = 4.6 \pm 2.6 \times 10^{-8} M_\odot$ (Lada et al., 2010). This relation is valid for high-density gas, and thus appropriate for star-forming clumps, and is consistent with the independently-derived SFRs and gas masses of star-forming clumps reported in a lensed $z = 2.3$ galaxy by Swinbank et al. (2011). Adopting this conversion results in characteristic masses, M_0, from our clump luminosity functions of

$$\frac{M_0}{M_\odot} = \begin{cases} 4^{+3}_{-2} \times 10^7, & z = 0 \\ 1.0^{+0.2}_{-0.2} \times 10^8, & 1 < z < 1.5 \\ 9^{+7}_{-7} \times 10^8, & 1.5 < z < 3 \\ 3^{+2}_{-2} \times 10^9, & z > 3. \end{cases}$$

We can also relate the SFR surface density, Σ_{SFR}, of clumps to the disc surface density, Σ_0, using the Kennicutt-Schmidt law. The relationship between the surface density of gas, $\Sigma_{\rm gas}$, and $\Sigma_{\rm SFR}$ found by (Kennicutt, 1998b) is

$$\frac{\Sigma_{\rm SFR}}{M_\odot\,{\rm yr}^{-1}{\rm kpc}^{-2}} = A\left(\frac{\Sigma_{\rm g}}{M_\odot{\rm pc}^{-2}}\right)^n, \tag{5.5.13}$$

where $A = (2.5 \pm 0.7) \times 10^{-4}$ and $n = 1.4 \pm 0.15$. The disc surface density Σ_0 is a combination of gas and stars ($\Sigma_{\rm g}$ and Σ_* respectively), which contribute differently to the disc stability. Following Rafikov (2001), we use

$$\Sigma_0 = \Sigma_{\rm g} + \left(\frac{2}{1+f_\sigma^2}\right)\Sigma_*, \tag{5.5.14}$$

where $f_\sigma = \sigma_*/\sigma_{\rm g} \approx 2$ is the ratio of the velocity dispersion of the stars to that of the gas (Korchagin et al., 2003). We define the gas fraction, $f_{\rm gas}$, such that

$$f_{\rm gas} = \frac{M_{\rm gas}}{M_{\rm gas} + M_*} \approx \frac{\Sigma_{\rm g}}{\Sigma_{\rm g} + \Sigma_*}, \tag{5.5.15}$$

if we measure the gas and stars over the same area. Combining Equations 5.5.13, 5.5.14 and 5.5.15, we have

$$\Sigma_{\rm SFR} = A\left(\Sigma_0\left(\frac{f_{\rm gas}\,(1+f_\sigma)}{f_{\rm gas}\,(1+f_\sigma)+2\,(1-f_{\rm gas})}\right)\right)^n . \tag{5.5.16}$$

Thus, from Equations 5.5.12 and 5.5.16, we find that the characteristic mass, M_0, and the clump SFR surface density, $\Sigma_{\rm SFR}$, depend on Σ_0, κ and $f_{\rm gas}$. In order to understand how M_0 and $\Sigma_{\rm SFR}$ evolve with redshift, we therefore need to understand the evolution of Σ_0, κ and $f_{\rm gas}$.

We can estimate Σ_0 and $f_{\rm gas}$ from our data using the $\Sigma_{\rm SFR}$ derived from Hα or Hβ and applying the Kennicutt-Schmidt law from Equation 5.5.13 to derive $\Sigma_{\rm gas}$. To estimate Σ_*, we use the total M_* from the SED fitting and apportion the stellar mass according to the fractional flux in each pixel of the reddest available *HST* image. We then combine the $\Sigma_{\rm gas}$ and Σ_* maps to create a map of Σ_0.

In the upper two panels of Figure 5.11, we compare our data to predictions for the evolution of $f_{\rm gas}$ and Σ_0. The predicted $f_{\rm gas}$ evolution indicated by the shaded region is the empirical relation $f_{\rm gas} \propto (1+z)^{(2.0\pm0.5)}$ from Geach et al. (2011), and we also show a prediction from semi-analytic models (Lagos et al., 2012, Lacey et al. in prep). We also show some recent data from other high-z samples, including more active (U)LIRGs and lensed galaxies whose gas content has been observed directly. There are many uncertainties in our estimate of $f_{\rm gas}$, specifically, the assumption of a constant Kennicutt-Schmidt law and in the reliability of the SED-derived stellar masses; nonetheless, we note that our estimate for MACSJ2135 (the 'Cosmic Eye') of $M_{\rm gas} \sim 10^9\,{\rm M}_\odot$ is very close to the CO-derived value of $M_{\rm gas} = (9.0 \pm 1.6) \times 10^8\,{\rm M}_\odot$ (Riechers et al., 2010).

The evolution of Σ_0 with redshift depends both on the evolution of $f_{\rm gas}$ and on

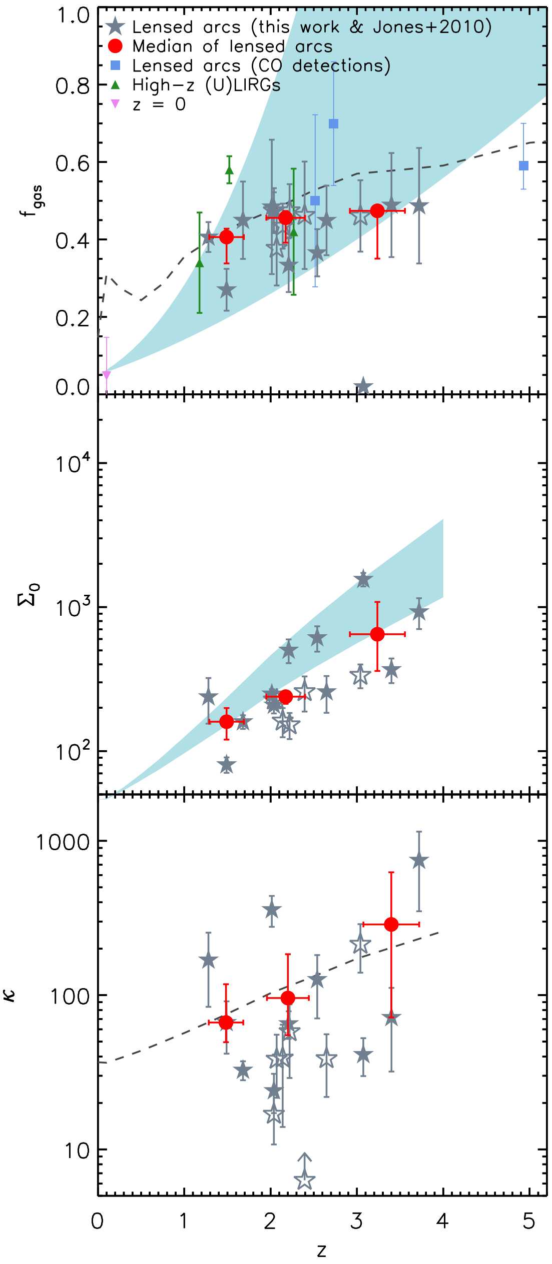

Figure 5.11. Evolution of the gas fraction, $f_{\rm gas}$, disc surface density Σ_0 and epicyclic frequency, κ, with z. In each panel, individual galaxies are represented by grey stars, with filled stars representing galaxies identified as rotating discs, and unfilled stars the mergers and dispersion-dominated systems. Medians in three redshift bins are indicated by red circles with error bars denoting the interquartile ranges. In the $\kappa - z$ plot, we include only disc-like systems in the median. *Upper:* The shaded region shows evolution of $f_{\rm gas} \propto (1+z)^{(2\pm0.5)}$ (Geach et al., 2011). For comparison, we also show samples at $z = 0$ (Leroy et al., 2008), medians of high-z (U)LIRGs (Daddi et al., 2010b; Tacconi et al., 2010), and lensed galaxies with CO detections (Kneib et al., 2005; Livermore et al., 2012b; Riechers et al., 2010). The dashed line is from semi-analytic models (Lacey et al in prep). *Centre:* The shaded region represents the predicted mass evolution from the models of Dutton et al. (2011) combined with the empirical $f_{\rm gas}$ evolution. *Lower:* The dashed line indicates the prediction from Dutton et al. (2011). In all cases, there is a lot of scatter in the data, but the general trends are consistent with predictions.

the change in total mass of a galaxy with redshift. The shaded region in Figure 5.11 incorporates both the empirical $f_{\rm gas}$ evolution of Geach et al. (2011) and mass evolution from the simulations of Dutton et al. (2011). There is a lot of scatter in the data, but the general trend indicated by the medians in three redshift bins, marked in red in Figure 5.11, are consistent with predictions.

We estimate κ by taking the velocity at the half-light radius $r_{1/2}$ along the dynamical axis from the disc fitting, where there is no inclination correction for the radius. This measurement is highly uncertain as the measurement of $r_{1/2}$ is affected by the clumpy morphologies and the irregular source plane PSF, and the measurement of the velocity includes uncertainty in the inclination. Nonetheless, we again find that although there is a lot of scatter in the data, the general trend is consistent with the predictions of Dutton et al. (2011).

Using these models for the evolution of $f_{\rm gas}$, Σ_0 and κ, we should be able to predict how the star formation surface density of clumps, $\Sigma_{\rm clump}$ and the characteristic mass, M_0, evolve. In Figure 5.12 we present an updated version of the figure in Livermore et al. (2012a, Figure 9) including the IFU data. We find that the evolution in the break of the clump mass function and in the surface brightness of clumps is consistent with the model predictions given by Equations 5.5.12 and 5.5.16 given evolution in the galaxy mass, gas fraction and dynamics. This indicates that galaxies at high redshift appear clumpy because their gas-rich discs fragment on larger scales, leading to star-forming clumps that dominate the morphology of the galaxy. Thus, despite the different appearance of high-redshift clumpy galaxies to local spirals, we find that they do not require a different 'mode' of star formation;

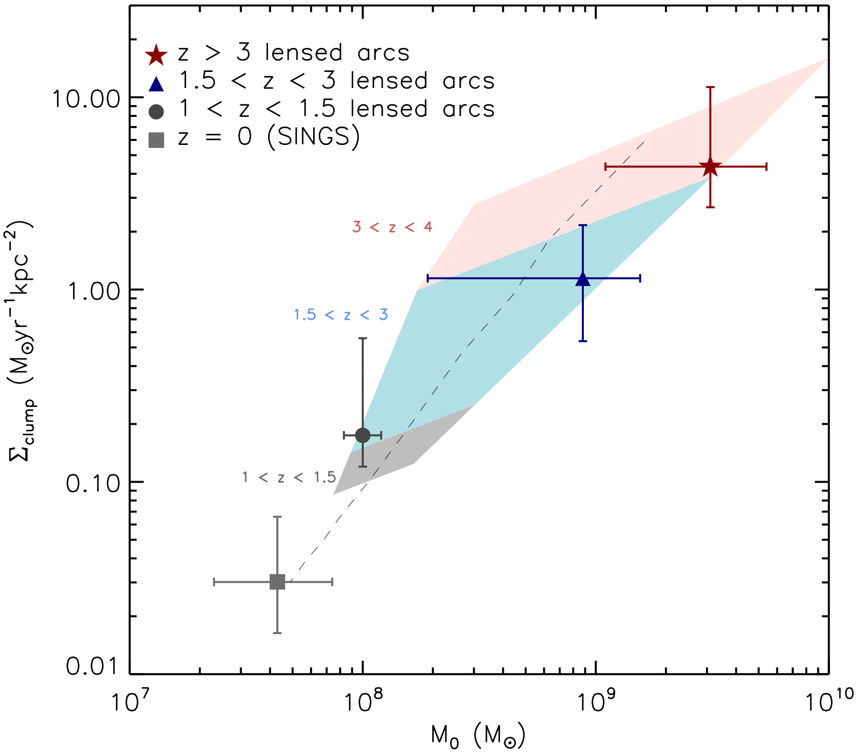

Figure 5.12. Evolution of clump surface brightness $\Sigma_{\rm SFR}$ and the characteristic mass M_0 derived from the clumps luminosity functions. The dashed line shows a predicted track based on Equations 5.5.12 and 5.5.16 assuming evolution in mass and epicyclic frequency from the simulations of Dutton et al. (2011) and gas fraction evolution of $f_{\rm gas} \propto (1+z)^2$ (Geach et al., 2011), with $f_\sigma = 2$. The shaded regions indicate the predicted locations of clumps in each redshift bin, for a range of gas fractions $f_{\rm gas} \propto (1+z)^{(2.0\pm0.5)}$. The data are consistent with the model, demonstrating that the 'clumpy' morphologies of high-z galaxies are driven by evolution in their gas fractions and dynamics.

.

the clumps can arise naturally as a consequence of the larger gas reservoirs.

5.5.2 The origin of the velocity dispersion

Galaxies at high redshift are observed to have high velocity dispersions (e.g. Epinat et al., 2009; Förster Schreiber et al., 2009, 2006; Law et al., 2009, 2007; Wright et al., 2009), and in §5.4.2 we found an excess of clumps with higher σ than would be expected for virialised systems.

There is some disagreement in the literature about the processes that drive the high velocity dispersions. Simulations of high-redshift galaxies have suggested that they are driven by inflows of cold gas, which in turn fuels the star formation (Dekel et al., 2009; Genel et al., 2012).

Another explanation for high velocity dispersions is turbulence driven by the energy from young stars. Green et al. (2010) noted a correlation between SFR and σ in galaxies with $L_{\mathrm{H}\alpha} > 10^{42} \mathrm{erg\,s^{-1}}$ and attributed this to star formation feedback (see also Hopkins et al., 2011; Lehnert et al., 2013, 2009; Wisnioski et al., 2012b). Direct observational evidence for this scenario comes from broad components in Hα emission seen in high signal-to-noise spectra of $z \sim 2$ star-forming galaxies (Genzel et al., 2011; Newman et al., 2012a,b). In Figure 5.13 we compare the mean flux-weighted velocity dispersion σ to the total Hα luminosity in our sample (where the latter is calculated from the Hβ flux where necessary, assuming case B recombination and a Balmer decrement calculated from the dust extinction values in Table 5.7). This is the equivalent of the right-hand panel of Figure 5.9 for the galaxies as a whole rather than the individual star-forming clumps. We do not see any correlation

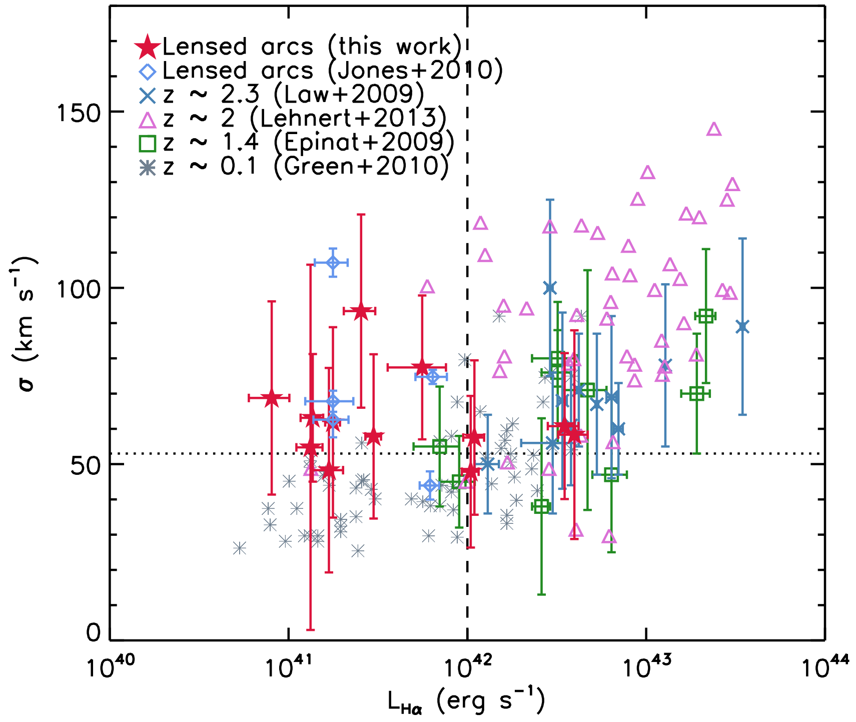

Figure 5.13. The flux-weighted mean local velocity dispersions, σ, against galaxy Hα luminosity, $L_{\mathrm{H}\alpha}$, in our sample and in comparison samples at $z \sim 0.1$ (Green et al., 2010), $z \sim 1.4$ (Epinat et al., 2009), $z \sim 2$ (Lehnert et al., 2013) and $z \sim 2.3$ (Law et al., 2009). The velocity dispersions are deconvolved for instrumental resolution, and the dotted line indicates the limit above which our tests indicate we can reliably measure the line broadening. Our sample is in agreement with the correlation noted by (Green et al., 2010) at $L_{\mathrm{H}\alpha} > 10^{42}\mathrm{erg\,s^{-1}}$, although the majority of our sample has $L_{\mathrm{H}\alpha}$ below this limit.

between $L_{\mathrm{H}\alpha}$ and σ in our data, although they are entirely consistent with the trend observed by Green et al. (2010). Since lensing allows us to probe more representative galaxies at high-z, only seven of the galaxies in our sample have $L_{\mathrm{H}\alpha} > 10^{42}\mathrm{erg\,s^{-1}}$. It is possible that the lack of correlation in all of the samples below this limit is due to the resolution limit in σ. We do not find such high values for σ as Lehnert et al. (2013), which could be an effect of the spatial resolution over which σ is measured.

A further possible driver of turbulence in high-redshift galaxies is gravitational instability. In an unstable ($Q < 1$) disc with insufficient turbulence to oppose self-gravity, instabilities will kinematically heat the gas and drive an increase in turbulence. The velocity dispersion will increase until the disc becomes stable ($Q > 1$), at which point the energy dissipates and velocity dispersion decreases until the disc is once more unstable. Thus, discs effectively self-regulate to maintain marginal stability such that $Q \sim 1$ (Burkert et al., 2010; Krumholz & Dekel, 2010).

In reality, there is no reason to consider the above arguments mutually exclusive. High velocity dispersions are required as support against self-gravity in order to form the large clumps that we observe; this follows from Equation (5.5.12) in combination with $\sigma = \kappa R$ and the Jeans' mass

$$M_J = \frac{3R}{2G}\sigma, \tag{5.5.17}$$

(see also Livermore et al., 2012a). We then have

$$\sigma \propto \left(\frac{\pi G \Sigma_0}{\kappa}\right)^3 . \tag{5.5.18}$$

As discussed in Section 5.5.1 with respect to M_J, the evolution of σ would be

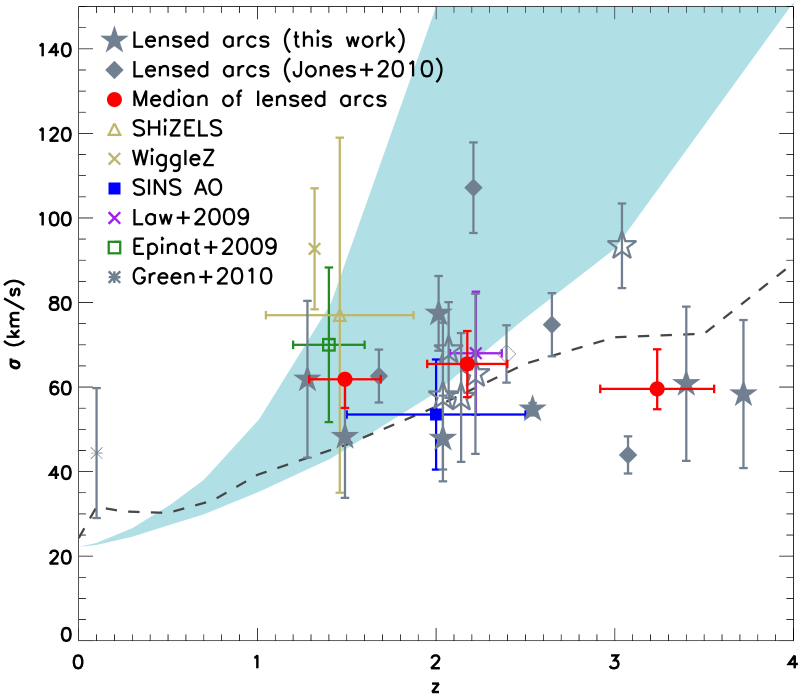

Figure 5.14. Evolution of the mean local velocity dispersion, σ, as a function of redshift, z. For the lensed arcs, filled symbols represent galaxies identified as rotating discs, and open symbols are mergers or dispersion-dominated systems. Medians in three redshift bins - $z < 2$,$2 < z < 3$ and $z > 3$ - are indicated by red circles with error bars denoting the interquartile ranges. The shaded region shows the predicted evolution according to Equation (5.5.18) assuming $f_{\text{gas}} \propto (1+z)^{(2.0\pm0.5)}$ (Geach et al., 2011) and gas mass, size and rotational velocity evolution from Dutton et al. (2011). The dashed line is the prediction using the gas fraction evolution from semi-analytic models (Lacey et al. in prep). We also plot the medians of a range of comparison samples (Epinat et al., 2009; Green et al., 2010; Law et al., 2009; Newman et al., 2013; Swinbank et al., 2012; Wisnioski et al., 2011). Both predictions are a reasonable fit to the data in the lower redshift bins, but the semi-analytic models predict a turnover at higher redshift that is a better match for our $z > 3$ galaxies. However, we note that the sample size is small, and furthermore that gravitationally lensed galaxies represent the fainter end of the population, and so we do not observe the high gas fractions that might be seen in the population as a whole at this epoch. Nonetheless, the data are approximately consistent with a model in which high velocity dispersions at high redshift are driven by gravitational instabilities, though as discussed in the text, this is unlikely to be the only contributing factor.

expected to increase with redshift as a result of higher gas fractions at high-z, as this evolution is stronger than that in κ. We plot the mean clump velocity dispersion for each galaxy as a function of redshift in Figure 5.14, in comparison with the prediction from Equation (5.5.18) based on redshift-evolution of galaxy size, mass and rotation from Dutton et al. (2011) and gas fraction from both Geach et al. (2011) and semi-analytic models (Lacey et al. in prep). We note that at high-z the σ values predicted using the empirical relation become arbitrarily large; this is because $f_{\rm gas}$ is permitted to increase without bound, whereas in practice there must be a turnover at high-z. Considering the large number of assumptions and the small sample size, the predictions are a reasonable fit to the data. However, there is an excess of galaxies with higher σ than expected, which indicates an additional contribution to the turbulent velocities. A robustly-selected sample would be required to test for the true redshift evolution of the population as a whole.

In order to gain some insight into the cause of the high velocity dispersions, we can make use of the improved spatial resolution afforded by gravitational lensing to investigate the origin of the high σ values within galaxies. If the high velocity dispersions are due to turbulence caused by star formation, we might observe the highest σ values in regions of galaxies with the highest star formation rates, i.e. within clumps. In Figure 5.15 we compare the disc surface density Σ_0 to the local velocity dispersion σ for each pixel in each galaxy, with the pixels colour-coded by star formation rate surface density $\Sigma_{\rm SFR}$. The Σ_0 maps are constructed by combining stellar mass and gas - derived from the star formation maps by assuming the Kennicutt-Schmidt law - using Equation 5.5.14 with the method described in

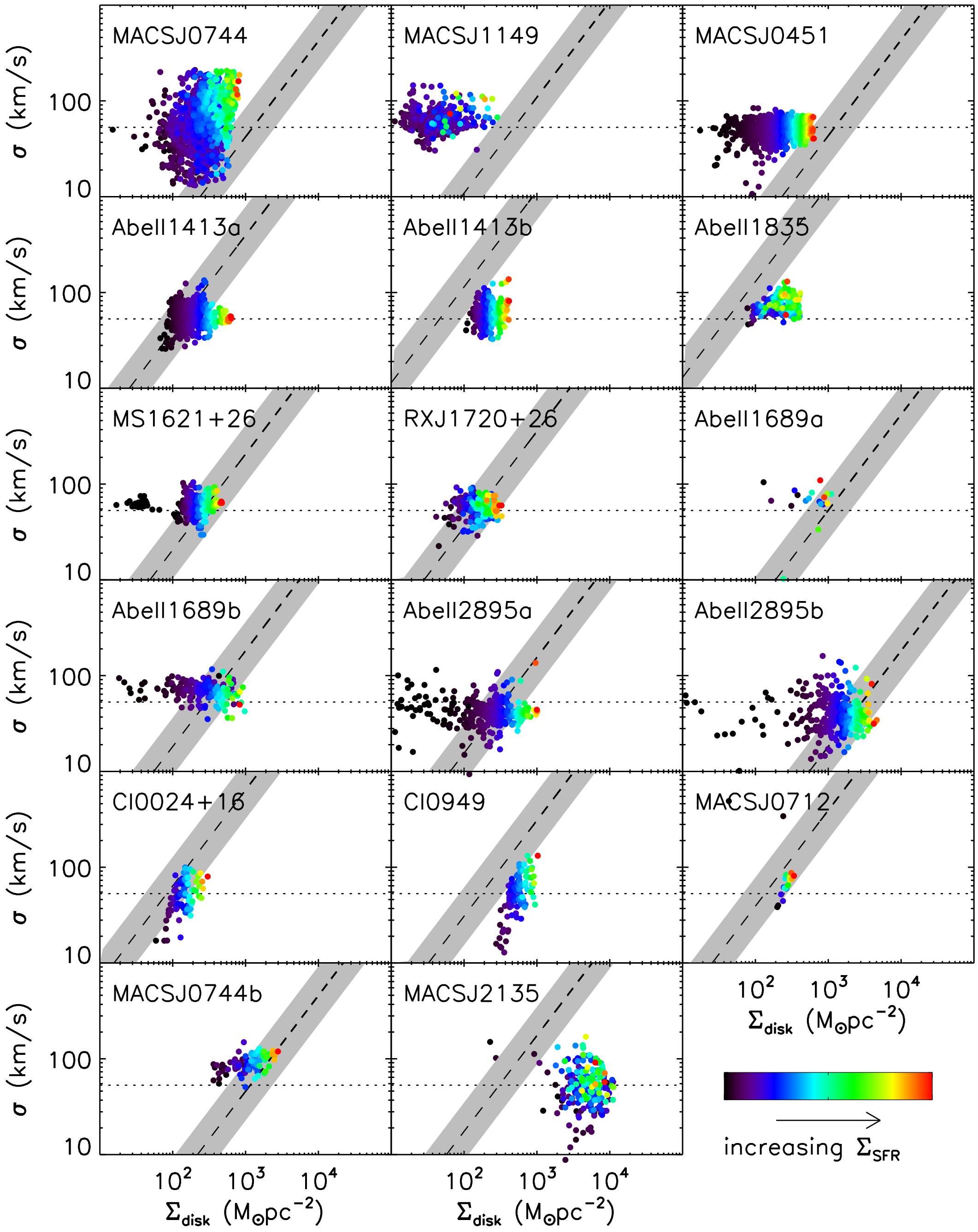

Figure 5.15. Comparison between disc surface density Σ_0 and local velocity dispersion σ in each pixel. As neither surface brightness nor line width are affected by gravitational lensing, we plot pixels from the image plane. Pixels are colour-coded by SFR surface density $\Sigma_{\rm SFR}$, on different scales in each panel so that the full range is visible. By deconvolving the line widths for instrumental resolution, we observe arbitrarily low values of σ, but the dotted lines indicate the lower limit above which we are confident we reliably detect the actual line width. The peak in $\Sigma_{\rm SFR}$ is generally seen below the peak in σ for each galaxy, suggesting that the velocity dispersion is not dominated by turbulence due to feedback from local star formation. The dashed line shows a Toomre parameter $Q = 1$, with the shaded region indicating the range $0.5 < Q < 2$. Regions below this line have lower Q and should therefore be more unstable to fragmentation. Most galaxies have $Q \sim 1$ with regions of high $\Sigma_{\rm SFR}$ generally having lower Q.

Section 5.5.1. As gravitational lensing does not affect surface brightness or line width, we use the image plane where the pixels are independent and the alignment of *HST* and IFU imaging is more straightforward. In most cases Σ_0 is dominated by the gas component and, as this is derived from $\Sigma_{\rm SFR}$, this introduces a correlation between Σ_0 and $\Sigma_{\rm SFR}$ that is likely to be stronger than in reality. As can be seen from Figure 5.15, the peak in $\Sigma_{\rm SFR}$ does not generally coincide with the peak in σ. Thus, if the local velocity dispersion is dominated by turbulence from star formation, it does not seem to be localised to the regions in which stars are forming most rapidly.

The conclusion that regions of intense star formation have low σ for their SFRs was also reached by Swinbank et al. (2012) and Genzel et al. (2011). The latter interpreted this as a low Toomre parameter Q, where they defined a $Q_{\rm gas}$ based only on the gas surface density $\Sigma_{\rm gas}$. As their $\Sigma_{\rm gas}$ is derived from $\Sigma_{\rm SFR}$ by assuming the Kennicutt-Schmidt law, a low Q is equivalent to a low $\sigma/\Sigma_{\rm SFR}$.

We also show in Figure 5.15 a line for a Toomre parameter $Q = 1$, where Q is defined as in Equation 5.5.10 using the local disc surface density and σ and κ for the disc as a whole. The absolute values of Q are highly uncertain due to the number of assumptions involved in estimating Σ_0. We also test the effect of adopting the method of Romeo & Wiegert (2011) for calculating Q from a combination of gas and stars, which weights the more stable component more highly. Using their method results in systematically higher Q by a factor $\sim 1.5\times$.

As a guide, we shade the region between $Q = 0.5$ and $Q = 2$ according to Equation 5.5.10. We find that most of the galaxies lie on or close to the $Q = 1$ line, supporting the idea of self-regulation. While there is uncertainty in the absolute value, variations in Q across the disc are more robust. Tracks of constant Q run parallel to the $Q = 1$ line shown, with lower Q values lying below this line. We can therefore see that regions with high $\Sigma_{\rm SFR}$ tend to have low Q; i.e. they are more unstable to collapse, and hence forming stars more rapidly. With the current data, $\Sigma_{\rm SFR}$ must be used to derive Q, and so a thorough investigation of this relationship would require an independent measure of Σ_0 from CO observations.

Although we find that most galaxies have $Q \sim 1$ on average, it does not not imply that self-regulation due to disc instabilities *drives* the velocity dispersion. On the contrary, as the high-σ is required to stabilise massive discs, it could arise as a result of accretion of cold gas as predicted in simulations. Yet, what happens when stars begin to form? Turbulence opposes self-gravity and hence inhibits star formation (although, as discussed by Ostriker & Shetty (2011), there is also a competing effect whereby turbulence can cause local overdensities that trigger star formation). As a cloud collapses, σ would increase if energy is conserved, contrary to our observations. The energy must therefore be lost through radiation and dissipation, which equalises the velocity dispersion between the clump and the disc. This also matches the model of Ceverino et al. (2012), who predict that there will be no enhanced velocity dispersion in star-forming clumps. Other simulations predict a time delay between the burst of star formation and the increase in σ (Hopkins et al., 2012), which might also explain why we do not see spatial correlation between velocity dispersion and ongoing star formation.

It is the nature of dynamical studies of high-redshift galaxies that we only select galaxies with active star formation. Even with gravitational lensing, where lower star formation rates are accessible, an observed emission line flux of $\gtrsim 10^{-16}\mathrm{erg\,s^{-1}\,cm^{-2}}$ is required for the galaxy to be targeted for integral field spectroscopy, equating to a minimum SFR $\sim 1\,\mathrm{M_\odot yr^{-1}}$ after accounting for lensing magnification. Thus, while it is possible that cold gas accretion drives the initial high turbulence, at the stage in which we observe the galaxies there is undoubtedly at least a contribution from gravitational instabilities that triggered star formation, and the feedback from the young stars themselves (see also Elmegreen & Burkert (2010) for a detailed discussion). While our data support the idea of self-regulation in star-forming galaxies such that $Q \sim 1$, it is not clear that the possible mechanisms for driving up σ to stabilise the disc can be differentiated in star-forming galaxies with current data.

5.6 Conclusions

We have presented integral field spectroscopy around the Hα/[NII] or Hβ/[OIII] emission lines of 12 gravitationally lensed galaxies at $1 < z < 4$, obtained with VLT/SINFONI, Keck/OSIRIS and Gemini/NIFS. We combine these data with 5 galaxies from Jones et al. (2010) and investigate the dynamics and star formation properties of 17 high-redshift galaxies. The galaxies all benefit from magnification due to gravitational lensing, increasing the flux by factors of $1.4-90\times$ and providing spatial resolution of $\sim 100\,\mathrm{pc}$.

Our combined sample have stellar masses $M_* \sim 4\times10^8 - 6\times10^{10}\mathrm{M_\odot}$ and dust extinctions of $A_V \sim 0.3 - 1.1$. The intrinsic star formation rates derived from the Hα (or Hβ) emission, after correcting for lensing and dust extinction, are SFR$\sim 0.8-40\mathrm{M_\odot yr^{-1}}$. The use of gravitational lensing therefore allows us to probe the representative star-forming population at this epoch, with lower M_* and SFRs than other high-z surveys.

We fit rotating disc models to the sample to derive inclinations and dynamical axes, from which we extract rotation curves and velocity dispersion profiles. All of the galaxies in the combined sample have velocity gradients, and 15 out of 17 are well-fit by an arctan function indicative of rotation. Of the sample, 65% have velocity profiles indicative of rotation, centrally-peaked velocity dispersion profiles and sufficiently high v/σ to be classed as possible rotating discs. Of the remainder, 29% have disturbed profiles that may be indicative of merging or interacting systems. There is one galaxy we class as 'dispersion-dominated,' though we note that we may not have observed the full velocity gradient in this galaxy. The merger fraction is in good agreement with other high-z kinematic surveys (e.g. Epinat et al., 2012; Förster Schreiber et al., 2009; Law et al., 2009; Wright et al., 2009), while, like Newman et al. (2013), we find that higher spatial resolution causes a higher fraction of the remainder to be classed as rotating discs.

As gravitational lensing allows us to probe intrinsically smaller galaxies, we extend relationships observed between galaxy size, velocity and v/σ in unlensed samples to smaller sizes. However, we observe a large degree of scatter in these relations. We obtain best-fit relations of $v_{\rm rot} \sim 23\, r_{1/2} + 60$ and $\log\left(v_{\rm rot}/\sigma\right) \sim 0.37 \log\left(r_{1/2}\right) + 0.09$, indicating that larger galaxies generally have a higher contribution to their kinematic support from ordered rotation compared to random motions.

We find that v/σ increases with M_* as $\log\left(M_*\right) \sim 1.2 \log\left(v_{\rm rot}/\sigma\right) + 9.7$. This extends this relation to lower M_* than previous high-z samples and indicating that galaxies become more dynamically settled as they increase in stellar mass.

We find that the sample is consistent with the local stellar mass Tully-Fisher relation with no coherent evidence for redshift evolution, in common with the work of Miller et al. (2012). Some of the highest-redshift galaxies are systematically offset, which may be a hint of evolution in the zero-point, but at a statistically insignificant level. We further demonstrate that the rotation in our sample, which comprises systematically smaller sizes than unlensed studies, could be dominated by baryons (see also Miller et al., 2011).

We extend the work of Jones et al. (2010) and Livermore et al. (2012a) by detecting 50 star-forming clumps in our sample and study their luminosities, sizes and velocity dispersions. In common with previous work, we find that the surface brightness evolves with redshift, but we extend this evolution to $z > 3$. The average star formation density in the brightest clumps evolves with redshift as $\log\left(\Sigma_{\rm clump}/{\rm M_\odot\,yr^{-1}\,kpc^{-2}}\right) = (3.5 \pm 0.5)\log(1+z) - (1.7 \pm 0.2)$. However, we find that the clumps have similar velocity dispersions to unlensed high-z samples while being smaller and less luminous; thus, they introduce a much larger degree of scatter into the $L-\sigma$ and $\sigma-r$ relations observed in other studies. This could be an indication that these clumps are not virialised, and that their velocity dispersions may have additional contributions from star formation feedback or gravitational instability.

We construct luminosity functions of the clumps, and find that they can be fit by a Schechter function in which the break evolves to higher luminosities at higher redshifts. We find that the characteristic luminosity evolves as $\log{(L_0/\mathrm{erg\,s^{-1}})} = (2.0 \pm 0.7)\log{(1+z)} + (41.0 \pm 0.2)$. We show that both this evolution and that of the clump surface brightnesses can be explained by evolution in the disc surface density, gas fraction and epicyclic frequency, as described by Livermore et al. (2012a). We use the IFU data to test predictions of the redshift evolution of these quantities from simulations, and find that they are consistent, albeit with a large degree of scatter. This supports the picture in which 'clumpy' galaxies arise at high-z because gas-rich, turbulent discs fragment on larger scales, resulting in star forming regions large enough to dominate the morphology of the galaxy. This clearly motivates more direct observations of molecular gas in high-redshift galaxies to test this idea.

We also find that our sample is consistent with a correlation between $L_{\mathrm{H}\alpha}$ and σ at $\log L_{\mathrm{H}\alpha} > 42$, which has been used to show that turbulence in high-z galaxies is driven by star formation feedback (Green et al., 2010; Lehnert et al., 2013, e.g.). We show that if σ is driven by self-regulation to maintain $Q \sim 1$ then it would be expected to increase with redshift due to the increasing gas fractions. Using the high spatial resolution of our data, we test the idea that the high σ is caused by star formation feedback, and find that regions with high SFR surface densities do not have high σ. By comparing the total disc surface density in these regions to the local σ, we find that galaxies on average tend to have a Toomre parameter $Q \sim 1$. Star-forming regions have systematically lower Q, indicating that they form as a result of gravitational instabilities. Thus, we conclude that the turbulence is likely caused by a combination of gravitational instability and star formation feedback, as they are related processes, but that any energy injected into the ISM directly by stars must be radiated or dissipated such that the turbulent velocity dispersion is not spatially correlated with ongoing star formation.

In studying the galaxy-wide kinematics, the star-forming clumps and the turbulence of high-z lensed galaxies, we have found throughout that these properties are all driven primarily by the galaxies' gas content, a factor that remains relatively unexplored due to the small number of observations of molecular gas in normal high-redshift star-forming galaxies. It is to be hoped that the redshift evolution of gas fractions (e.g. Geach et al., 2011; Livermore et al., 2012b) and the universality of the Kennicutt-Schmidt law can be tested as ALMA in full science operations opens up the more normal star-forming population.

Chapter 6

Summary

6.1 Key Results

In this thesis, we have presented a detailed study of the properties of high-redshift star-forming galaxies that are gravitationally lensed by foreground clusters. The lensing magnification provides a unique opportunity to study the 'normal' star-forming population that is inaccessible to unlensed surveys with current facilities, in a level of detail comparable to that achievable at $z \sim 0.1$.

In Chapter 3 we began by using narrowband filters on *HST/WFC3* to image the Hα emission in eight lensed galaxies at $z \sim 1 - 1.5$. The galaxy morphologies seen in Hα tend to be dominated by a few large, bright regions, termed star-forming 'clumps.' The high resolution of *HST* combined with the lensing magnification results in effective spatial resolution of order $\sim 100\,\mathrm{pc}$, allowing direct comparison to star formation in the local Universe, which occurs in HII regions on $\sim 100\,\mathrm{pc}$ scales.

The first key result of this work was that star-forming clumps follow similar SFR-size scaling relations at all redshifts (SFR $\underset{\sim}{\propto}$ r^2), with evolution in the normalisation towards higher surface brightnesses at higher redshifts.

The second key result of Chapter 3 is the evolution in the luminosity function of star-forming clumps, towards a higher cut-off luminosity (or mass) at higher redshift.

We link these two results with a simple theoretical model in which gas collapses in marginally stable disks, and the 'cut-off' in the clump luminosity function represents the largest clumps on the scale of the Jeans mass. In this picture, the main driver of clump size (and hence mass and luminosity) is the disk surface density, though there is also a competing effect from higher epicyclic frequencies in more compact high-z galaxies, which stabilise the disk and prevent collapse on the largest scales.

We have therefore shown that there is no requirement to invoke a second 'mode' of star formation to explain the intense SFRs seen in high-redshift galaxies. Rather, they can be explained with the same physical processes as star-forming regions in the local Universe, but occurring on larger scales due to the different conditions within high-redshift galaxies. The disk surface density is dominated by the gas component, and hence depends strongly on the galaxy's gas fraction. In the more gas-rich disks at high redshift, the clumps appear larger and more luminous, and therefore come to dominate the host galaxy's morphology, giving rise to its 'clumpy' appearance.

This result demonstrates the importance of understanding the evolution of molecular gas content in high-redshift galaxies. We therefore go on to address this in Chapter 4.

Observations of molecular gas at high redshift are challenging, and have therefore been limited to the most extreme, highly star-forming examples. With the use of gravitational lensing, we can access a more representative example. We therefore observed a $z \sim 5$ galaxy lensed by the cluster MS1358+62 with the IRAM Plateau de Bure Interferometer at the frequency of the CO(5–4) emission line.

Even with the lensing magnification, the line is faint; we obtain a $\sim 4\,\sigma$ detection with a line flux of $0.104 \pm 0.024\,\mathrm{Jy\,km\,s^{-1}}$. The inferred molecular gas mass is $M_{\mathrm{gas}} = 1^{+1}_{-0.6} \times 10^{9}\,\mathrm{M_{\odot}}$, implying a gas fraction $f_{\mathrm{gas}} = 0.59^{+0.11}_{-0.06}$. This is broadly consistent with predicted trends for the redshift evolution of gas fractions, though clearly a large sample will be required to test this further.

In addition to the gas fractions, the other driver of star formation properties in galaxies that we identified in Chapter 3 was the dynamics. If the epicyclic frequency is higher, the disk will be stabilised against collapse, reducing the scale of star-forming clumps. Higher turbulent velocity dispersions also provide support against collapse. These quantities could not be measured from the narrowband imaging data in Chapter 3, and were instead assumed from models. We therefore progressed in Chapter 5 to direct observations of the galaxy kinematics with Integral Field Spectroscopy (IFS).

The advantage of IFS is that it provides a spectrum for every spatial pixel. The mean wavelength of the emission line at a given position gives the line-of-sight velocity, the line width gives the velocity dispersion, and the integral measures the line flux. We therefore made maps of each quantity, and carried out a study of the star formation morphologies similar to that in Chapter 3 whilst simultaneously considering the galaxy kinematics. We were also able to estimate the stellar masses and the level of extinction due to dust by modelling the galaxy SEDs from continuum emission.

The new observations of 12 lensed galaxies presented in Chapter 5 represents a significant increase in the sample size over other studies of lensed galaxies with IFS. We combine these data with 5 galaxies at $z \sim 2$ from Stark et al. (2008) and Jones et al. (2010), to form a combined sample of 17 star-forming galaxies at $1 < z < 4$. Due to the use of lensing, these galaxies tend to be more representative of the population as a whole than those accessible to unlensed work, with stellar masses in the range $M_* \sim 4 \times 10^8 - 6 \times 10^{10}\mathrm{M}_\odot$ and dust-corrected star formation rates derived from Hα (or Hβ) SFR$\sim 0.8 - 40\mathrm{M}_\odot\mathrm{yr}^{-1}$.

Of the sample, 65% were shown to have velocity profiles indicative of rotation, centrally-peaked velocity dispersion profiles and sufficiently high v/σ to be classed as possible rotating discs. Of the remainder, 29% have disturbed profiles that may be indicative of merging or interacting systems. There is one galaxy we class as 'dispersion-dominated,' though we note that we may not have observed the full velocity gradient in this galaxy. For comparison, unlensed surveys tend to find approximately equal splits between rotating disks, dispersion-dominated galaxies and mergers, although increasing spatial resolution with adaptive optics systems is beginning to demonstrate that many galaxies classified as dispersion-dominated turn out to be rotating when observed at higher resolution where beam-smearing does not contribute so significantly to the velocity dispersion. This highlights the importance of understanding the effect of spatial resolution when measuring galaxy kinematics.

The high resolution of the lensed observations also allowed us to extend previously-observed relationships to smaller galaxies. We show that the correlation between v/σ and M_* extends to low-mass galaxies, indicating that galaxy kinematics become more ordered as they build up stellar mass.

We find no convincing evidence for evolution in the stellar mass Tully-Fisher relation; the lensed galaxies are consistent with the relation observed at $z = 0$, though with considerable scatter. Due to the small sizes of the lensed galaxies as seen in nebular line emission, the dynamics are dominated by baryonic material.

We were also able to carry out a similar analysis to that in Chapter 3 of the star-forming clumps extracted from maps of the Hα or Hβ emission lines. A similar evolution in both the clump surface brightnesses and the luminosity functions to those seen in Chapter 3 were observed in these data, with the evolution now extending to $z > 3$. With the new IFS data, however, we were able to measure the kinematics directly, and we presented tentative evidence that the epicyclic frequency does evolve in line with the predictions from semi-analytic models, supporting the theoretical model presented in Chapter 3.

The IFS observations also allowed us to measure velocity dispersions in the clumps, but contrary to previous unlensed studies we did not observe any correlation within the lensed sample between velocity dispersion and either luminosity or size. This could indicate that the clumps are not virialised, or that there are resolution effects in the data, or a combination of the two.

We finished Chapter 5 by exploring the origin of the velocity dispersion in more detail. Using the high spatial resolution of the lensed data, we compared the disc surface density to the local velocity dispersion, and found that the velocity dispersion is not necessarily enhanced in dense or highly star-forming regions. We therefore concluded that the high velocity dispersion in high-redshift galaxies are probably driven by gravitational instabilities, although as these instabilities lead to star formation, there is likely to be a contribution from star formation feedback that does not remain localised to the star-forming region.

6.2 Future Work

The work presented in this thesis has demonstrated the potential of gravitationally lensed galaxies as a laboratory for probing the spatially resolved properties of distant galaxies. We conclude by discussing the future prospects for this work, and its implications for the future of high-resolution studies of high-redshift galaxies with the next generation of telescopes.

6.2.1 Further work with lensed galaxies

This work has concentrated on the star formation within lensed galaxies, but the wealth of data accumulated for the current sample presents a number of other opportunities to investigate other properties of these galaxies.

The first of these is the spatially-resolved metallicity properties. The author was involved in the pilot study of the metallicity gradient of MACSJ1149 (discussed in Chapters 3 and 5) by Yuan et al. (2011), and we intend to extend this work to the rest of the sample using the [Nii]/Hα or [Oiii]/Hβ metallicity indicators from the data presented in Chapter 5. The spatial distribution of metallicity can be used to differentiate between 'inside-out' and 'outside-in' formation scenarios, and probes the interplay of accretion, enrichment and outflows that together set the properties of the interstellar medium.

An additional prospect for expanding on the work on this sample lies in spatially resolved stellar population models. This has been explored with another pilot study on MACSJ1149 in which the author was involved, by Adamo et al. (2013). For those clusters with extensive multi-wavelength archival data, we can fit SEDs on a pixel-by-pixel basis to compare the stellar populations in different regions of the galaxy. We created crude stellar mass maps in Chapter 5 for the purpose of estimating the disk surface density, but a more robust mass map constructed with resolved stellar population synthesis modelling could be used to compare the distribution of stars to that of star formation. Work in this area with unlensed galaxies on $\sim$kpc scales has revealed that the distributions are not correlated, i.e. that star clusters are not coincident with star-forming clumps (Wuyts et al., 2012). With the lensed sample, we could test this on smaller spatial scales and in more representative galaxies.

We can also use spatially-resolved stellar population models in conjunction with the star formation properties presented in this thesis to estimate the ages of star-forming clumps. Simulations have predicted that these clumps should migrate towards the centre of the galaxy, where they combine to form bulges seen in present-day spirals (Bournaud et al., 2011; Ceverino et al., 2010; Dekel et al., 2009). Estimating the ages of the clumps is one means of testing whether they are sufficiently long-lived for this process to be possible. The distribution of ages with galactocentric radius may even provide evidence for the migration process in progress.

If the clumps are not sufficiently long-lived to migrate to the galaxy centre, one likely disruption process is feedback from star formation. Deep spectroscopy of unlensed star-forming galaxies shows evidence of a broad component to the emission lines in star-forming clumps, possibly indicative of a fast outflow (Genzel et al., 2011; Newman et al., 2012b). The signal-to-noise required for these broad components to be identified is higher than that of the data in Chapter 5, but could be achieved with additional observations of a small sample in order to explore the outflow hypothesis in less extreme star-forming galaxies.

Another opportunity for studying the outflows from star-forming galaxies lies in the absorption lines in the UV. One of the key results from spectroscopic surveys of Lyman Break Galaxies (LBGs) is that 'superwinds' (ISM material blueshifted by up to 400 km/s) are common (e.g. Pettini et al., 2001; Steidel et al., 2010). Further studies at a range of redshifts have found increasing evidence that outflows are driven by star formation (e.g. Erb et al., 2012; Martin et al., 2012), with an apparent 'threshold' of star formation surface density of $\Sigma_{\rm SFR} \sim 0.1$ $\rm M_{\odot}\,yr^{-1}kpc^{2}$ for the launch of outflows (Kornei et al., 2012), which is comparable to the surface densities of star-forming clumps in high-redshift galaxies (see Chapters 3 and 5).

Studies of outflows at high redshift have focused by necessity on integrated spectra. Whilst the bulk velocity of the outflows can be inferred from integrated spectroscopy alone, in order to constrain the mass (and hence kinetic energy) in the wind, spatial information is required. For example, where do the winds originate? Are they associated with star-forming regions, or are they decoupled from the galaxy? Does the outflowing material eventually fall back onto the galaxy, or is it injected into the intergalactic medium? Addressing these questions requires spatially-resolved spectroscopy on scales comparable to the star-forming regions.

Currently, prospects for this work are limited by the available observational facilities. In high-redshift galaxies, the UV absorption lines are observed in the optical region of the spectrum, where there are no adaptive optics corrections. Even with gravitationally-lensed galaxies, therefore, it is currently only possible to resolve these spectral lines on $\sim$kpc scales. However, this will change with the installation of the Multi Unit Spectroscopic Explorer (MUSE) on the VLT, an optical IFU with an adaptive optics (AO) system (Bacon et al., 2010). Once MUSE is operating with AO correction, combining its high spatial resolution with the magnification of gravitational lensing will provide a powerful probe of the spatial distribution of feedback processes of distant star-forming galaxies.

Throughout this thesis, we have noted the importance of gas fractions in governing galaxy evolution. In Chapters 3 and 5, we noted that the turbulent, gas-rich disks of high-redshift galaxies appear to be main driver of the intense star formation seen in distant clumpy galaxies. Yet, as discussed in Chapter 4, direct observations of the gas are challenging even with the benefit of gravitational lensing, and the evolution of gas fraction with redshift remains poorly constrained. With the Atacama Large Millimetre/submillimetre Array (ALMA) in full science operations, it should become possible to detect the CO emission in the current sample of lensed galaxies. This will enable us to better understand the Kennicutt-Schmidt law - which is assumed to be redshift-invariant throughout this thesis - and how the changing composition of the interstellar medium has influenced the evolution of star-forming galaxies.

There are also good prospects for increasing the sample size of lensed galaxies in the near future, with the *Hubble Space Telescope* Frontier Fields programme. This will take multiwavelength observations of six lensing clusters over the next three years, potentially enabling the detection of previously inaccessible galaxies at $5 < z < 10$.

Advances in facilities are also likely to revolutionise the field. Over the coming decade, the next generation of $\sim 30\,\mathrm{m}$ telescopes, with their increased light-gathering power and unprecedented spatial resolution, will offer significant advances over current facilities. In addition, the *James Webb Space Telescope (JWST)*, currently scheduled to launch in 2018, will offer increased sensitivity and spatial resolution in the near-infrared from space, and will offer the first space-based integral field unit.

6.2.2 The limitations of gravitational lensing

This thesis has demonstrated the power of gravitational lensing for making detailed observations of high-redshift galaxies that are inaccessible to current unlensed surveys. However, there are a number of difficulties associated with the use of lensed galaxies.

One notable difficulty is the amount of observing time required. The lenses must first be located from existing surveys, and then spectroscopy of as many lensed arcs as possible is required in order to model the mass of the foreground cluster. Only then can the detailed observations of the target lensed galaxy be made. Analysis is then complicated by the need to reconstruct the source-plane image of the galaxy.

The time investment required means that the sample size is, by necessity, extremely limited, with the sample presented in this thesis representing the largest selection of lensed galaxies with spatially resolved studies compiled to date. The sample is subject to selection effects that are difficult to quantify, as the intrinsic magnitude limit is dependent on the magnification of the foreground cluster.

There are also additional sources of error inherent in studies of lensed galaxies due to uncertainty in the modelling of the mass distribution of the lensing cluster.

We have quantified the error in magnification in this thesis as typically $20-30\,\%$ over the whole galaxies, but in practice these errors will vary across the galaxy images, with errors in the immediate vicinity of critical lines likely much higher.

Finally, one of the largest sources of difficulty for the spatially resolved studies presented in Chapters 3 and 4 is that the magnification acts preferentially in one direction. This leads to a distorted, elliptical effective PSF in the source plane. In the most extreme cases, improved resolution is only achieved along one axis. We have sought to account for this throughout this work, but it does inevitably introduce additional uncertainties into any morphological analysis. To compound the problem, the galaxies with the most asymmetric magnifications are the ones that appear as the most extended arcs on the sky, and are thus more likely to be identified as lensed and selected for follow-up.

The only means of entirely eliminating the problems associated with gravitational lensing is to achieve the same depth and spatial resolution in unlensed sources, which requires large telescopes. The next generation of $\sim 30\,\mathrm{m}$ telescopes (the European Extremely Large Telescope (E-ELT), the Giant Magellan Telescope (GMT) and the Thirty Metre Telescope (TMT)) can theoretically offer a $\sim 4\times$ improvement in spatial resolution accompanied by a $> 10\times$ increase in light-gathering area. Within the next decade, therefore, it should become possible to carry out the kind of analysis detailed in this thesis on unlensed galaxies. This will enable us to place this work in proper context, and to understand the detailed properties of galaxies in an unprecedented level of detail.

6.3 Conclusions

In this thesis, we have harnessed the power of gravitational lensing to study the star formation in high-redshift galaxies. By taking advantage of the magnification of distant sources by foreground lensing clusters, We have shown that although the most distant galaxies appear very different to those found locally, with irregular, clumpy morphologies, they can be explained by the same physics that govern star formation in the local Universe.

The next steps are to expand this work into other observable features of the lensed galaxies, such as metallicity gradients and outflows. In the long term, the next generation of telescopes on the ground and in space will potentially open up the general, unlensed population to observations in the level of detail that are currently possible only in lensed cases. As such, this work has acted as a preview of the capabilities of the extremely large telescopes of the future.

Bibliography

Adamo A., Östlin G., Bastian N., Zackrisson E., Livermore R. C., Guaita L., 2013, ApJ, 766, 105

Alpher R. A., Herman R., 1948, Nature, 162, 774

Alpher R. A., Herman R., Gamow G. A., 1948, Physical Review, 74, 1198

Arp H., 1966, ApJS, 14, 1

Arsenault R., Roy J.-R., Boulesteix J., 1990, A&A, 234, 23

Baade W., 1938, ApJ, 88, 285

Babcock H. W., 1939, Lick Observatory Bulletin, 19, 41

Bacon R. et al., 2010, in Society of Photo-Optical Instrumentation Engineers (SPIE) Conference Series.

Baker A. J., Tacconi L. J., Genzel R., Lehnert M. D., Lutz D., 2004, ApJ, 604, 125

Baldry I. K., Glazebrook K., 2003, ApJ, 593, 258

Baldry I. K., Glazebrook K., Brinkmann J., Ivezić Ž., Lupton R. H., Nichol R. C., Szalay A. S., 2004, ApJ, 600, 681

Bartelmann M., Schneider P., 2001, Phys. Rep., 340, 291

Bastian N., Emsellem E., Kissler-Patig M., Maraston C., 2006, A&A, 445, 471

Baugh C. M., Cole S., Frenk C. S., 1996, MNRAS, 283, 1361

Begelman M. C., Shlosman I., 2009, ApJ, 702, L5

Benson A. J., 2012, New Astronomy, 17, 175

Benson A. J., Bower R. G., Frenk C. S., Lacey C. G., Baugh C. M., Cole S., 2003, ApJ, 599, 38

Bessel F. W., 1838, MNRAS, 4, 152

Blair A., 1990, Journal of the History of Ideas, 51, 355

Blanton M. R. et al., 2003, ApJ, 594, 186

Bordalo V., Telles E., 2011, ApJ, 735, 52

Bothwell M. S. et al., 2013, MNRAS, 429, 3047

Boulting W., 1972, Giordano Bruno: his life, thought and martyrdom. Arno Pr

Bournaud F. et al., 2011, ApJ, 730, 4

Bournaud F., Dekel A., Teyssier R., Cacciato M., Daddi E., Juneau S., Shankar F., 2011, ApJ, 741, L33

Bournaud F., Elmegreen B. G., 2009, ApJ, 694, L158

Bournaud F., Elmegreen B. G., Teyssier R., Block D. L., Puerari I., 2010, MNRAS, 409, 1088

Bower R. G., Benson A. J., Malbon R., Helly J. C., Frenk C. S., Baugh C. M., Cole S., Lacey C. G., 2006, MNRAS, 370, 645

Branch D., Tammann G. A., 1992, ARA&A, 30, 359

Burgers J. M., 1974, The Nonlinear Diffusion Equation. D. Reidal Publishing Co.

Burkert A. et al., 2010, ApJ, 725, 2324

Carilli C. L. et al., 2010, ApJ, 714, 1407

Carman C. C., 2009, Arch. Hist. Exact Sci., 63, 205

Ceverino D., Dekel A., Bournaud F., 2010, MNRAS, 404, 2151

Ceverino D., Dekel A., Mandelker N., Bournaud F., Burkert A., Genzel R., Primack J., 2012, MNRAS, 420, 3490

Chabrier G., 2003, PASP, 115, 763

Chandrasekhar S., 1931, ApJ, 74, 81

Christianidis J., Dialetis D., Gavroglu K., 2002, History of Science, 40, 147

Coe D., Fuselier E., Benítez N., Broadhurst T., Frye B., Ford H., 2008, ApJ, 681, 814

Colgate S. A., 1979, ApJ, 232, 404

Combes F. et al., 2012, A&A, 538, L4

Conselice C. J., Bundy K., Ellis R. S., Brichmann J., Vogt N. P., Phillips A. C., 2005, ApJ, 628, 160

Coppin K. E. K. et al., 2010, MNRAS, 407, L103

Coppin K. E. K. et al., 2007, ApJ, 665, 936

Couch W. J., Barger A. J., Smail I., Ellis R. S., Sharples R. M., 1998, ApJ, 497, 188

Courteau S., 1997, AJ, 114, 2402

Cowie L. L., Hu E. M., Songaila A., 1995, AJ, 110, 1576

Cox P. et al., 2011, ApJ, 740, 63

Crain R. A. et al., 2009, MNRAS, 399, 1773

Cresci G., Davies R. I., Baker A. J., Mannucci F., Lehnert M. D., Totani T., Minowa Y., 2006, A&A, 458, 385

Cresci G. et al., 2009, ApJ, 697, 115

Croton D. J. et al., 2006, MNRAS, 365, 11

Daddi E. et al., 2010a, ApJ, 713, 686

Daddi E. et al., 2010b, ApJ, 714, L118

Danielson A. L. R. et al., 2011, MNRAS, 410, 1687

Danver C.-G., 1942, Annals of the Observatory of Lund, 10, 3

Davies L. J. M., Bremer M. N., Stanway E. R., Birkinshaw M., Lehnert M. D., 2010, MNRAS, 408, L31

de Vaucouleurs G., 1972, in Evans D. S., Wills D., Wills B. J., eds, IAU Symposium Vol. 44, External Galaxies and Quasi-Stellar Objects. p. 353

Dekel A., Sari R., Ceverino D., 2009, ApJ, 703, 785

Dicke R. H., Peebles P. J. E., Roll P. G., Wilkinson D. T., 1965, ApJ, 142, 414

Dickinson M., Papovich C., Ferguson H. C., Budavári T., 2003, ApJ, 587, 25

Dobbs C. L., Burkert A., Pringle J. E., 2011, MNRAS, 413, 2935

Domínguez A. et al., 2013, ApJ, 763, 145

Dressler A., 1980, ApJ, 236, 351

Dressler A. et al., 1997, ApJ, 490, 577

Dutton A. A. et al., 2011, MNRAS, 410, 1660

Dyson F. W., Eddington A. S., Davidson C., 1920, Royal Society of London Philosophical Transactions Series A, 220, 291

Eastwood B. S., 2001, Journal for the History of Astronomy, 32, 281

Ebeling H., Barrett E., Donovan D., Ma C.-J., Edge A. C., van Speybroeck L., 2007, ApJ, 661, L33

Ebeling H., Edge A. C., Bohringer H., Allen S. W., Crawford C. S., Fabian A. C., Voges W., Huchra J. P., 1998, MNRAS, 301, 881

Ebeling H., Edge A. C., Henry J. P., 2001, ApJ, 553, 668

Ebeling H., Edge A. C., Mantz A., Barrett E., Henry J. P., Ma C. J., van Speybroeck L., 2010, MNRAS, 407, 83

Eggen O. J., Lynden-Bell D., Sandage A. R., 1962, ApJ, 136, 748

Einstein A., 1916, Annalen der Physik, 354, 769

Eisenhauer F. et al., 2003, in Iye M., Moorwood A. F. M., eds, Society of Photo-Optical Instrumentation Engineers (SPIE) Conference Series Vol. 4841, Society of Photo-Optical Instrumentation Engineers (SPIE) Conference Series. pp 1548–1561

Elmegreen B. G., Burkert A., 2010, ApJ, 712, 294

Elmegreen B. G., Elmegreen D. M., 2005, ApJ, 627, 632

Elmegreen B. G., Elmegreen D. M., Fernandez M. X., Lemonias J. J., 2009, ApJ, 692, 12

Elmegreen B. G., Elmegreen D. M., Hirst A. C., 2004, ApJ, 612, 191

Elmegreen D. M., Elmegreen B. G., Ravindranath S., Coe D. A., 2007, ApJ, 658, 763

Elmegreen D. M., Elmegreen B. G., Sheets C. M., 2004, ApJ, 603, 74

Epinat B. et al., 2009, A&A, 504, 789

Epinat B. et al., 2012, A&A, 539, A92

Erb D. K., Quider A. M., Henry A. L., Martin C. L., 2012, ApJ, 759, 26

Fall S. M., Efstathiou G., 1980, MNRAS, 193, 189

Feast M., Whitelock P., 1997, MNRAS, 291, 683

Fitzpatrick R., , 2010, A Modern Almagest, `http://farside.ph.utexas.edu/books/Syntaxis/Syntaxis.html`

Flores H., Hammer F., Puech M., Amram P., Balkowski C., 2006, A&A, 455, 107

Forman W., Jones C., Tucker W., 1985, ApJ, 293, 102

Förster Schreiber N. M. et al., 2009, ApJ, 706, 1364

Förster Schreiber N. M. et al., 2006, ApJ, 645, 1062

Förster Schreiber N. M., Shapley A. E., Erb D. K., Genzel R., Steidel C. C., Bouché N., Cresci G., Davies R., 2011, ApJ, 731, 65

Förster Schreiber N. M. et al., 2011, ApJ, 739, 45

Franx M., Illingworth G. D., Kelson D. D., van Dokkum P. G., Tran K., 1997, ApJ, 486, L75

Freedman W. L. et al., 2001, ApJ, 553, 47

Fu J., Guo Q., Kauffmann G., Krumholz M. R., 2010, MNRAS, 409, 515

Fuentes-Masip O., Muñoz-Tuñón C., Castañeda H. O., Tenorio-Tagle G., 2000, AJ, 120, 752

Gamow G., 1954, AJ, 59, 200

Garn T. et al., 2010, MNRAS, 402, 2017

Geach J. E., Smail I., Moran S. M., MacArthur L. A., Lagos C. d. P., Edge A. C., 2011, ApJ, 730, L19+

Genel S., Dekel A., Cacciato M., 2012, MNRAS, 425, 788

Genzel R. et al., 2008, ApJ, 687, 59

Genzel R. et al., 2011, ApJ, 733, 101

Genzel R. et al., 2006, Nature, 442, 786

Gershtein S. S., Zel'dovich Y. B., 1966, Soviet Journal of Experimental and Theoretical Physics Letters, 4, 120

Gilbank D. G., Baldry I. K., Balogh M. L., Glazebrook K., Bower R. G., 2010, MNRAS, 405, 2594

Gingerich O., 1972, QJRAS, 13, 346

Gingerich O., 2004, The book nobody read : chasing the revolutions of Nicolaus Copernicus. New York, NY: Walker

Gingerich O., 2005, in Turatto M., Benetti S., Zampieri L., Shea W., eds, Astronomical Society of the Pacific Conference Series Vol. 342, 1604-2004: Supernovae as Cosmological Lighthouses. p. 3

Gini C., 1912, Memorie di metodologia statistica

Glazebrook K., 2013, astro-ph/1305.2469

Gnerucci A. et al., 2011, A&A, 528, A88

Goldstein B. R., 1967, Transactions of the American Philosophical Society, 57, 3

Goldstein B. R., 2002, Journal for the History of Astronomy, 33, 219

Gonzalez J. E., Lacey C. G., Baugh C. M., Frenk C. S., Benson A. J., 2011, ArXiv e-prints

Gonzalez Delgado R. M., Perez E., 1997, ApJS, 108, 199

Gott III J. R., Thuan T. X., 1976, ApJ, 204, 649

Granada M. A., 2008, Journal for the History of Astronomy, 39, 469

Graney C. M., 2012, Journal for the History of Astronomy, 43, 215

Green A. W. et al., 2010, Nature, 467, 684

Guilloteau S. et al., 1992, A&A, 262, 624

Guilloteau S., Lucas R., 2000, in J. G. Mangum & S. J. E. Radford ed., Astronomical Society of the Pacific Conference Series Vol. 217, Imaging at Radio through Submillimeter Wavelengths. p. 299

Gushee V., 1941, The History of Science Society, 33, 197

Hall A. R., Hall M. B., 1978, Unpublished scientific papers of Isaac Newton: a selection from the Portsmouth collection in the University Library, Cambridge.. Cambridge (UK): Cambridge Univ. Press

Herschel W., 1785, Philosophical Transactions of the Royal Society of London, pp 213–266

Herschel W., 1786, Royal Society of London Philosophical Transactions Series I, 76, 457

Herschel W., 1791, Royal Society of London Philosophical Transactions Series I, 81, 71

Hertzsprung E., 1913, Astronomische Nachrichten, 196, 201

Hopkins A. M., 2004, ApJ, 615, 209

Hopkins A. M., Beacom J. F., 2006, ApJ, 651, 142

Hopkins P. F., 2012, MNRAS, 423, 2016

Hopkins P. F., Quataert E., Murray N., 2011, MNRAS, 417, 950

Hopkins P. F., Quataert E., Murray N., 2012, MNRAS, 421, 3488

Hoskin M. A., 1976, Journal for the History of Astronomy, 7, 169

Hoyle F., 1948, MNRAS, 108, 372

Hoyle F., Narlikar J. V., 1962, The Observatory, 82, 13

Hubble E., 1929, Proceedings of the National Academy of Science, 15, 168

Hubble E. P., 1925, The Observatory, 48, 139

Hubble E. P., 1926, ApJ, 64, 321

Hubble E. P., 1936, Realm of the Nebulae. New Haven: Yale University Press

Ivison R. J., Papadopoulos P. P., Smail I., Greve T. R., Thomson A. P., Xilouris E. M., Chapman S. C., 2011, MNRAS, pp 46–+

Ivison R. J., Smail I., Papadopoulos P. P., Wold I., Richard J., Swinbank A. M., Kneib J., Owen F. N., 2010, MNRAS, 404, 198

Jeans J., 1928, Astronomy and cosmogony. Dover Publications

Johnson F. R., Larkey S. V., Digges T., 1934, The Huntingdon Library Bulletin, 5, 69

Jones K. G., 1991, Pract. Astron. Handb., Vol. 2,, 2

Jones T., Ellis R., Jullo E., Richard J., 2010, ApJ, 725, L176

Jones T. A., Swinbank A. M., Ellis R. S., Richard J., Stark D. P., 2010, MNRAS, 404, 1247

Jullo E., Kneib J., Limousin M., Elíasdóttir Á., Marshall P. J., Verdugo T., 2007, New Journal of Physics, 9, 447

Jullo E., Kneib J.-P., 2009, MNRAS, 395, 1319

Kahn F. D., Woltjer L., 1959, ApJ, 130, 705

Kant I., 1755, Allgemeine Naturgeschichte und Theorie des Himmels. Zeitz, Bei W. Webel, 1798. Neue aufl.

Kassin S. A. et al., 2012, ApJ, 758, 106

Kassin S. A. et al., 2007, ApJ, 660, L35

Kennicutt Jr. R. C., 1988, ApJ, 334, 144

Kennicutt Jr. R. C., 1998a, ARA&A, 36, 189

Kennicutt Jr. R. C., 1998b, ApJ, 498, 541

Kennicutt Jr. R. C. et al., 2003, PASP, 115, 928

Kennicutt Jr. R. C., Edgar B. K., Hodge P. W., 1989, ApJ, 337, 761

Kneib J., 1993, PhD thesis, Ph. D. thesis, Université Paul Sabatier, Toulouse, (1993) Kneib J., Neri R., Smail I., Blain A., Sheth K., van der Werf P., Knudsen K. K., 2005, A&A, 434, 819

Knop R. A. et al., 2003, ApJ, 598, 102

Knudsen K. K., van der Werf P. P., Kneib J., 2008, MNRAS, 384, 1611

Koekemoer A. M., Fruchter A. S., Hook R. N., Hack W., 2002, in S. Arribas, A. Koekemoer, & B. Whitmore ed., The 2002 HST Calibration Workshop : Hubble after the Installation of the ACS and the NICMOS Cooling System. p. 337

Kokowski M., ed. 2006, Ptolemy, Copernicus and Kepler on linear distances

Korchagin V. I., Girard T. M., Borkova T. V., Dinescu D. I., van Altena W. F., 2003, AJ, 126, 2896

Kornei K. A., Shapley A. E., Martin C. L., Coil A. L., Lotz J. M., Schiminovich D., Bundy K., Noeske K. G., 2012, ApJ, 758, 135

Korngut P. M. et al., 2011, ApJ, 734, 10

Kowal C. T., 1968, AJ, 73, 1021

Kroupa P., 2001, MNRAS, 322, 231

Krumholz M. R., Dekel A., 2010, MNRAS, 406, 112

Lada C. J., Lombardi M., Alves J. F., 2010, ApJ, 724, 687

Lagos C. d. P., Bayet E., Baugh C. M., Lacey C. G., Bell T. A., Fanidakis N., Geach J. E., 2012, MNRAS, 426, 2142

Law D. R., Steidel C. C., Erb D. K., Larkin J. E., Pettini M., Shapley A. E., Wright S. A., 2009, ApJ, 697, 2057

Law D. R., Steidel C. C., Erb D. K., Pettini M., Reddy N. A., Shapley A. E., Adelberger K. L., Simenc D. J., 2007, ApJ, 656, 1

Leavitt H. S., 1908, Annals of Harvard College Observatory, 60, 87

Leavitt H. S., Pickering E. C., 1912, Harvard College Observatory Circular, 173, 1

Lehnert M. D., Le Tiran L., Nesvadba N. P. H., van Driel W., Boulanger F., Di Matteo P., 2013, astro-ph/1304.7734

Lehnert M. D., Nesvadba N. P. H., Le Tiran L., Di Matteo P., van Driel W., Douglas L. S., Chemin L., Bournaud F., 2009, ApJ, 699, 1660

Leroy A. K., Walter F., Brinks E., Bigiel F., de Blok W. J. G., Madore B., Thornley M. D., 2008, AJ, 136, 2782

Lilly S. J., Le Fevre O., Hammer F., Crampton D., 1996, ApJ, 460, L1+

Limousin M. et al., 2007, ApJ, 668, 643

Livermore R. C. et al., 2012a, MNRAS, 427, 688

Livermore R. C. et al., 2012b, ApJ, 758, L35

Lynds R., Petrosian V., 1986, in Bulletin of the American Astronomical Society. p. 1014

Lyubimov V. A., Novikov E. G., Nozik V. Z., Tretyakov E. F., Kosik V. S., 1980, Phys. Lett., B94, 266

Madau P., Ferguson H. C., Dickinson M. E., Giavalisco M., Steidel C. C., Fruchter A., 1996, MNRAS, 283, 1388

Maraston C., 2005, MNRAS, 362, 799

Martin C. L., Shapley A. E., Coil A. L., Kornei K. A., Bundy K., Weiner B. J., Noeske K. G., Schiminovich D., 2012, ApJ, 760, 127

McCarthy I. G., Schaye J., Font A. S., Theuns T., Frenk C. S., Crain R. A., Dalla Vecchia C., 2012, MNRAS, 427, 379

McConnachie A. W., Irwin M. J., Ferguson A. M. N., Ibata R. A., Lewis G. F., Tanvir N., 2005, MNRAS, 356, 979

McGregor P. J. et al., 2003, in Iye M., Moorwood A. F. M., eds, Society of Photo-Optical Instrumentation Engineers (SPIE) Conference Series Vol. 4841, Society of Photo-Optical Instrumentation Engineers (SPIE) Conference Series. pp 1581–1591

McKellar A., 1941, Publications of the Dominion Astrophysical Observatory Victoria, 7, 251

McLure R. J., Cirasuolo M., Dunlop J. S., Foucaud S., Almaini O., 2009, MNRAS, 395, 2196

Messier C., 1781, Connoissance des Temps for 1784, pp 227–267

Miller S. H., Bundy K., Sullivan M., Ellis R. S., Treu T., 2011, ApJ, 741, 115

Miller S. H., Ellis R. S., Sullivan M., Bundy K., Newman A. B., Treu T., 2012, ApJ, 753, 74

Miller S. H., Sullivan M., Ellis R. S., 2013, ApJ, 762, L11

Mo H. J., Mao S., White S. D. M., 1998, MNRAS, 295, 319

Murray N., Ménard B., Thompson T. A., 2011, ApJ, 735, 66

Nakamura O., Fukugita M., Yasuda N., Loveday J., Brinkmann J., Schneider D. P., Shimasaku K., SubbaRao M., 2003, AJ, 125, 1682

Neri R. et al., 2003, ApJ, 597, L113

Nesvadba N. P. H. et al., 2006, ApJ, 650, 661

Nesvadba N. P. H. et al., 2007, ApJ, 657, 725

Newman S. F. et al., 2012a, ApJ, 761, 43

Newman S. F. et al., 2013, ApJ, 767, 104

Newman S. F. et al., 2012b, ApJ, 752, 111

Nichol J. P., 1846, Thoughts on some important points relating to the system of the world.. Edinburgh, W. Tait

Noll S., Burgarella D., Giovannoli E., Buat V., Marcillac D., Muñoz-Mateos J. C., 2009, A&A, 507, 1793

Norgaard-Nielsen H. U., Hansen L., Jorgensen H. E., Aragon Salamanca A., Ellis R. S., Couch W. J., 1989, Nature, 339, 523

Oort J. H., 1940, ApJ, 91, 273

Ostriker E. C., Shetty R., 2011, ApJ, 731, 41

Ostriker J. P., Peebles P. J. E., 1973, ApJ, 186, 467

Ouchi M. et al., 2004, ApJ, 611, 660

Partridge R. B., 1980, Phys. Scr, 21, 624

Patel S. G. et al., 2013, astro-ph/1304.2395

Peebles P. J. E., 1982, ApJ, 263, L1

Pello R., Sanahuja B., Le Borgne J.-F., Soucail G., Mellier Y., 1991, ApJ, 366, 405

Penzias A. A., Wilson R. W., 1965, ApJ, 142, 419

Perlmutter S. et al., 1999, ApJ, 517, 565

Perlmutter S., Schmidt B. P., 2003, in Weiler K., ed., Lecture Notes in Physics, Berlin Springer Verlag Vol. 598, Supernovae and Gamma-Ray Bursters. pp 195–217

Pettini M., Shapley A. E., Steidel C. C., Cuby J., Dickinson M., Moorwood A. F. M., Adelberger K. L., Giavalisco M., 2001, ApJ, 554, 981

Pizagno J. et al., 2005, ApJ, 633, 844

Planck Collaboration et al., 2013a, astro-ph/1303.5062

Planck Collaboration et al., 2013b, astro-ph/1303.5076

Prickard A. O., 1911, Plutarch on the face which appears on the orb of the Moon. Winchester: Warren and Son

Puech M. et al., 2008, A&A, 484, 173

Pumfrey S., 2011, The British Journal for the History of Science, 44, 29

Rafikov R. R., 2001, MNRAS, 323, 445

Richard J., Jones T., Ellis R., Stark D. P., Livermore R., Swinbank M., 2011, MNRAS, 413, 643

Richard J. et al., 2007, ApJ, 662, 781

Richard J. et al., 2010, MNRAS, 404, 325

Richard J., Stark D. P., Ellis R. S., George M. R., Egami E., Kneib J., Smith G. P., 2008, ApJ, 685, 705

Riechers D. A. et al., 2010, ApJ, 720, L131

Riechers D. A., Carilli C. L., Walter F., Momjian E., 2010, ApJ, 724, L153

Riechers D. A. et al., 2011, ApJ, 733, L12+

Riechers D. A., Hodge J., Walter F., Carilli C. L., Bertoldi F., 2011, ApJ, 739, L31

Riess A. G. et al., 1998, AJ, 116, 1009

Roberts M. S., Haynes M. P., 1994, ARA&A, 32, 115

Roberts M. S., Whitehurst R. N., 1975, ApJ, 201, 327

Rodríguez-Zaurín J., Arribas S., Monreal-Ibero A., Colina L., Alonso-Herrero A., Alfonso-Garzón J., 2011, A&A, 527, A60+

Romeo A. B., Wiegert J., 2011, MNRAS, 416, 1191

Ronan C. A., 1991, Journal of the British Astronomical Association, 101, 335

Rosen E., 1965, Kepler's Conversation with Galileo's Sidereal Messenger. Johnson Reprint Corporation

Rozas M., Richer M. G., López J. A., Relaño M., Beckman J. E., 2006, A&A, 455, 539

Rozas M., Sabalisck N., Beckman J. E., 2001, Ap&SS, 276, 413

Rubin V. C., Ford Jr. W. K., 1970, ApJ, 159, 379

Rubin V. C., Ford W. K. J., . Thonnard N., 1980, ApJ, 238, 471

Salpeter E. E., 1955, ApJ, 121, 161

Sand D. J., Treu T., Ellis R. S., Smith G. P., 2005, ApJ, 627, 32

Sandage A., 1962, in McVittie G. C., ed., IAU Symposium Vol. 15, Problems of Extra-Galactic Research. p. 359

Sandage A., 1989, JRASC, 83, 351

Sandage A., 1999, ApJ, 527, 479

Sandage A., Sandage M., Kristian J., 1975, Galaxies and the universe. Stars and Stellar Systems, University of Chicago Press

Sanders D. B., Scoville N. Z., Soifer B. T., 1991, ApJ, 370, 158

Sanders D. B., Solomon P. M., Scoville N. Z., 1984, ApJ, 276, 182

Sawyer Hogg H., 1952, JRASC, 46, 195

Scalo J. M., 1986, Fund. Cosmic Phys., 11, 1

Schmidt W., Federrath C., Hupp M., Kern S., Niemeyer J. C., 2009, A&A, 494, 127

Shapley H., 1919, ApJ, 49, 311

Shapley H., Shapley M. B., 1919, ApJ, 50, 107

Shen S., Mo H. J., White S. D. M., Blanton M. R., Kauffmann G., Voges W., Brinkmann J., Csabai I., 2003, MNRAS, 343, 978

Slipher V. M., 1917, Proceedings of the American Philosophical Society, 56, 403

Smith G. P. et al., 2009, ApJ, 707, L163

Smith G. P., Treu T., Ellis R. S., Moran S. M., Dressler A., 2005, ApJ, 620, 78

Smith S., 1936, ApJ, 83, 23

Smoot G. F. et al., 1992, ApJ, 396, L1

Sobral D., Best P. N., Matsuda Y., Smail I., Geach J. E., Cirasuolo M., 2012a, MNRAS, 420, 1926

Sobral D., Best P. N., Matsuda Y., Smail I., Geach J. E., Cirasuolo M., 2012b, MNRAS, 420, 1926

Solomon P. M., Downes D., Radford S. J. E., Barrett J. W., 1997, ApJ, 478, 144

Solomon P. M., Vanden Bout P. A., 2005, ARA&A, 43, 677

Soucail G., Fort B., Mellier Y., Picat J. P., 1987, A&A, 172, L14

Stanway E. R., Bremer M. N., Davies L. J. M., Birkinshaw M., Douglas L. S., Lehnert M. D., 2008, ApJ, 687, L1

Stark A. A., Lee Y., 2006, ApJ, 641, L113

Stark D. P., Ellis R. S., Bunker A., Bundy K., Targett T., Benson A., Lacy M., 2009, ApJ, 697, 1493

Stark D. P., Ellis R. S., Chiu K., Ouchi M., Bunker A., 2010, MNRAS, 408, 1628

Stark D. P., Swinbank A. M., Ellis R. S., Dye S., Smail I. R., Richard J., 2008, Nature, 455, 775

Steidel C. C., Erb D. K., Shapley A. E., Pettini M., Reddy N., Bogosavljević M., Rudie G. C., Rakic O., 2010, ApJ, 717, 289

Stephenson B., ed. 1987, Kepler's physical astronomy Studies in the History of Mathematics and Physical Sciences Vol. 13. New York, Springer-Verlag

Storey P. J., Zeippen C. J., 2000, MNRAS, 312, 813

Struck-Marcell C., Tinsley B. M., 1978, ApJ, 221, 562

Swinbank A. M., Bower R. G., Smith G. P., Smail I., Kneib J., Ellis R. S., Stark D. P., Bunker A. J., 2006, MNRAS, 368, 1631

Swinbank A. M., Bower R. G., Smith G. P., Wilman R. J., Smail I., Ellis R. S., Morris S. L., Kneib J., 2007, MNRAS, 376, 479

Swinbank A. M. et al., 2011, ApJ, 742, 11

Swinbank A. M., Smail I., Sobral D., Theuns T., Best P. N., Geach J. E., 2012, ApJ, 760, 130

Swinbank A. M., Sobral D., Smail I., Geach J. E., Best P. N., McCarthy I. G., Crain R. A., Theuns T., 2012, MNRAS, 426, 935

Swinbank A. M. et al., 2009, MNRAS, 400, 1121

Tacconi L. J. et al., 2010, Nature, 463, 781

Tammann G. A., 1979, Mitteilungen der Astronomischen Gesellschaft Hamburg, 46, 10

Terlevich R., Melnick J., 1981, MNRAS, 195, 839

Tonry J. L. et al., 2003, ApJ, 594, 1

Toomer G. J., 1974, Arch. Hist. Exact Sci., 14, 126

Toomer, G. J. 1998, Ptolemy's Almagest. Princeton University Press

Toomre A., 1964, ApJ, 139, 1217

Toomre A., Toomre J., 1972, ApJ, 178, 623

Trujillo I. et al., 2006, ApJ, 650, 18

Tully R. B., Fisher J. R., 1977, A&A, 54, 661

Vergani D. et al., 2012, A&A, 546, A118

Verma A., Lehnert M. D., Förster Schreiber N. M., Bremer M. N., Douglas L., 2007, MNRAS, 377, 1024

Vogt N. P., Forbes D. A., Phillips A. C., Gronwall C., Faber S. M., Illingworth G. D., Koo D. C., 1996, ApJ, 465, L15

Vogt N. P. et al., 1997, ApJ, 479, L121

Walter F. et al., 2012, Nature, 486, 233

Walter F., Weiß A., Riechers D. A., Carilli C. L., Bertoldi F., Cox P., Menten K. M., 2009, ApJ, 691, L1

Webb S., 1999, Measuring the Universe: The Cosmological Distance Ladder. Springer Praxis Books / Space Exploration, Springer

Whitaker K. E., van Dokkum P. G., Brammer G., Franx M., 2012, ApJ, 754, L29

White S. D. M., Frenk C. S., Davis M., 1983, ApJ, 274, L1

White S. D. M., Rees M. J., 1978, MNRAS, 183, 341

Williams J. P., de Geus E. J., Blitz L., 1994, ApJ, 428, 693

Williams R. J., Quadri R. F., Franx M., van Dokkum P., Toft S., Kriek M., Labbé I., 2010, ApJ, 713, 738

Wisnioski E., Glazebrook K., Blake C., Poole G. B., Green A. W., Wyder T., Martin C., 2012a, MNRAS, p. 2831

Wisnioski E., Glazebrook K., Blake C., Poole G. B., Green A. W., Wyder T., Martin C., 2012b, MNRAS, 422, 3339

Wisnioski E. et al., 2011, MNRAS, 417, 2601

Wolf M., 1908, Publikationen des Astrophysikalischen Instituts Koenigstuhl-Heidelberg, 3, 109

Wright S. A. et al., 2007, ApJ, 658, 78

Wright S. A., Larkin J. E., Law D. R., Steidel C. C., Shapley A. E., Erb D. K., 2009, ApJ, 699, 421

Wuyts S. et al., 2012, ApJ, 753, 114

Young J. S., Scoville N. Z., 1991, ARA&A, 29, 581

Yuan T.-T., Kewley L. J., Swinbank A. M., Richard J., Livermore R. C., 2011, ApJ, 732, L14+

Zel'dovich Y. B., 1970, A&A, 5, 84

Zwicky F., 1933, Helvetica Physica Acta, 6, 110

Zwicky F., 1937, ApJ, 86, 217